Thermodynamic simulation and exergy analysis of a hydrogen SI engine

A Thesis Submitted for the Degree of Doctor of Philosophy

 $\mathbf{B}\mathbf{y}$

Dardan Naim Rrustemi

 $\begin{tabular}{ll} Department of Mechanical and Aerospace Engineering, \\ Brunel University London \end{tabular}$

2024

This thesis is dedicated to my family.

Abstract

Concerns of limited fossil fuel reserves, environmental pollution from their extraction, processing, and use, and health effects from localised tailpipe emissions are leading to a transition of the transportation sector towards low-carbon and carbon-free alternative fuels for internal combustion engines. As an alternative fuel hydrogen has the potential to significantly reduce tailpipe greenhouse gas emissions, and offers advantages in terms of its combustion properties. To understand hydrogen combustion in an internal combustion engine and the upper limit of efficiency, single- and two-zone combustion models exploiting the second law of thermodynamics are developed to assess the origins of the exergy losses. The single-zone model provides detailed analysis of the boosted operation strategy, showing that thermal efficiency increases significantly for lean-burn hydrogen mixtures. Operating hydrogen engines at high loads presents challenges arising from combustion abnormalities as increasing intake air pressure raises in-cylinder temperature, significantly increasing knock occurrence and nitric oxide emissions. However, low-temperature combustion through lean-burn and water injection has potential to mitigate combustion abnormalities and reduce nitric oxide emissions; the addition of water modulates the rate at which combustion occurs. A newly developed laminar flame speed correlation for hydrogen-air combustion accounts for water addition under engine-relevant conditions. The applicability of this new correlation is demonstrated by incorporating this empirical correlation into a two-zone combustion model to predict engine performance, combustion abnormalities and nitric oxide emissions. The simulation of a water-diluted hydrogen engine indicates that emission control and knock mitigation are achievable, but requires careful optimization to avoid significant reducing thermal efficiency. The simulations allow the production of a hydrogen operational map based on the indicated specific fuel consumption, nitric oxide, thermal efficiency, equivalence ratio, and water addition. A comprehensive exergy analysis of a hydrogen engine evaluates efficiency, irreversibility, and emissions, quantifying losses for each engine condition: intake manifold air pressure, fuel mixture, compression ratio, water addition, and spark timing. This enables a discussion of the compromises for designing and managing hydrogen-fuelled SI engines at various operating conditions, including equivalence ratios, spark timings, compression ratio, and boosted manifold air pressure.

Acknowledgements

I would like to extend my gratitude to those who supported and guided me throughout my PhD pursuit. I am especially grateful to my supervisors, Dr. Colin Axon and Professor Lionel Ganippa, for their invaluable expertise, insightful feedback, and consistent encouragement. I would also like to thank my parents for their continuous support and for providing me the opportunity to study in the UK. Finally, I express my appreciation to all those who have directly or indirectly contributed to my academic and personal development. Your support and encouragement are greatly appreciated.

Contents

	List	of figur	res	vi
	List	of table	es	X
	Non	nenclati	ure	xi
1	Intr	oducti	ion	1
	1.1	Energ	y used in transportation	2
	1.2	Altern	native fuels	4
	1.3	Hydro	ogen as a fuel	5
	1.4	Aim a	and objectives	7
	1.5	Thesis	s outline	7
	1.6	Resear	rch contribution and novelty	8
2	${ m Lite}$	erature	e review	11
	2.1	Hydro	ogen use in engines	11
		2.1.1	Hydrogen port injection	12
		2.1.2	Hydrogen direct injection	13
	2.2	Therm	nal efficiency	14
		2.2.1	Boosted hydrogen engine	15
		2.2.2	Lean-burn hydrogen engine	17
		2.2.3	Hydrogen combustion abnormalities	18
		2.2.4	Water injection	20
	2.3	Hydro	ogen combustion model	21
		2.3.1	Hydrogen laminar flame speed correlation	23
		2.3.2	Heat transfer	25
	2.4	Exerg	v analysis of the ICE	26

	2.5	Summarising the research gaps	27
3	Me	thodology	29
	3.1	Single-zone combustion model	30
	3.2	Two-zone combustion model	32
		3.2.1 Mass fraction burned	36
	3.3	Heat transfer	44
	3.4	Auto-ignition delay time and knock	46
	3.5	NO emissions	47
	3.6	Physical and chemical exergy	48
		3.6.1 Exergy transfers	56
		3.6.2 Combined top-down and bottom-up exergy approach	57
4	Sin	ngle-zone model of a hydrogen SI engine	59
	4.1	Incorporating the laminar flame speed sub-model	59
	4.2	Validating the single-zone combustion model	63
	4.3	Hydrogen SI engine combustion performance	67
	4.4	Knock model	74
	4.5	Hydrogen engine load	77
	4.6	Indicated thermal efficiency and indicated specific fuel consumption $% \left(1\right) =\left(1\right) \left(1\right) +\left(1\right) \left(1\right) \left(1\right) +\left(1\right) \left($	81
	4.7	Nitric oxide emissions	85
	4.8	Mapping hydrogen SI engine	88
	4.9	Summary	90
5	Lan	ninar flame speed correlation	92
	5.1	Chemical kinetic simulations	93
	5.2	LFS correlation	97
	5.3	LFS correlation with water addition	100
	5.4	Hydrogen with water addition LFS at engine-relevant conditions	103
	5.5	Effect of water addition on LFS correlation	103
	5.6	Residual analysis	109
	5.7	Summary	112

6	An	improved and extended two-zone model to study the effect	of
	wat	ter dilution	113
	6.1	Model validation	. 113
		6.1.1 Comparing the performance of the single- and two-zone mode	els 116
	6.2	Hydrogen engine model performance	. 117
		6.2.1 Laminar flame speed at engine relevant conditions	. 118
		6.2.2 In-cylinder characteristics	. 120
	6.3	IMEP and ITE	. 126
	6.4	Indicated specific fuel consumption and NO emissions	. 129
	6.5	Knock prediction	. 130
	6.6	Hydrogen operating regimes	. 134
	6.7	Summary	. 137
7	Exe	ergy analysis of the lean-burn hydrogen SI engine	139
	7.1	Entropy generation	. 139
		7.1.1 Hydrogen SI engine exergy	. 142
		7.1.2 Effect of spark timing on exergetic processes	. 146
		7.1.3 MAP effect on the exergy split	. 148
		7.1.4 Compression ratio effect on the exergy split	. 149
		7.1.5 Low heat rejection effect on the exergy split	. 151
		7.1.6 Effect of water addition on the exergy split	. 152
	7.2	Combined top-down and bottom-up approach	. 156
	7.3	Summary	. 156
8	Cor	nclusions and future work	158
	8.1	Single-zone model	. 159
	8.2	Laminar flame speed correlation	. 160
	8.3	Two-zone model	. 163
	8.4	Understanding the fundamentals of ICE energy losses	. 164
	8.5	Limitations and future work	. 166
	Refe	erences	. 168

List of Figures

1.1	World transportation energy consumption by source	3
1.2	Production pathways of current and future fuels	5
2.1	Hydrogen injection and ignition strategies	12
2.2	Efficiency at different air and compression ratios	15
2.3	IMEP for lean hydrogen and stoichiometric gasoline	17
3.1	Zonal division in two-zone model	34
3.2	Zonal division in entrained combustion model	36
3.3	Turbulent length scales during intake	38
3.4	Turbulent kinetic energy with crank angle	41
3.5	Flame sphere and geometry illustration	43
3.6	Thermal system and environmental interaction	49
3.7	System, restricted dead state, and true dead state	55
3.8	Exergy analysis schematic	57
4.1	Laminar burning velocity of hydrogen-air mixture	62
4.2	Laminar flame speed of hydrogen at engine-relevant conditions	62
4.3	In-cylinder pressure and heat release rate of hydrogen-air mixture $$	65
4.4	IMEP and maximum in-cylinder pressure	66
4.5	Simulated and experimental fuel mass variation with MAP $\ \ldots \ \ldots$	66
4.6	In-cylinder pressure and AHRR at different boosting pressures	69
4.7	Maximum in-cylinder pressure at boosted and lean conditions $\ \ . \ \ . \ \ .$	70
4.8	Mass fraction burned profile with crank angle at MAP $\ \ldots \ \ldots \ \ldots$	72
49	Combustion duration for various λ and MAP values	73

4.10	Location of CA50 for various λ and MAP values	73
4.11	Location of CA50 at different loads for various λ and MAP values $$	74
4.12	Hydrogen autoignition delay at different temperatures and pressures $.$	76
4.13	Autoignition delay at different pressures, temperatures, and ϕ	76
4.14	Knock integral for different conditions and spark timings	77
4.15	IMEP variation with spark timing and MAP at $\lambda = 1.82$	79
4.17	IMEP variation with spark timing and λ	79
4.16	IMEP variation with spark timing.	80
4.18	Indicated thermal efficiency at various MAP and lean conditions	82
4.19	ISFC at different λ	83
4.20	ISFC at different λ and spark timings	84
4.21	ISFC at different λ and MAP	84
4.22	NO emissions at various λ and MAP	86
4.23	NO emissions at various λ and MAP	87
4.24	NO emissions at $\lambda=1.82$ for different spark timings and MAP values	87
4.25	NO emissions and thermal efficiency at different λ and spark timings	88
4.26	The operation of hydrogen SI engines	89
4.27	The operation of boosted hydrogen SI engines	90
5.1	Laminar burning velocities at various equivalence ratios	95
5.2	Hydrogen LFS with water addition at various equivalence ratios $\ . \ . \ .$	96
5.3	Chemical kinetic and correlation S_{l0} values	96
5.4	Alpha values at various $\phi,$ pressures, and temperatures for hydrogen .	100
5.5	Chemical kinetic and new correlation LFS values	101
5.6	Chemical kinetic and correlation LFS values with deviations	102
5.7	Comparison of chemical kinetic and correlation LFS values	105
5.8	Hydrogen LFS values with water additions at various pressures and ϕ	108
5.9	Hydrogen LFS values with water additions and operating conditions .	109
5.10	Standard error and residuals for the new LFS correlation	111
5.11	Residuals between chemical kinetics and correlation LFS	111
6.1	Simulated in-cylinder pressure vs. experimental values	114

0.2	Simulated in-cylinder pressure vs. experimental values for various
	heat transfer coefficients
6.3	Simulated in-cylinder pressure compared to experimental data 117
6.4	Hydrogen laminar flame speed values at different conditions 119
6.5	LFS values with equivalence ratios, temperature, and water addition . 120
6.6	In-cylinder pressure and AHRR for various ϕ and water additions 121
6.7	Maximum in-cylinder pressure at various ϕ and water additions 122
6.8	Maximum in-cylinder pressure of hydrogen at various ϕ and MAP $$ 123
6.9	Simulated IMEP with spark timings, equivalence ratios, and MAP 124
6.10	Simulated IMEP with spark timings and water additions 125
6.11	Simulated mass fraction burned profiles
6.12	IMEP at various MAP, water additions, and ϕ
6.13	ITE at various MAP, water additions, and ϕ
6.14	ISFC at various MAP, water additions, and ϕ
6.15	NO emissions at various MAP, water additions, and ϕ
6.16	Knock integral at various MAP and ϕ
6.17	Hydrogen autoignition delay time at various temperatures and ϕ 132
6.18	Knock integral at various water additions and ϕ
6.19	Hydrogen autoignition delay time with temperature and water additions 134
6.20	Hydrogen SI engine operation at 120 kPa with water addition 136
6.21	Boosted lean burn hydrogen SI engine operation with water addition 137
7.1	Entropy generation in hydrogen-fuelled SI engine
7.2	Entropy generation by combustion at ϕ of 0.9
7.3	In-cylinder exergy balance for ϕ of 0.9 and 0.45
7.4	Exergy split and NO emissions for various equivalence ratios 145
7.5	Exergy split and NO emissions for various spark timings 147
7.6	Exergy split and NO emissions for various MAP and ϕ
7.7	Compression ratio effect on exergy split and NO emissions 150
7.8	Exergy split for various ϕ and heat-loss percentages
7.9	Hydrogen/air chemical exergy with water additions

7.10	Exergy split for ϕ of 0.9 with water additions							153
7.11	Exergy split for a lean-burn hydrogen engine .							155

List of Tables

3.1	Constants for gas velocity model for different processes
4.1	Hydrogen LFS correlations from various studies 61
4.2	Simulated IMEP
4.3	SI engine specifications used in simulations
4.4	Operating conditions used for the simulations
4.5	Representative pressures used for each operating condition
5.1	Coefficients used in correlation
6.1	Conditions used in the hydrogen engine numerical model
7.1	Exergy balance for the case of ϕ of 0.90
A1	Pseudocode for single-zone combustion model
A2	Pseudocode for two-zone combustion model

Nomenclature

Acronyms

AFR Air/fuel ratio

AHRR Apparent heat release rate

aTDC After top dead centre

bTDC Before top dead centre

CA Crank angle

CA50 Location of 50% mass fraction burned

CI Compression ignition

CO₂ Carbon dioxide

CR Compression ratio

EGR Exhaust gas recirculation

EVO Exhaust valve opening

Exh Exhaust

H₂ Hydrogen

H₂O Water

ICE Internal combustion engine

IMEP Indicated mean effective pressure

ISFC Indicated specific fuel consumption

ITE Indicated thermal efficiency

IVC Intake valve closing

KI Knock integral

LFS Laminar flame speed

MAP Manifold air pressure (Pa)

MBT Minimum advance for best torque

MFB10-90 10-90% mass fraction burned

MFB50 50% mass fraction burned

NO Nitric oxide

NOx Oxides of nitrogen

N₂ Nitrogen

 O_2 Oxygen

RON Research octane number

SI Spark ignition

soc Start of combustion

ST Spark timing

TDC Top dead centre

TM Thermo-mechanical

Symbols

a, m Wiebe efficiency and form factors

b Burned

c Specific heat

f Fuel

h Specific enthalpy

i Species index

j Environmental species index

k Heat transfer coefficient

m Mass

N Engine speed

n Number of moles

P Pressure

Q Heat

R Universal gas constant

s Specific entropy

T In-cylinder temperature

U Internal energy

u Specific internal energy

v Specific volume

V Volume

W Work

X Exergy

 λ Excess air ratio

 μ Chemical potential

 σ Stefan-Boltzmann constant

 ϕ Equivalence ratio

Subscripts

0 Initial conditions

b Burned

Exh Exhaust

f Fuel

ht Heat transfer

i Species index

j Environmental species index

soc Start of combustion

Chapter 1

Introduction

The internal combustion engine (ICE) has played a significant role in shaping the modern world for almost a century and, for the foreseeable future, will remain the most widely used engine for transportation. As the global energy demand increases and oil reserves dwindle, the efficiency of ICEs must improve, and the emissions reduce from where they stand today. The international community agreed to reduce emissions due to human activity through the Paris Agreement [1] approved by 196 countries during the United Nations Climate Change Conference (COP21) in 2015. The primary objective is to restrict the rise in the global temperature to below 2°C above pre-industrial levels, later reduced to 1.5°C. To accomplish this, the agreement calls for greenhouse gas (GHG) emissions to peak by 2025 and then decrease by 43% by 2030, including emissions due to all forms of transport. The energy sector is the greatest contributor to GHG emissions, accounting for more than three-quarters of total GHG emissions [2].

In Europe, GHG emissions from the transportation sector increased steadily from 2013, accounting for approximately a quarter of the EU's overall GHG emissions in 2023. Although measures are in place, it is projected that road transport emissions will not decrease to the 1990 level until 2032 [3]. However, emissions from aviation and maritime are expected to keep increasing [4]. Road vehicles account for over two-thirds of EU transport-related emissions [5] and approximately 72% of the total emissions in the transportation sector worldwide [6]. Vehicle tailpipe emissions from directly combusting fossil fuels have health consequences [7]; therefore, using

alternative fuels may offer additional benefits to society.

The efficiency of the ICE in its different forms and systems has improved steadily. For stationary power plants, the efficiencies now exceed 60% [8], and by optimizing the heat recovery steam generator and integrating gas turbine reheat, the efficiency could exceed 65% [9]. Distributed power generation reduces grid losses while maintaining efficiencies above 50% of the lower heating value. For transportation, ICEs power approximately 99.8% globally, with around 95% of the energy delivered as liquid fuels derived from petroleum [10]. ICEs are projected to remain the dominant source of energy for transportation, accounting for 85-90\% of the total transportation sector by 2040 [11]. The energy efficiency of road vehicle ICEs is relatively low, typically around the low 40% range for spark-ignition engines and the low 50% range for compression-ignition engines [12]. The higher thermal efficiency of the CI engine compared to the SI engine is explained by the higher compression ratio of the CI engine. The CI engine operates with direct injection, which eliminates throttling losses [13]. Additionally, the diesel engine operates under lean burn conditions, which improves the specific heat ratio. In contrast, the conventional port-injected SI operating conditions are limited by combustion abnormalities, hence requiring lower compression ratios, and may suffer from throttling losses [14]. These factors reducze the engine thermal efficiency. However, hydrogen-fuelled SI engines can mitigate some of these limitations. Hydrogen's high flame speed allows for stable combustion with lean burn mixtures, and its wide flammability limits enable throttling losses to be reduced [15].

By using alternative fuel, it is claimed that ICEs may achieve efficiencies of up to 50% [11]. Nevertheless, continuous advancements in hybrid systems and waste heat recovery technologies may enhance these projected efficiencies.

1.1 Energy used in transportation

Worldwide, the transportation sector accounts for a fifth of total energy use and carbon dioxide emissions. This is projected to remain constant until 2050, even though the energy consumption is increasing each year, although the ratio of fossil

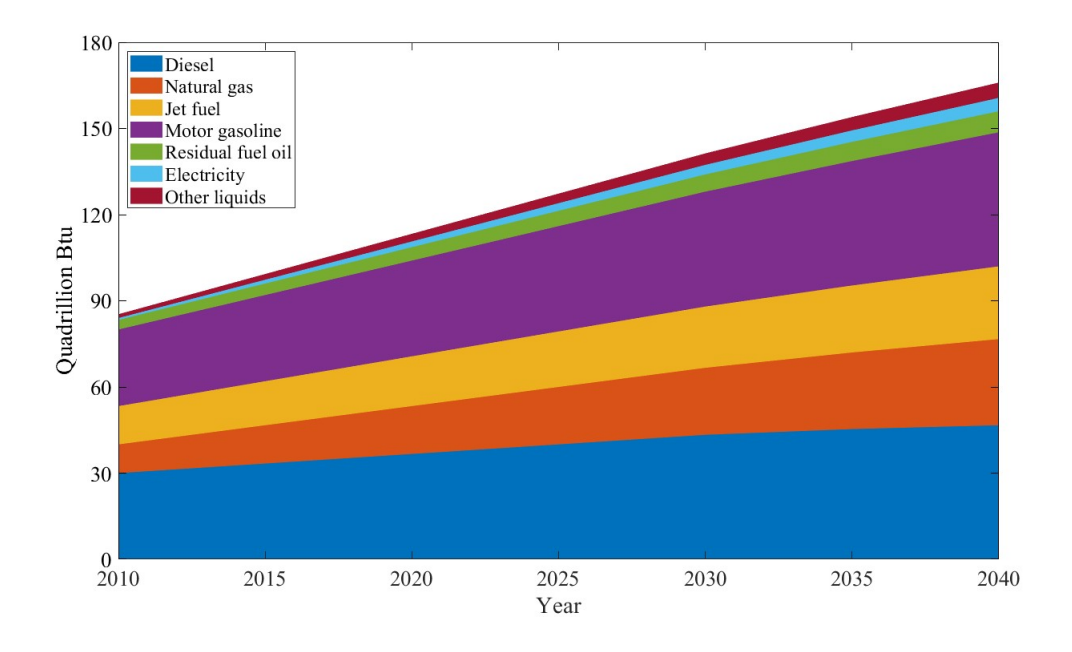


Figure 1.1: World transportation energy consumption by source [3].

energy use in transportation is projected to decline from 96% in 2012 to 88% in 2040 [16]. The global transportation sector's liquid fuel consumption is expected to grow by 907.2 Mtoe from 2012 to 2040 (Figure 1.1) with motor gasoline (including ethanol blends) as the largest source, followed by diesel (including biodiesel). Since 2010, energy consumption has increased: diesel by 327.6 Mtoe, jet fuel by 252.0 Mtoe, and motor gasoline by 226.8 [3].

A combination of increasing energy demand, rising costs, and environmental regulation has encouraged the development of electric vehicles (EV) and non-petroleum fuels. However, battery EVs are not 'clean' unless the electricity sector is decarbonised using renewable energy sources [17]. EU sales of EVs have been growing and in 2022 accounted for 21.6% of the total new car registrations [18]. However, there is evidence that sales growth may be slowing as the resale value of EVs is lower than projected. While electric and hybrid vehicles have shown some degree of success, the electrification of vehicles is more suitable for light-duty operation due to limitations in power density and low energy storage capacity [19]. An important barrier to the widespread adoption of EVs in developing countries is the lack of reliable and stable electricity supply [20]. Developing countries face significant infrastructure and finance obstacles when expanding their electric grid for basic provision,

before the additional demand from EVs [21]. Furthermore, even where electricity is accessible, frequently it originates from fossil fuel power plants, thereby compromising the environmental advantages of EVs [22]. Electrification might be promising for light-duty applications in developed countries, but other solutions could be more suitable for countries with unstable electricity infrastructure and for heavy-duty applications. Therefore, developing non-fossil fuels for ICEs is important for reducing tailpipe emissions and achieving greater efficiencies to meet the energy demands of the transportation sector.

1.2 Alternative fuels

Some alternative fuels (Figure 1.2) are available in the market, with others still at the development stage. Alternative fuels could improve energy sustainability using renewable energy sources by reducing the use of fossil reserves [23]. Moreover, some alternative fuels have superior chemical and physical properties compared to traditional fossil fuels [24]. For example, biofuels derived from vegetable oil, corn, or methanol could halve the GHG emissions on a well-to-wheel basis compared to traditional petroleum-based fuels [25]. Currently, alternative ICE fuels account for only 5\% of the total transportation sector fuel demand. In the EU, the share of the transportation sector's energy consumption powered by renewable sources increased from 2% in 2005 to 8.7% in 2022 [26]. This was because transportation energy demand is projected to increase by 1.2% yearly [27]. According to the World Energy Outlook 2023 [3], the total installed capacity of solar and wind energy available worldwide by 2030 is estimated to be more than 4240 GW. It is expected that solar alone could contribute more than 500 GW each year. China's objective is to reach a solar and wind capacity of more than 1450 GW by the year 2030. India aims to achieve a non-fossil fuel capacity of 500 GW by 2030, with a substantial contribution from solar and wind energy. The EU aims to achieve 50% of its new electricity consumption through renewable sources, primarily by installing a minimum of 1,200 GW of solar and wind power capacity by 2030. As solar and wind are intermittent, it is logical to generate so-called 'green' hydrogen by electrolysis when renewable energy

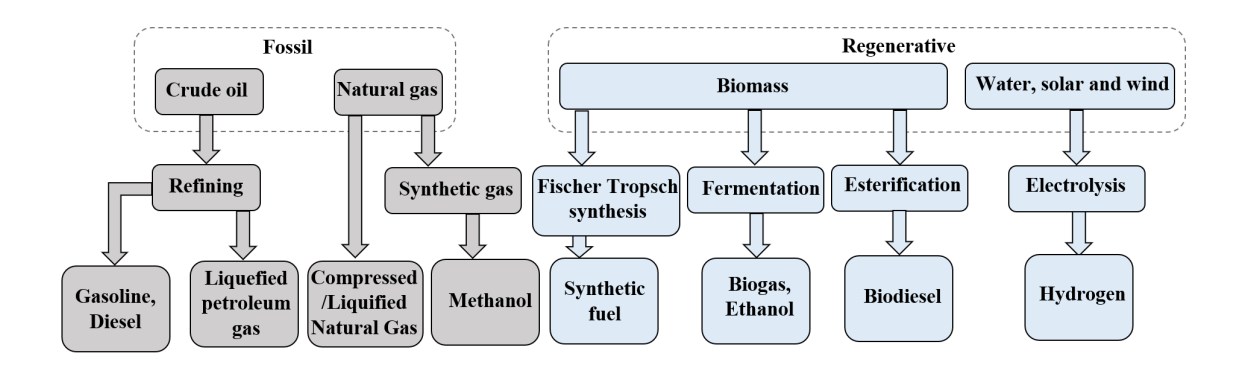


Figure 1.2: Production pathways of current and future fuels.

production exceeds demand, which might decrease GHG emissions and dependence on fossil fuels [28].

1.3 Hydrogen as a fuel

Hydrogen is the most abundant element in the universe, however, its use as the main fuel for industrial applications, power generation, or vehicles is challenged by the current production method [29]. Currently, hydrogen is produced using nonrenewable fuels and inefficient processes [30], and challenges exist for storage and safe transportation [31]. However, several countries are making significant financial commitments to hydrogen energy research. Since 2019, China has initiated more than 30 projects focused on green hydrogen, and the EU has a target of achieving a renewable hydrogen electrolyser capacity of 40 GW by 2030 (2022). There are two paths through which hydrogen could be implemented into vehicles: 1) burning hydrogen in ICEs, and 2) using hydrogen fuel cells [32]. Research has been invested in both paths, but burning hydrogen in ICEs is considered more cost-effective currently as it can be implemented with minimal modifications. However, the hydrogenfuelled ICE has lower efficiency compared to fuel cells and still produces nitrogen oxide emissions during combustion, raising concerns on the long-term environmental benefits [33]. Hydrogen fuel cells offer higher energy conversion efficiency and zero tailpipe emissions [32], but require an electric drivetrain making them competitors to batteries and not a modified ICE. Fuel cell research is addressing production costs, sensitivity to hydrogen purity, and limited durability in certain applications [34]. Any distribution infrastructure developed for hydrogen ICEs would also benefit fuel cell vehicles if they become competitive in terms of performance, emissions, and price when compared to traditional petroleum [35].

For hydrogen to be adopted as a fuel for ICEs, it needs to provide equivalent durability, safety, and range as traditional hydrocarbon fuels [36]. To make hydrogen vehicles economically viable, difficult problems in hydrogen generation, delivery, and storage must be solved. Compared to traditional liquid fuels like gasoline, hydrogen has unique qualities that make it an attractive fuel for ICE applications [37]. When using hydrogen as a transport fuel, special consideration must be given to its low density of $0.08 \, \text{kg/m}^3$ at 300 K and 1 atm, its broad flammability limits of 4 to 75 vol percent in the air, and its low minimum ignition energy of $0.02 \, \text{mJ}$ [38]. Because of the wide range of flammability, the hydrogen engine suffers from severe combustion abnormalities such as pre-ignition and backfire, leading to knock [39].

The use of a hydrogen/air mixture in ICEs started with Rivaz in 1806 [40]. Then, Ricardo in 1924 investigated the effect of the equivalence ratio on the knock regions of a hydrogen engine [41]. The first hydrogen engine was produced by the Erren Engineering Company, where it was proposed to use slightly pressurized hydrogen in the chamber instead of using a carburettor [42]. Since the energy crisis of 1973, intense research programmes into alternative fuels, particularly hydrogen, have been implemented in multiple countries [43]. Despite the considerable historical and recent interest in hydrogen as a fuel, several research gaps remain. While hydrogen's combustion characteristics have been widely studied [44, 45, 46, 15, 47], there is a need for mapping the hydrogen SI engine performance and emissions over a wide range of realistic operating conditions. Furthermore, as the product of burning hydrogen is water, an empirical correlation that can be used in numerical combustion models to capture the effect of water addition on hydrogen flame speed under enginerelevant conditions does not exist. Moreover, a comprehensive exergy analysis of hydrogen-fuelled engines investigating the fundamental origins of losses, the limits to efficiency, and the engineering trade-offs required to reduce losses remains scarce. These gaps underline the need for a comprehensive hydrogen combustion model and exergy analysis to support the design and optimisation of hydrogen internal

combustion engines.

1.4 Aim and objectives

The aim is to estimate the upper limit of efficiency for a hydrogen-fuelled ICE and investigate the in-cylinder engine processes leading to losses. To achieve the aim, the following objectives must be met:

- Develop a single-zone combustion model to comprehensively map the performance, emissions, and combustion abnormalities of a hydrogen SI engine under various operating conditions.
- Develop an empirical correlation to predict the laminar flame speed of hydrogenair combustion with water addition under lean mixture engine operating conditions.
- Develop a two-zone combustion model and implement the new laminar flame speed correlation .
- Conduct an exergy analysis to investigate how exergy splits between the various engine processes and assess the maximum possible efficiency of a hydrogen ICE.

1.5 Thesis outline

The thesis is structured as follows:

- Chapter 1 provides an overview of energy consumption and the role of ICEs in the transportation sector. It highlights the importance of improving engine efficiency and adopting better energy utilization strategies and sets out the basis of hydrogen as an alternative fuel in ICEs.
- Chapter 2 provides an overview of hydrogen use in ICEs under different operating conditions. The chapter reviews hydrogen operational strategies to

improve performance, reduce emissions, and mitigate combustion abnormalities.

- Chapter 3 details the methodology of hydrogen combustion engine modelling processes and introduces new model components to advance the established models. It also provides a detailed methodology for the application of the second law of thermodynamics to hydrogen-fuelled SI engines under various operating conditions.
- Chapter 4 presents a detailed analysis of boosted lean-burn strategies by advancing a single-zone hydrogen combustion model.
- Chapter 5 proposes a new correlation to predict the laminar flame speed of hydrogen with and without water addition for engine-relevant operating conditions.
- Chapter 6 applies the empirical correlation proposed in Chapter 5 to a two-zone hydrogen combustion model. The chapter provides a comprehensive study of the performance, combustion abnormalities, and NO emissions of a boosted lean-burn hydrogen SI engine under a water injection environment.
- Chapter 7 investigates the exergy split between processes of a hydrogen-fuelled SI engine across a wide range of real-world operating conditions. The chapter addresses exergy management, discussing any compromises of a hydrogenfuelled SI engine.
- Chapter 8 summarises the outcomes, draws conclusions about the implications of the results, and proposes future directions for this research.

1.6 Research contribution and novelty

This work applies the second law of thermodynamics to hydrogen combustion in ICEs to estimate the limits to efficiency, emissions reductions, and develop strategies for managing the initial energy supplied to the engine to minimise losses and maximise useful energy output. This could help develop advanced combustion strategies

for ICEs in line with future emissions regulations. The single-zone combustion model was advanced by implementing the laminar flame speed to predict the combustion phasing of the hydrogen SI engine at various engine operating conditions. The two-zone model captures information about in-cylinder turbulence or burned/unburned gas separation and thus was suitable to study water addition and exergy analysis. The two-zone model predicts performance, emissions, and combustion abnormalities, and incorporates the new laminar flame speed correlation. Compared to computationally expensive 3D CFD models, the two-zone combustion model offered a faster and more cost-effective approach, which was shown to be sufficient for investigating hydrogen combustion and in-cylinder exergy analysis in hydrogen SI engines. This work has yielded five research outputs – four journal papers and a fully refereed conference paper:

- Rrustemi DN, Ganippa LC, Axon CJ. Investigation of boost pressure and spark timing on combustion and NO emissions under lean mixture operation in hydrogen engines. Fuel 2023; 353:129192. https://doi.org/10.1016/j.fuel.2023.129192.
- Rrustemi DN, Ganippa LC, Megaritis T, Axon CJ. New laminar flame speed correlation for lean mixtures of hydrogen combustion with water addition under high-pressure conditions. Int J Hydrog Energy 2024; 63:609–17. https://doi.org/10.1016/j.ijhydene.2024.03.177.
- Rrustemi DN, Ganippa LC, Megaritis T, Axon CJ. Predicting engine performance for hydrogen with water addition using a two-zone thermodynamic model. Fuel 2025;386:134137.
 https://doi.org/10.1016/j.fuel.2024.134137.
- Rrustemi DN, Ganippa LC, Axon CJ. Exergy analysis of lean-burn hydrogen-fuelled engine. Energy 2025;314:134110.
 https://doi.org/10.1016/j.energy.2024.134110.

Paper 1 studies the performance of a boosted lean-burn hydrogen SI engine under various spark timings, focusing on combustion characteristics, efficiency, fuel consumption, NO emissions, and knock regions. Paper 2 offers a newly developed laminar flame speed correlation of hydrogen-air combustion to account for the effects of water addition under engine-relevant conditions by using chemical kinetic laminar flame speed values. The laminar flame speed correlation was derived for pressures from 10 to 70 bar, temperatures from 400 to 800 K, equivalence ratios from 0.35 to 1, and water addition by mole from 0 to 20%. In Paper 3, a two-zone waterdiluted hydrogen combustion model was developed and extended for various engine operating conditions based on the laminar flame speed correlation provided in Paper 2. Additionally, sub-models for engine knock and NO emissions were implemented to provide a comprehensive study of the performance, combustion abnormalities, and NO emissions of a boosted lean-burn hydrogen SI engine under injection water environment. Paper 4 evaluates the hydrogen engine efficiency, irreversibility, as well as the NO emissions based on the two-zone combustion model provided in Paper 3. Consequently, the exergy losses were quantified for each hydrogen engine subcondition, such as intake manifold air pressure, equivalence ratio, compression ratio, and spark timing.

Chapter 2

Literature review

This review examines the use of hydrogen in ICEs, emphasizing hydrogen combustion properties, combustion modes, and strategies for enhancing the thermal efficiency of hydrogen SI ICEs. Operational strategies – boosting, compression ratio, lean-burn, and water injection – are discussed in the context of to increasing engine performance, reducing emissions, and mitigating combustion abnormalities. Finally, this review examines the application of the second law of thermodynamics to the hydrogen ICE to quantify the potential for performance improvement and emissions reductions.

2.1 Hydrogen use in engines

There are comprehensive reviews of hydrogen as a fuel for ICEs [43, 48]. The combustion abnormalities are due to high hydrogen flame speed and wide flammability range [49]; however, injection strategies might minimize or mitigate these problems [50]. The direct injection of hydrogen has shown benefits, including preventing backfire, improving thermal efficiency, and achieving higher engine power output [51, 52, 53]. In 2007, BMW demonstrated a hydrogen SI engine [54], which was shown to be the cleanest engine ever tested at the Argonne National Laboratory. Soon after, the MAN Group demonstrated a bus engine that could run independently either on hydrogen or gasoline. MAN conducted comprehensive investigations regarding safety, and the vehicles were able to cover more than 10,000 km running without any

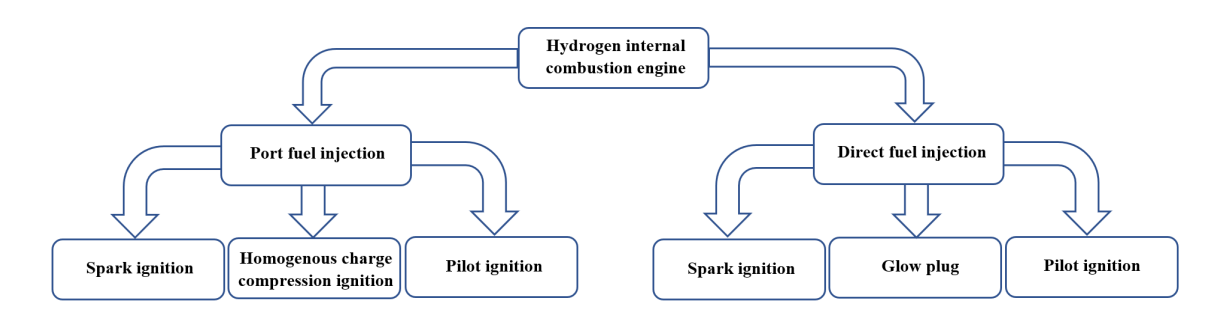


Figure 2.1: Various hydrogen injection and ignition strategies.

safety or running issues [55]. The Ford Motor Company also designed, developed, and demonstrated hydrogen engines for road vehicles [56]. Recently, most leading engine manufacturers or research institutions have invested in hydrogen engine research, if not in the demonstration or production stage.

The hydrogen-fuelled ICE has been shown to be operable in the main combustion modes (Figure 2.1). ICEs are divided into two categories based on the fuel injection mechanism: port injection and direct injection. In port injection, the hydrogen/air mixture starts mixing outside the combustion chamber and is defined as a premixed fuel. The port injection hydrogen ICE can be ignited using spark ignition (SI), homogeneous charge compression ignition (HCCI), and pilot ignition [57]. Pilot ignition (Figure 2.1) refers to the strategy of initiating combustion by injecting a small amount of high-cetane fuel to ignite the in-cylinder mixture. The direct injection hydrogen engine allows premixed, partially premixed, and non-premixed diffusion-controlled flames in the mixture formation of hydrogen, depending on the injection strategy [58]. A characteristic that differentiates various direct-injection modes is the fuel injection pressure [59]. The ignition strategies used in hydrogen direct injection are pilot ignition, glow plug, and spark ignition [60].

2.1.1 Hydrogen port injection

A port injection hydrogen engine might suffer from abnormal combustion, such as pre-ignition, knock, and backfire [61, 62, 63]. Additionally, hydrogen injection into the air intake might limit the engine power density. The SI port-injection mode is the most researched area, with the performance, control strategy, and emissions

summarized by White et al. [43]. Hydrogen's combustion properties allow it to be used in an HCCI engine, where the premixed hydrogen/air charge is introduced during the intake air stroke. Then, at the end of the compression process, the charge auto-ignites due to the elevated in-cylinder pressures and temperatures. The hydrogen HCCI combustion modes exploit the high flame speed of hydrogen [64]. Mixture formation is the most influential parameter on the performance and reliability of a hydrogen HCCI engine [65]. However, the drawback is the narrow operating ranges [64, 66]. Hydrogen engines can operate using the pilot injection strategy, which might enhance combustion rates due to the high flame speed [67, 68, 69, 70]. Finally, different injection and control strategies can be implemented into port injection hydrogen engines to mitigate NOx emissions and combustion abnormalities. While hydrogen port injection might be the most straightforward technology and could help with the fundamental understanding of hydrogen use in engines, the cost is in power output.

2.1.2 Hydrogen direct injection

The performance of a hydrogen engine can be improved by injecting hydrogen directly into the combustion chamber [52]. In direct injection, the mixture forms within the cylinder. Unlike port injection, direct injection allows the combination of fully or partially premixed [71]. Another benefit of hydrogen direct injection is the mitigation of combustion abnormalities such as pre-ignition and backfire [72]. Hydrogen pre-ignition is avoided using hydrogen direct injection by reducing the hydrogen mixture's exposure time to hot spots or fuel left from the previous cycle [73]. Also, the direct injection strategy allows greater hydrogen fuel masses to be injected, thereby increasing the load [74, 75]. Injection is performed at high pressures, allowing a wide range of engine operating conditions. The air-to-fuel stratification, apart from the injection pressure, is strongly influenced by the injection timing [65].

The SI hydrogen engine is well-established [48, 76], and the performance of a direct injection hydrogen engine is almost one-fifth greater than that of a standard gasoline port-injected engine [52]. However, the wall heat losses are greater for the hydrogen engine because of the smaller quenching distance [77]. The direct injection

of fuel can use various ignition strategies such as a glow plug, spark plug, and pilot ignition [78]. The glow plug is a heated surface placed inside the combustion chamber; its implementation in the hydrogen engine could benefit cold start conditions by increasing the in-cylinder charge temperature [50]. A glow plug is effective in controlling the combustion characteristics of a hydrogen engine, but it may reduce thermal efficiency by increasing the likelihood of pre-ignition [79] Also, the durability of glow plugs in the higher combustion temperatures may be reduced. Furthermore, improvements in volumetric efficiency and the high-pressure direct injection of hydrogen increases fuel efficiency by reducing the compression work required [80]. Even though the load could be increased by the direct injection of hydrogen, the power output remains inferior compared to that of a compression-ignited engine [81]. This is mainly due to the limitation of the operating condition (compression ratio) caused by combustion abnormalities. The emissions from a direct hydrogen injection engine could be further reduced by injecting water [82] or exhaust gas recirculation [83].

2.2 Thermal efficiency

The thermal efficiency of the Otto cycle is influenced by the compression ratio CR and specific heat ratio γ [84], given by:

$$\eta = 1 - \frac{1}{CR^{(\gamma - 1)}}$$
(2.1)

Figure 2.2 shows that enhancing thermal efficiency can be achieved via two paths: 1) by increasing the compression ratio, and 2) by increasing the specific heat ratio γ , which is strongly influenced by the air-to-fuel ratio [85]. Increasing the compression ratio improves thermal efficiency but is usually limited by combustion abnormalities [86]. However, increasing γ via lean-burn conditions increases efficiency. For traditional hydrocarbon fuels, increasing the air-to-fuel ratio was not preferred due to slow and unstable combustion [87]. Hydrogen, however, offers superior combustion characteristics such as high flame speed and wide range of flammability, enabling the stable lean-burn operation [88]. The lean-burn hydrogen ICEs offer greater thermal efficiency and lower engine-out emissions compared to traditional

hydrocarbon-fuelled ICEs [89]. Additionally, boosting could further enhance the efficiency of hydrogen ICE by increasing power output [90]. The boosted lean-burn hydrogen ICE could provide optimal thermal efficiency, emissions, and power output, making hydrogen a promising solution for future sustainable transportation.

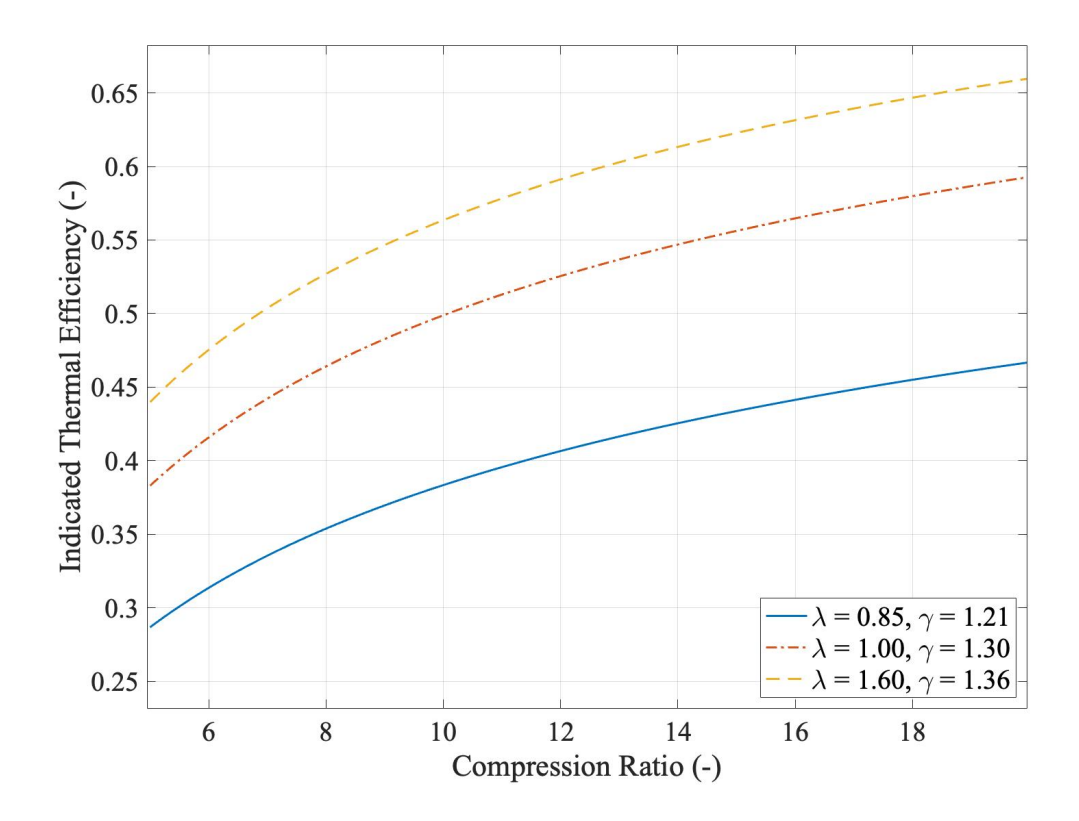


Figure 2.2: Ideal thermal efficiency at various excess air ratios, gamma and compression ratio.

2.2.1 Boosted hydrogen engine

The current limitations of pure hydrogen SI engines are low volumetric energy and high levels of NOx emissions [43, 48, 61, 91]. The lower volumetric energy reduces the performance of a naturally aspirated hydrogen SI engine, but this can be counteracted by boosting the intake manifold air pressure (MAP). The increase of the MAP could increase the load and thermal efficiency by:

• reducing engine friction by decreasing the engine size,

- lowering heat transfer through the walls by reducing the combustion chamber surface area,
- enhancing air-fuel mixing by increasing the mass flow rate across the inlet valves,
- using a compressor to better exploit the exhaust enthalpy.

By charging the intake pressure of a hydrogen SI engine, the same level of performance as a standard gasoline engine can be achieved at a very low level of fuel consumption [44]. Hence, the only limitation to this approach is operating at stoichiometric conditions due to the risk of backfire and pre-ignition [44]. Improvements have been reported in thermal efficiency and indicated mean effective pressure (IMEP) of up to 38.9% and 14.2%, respectively, by increasing the intake charge density, which allowed more fuel to be added while maintaining an equivalence ratio of 0.6, and still achieving relatively low NOx emissions [92]. The IMEP of a lean burn ($\phi = 0.6$) hydrogen SI engine is able to surpass the stoichiometric operation of gasoline IMEP at their corresponding MBT timings when the MAP was boosted by 10 kPa (Figure 2.3). With the load increasing on a hydrogen engine, backfire occurs, but it can be mitigated by varying the intake valve timing [93]. Also, hydrogen mixtures with an equivalence ratio up to 0.2 were able to be operated with stable combustion because of the boosting [94]. When the hydrogen/air mixture was operated at ultra-lean burn operation, the temperature was reduced below the threshold for NOx emission formation [95], hence suggesting the feasibility of achieving high-load hydrogen engines with no NOx emissions. Improvement of load and thermal efficiency were observed when the intake MAP was increased from the naturally aspirated condition up to 130 kPa [83]. Finally, the effect of supercharging hydrogen engines to improve performance has been demonstrated [63, 93, 96, 97, 98]. Although boosting intake air pressure enhances performance, this increases the in-cylinder temperature which strongly influences the NOx formation rate [99]. NOx formation in an ICE depends not only on the in-cylinder temperature but also on oxygen concentration and the residence time of the gases. Higher in-cylinder temperatures are typically observed with richer hydrogen/air mixtures [100]. Therefore, reducing NOx emissions can be achieved by increasing the air—fuel ratio (lean burn) or by using exhaust gas recirculation (EGR) to lower combustion temperatures. Increasing the EGR ratio decreases the load due to the increase of the combustion duration caused by the decrease of the flame speed with EGR rate [83]. NOx emissions reduce by increasing the EGR rate by decreasing the combustion energy (lower in-cylinder temperatures), and the effect of EGR had greater significance at the greater loads [101]. To improve the thermal efficiency beyond 40%, reducing heat loss is essential. The effect of lean-burn on decreasing cooling heat losses is greater than that of EGR [102], so higher thermal efficiency and lower emissions are expected [37, 62, 103, 104, 47].

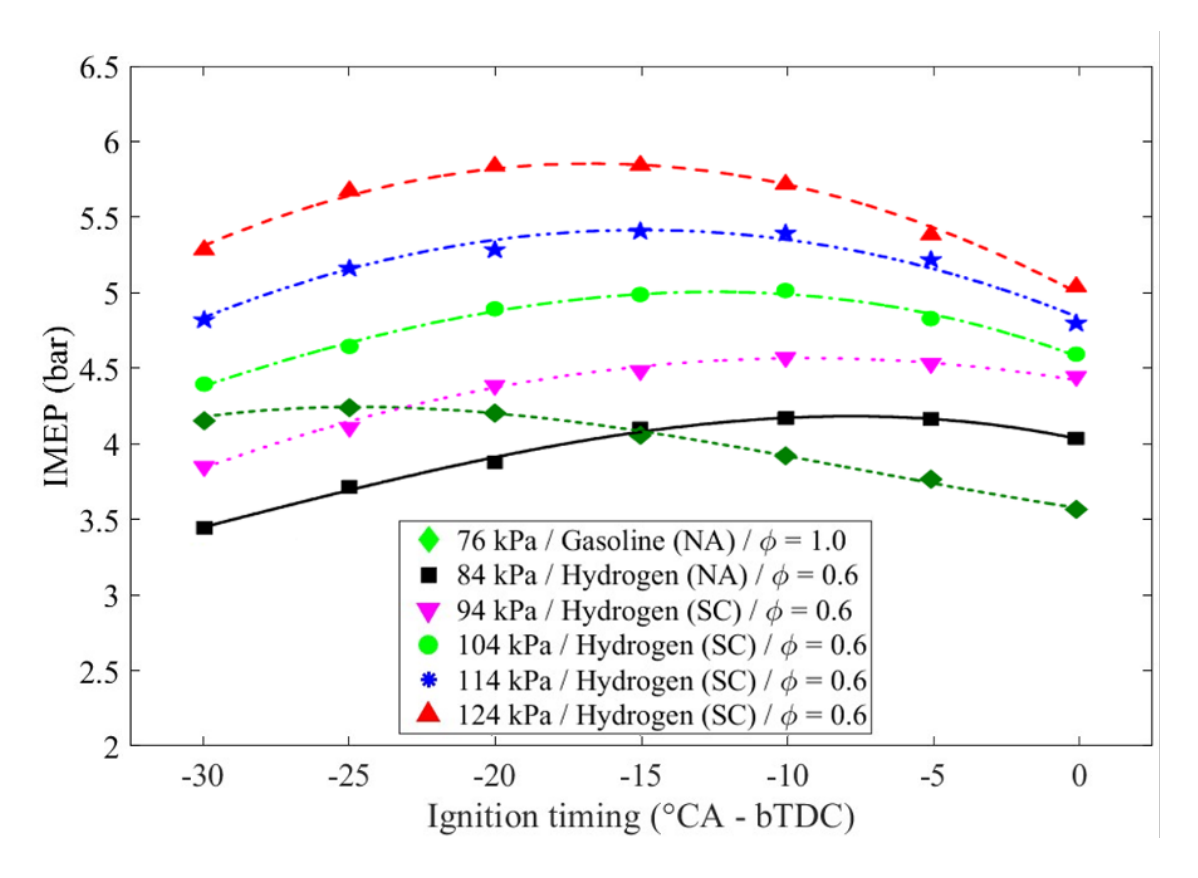


Figure 2.3: The IMEP of a lean-burn hydrogen engine at various MAP and the IMEP of naturally aspirated stoichiometric A/F gasoline [92].

2.2.2 Lean-burn hydrogen engine

Higher thermal efficiency requires greater work output, eventually leading to higher engine-out emissions. For traditional hydrocarbon fuels, the stoichiometric air-tofuel ratio has been used for more than two decades to achieve greater loads [105]. However, due to the superior combustion properties of hydrogen, a compromise between engine load and thermal efficiency could be achieved by operating at lean-burn mixtures. Lean-burn of an SI engine occurs when the relative air/fuel ratio (AFR) is greater than unity. Moreover, the high laminar flame speed (LFS) of hydrogen can be used to offset the slow burning tendencies of lean mixtures, offering greater combustion speed and stability [104]. The highest thermal efficiency was achieved when operating at an excess air ratio of 2, without significant power losses and relatively low NOx emissions [106]. The power was able to be kept high with the help of the engine speed and the boosting of the intake MAP. For lean burn mixtures, the exhaust losses reduced thermal efficiency. However, at greater equivalence ratios, the losses were mostly caused by the in-cylinder heat transfer because of the increase in the in-cylinder temperature. Furthermore, studies of the combustion range and the combustion regimes to maintain the engine at idling conditions show that the excess air ratio of the hydrogen/air mixture could be kept at a range from unity to 2.4 [107]. Experimental studies have demonstrated that hydrogen combustion can maintain stable operation at idle conditions with excess air ratios approaching 3 [107]. The optimal hydrogen SI engine operating condition was found to be for the excess air ratio from 1.8 to 2. Experiments on injection pressure and injection timing of a lean-burn turbocharged engine show that operating at ultra-lean mixtures significantly improved thermal efficiency [53]. The optimum operating condition was found to be at an excess air ratio of 2.3, resulting in a load of 10.9 bar with a thermal efficiency of 42% with relatively low NOx emissions less than 150 ppm.

2.2.3 Hydrogen combustion abnormalities

Mitigating abnormal combustion in hydrogen engines has implications for mixture formation, load control, and engine design. There are three main types of abnormal hydrogen combustion: knock, pre-ignition, and backfire [108]. Knock is characterized by the autoignition of the end-gas mixture, pre-ignition is caused by uncontrolled ignition from a hot spot, while backfire occurs during the intake process and is considered a premature form of pre-ignition [109]. The Ford Motor Company [106]

showed that knock in hydrogen engines occurred only for richer mixtures $\lambda < 1.3$, but this was not presented as an engine performance limiting factor. Whereas, Lee et al. [110] showed that knock from the boosting pressure has an opposite relationship with the equivalence ratio due to the drop of the in-cylinder gas temperature, but knock did not occur once the mixture became leaner than an equivalence ratio of 0.6. By increasing boost pressure, the lean-burn limit increased up to an equivalence ratio of 0.2 and the thermal efficiency could be increased up to 36.7%. Studies of the knock-free regimes for a hydrogen engine at various excess air ratios, compression ratios, and load provide evidence to justify the selected operating condition to avoid hydrogen knock [111, 110, 112, 39, 73].

Hydrogen engine knock can be estimated in the same way as the existing gasoline knock models by using the appropriate modelling modifications [39]. The aim of the knock model is to determine whether the engine knocks at a certain operating condition or not. The most commonly used method describes knock occurrence as a function of the autoignition delay [113]. Most of the knock models in the literature use the ignition delay coefficient method which was proposed by Livengood and Wu [114]. The ignition delay coefficient method uses a single step Arrhenius equation to predict the global ignition delay time of a mixture. However, because hydrogen behaves significantly differently from traditional hydrocarbon fuels, the available correlations cannot be used for hydrogen autoignition delay time predictions. Currently, there is no correlation available in the literature which predicts the hydrogen autoignition delay time at engine-relevant conditions. For various ranges of temperature, pressure, and equivalence ratios, the autoignition delay time could be calculated by simulating a closed homogeneous reactor using a chemical kinetic solver.

Backfire is persistent in hydrogen engines, particularly during premixed operation [109]. Due to hydrogen's low ignition energy and wide flammability range, backfire can arise from hot spots caused by residual gas, exhaust valves, or spark plugs [111]. Pre-ignition could also result from ignition energy that is not fully dissipated due to hydrogen's lower ion concentration [115]. Additionally, hydrogen's small quenching distance could allow combustion to propagate across the top of the

piston, which can occur during the intake valve opening, thus igniting the fresh charge [116]. Although hydrogen has low ignition energy, the autoignition temperature is high. Hence, pre-ignition could be mitigated by retarding the spark timing [106]. When the SI hydrogen engine is operating at boosted lean conditions, air dilution of the mixture significantly increases, which affects the combustion stability and can lead to autoignition, misfire, or knock [117]. However, Nguyen et al. [62] showed that the combustion remained stable without any backfire, misfire, or knock for ultra-lean mixtures ($\lambda = 2.8$) at part-load operation with a low engine speed.

2.2.4 Water injection

Water injection into the combustion chamber was discussed as early as 1920 by Ricardo, but he noted several problems such as the quantity and quality of the water [118]. For example, water injection is used in aircraft engines to control detonation [119]. For road vehicle engines, water injection is considered an alternative method to reduce emissions [120]. Water can be injected into the engine via direct or port injection [121]. Direct injection can be implemented using a fuel-like injector or special water injectors in the cylinder head [122].

The main advantage of water injection is to allow the engine to operate at higher loads due to the mitigation of abnormal combustion [82]. This is because water has a higher heat of vaporization, reducing the in-cylinder temperature [123]. Subramanian et al. [124] experimentally showed that injecting water into the intake manifold of a hydrogen SI engine was an effective way to control knock, leading to reductions of up to 80% in NOx emissions with relatively low losses in brake thermal efficiency. Similarly, reductions of NOx emissions up to 87% were achieved with a 2% increase in indicated specific fuel consumption, while the load was increased by 24% at the same NOx emissions compared to conditions without water injection [125]. For a fixed spark timing of 20° CA bTDC, the thermal efficiency of the hydrogen engine increased with the addition of water (0 to 4.05 mg/cycle) at an excess air ratio of 1.15. Additionally, advancing the timing of water injection is beneficial for engine performance [126]. Moreover, hydrogen allows for high rates of dilution with air, exhaust gas, or water before combustion stability deteriorates due to hydrogen's

wide flammability limits [51]. A further reduction in NOx emissions was observed as the level of water injection increased compared to the exhaust gas recirculation method.

Moreover, water injection facilitates rapid dilution [127]. The quantity of water direct injection is independent of the fuel and air flow and can be applied throughout the entire operating range of a hydrogen engine [126]. Additionally, during boosted manifold air pressure operation, water injection can serve as an alternative means of delivering exhaust gas to the compressor under high load conditions in hydrogen SI engines [128]. Despite the benefits of water injection in hydrogen engines, challenges remain such as the potential for oil-related emission accumulation and the need to supply the correct quantity of water while mitigating the risk of water freezing in cold weather [122]. However, experiments show that sourcing water from air conditioning condensate could address these challenges [129]. Equipping the supply line with a damping volume system could prevent system damage caused by water freezing [124]. Finally, since under EGR operation of a hydrogen engine, the water content in the cylinder increases, it is important to study the effect of water addition into a hydrogen engine.

2.3 Hydrogen combustion model

Thermodynamic methods provide fundamental understanding of the relationship between mechanical, thermal, and chemical processes in an ICE [113]. Engine models are divided into three types: zero-, one-, and multi-dimensional models [130]. The zero-dimensional models are computationally fast and inexpensive but do not have any spatial in-cylinder information. However, if treated correctly, it may be possible to obtain results comparable to multi-dimensional models [131].

In contrast the multi-dimensional CFD models use the Navier-Stokes equations coupled with detailed chemical kinetic mechanism to capture the flame development, turbulence with chemistry interaction and the emission species formation. The fast chemistry combustion model (FCCM) which assumes the flamelet like incylinder chemistry [132]. The extended coherent flame model (ECFM) captures the

pre-mixed turbulence flame propagation [133]. The ECFM model was adapted for hydrogen combustion by incorporating a specific laminar flame speed correlation and modified flame thickness expressions to account for hydrogen's high reactivity and diffusivity. allowing improved prediction of flame propagation and NOx emissions in hydrogen-fuelled SI engines[46]. Similar to the ECFM, the SAGE detailed chemistry solver and the G-equation enable the accurate simulation of the premixed and stratified hydrogen combustion, the hydrogen ignition dynamics, and the flame-turbulence interactions [134]. The usefulness of these models is their ability to predict the flame morphology [135, 136, 137] by simulating the detailed physics and chemistry. However, their high computational cost and complexity limit their practicality for wide-range parametric or optimization studies [138]. For applications focusing only on engine performance prediction, such as in-cylinder pressure and temperature, there is no need to model detailed flame morphology or combustion spatial information a zero-dimensional combustion model can provide sufficient accuracy.

The zero-dimensional combustion models are categorized as single-, two-, and multi-zone models, where the conservation of energy and the ideal gas laws are applied to calculate parameters of the combustion process [139], for example the mass fraction burned using the Wiebe function [140]. The Wiebe function is an S-shaped curve starting from zero to unity, providing the mass fraction of burned gases at any instant of the combustion process [113], with the parameters calculated using the least squares fitting method based on experimental data [141]. In recent years, research has focused on the use of a multi-zone Wiebe function, with its parameters predicted by machine learning techniques for a wide range of operating conditions [142, 143, 144].

The first hydrogen numerical model [145] used a two-zone model with the incylinder turbulence modeled using a semiempirical turbulent flame expression and NO emissions using the extended Zeldovich mechanism. This methodology has been used in other studies [146, 63]. Regarding hydrogen combustion, the specific heat ratio has been replaced by a polytropic index appropriate for hydrogen—air mixtures [147]. For zero-dimensional combustion modeling, the laminar flame speed (LFS)

is the most influential input. An extended correlation for predicting hydrogen/air LFS at lean-burn conditions was used to investigate the performance of the hydrogen port-injected engine [148]. Similarly, other correlations to predict the LFS of hydrogen have been made [149, 150]. Simulations using a two-zone hydrogen combustion model to study the effect of supercharging [151] noted difficulties in calculating stretch-free burning speeds, which have since been addressed [152]. Using the chemical kinetic mechanism, the hydrogen propagating flame was modeled using turbulent burning velocity [153] and by dividing the combustion chamber into three zones: unburned, flame, and burned. This showed good agreement between simulation and experimental in-cylinder pressure across a wide range of equivalence ratios, spark timings, and compression ratios.

2.3.1 Hydrogen laminar flame speed correlation

A notable difference between fuels is the laminar flame speed (LFS), an important parameter for turbulent flame calculations. The LFS is used to assess flame stability and characterize the transition between deflagration and detonation [154]. Generating hydrogen LFS data from experiments or chemical kinetic simulations across a wide range of operating conditions is time-consuming. Experimental data for hydrogen combustion at the elevated pressures of engine-relevant conditions are scarce, as the flames are unstable [152].

Hydrogen/air flames, with or without EGR dilution, will not be stable in any combustion application due to mechanisms such as hydrodynamic instability (Darrieus-Landau), which is caused by the variation in density between the burned and unburned hydrogen/air mixture, or Rayleigh-Taylor instabilities initiated by gravitational forces affecting the stability of the flames [155]. Flame instability is also affected by unequal diffusivity as flame propagation is influenced by the system temperature [156]. Heat transfer from the flame front into the unburned mixture and from the unburned zone into the flame front impacts flame stability. There are three main mechanisms for diffusion: 1) thermal diffusivity of the unburned mixture, 2) deficient reactant diffusivity, and 3) excess reactant diffusivity. The hydrogen flames at high pressure are more prone to Darrieus-Landau and thermo-diffusive instabili-

ties. These cause the flame to wrinkle, increasing the burning velocity [157] due to high turbulent burning velocity and laminar burning velocity ratios for lean burn hydrogen flames [158, 159, 160, 57]. The decrease of the equivalence ratio, and the unburned temperature, with increasing pressure causes the increase of intrinsic instability. The instability growth is associated with the expansion ratio or the increase of Zeldovich number, and with a reduction of the effective Lewis number [161].

The conditions for stable hydrogen flames can be predicted by using chemical kinetics models [150] once the kinetic mechanism is validated. Most of the available LFS correlations are fitted using a power law [162], where the influence of equivalence ratio, pressure and temperature are independent,

$$S_l(\phi, P, T_u, f) = S_{l0} \left(\frac{T_u}{T_0}\right)^{\alpha} \left(\frac{P}{P_0}\right)^{\beta}$$
(2.2)

The LFS S_l is a function of equivalence ratio ϕ , unburned gas temperature T_u , and pressure P at a reference pressure P_0 and temperature T_0 . The terms S_{l0} , α and β represent the flame speed at a reference condition, and temperature and pressure power coefficients, respectively. The power coefficients α and β differ for each fuel and can be determined from experimental or numerical approaches [163]. Most correlations [149, 150] only express the power coefficients α and β as dependent on the equivalence ratio. However, numerous experimental studies show β varying with both pressure and equivalence ratio [154, 163, 164]. Additionally, Verhelst et al. [152] demonstrated a strong relationship between the effects of pressure and equivalence ratio on the hydrogen LFS. To account for the observed nonlinear effects of the pressure on the hydrogen LFS, integration of the coupled effects of the equivalence ratio and pressure to calculate the reference flame speed S_{l0} and pressure exponent β has been achieved [152]. The gasoline LFS correlation using the power law formulation [162] was unable to capture the non-power behaviors [165]. The observed coupling of temperature-pressure dependence on the LFS was resolved by incorporating a logarithmic dependence of the flame speed on the temperature and pressure terms. For methane LFS fitting, it was proposed [164] to modify the powerlaw [162] by incorporating the pressure effect on the temperature power coefficient

and by incorporating the temperature effect into the pressure power coefficient at various equivalence ratios [154]. Whereas, a temperature scaling factor at various equivalence ratios was introduced to fit the LFS of gasoline [166], and the same approach was used for fitting the LFS for various sets of toluene reference fuels [167]. The hydrogen LFS could be correlated using the power law [162] and the effects of the equivalence ratio and pressure coupled to calculate the reference flame speed S_{l0} and pressure exponent β [152]. The addition of water in hydrogen-air combustion has three main effects on flame speed: 1) a dilution effect reducing the net reaction rate, 2) a thermal-diffusion effect altering the thermodynamic and transport properties of the reactants, and 3) a chemical effect occurring due to the participation of the diluent in elementary kinetic reactions [168]. The chemical effect alters the reaction mechanisms not only by the presence of water in the elementary reactions, but the presence of water vapor also facilitates the third-body stabilization reactions [169]. Initial studies on hydrogen oxidation reactions established the basis for modeling hydrogen LFS [163], and substantial improvements have been made in recent decades in refining the reaction rates and mechanisms, all validated against various pressures, temperatures, and equivalence ratios.

2.3.2 Heat transfer

The hydrogen engine experiences a greater heat flux compared to carbon-based fuels. The heat transfer of an engine is commonly calculated using the correlations proposed by Woschni [170], Annand [171], and Hohenberg [172]. The correlations of Woschni and Annand are incapable of predicting the heat flux in a hydrogen engine when comparing a multi-zone model's maximum in-cylinder pressure and total heat release results with experimental data across various compression ratios, equivalence ratios, and spark timings [173], because the heat flux cannot be modeled with a characteristic velocity [174]. In addition, hydrogen's shorter quenching distance allows the flame to propagate closer to the cylinder walls leading to increased wall heat transfer. A hydrogen heat transfer model was proposed for specific operating conditions, though it requires more detailed information about hydrogen combustion [175]. Additionally, Shudo-Suzuki [176] developed a correlation for predicting heat

transfer in a hydrogen engine, stating that the Woschni correlation underpredicts the heat transfer due to increased heat flux compared to traditional hydrocarbon fuels [174]. However, if the Woschni correlation coefficient is properly tuned, the hydrogen heat transfer can be predicted accurately by multiplying the heat transfer coefficient by a factor of 2.2. This enabled the correlation to capture the performance of a hydrogen-fuelled SI engine under various operating conditions [177].

2.4 Exergy analysis of the ICE

Exergy is a useful concept for evaluating the performance of ICEs by identifying and quantifying the thermodynamic inefficiencies (losses) of the underlying irreversible processes [178, 179]. Exergy analysis can be conducted using experimental measurements or modeling engine components and systems [180]. The early work applying the second law to ICEs investigated the performance improvement of diesel [181] and gasoline [182] engines by identifying the exergy destruction associated with irreversibility. Unlike energy analysis, exergy analysis accounts for the quality of energy and captures the trade-offs between useful work output, combustion irreversibility, and the exergy carried away by exhaust gases. ICE exergy studies from 1960 to 2006 have been summarized [180, 183], while more recent studies focus on combustion strategies [184, 185, 186], alternative fuels [187, 188], and waste recovery systems [189, 190, 191]. Quantification of premixed and diffusion flames shows the main cause of entropy generation is the chemical reaction in premixed flames, whereas heat conduction was the primary cause in diffusion flames [192]. Previous studies using diesel and gasoline have incorporated detailed numerical chemical analyses into the combustion process to study the effect of operating conditions on exergy destruction or the potential relationship between various engine operating conditions [190, 193, 186]. Investigations of exergy destruction caused by the combustion process for a range of initial reactant temperatures, pressures, and equivalence ratios concluded that the initial reactants' temperature had the highest impact compared to other parameters [178]. Furthermore, the reactants' temperature and equivalence ratio were the most influential parameters regarding the exergy destruction [194, 193].

These previous studies do not translate directly to hydrogen engines because the physical and chemical properties of pure hydrogen differ significantly from hydrocarbon fuels. Exergy and energy analyses of a hydrogen HCCI engine with EGR concluded that engine speed had a smaller effect on exergy destruction compared to other parameters [195]. Increasing the intake temperature reduces combustion losses by reducing combustion-related entropy generation. Investigating the exergy split of a hydrogen SI engine at various equivalence ratios and spark timings showed for leaner fuel mixtures, exergy due to combustion irreversibility increased, mainly due to the decreasing combustion temperature [196]. However, when the spark timing was retarded, the exergy transfer to heat decreased, and the exergy carried by the exhaust gases increased. For a turbocharged hydrogen engine the load was the main influence on the exergy allocation [186]. Hydrogen as a combustion enhancer has also been studied [197, 198, 199, 200].

2.5 Summarising the research gaps

From the literature, it can be seen that there are no single- or two-zone studies correlating equivalence ratio, spark timing, compression ratio, and intake pressure to investigate the combustion characteristics, NO emissions, and knocking regions of a hydrogen SI engine with water addition. Water modulates the LFS in addition to its thermal and chemical effects on the reactive mixture, but no correlation for hydrogen-air combustion exists to account for the effects under engine-relevant conditions. Integrating this empirical correlation into a two-zone combustion model for predicting the performance, abnormalities in combustion, and NO emissions of a boosted lean-burn hydrogen SI engine operating in a water injection environment, the applicability of a new LFS can be demonstrated. By using a two-zone hydrogen combustion model, the indicated specific fuel consumption, NO, thermal efficiency, equivalence ratio, and water addition can be used to create an operational map for hydrogen. A comprehensive exergy analysis of hydrogen engines to assess efficiency has not been conducted, but the literature indicates the second law of thermody-

namics is well suited to studying the performance of ICE using alternative fuels.

Chapter 3

Methodology

Combustion modelling is a useful tool for understanding and optimizing ICEs. By accurately simulating the combustion process, the model can provide insights into in-cylinder properties, emissions, and efficiency that might be difficult and timeconsuming to obtain experimentally. Developing and validating combustion and emission models requires an understanding of the governing physics and chemistry. This chapter describes the theoretical development and implementation of single and two-zone combustion models to predict the performance, combustion abnormalities, and NO emissions of a boosted lean burn hydrogen spark ignition engine at various operating conditions. The operating conditions are described using equivalence ratio, manifold air pressure, start of combustion, and water addition rate. A detailed methodology of the second law of thermodynamics application to a hydrogen-fuelled ICE is given. The single-zone thermodynamic model is modified by incorporating a LFS sub-model. The two-zone hydrogen combustion model is advanced by incorporating an in-cylinder turbulence model based on input from advanced computational fluid dynamics simulations. Both the single and two-zone hydrogen combustion models incorporate sub-models for: NO emission, hydrogen adapted heat transfer, and knock integral prediction. The application is to study the nitric oxide emissions from a hydrogen-fuelled SI engine under boosted and lean burn operating conditions with and without water addition. The sub-models for LFS, heat transfer, NO emissions, and knock are calibrated using published experimental data for the hydrogen-fuelled SI engine.

3.1 Single-zone combustion model

Single-zone engine combustion models are simple, but can yield useful results. The zero-dimensional representation of the combustion process neglects the in-cylinder spatial information and therefore the thermodynamic state of the in-cylinder mixture is only given as a function of time or crank angle resolved. The combustion process was modelled by using the Wiebe function, which provides the mass fraction burned MFB as a function of the crank angle [113]. The function is written as:

$$MFB = 1 - e^{-a\left(\frac{\theta - \theta_{soc}}{\theta_{dur}}\right)^{m+1}}$$
(3.1)

where θ is the instantaneous crank angle, θ_{soc} is start-of-combustion crank angle, a and m are efficiency and form factors, respectively. The MFB in Equation (3.1) was linked to pressure and temperature through the laminar flame speed. The pressure and temperature are extracted from their motoring values at the start of combustion, respectively, and used in an empirical correlation that accounts for equivalence ratio, pressure, and temperature to calculate the flame speed. As, long as the hydrogen combustion can be accurately phased with similar combustion duration and profile as experimental data, the engine performance and emissions results will be reliable [201]. Furthermore, the small changes in the combustion profile or duration would only have a marginal effect on the in-cylinder pressure and could not invalidate the proposed analytical combustion methodology. The Wiebe function parameters are calibrated and validated with experimental data for each case presented (Chapters 4 and 6). Following the spark discharge it is assumed that flame grows spherically with a speed close to LFS. Then the LFS correlation is used to estimate the influence of the equivalence ratio, initial pressure, temperature and residual gas content upon the total burn duration at various engine speed and compression ratios [202]. For optimal performance, the CA50 location can be fixed at 8 °CA aTDC [140]. The specific heat ratio is replaced by a polytropic index appropriate for hydrogen-air mixtures [147]. The calculations are based on parametrising the Otto cycle considering spark advance and varying air-fuel ratios [203]. It is possible to describe in-cylinder pressure as a function of intake manifold pressure, temperature, crank angle, air-fuel ratio, and spark timing [204]. The calculations include the processes from the intake valve closing (IVC) to the exhaust valve opening (EVO). Firstly, the compression and expansion processes are modelled using a polytropic relation, then combustion will be obtained interpolating these two asymptotes using the Weibe function. The compression is modelled using the polytropic relation. First, the polytropic coefficient k and the reference point at IVC are needed. Equations 3.2 and 3.3 describe the compression pressure and temperature, respectively,

$$P_c(\theta) = P_{in} \left(\frac{V_d}{V(\theta)}\right)^k \tag{3.2}$$

$$T_c(\theta) = T_{in} \left(\frac{V_d}{V(\theta)}\right)^{k-1} \tag{3.3}$$

The initial pressure is the manifold pressure at the reference crank angle position. Due to simplicity the pressure drop across the valves is neglected,

$$P_{in} = P_{im}(\theta_{ivc}) \tag{3.4}$$

However, obtaining the initial temperature is challenging since it is influenced by residual gases. Assuming no changes in the chemical composition of the charge, the initial temperature can be calculated using a fraction of residual gases and intake manifold temperature. Expansion is modelled as a polytropic process using the polytropic coefficient k,

$$P_e(\theta) = P_3 \left(\frac{V_c}{V(\theta)}\right)^k \tag{3.5}$$

$$T_e(\theta) = T_3 \left(\frac{V_c}{V(\theta)}\right)^{k-1} \tag{3.6}$$

values of P_3 and T_3 refer to the third state in the ideal Otto cycle and are obtained from the temperature increase caused by combustion, expressed as:

$$\Delta T = \frac{(1 - x_r)Q_{hv}n_f(\lambda)}{\left(\lambda\left(\frac{A}{F}\right)_{st} + 1\right)c_v}$$
(3.7)

So, the temperature at state three is calculated using the temperature at the end of compression and the temperature increase during combustion:

$$T_3 = T_2 + \Delta T \tag{3.8}$$

hence,

$$P_3 = P_2 \frac{T_3}{T_2} \tag{3.9}$$

The pressure and temperature during the combustion process are given by:

$$P_{comb}(\theta) = (1 - f(\theta))P_c(\theta) + f(\theta)P_e(\theta)$$
(3.10)

$$T_{comb}(\theta) = (1 - f(\theta))T_c(\theta) + f(\theta)T_e(\theta)$$
(3.11)

3.2 Two-zone combustion model

In the two-zone combustion model, the mass inside the combustion chamber (incylinder charge) is divided into two zones (Figure 3.1): 1) the burned products, and 2) the unburned reactants, where both of the control volumes are assumed to be a mixture of ideal gases [112]. Later an entrained region is added to the two-zone model. This will allow the calculation of the mass fraction burned.

The chemical composition of the unburned reactants is assumed to be known throughout the simulation. The burned zone is classified in terms of the crank angle position with respect to the flame front, rather than a specific chemical composition. Each of the control volumes is assumed to have uniform temperature with no composition- or density-gradient occurring between the unburned and burned zones at any time [205]. The mass was assumed to be exchanged between the zones without mass loss due to blow-by. The cylinder chamber walls are assumed to have a constant and uniform temperature throughout the cycle. The flame front is considered to be of zero thickness, allowing the assumption that the fuel mass is consumed in the flame front in any instant [206]. Both the unburned and burned zones are treated as ideal gases, and it is assumed that there is no heat transfer between the two zones. Thus, the following equations would be applicable at any crank angle position throughout the combustion process:

$$V = V_b + V_u \tag{3.12}$$

$$m = m_b + m_u \tag{3.13}$$

$$PV_u = m_u R_u T_u (3.14)$$

$$PV_b = m_b R_b T_b \tag{3.15}$$

where P and V are the pressure and volume of each control volume, respectively. The total in-cylinder mixture mass is the sum of the burned zone mass, m_b , and the unburned zone mass, m_u . R is the gas constant. Thus, the equation of state can be written as:

$$PV = m_u R_u T_u + m_b R_b T_b \tag{3.16}$$

or,

$$PV = mR_u T_u + m_b (R_b T_b - R_u T_u) (3.17)$$

Based on the assumptions and after rearranging the equation of state, the first law, and the equation of mass conservation, the following first-order differential equations are derived to model the combustion process. The subscript u refers to the unburned zone and b refers to the burned zone, respectively:

$$\frac{dT_u}{d\theta} = \frac{1}{m_u c_{pu}} \left(V_u \frac{dP}{d\theta} + \frac{dQ_u}{d\theta} \right) \tag{3.18}$$

$$\frac{dT_b}{d\theta} = \frac{1}{m_u c_{pu}} \left[P \frac{dV}{d\theta} - (R_b T_b - R_u T_u) \frac{dm_b}{d\theta} - \frac{R_u}{c_{pu}} \left(V_u \frac{dP}{d\theta} + \frac{dQ_u}{d\theta} \right) + V \frac{dP}{d\theta} \right]$$
(3.19)

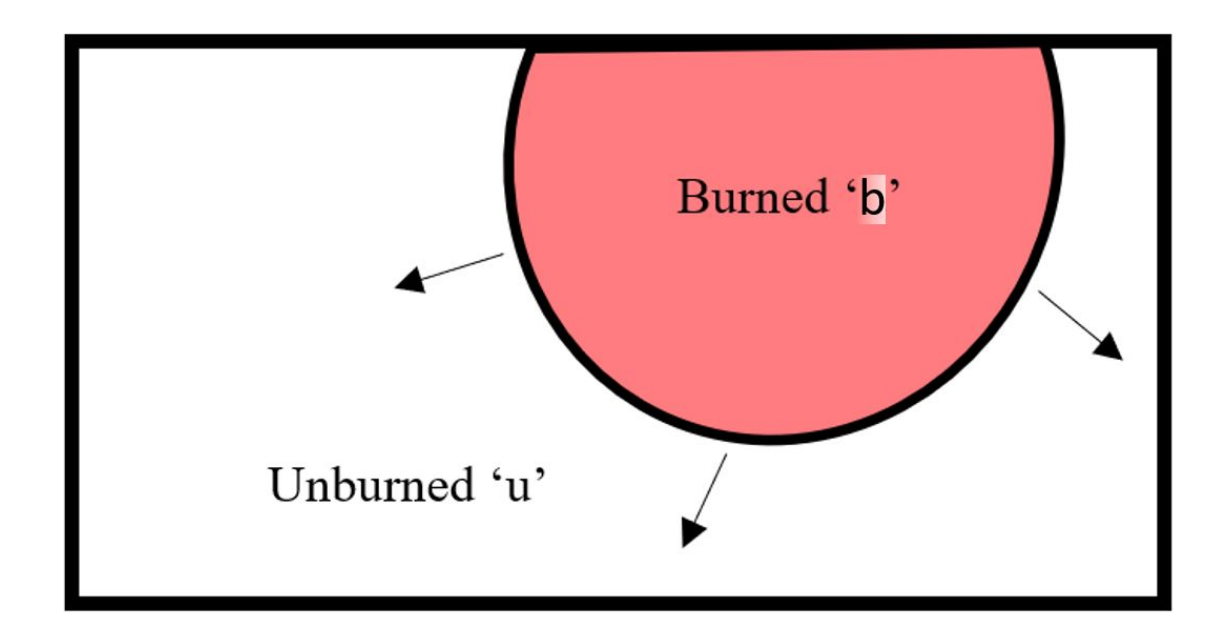


Figure 3.1: Zonal division for the two-zone combustion model.

$$\frac{dP}{d\theta} = \frac{1}{\frac{c_{vu}}{c_{pu}}V_u - \frac{c_{vb}R_u}{R_bc_{pu}}V_u + \frac{c_{vb}}{R_b}V} \times \left\{ \left(1 + \frac{c_{vb}}{R_b}\right)P\frac{dV}{d\theta} - \frac{dQ}{d\theta} + \left[(u_b - u_u) - c_{vb}\left(T_b - \frac{R_u}{R_b}T_u\right) \right] \frac{dm_b}{d\theta} + \left(\frac{c_{vu}}{c_{vb}} - \frac{c_{vb}R_u}{R_bc_{pu}}\right) \frac{dQ_u}{d\theta} \right\}$$
(3.20)

Where T_u and T_b are the temperatures of the unburned and burned zones, respectively. θ is the crank angle, m_u and m_b are the masses of the unburned and burned gases, and c_{pu} is the specific heat at constant pressure of the unburned mixture. Similarly, c_{vu} and c_{vb} are the specific heat capacities at constant volume of the unburned and burned gases, respectively. V_u refers to the volume of the unburned zone, while V is the volume of the combustion chamber. P is the in-cylinder pressure. R_u and R_b are the gas constants of the unburned and burned gases, respectively. The terms $\frac{dQ_u}{d\theta}$ and $\frac{dQ}{d\theta}$ represent the rates of heat transfer in the unburned zone and the total heat transfer, respectively. The total heat transfer, assuming a zero-dimensional heat flow, is given by:

$$\frac{dQ}{d\theta} = \frac{dQ_u}{d\theta} + \frac{dQ_b}{d\theta} \tag{3.21}$$

The two-zone combustion model was advanced by adding a third zone, usually referred to as the entrainment model [89]. Describing the flame surface shape is trivial using the entrainment model, since the turbulence cannot be spatially resolved. The entrainment model divides the combustion chamber into three zones (Figure 3.2) as:

- The unburned zone 'u' consists of the homogeneous fresh mixture,
- The burned zone 'b' consists of the burned mixture after the complete reaction,
- The entrained zone 'e' consists of the entrained mass but not yet burned.

With this zonal division, the entrainment model is able to compute the incylinder properties of the burned and unburned zones, and also offers the density changes within the flame front in comparison with the two-zone combustion model. The in-cylinder pressure and temperatures were calculated using the two-zone approach (Equations 3.18-3.20), and the mass fraction burned profile was calculated using the entrainment model, which considers the delay of burning of the charge with respect to the flame front.

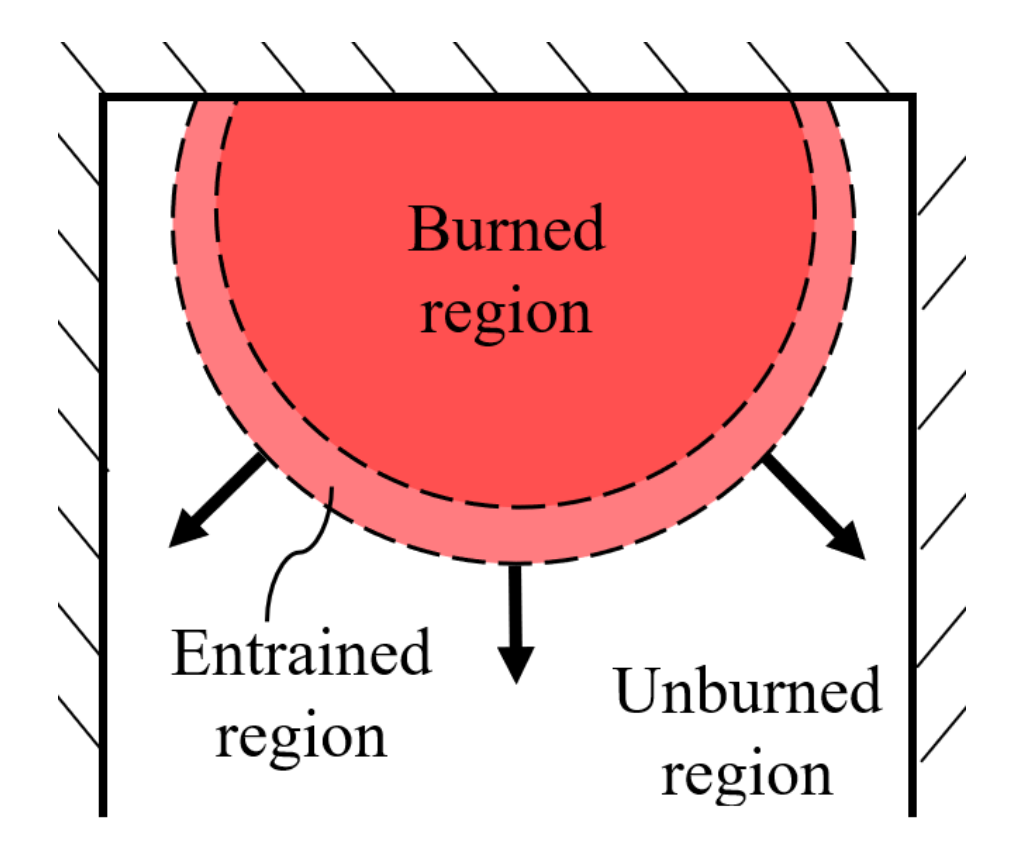


Figure 3.2: The zonal division for the entrained combustion model.

3.2.1 Mass fraction burned

An entrained region is needed to describe the effect of eddies generated inside the chamber. The eddies are characterized by change in density and volume of the combustion chamber. Eddies give rise to turbulence which has effect of increasing the flame speed. Hence, the flame was assumed to be travelling at the local LFS because the eddies generated during the intake process persist during combustion [207]. As it is assumed that the charge is homogeneous, the combustion process can be modelled as the propagation of a flame front with finite thickness. The propagation rate is determined by the rate at which the eddies are entrained, u_e [208]. The rate of the entrainment of the resting unburned gas is:

$$\dot{m}_e = \rho_u A_F u_e = \rho_u A_F (S_L + u')$$
 (3.22)

where \dot{m}_e is the entrained mass by the flame front, ρ_u is the unburned mixture

density, A_F is the flame front area, S_L is the LFS, and u' is the in-cylinder turbulence intensity. The density of the reactants was calculated based on the volume and mass of the unburned zone, while the burned zone density was calculated numerically by differentiating the mass fraction burned. Note that the cylindrical flame front starts at the centre of the spark plug and the flame front separates the zones. The rate at which the mixture is burned for a given time step is:

$$\dot{m}_b = \frac{m_e - m_b}{\tau_b} \tag{3.23}$$

The characteristic burning time, τ_b , was obtained by taking the ratio of the Taylor micro-scale length l_e to the laminar flame speed u, corrected by a factor C_{τ} .

$$\tau_b = C_\tau \frac{l_e}{u_l} \tag{3.24}$$

The mass fraction burned is given by Equation 3.23. To calculate this:

- 1. Calculate the turbulence intensity.
- 2. Calculate the LFS.
- 3. Calculate the thermodynamic properties of the in-cylinder mixture.
- 4. Calculate the flame area.

Turbulence in the fuel mixture occurs in the entrained zone which are modelled as eddies. The turbulence spans several length scales and is visualized in terms of eddies. An eddy is characterized by its local turbulence scale (mathematically is terms of wavelengths). Turbulent flows are dissipative, since turbulence is known to be a cascade process. Turbulence decays from large eddies to smaller eddies by transferring kinetic energy, with the smallest eddies dissipating as heat through molecular viscosity [209]. Figure 3.3 is a graphical representation of the common turbulence structures and length scales: integral length scale, Kolmogorov and Taylor length scales. The largest eddies are defined by the integral length scale which create velocity gradients resulting in turbulent stresses. These turbulent stresses create smaller eddies measured by Taylor length scale continually forming smaller

eddies measured by the Kolmogorov scale [210]. The energy transfer from large to small scales is determined by the interaction of these turbulence structures, with dissipation occurring at the smallest scales [211].

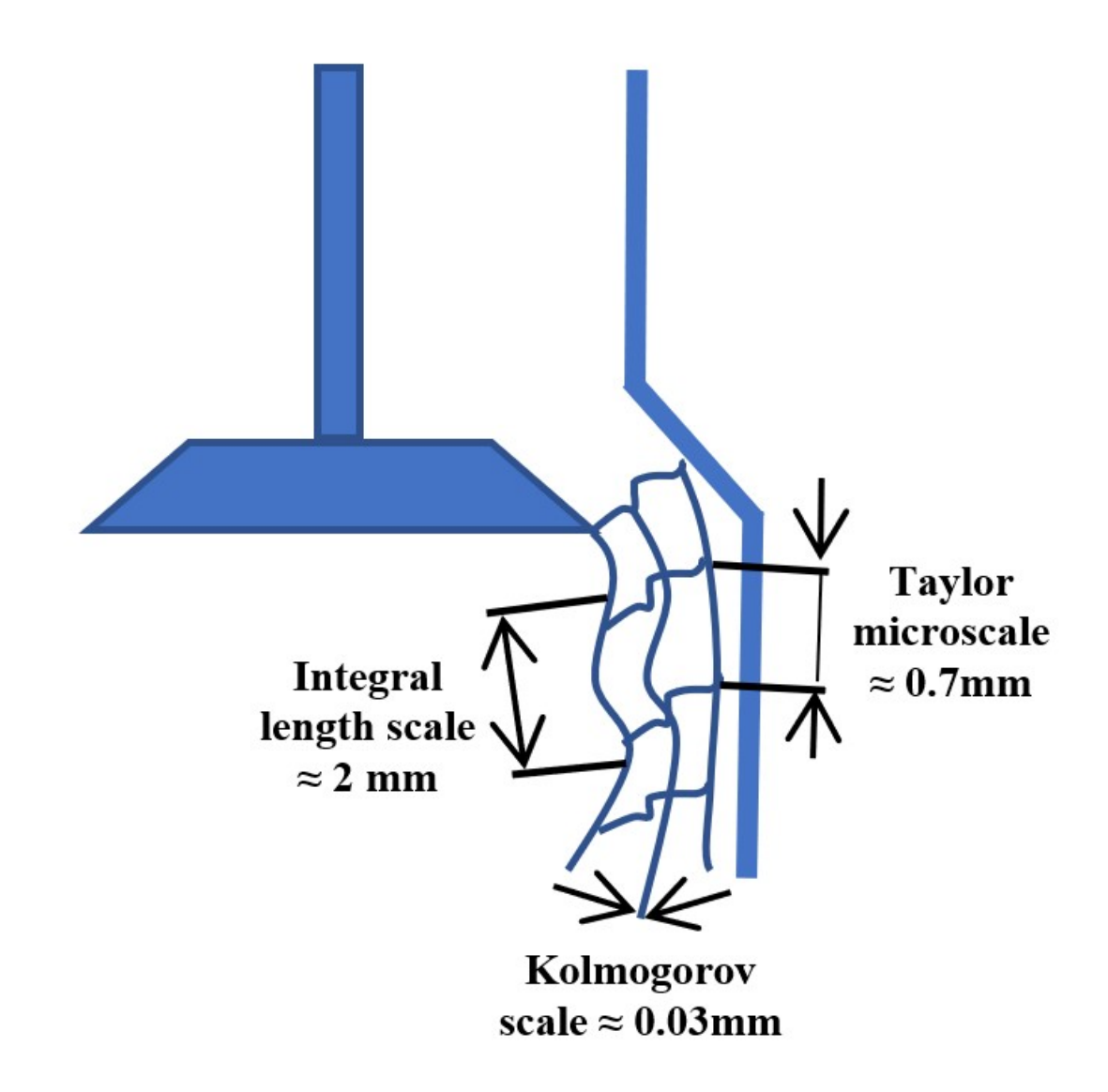


Figure 3.3: Typical length scales of turbulent structure during the intake process.

The largest scale (integral length scale) is a measure of the energy contained in the eddies. In ICE processes, the integral length scale is limited by the geometry of the cylinder. One of the accepted turbulent integral length scales l_I approaches is only associated with the cylinder geometry:

$$l_I = C_l \left(\frac{V_{cylinder}}{V_{cylinder,mean}}\right)^{\frac{1}{3}} \tag{3.25}$$

However, this approach does not accurately predict the global information of in-cylinder turbulence integral length scale for a wide variety of engine operating conditions, leading to a wrong Damköhler number and therefore uncertain turbulent speeds. Hunzinger et al. (2006) accounted for the flow structures by limiting intake valve lift L_{iv} and turbulence developed after intake valve closure k_{IVC} . Therefore, the integral turbulent length scale l_I is determined to be proportional to the turbulent kinetic energy (TKE):

$$l_I = L_{IV}^a \sqrt{\frac{k_{IVC}}{k}} \tag{3.26}$$

The variable k represents the in-cylinder turbulent kinetic energy, and the integral turbulent length scale was assumed to be proportional to k. The TKE produced by shearing forces on complex charge motion and intake flow is addressed by incorporating 3D CFD results back into the quasi-dimensional model of TKE during IVC. The main determinant of the combustion regime is described by the turbulent Damköhler number. The Damköhler number Da is the ratio of the characteristic turnover time τ_t of the largest eddies in the flow to the characteristic transient time τ_L through the laminar flame front:

$$Da = \frac{\tau_t}{\tau_L} = \frac{\frac{\lambda}{u'}}{\frac{\delta_L}{S_L}} = \frac{\lambda}{u'} \frac{S_L}{\delta_L} = \frac{\lambda}{u'} \frac{S_L}{\frac{v}{S_L}}$$
(3.27)

The flame thickness δ_L does not create a sharp boundary between the burned and unburned gases; instead, the species concentration, density, and temperature gradually transition between the two zones. The turbulence model must provide the velocity fluctuations u' from Reynolds' decompositions and the turbulent length scale L. A simple isotropic assumption can be used: $u' = \sqrt{\frac{2}{3}k}$. As per the laminar flame thickness, the distance between the unburned and burned gases can be difficult to quantify because the change between zones occurs gradually (over several mm). Therefore, the laminar boundary layer thickness is defined as a characteristic length for a given engine operational condition. In this study, the laminar layer thickness

is defined as a hydrodynamic length $\delta_L = \frac{v}{S_L}$ where v is the kinematic viscosity.

The Damköhler Da number is high when the flame front reaches the resting unburned mixture before the turbulence distorts it, which can lead to less in-cylinder turbulence with respect to laminar burning speed. When the (Da) number is low, it indicates that the chemical reaction rate is slower than the time it takes for turbulence to distort the flow. This means that turbulence has a greater influence on the unburned mixture. In summary, in SI engine operations, the flame propagation is dominated by the chemical reaction when the Da number is high, but dominated by turbulence when the Da number is low.

An accurate turbulence model should be able to describe the turbulence at various engine operating conditions and geometries. Without spatial information, the most commonly used approach for turbulence modeling is a combined k- ϵ equation. The calculation of the in-cylinder turbulent kinetic energy (TKE) is done using a zero-dimensional k- ϵ equation, where the source terms are turbulence production and dissipation rate:

$$\frac{dk}{dt} = \left(\frac{dk}{dt}\right)_{prod} - \epsilon \tag{3.28}$$

TKE produced by means of compression and expansion is expressed as:

$$\left(\frac{dk}{dt}\right)_{prod} = \frac{dk}{dt} = \frac{2}{3} \frac{k}{\rho} \frac{d\rho}{dt}$$
(3.29)

with:

$$\frac{d\epsilon}{dt} = \frac{4}{3} \frac{\epsilon}{\rho} \frac{d\rho}{dt} - C_2 \frac{\epsilon^2}{k} \tag{3.30}$$

The integral length scale l_I is determined to be proportional to the TKE k, and is calculated by:

$$l_I = L_{IV} \sqrt{\frac{k_{IVC}}{k}} \tag{3.31}$$

where L_{IV} is the intake valve lift and k_{IVC} is the TKE at IVC, determined using a 3D CFD (Converge) tool. A steady discharge analysis for each operating condition is performed. The in-cylinder turbulence is modeled by assuming that

the turbulence is isotropic and no turbulence is produced by boundary layer flow or diffusion.

In Figure 3.4, the zero-dimensional and three-dimensional TKE are compared for manifold air pressures (MAPs) for a premixed hydrogen/air mixture, showing that the zero-dimensional k- ϵ turbulence model performed well at predicting in-cylinder TKE compared to a 3D CFD simulation.

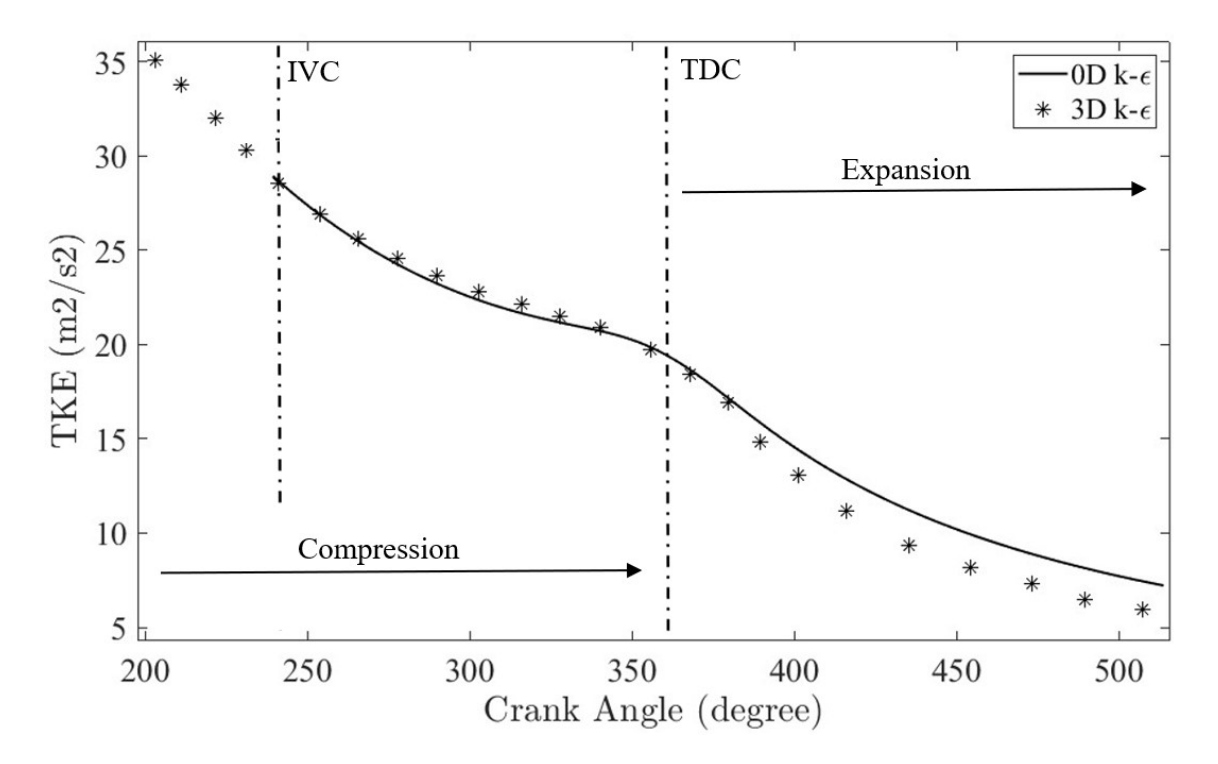


Figure 3.4: Turbulent kinetic energy (TKE) with crank angle (MAP=100 kPa, IVC=240 °CA, CR=11.5).

If the flame propagation is assumed to be perfectly spherical and the centre of the flame is fixed at a coordinate (independent of the real ignition coordinate), the flame front can be expressed as a function of the sphere radius r_f , piston position s_{pist} , and flame centre r_s [208]:

$$A_e = f(r_f, s_{pist}, r_s) (3.32)$$

The LFS is calculated from an empirical correlation for hydrogen/air mixtures at engine-relevant conditions. The LFS correlation is given in the form of:

$$S_L = S_{L,0}(\phi) \left(\frac{T_u}{T_o}\right)^{\alpha} \left(\frac{P}{P_o}\right)^{\beta} \tag{3.33}$$

where $S_{L,0}$ is the LFS measured at ambient conditions at a given equivalence ratio ϕ , when T_u corresponds to ambient temperature T_o and P corresponds to ambient pressure P_o , and α and β are mixture strength-dependant constants. The empirical LFS correlation of hydrogen at various engine-relevant operating conditions is discussed in Chapter 5.

Equation 3.32 requires the entrained flame area A_e to be determined, and it is computed using an approach proposed by Blizard and Keck [208] with the following assumptions:

- 1. Perfectly spherical flame propagation.
- 2. Wall and flame contact are defined as 'dead' state.
- 3. The centre of flame ignition is defined as a fixed coordinate (independent from the real position).
- 4. Flat piston geometry and pancake-shaped combustion chamber.

The flame surface sub-model calculates the flame radius corresponding to the burned volume (see Figure 3.5). The flame surface area between the unburned and burned zones, as well as the contact area with the chamber walls, was used to calculate the heat transfer. Integrating the burned mass gives the mass fraction burned.

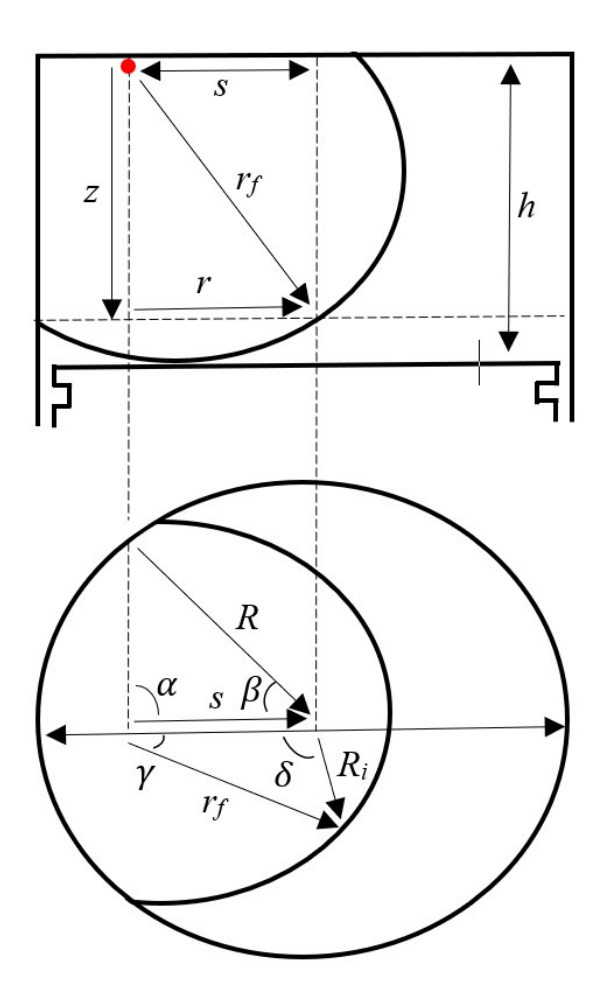


Figure 3.5: Illustration of the flame sphere (top) and the flame geometry at a given position z (bottom).

The radius of the flame at a position z is given by:

$$r = \sqrt{r_f^2 - z^2} (3.34)$$

The angles α , β , γ , and δ within the triangles constructed by the flame propagation are given by:

$$\alpha = \arccos\left(\frac{s^2 + r^2 - R^2}{2sr}\right) \tag{3.35}$$

$$\beta = \arccos\left(\frac{s^2 + R^2 - r^2}{2sr}\right) \tag{3.36}$$

$$\gamma = \arccos\left(\frac{s^2 + r^2 - R_i^2}{2sr}\right) \tag{3.37}$$

$$\delta = \arccos\left(\frac{s^2 + R_i^2 - r^2}{2sR_i}\right) \tag{3.38}$$

The flame front and entrained volume can be written as:

$$A_f = 2r_f \int_0^h \alpha \, dz \tag{3.39}$$

$$V_f = \int_0^h \left(\alpha r^2 + \beta R^2 - r_s R \sin \beta\right) dz \tag{3.40}$$

3.3 Heat transfer

Hydrogen behaves completely differently from traditional hydrocarbon fuels due to the increased heat flux inside the chamber for hydrogen combustion [175]. Since most of the heat transfer models are based on traditional hydrocarbon fuel, various heat transfer models are examined to find the most suitable for hydrogen [212]. The focus remains on the convective heat transfer because, for SI engines, the radiation mode is not as significant as it would be for compression ignition engines [213]. All heat transfer models assume that the heat transfer process occurring in the engine is quasi steady-state. All of the common zero and quasi-dimensional heat transfer models for wall heat flux are based on the Newtonian approach:

$$\frac{dQ_{loss}}{dt} = \alpha \Delta T \tag{3.41}$$

with α being the wall heat transfer coefficient and the temperature difference between the in-cylinder mixture and the chamber walls. Then, from the first law of thermodynamics, the heat release is given by:

$$dQ_{ch} = dU + dW + dQ_{loss} (3.42)$$

where the change of energy during combustion equals the change of the internal energy and the work done by the system. The derived heat release rate accounting for heat loss was modelled as:

$$\frac{dQ}{d\theta} = \frac{\gamma}{\gamma - 1} p \frac{dV}{d\theta} + \frac{1}{\gamma - 1} V \frac{dp}{d\theta} - dQ_{loss}$$
 (3.43)

In Equation 3.43, γ is the specific heat ratio of the mixture, p is the in-cylinder pressure, V is the instantaneous volume, and dQ_{loss} is the convective heat loss modelled using the Woschni correlation [170] as:

$$h_w = C \left[b^{-0.2} P^{0.8} T^{-0.55} U^{0.8} \right] \tag{3.44}$$

where b is the cylinder bore, P is the in-cylinder pressure, T is the in-cylinder temperature, and U_s is the average gas velocity. The average gas velocity is proportional to the mean piston speed, and to capture the density variations, the average gas velocity can be given as:

$$U_{s} = \left[C_{1}U_{p} + C_{2} \frac{T_{IVC}V_{d}}{V_{IVC}P_{IVC}} (P - P_{m}) \right]$$
(3.45)

where V_d is the displacement volume, P is the instantaneous pressure, V_{IVC} , P_{IVC} , and T_{IVC} are the cylinder volume, pressure, and temperature at a reference point taken at IVC, and P_m is the monitored pressure at the same crank angle as the piston instantaneous pressure p. U_p is the mean piston speed, which shows the distance traveled by the piston in one revolution per time required to complete the revolution at a particular engine rotational speed N. Constants C_1 and C_2 needed to model the gas velocity for each process are given in Table 3.1. The mean velocity is given as where the engine rotational speed is set to be 2000 revolutions per minute [214].

The mean piston speed is given by:

$$U_p = \frac{2sN}{60} \tag{3.46}$$

For the heat transfer sub-model to match the actual hydrogen heat release, the heat transfer coefficient in the standard Woschni correlation is multiplied by a factor of 2.2 [177]. This adjustment is due to the low quenching distance of hydrogen and the high burning velocity, resulting in greater cooling losses. Additionally, for

Table 3.1: Constants for gas velocity model for different processes.

Process	C_1	$\mathbf{C_2}$
Scavenging	6.18	0
Compression	2.28	0
Combustion and expansion	2.28	0.00324

hydrogen/air mixtures, the constant specific heat ratio is replaced by a temperature-dependent polytropic index that accounts for hydrogen-air mixtures [147].

3.4 Auto-ignition delay time and knock

Combustion abnormalities are the main factor limiting the thermal efficiency of SI engines and are related to charge density, compression ratio, and early spark timing [113]. Knock is defined as the autoignition of the unburned mixture at the end-gas when temperature and pressure are high, governed by the time available for a reactive mixture quicker than the autoignition delay time. Auto-ignition chemistry, leading to the onset of knock, τ_{knock} , is determined by integrating the inverse of the ignition delay time, τ [114]. Knock occurs when the value of the knock integral, KI, reaches unity:

$$KI = \int_{0}^{\tau_{knock}} \frac{dt}{\tau} \tag{3.47}$$

Since an Arrhenius correlation for hydrogen combustion is not available for varying equivalence ratios, the autoignition delay time for a hydrogen-air mixture was simulated using detailed chemical kinetics. The hydrogen autoignition delay time τ at various pressures, temperatures, equivalence ratios, and water addition was evaluated numerically using the Converge software [215]. A constant volume homogeneous reactor model was used to solve the energy equations. The equivalence ratio, pressure, and temperature were assumed to be spatially uniform throughout the reactor. Hence, the purpose of the model was to estimate the progress of the kinetic reactions as a function of time. The autoignition delay time values were generated using a reduced reaction kinetic mechanism [216]. The simulated data of the

autoignition delay time at different unburned mixture temperatures, pressures, and water additions were fitted using a least squares algorithm to obtain an expression for each equivalence ratio considered.

The proposed knock model only captures the autoignition of the unburned mixture at the end-gas. The presence of hot spots or emissions from unburned hydrogen of the previous cycle can also cause pre-ignition [45]. In this study, pre-ignition was not considered since the hot spots could not be identified for zero-dimensional models. However, the Arrhenius correlation presented in Equation 3.47 does not consider the direct chemical effects of equivalence ratio as well as the residual burnt gas effects on the autoignition delay time.

3.5 NO emissions

The major causes of nitrogen oxide emissions during combustion are the oxidation of nitrogen-containing compounds in the fuel (also known as fuel-bound NO), the production of NO in the flame zone, and the oxidation of nitrogen-containing molecules in the post-flame zone (thermal NO). This study concentrates on post-flame oxidation of NO because it is the primary cause of NO emissions from ICEs. The formation of NO is highly dependent on in-cylinder temperatures, oxygen concentration, and residence time for the reaction to take place. It can be assumed that, except for NO, all other species are in thermodynamic equilibrium due to fast reaction rates.

NO is formed at temperatures usually above 1800 K, and its formation is driven by the temperature of the burned gases. Therefore, eight non-linear equations based on the equilibrium constant expressions for reactions, along with four linear equations obtained from the conservation of the atomic mass of O, H, N, and C, can be written. Numerical solutions of these equations at an assumed corresponding combustion temperature determine the equilibrium mole number of each product. Then, the accuracy of the first law of thermodynamics is checked according to the calculated composition and the corresponding temperature. If the balance of internal energy of the reactants and products is not achieved within the stipulated

accuracy range, the combustion temperature is modified using the Newton-Raphson method until a solution is achieved.

The formation of NO is rate-limited due to its high dependency on temperature. Therefore, the extended Zeldovich mechanism has been used as the basic model for non-equilibrium NO formation [217]:

$$O + N_2 \rightleftharpoons NO + N$$

 $N + O_2 \rightleftharpoons NO + O$
 $N + OH \rightleftharpoons NO + H$ (3.48)

The system of reactions can be simplified and calculated as a single differential equation:

$$\frac{d[NO]}{dt} = 2R_1 \frac{1 - \left(\frac{[NO]}{[NO]_e}\right)^2}{1 + \frac{[NO]}{[NO]_e} \frac{R_1}{R_2 + R_3}}$$
(3.49)

where R_i are equilibrium rates defined by rate constants as:

$$R_{1} = k_{1}^{+}[O]_{e}[N_{2}]_{e} = k_{1}^{-}[NO]_{e}[N]_{e}$$

$$R_{2} = k_{2}^{+}[N]_{e}[O_{2}]_{e} = k_{2}^{-}[NO]_{e}[O]_{e}$$

$$R_{3} = k_{3}^{+}[N]_{e}[OH]_{e} = k_{3}^{-}[NO]_{e}[H]_{e}$$
(3.50)

3.6 Physical and chemical exergy

If a thermal system with the properties p, T, and N_k is interacting with its surroundings at P_0 , T_0 , and N_i , the interaction between this system and its surroundings occurs through the exchange of matter and heat, and the input or output of work, as illustrated in Figure 3.6. To determine how much useful work can be extracted from this system, it is assumed that the energy reservoir (the source) is large but finite, such that the intensive properties during the interaction of the system with the surroundings will not change.

The second assumption is that the reservoir equilibrates quickly, meaning that all the entropy is generated inside the system only.

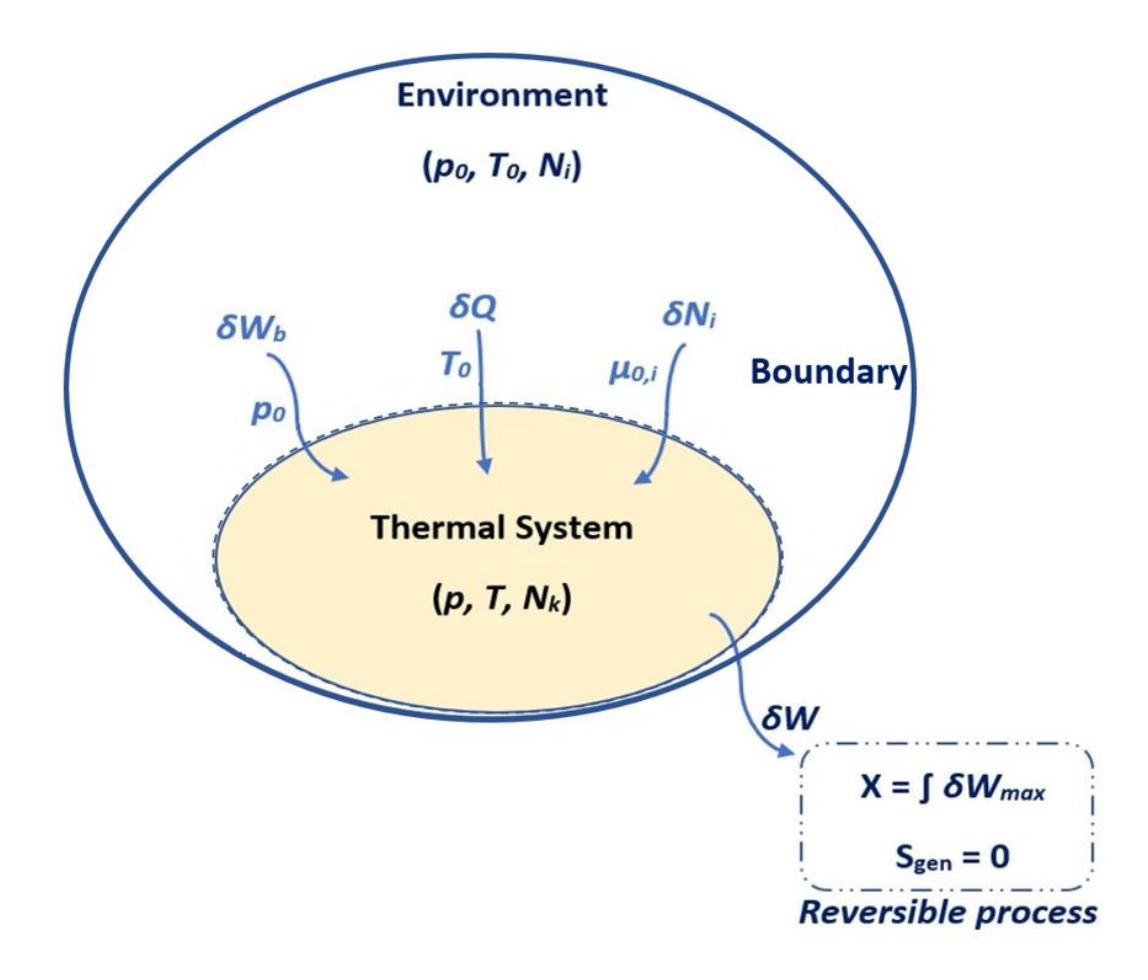


Figure 3.6: The thermal system with properties p, T, and N_k interacts with its surrounding environment characterized by P_0 , T_0 , and N_i .

For such a system, the first law of thermodynamics takes the form:

$$dU = \delta Q - \delta W_b + \sum_{k} \bar{h}_k \delta N_k - \delta W \tag{3.51}$$

where the change in internal energy increases with heat transfer δQ , and energy transferred per chemical specie $\sum_k \bar{h}_k \delta N_k$, where \bar{h}_k is the molar enthalpy and N_k is the number of moles of chemical species k, respectively. Internal energy decreases due to boundary work δW_b and work done outside the system δW .

To consider the entropy of the system, the second law of thermodynamics takes the form:

$$dS = \frac{\delta Q}{T_0} + \sum_{k} \bar{s}_k \delta N_k + \delta S_{gen} \tag{3.52}$$

where the change of entropy for this specific system increases with heat transfer with respect to the boundary temperature $\frac{\delta Q}{T_0}$, and with matter exchange $\sum_k \bar{s}_k \delta N_k$. The last term δS_{gen} expresses the entropy generated inside the system.

Rearranging Equation 3.51 to solve for δQ :

$$\delta Q = dU + \delta W_b - \sum_k \bar{h}_k \delta N_k + \delta W \tag{3.53}$$

Now, substituting δQ from Equation 3.53 into Equation 3.52:

$$dS = \frac{dU + \delta W_b - \sum_k \bar{h}_k \delta N_k + \delta W}{T_0} + \sum_k \bar{s}_k \delta N_k + \delta S_{gen}$$
 (3.54)

Multiplying through by T_0 :

$$T_0 dS = dU + \delta W_b - \sum_k \bar{h}_k \delta N_k + \delta W + T_0 \sum_k \bar{s}_k \delta N_k + T_0 \delta S_{gen}$$
 (3.55)

and solving for useful work (exergy) of the system δW :

$$\delta W = -dU - P_0 dV + T_0 dS + \sum_{k} (\bar{h}_k - T_0 \bar{s}_k) \delta N_k - T_0 \delta S_{gen}$$
 (3.56)

where the final term $T_0 \delta S_{gen}$ represents the destruction of the exergy and must be ≥ 0 .

The chemical potential $\mu_{k,0}$ is used for measuring the energy available for work when the particle number k changes due to a chemical reaction. The $\mu_{k,0}$ can be calculated as the partial derivative of Gibbs energy G with respect to k, at temperature T and pressure P:

$$\mu_{k,0} = \left(\frac{dG}{dN_l}\right)_{P,T,N_{l\neq k}} = h_k - T_0 s_k \tag{3.57}$$

where the Gibbs energy quantifies the maximum reversible work that could be extracted by a system at constant T and P. The Gibbs energy is given by G = H - TS, where H is the enthalpy, T is the temperature, and S is the entropy.

The reversible work δW_{rev} represents the maximum useful work that can be extracted from a system under reversible conditions. Moreover, reversible work is a fundamental concept for calculating the exergy, which is a measure of the maximum useful work potential that could be extracted from a system when it reaches equilibrium with its environment. By assuming $\delta S_{gen} = 0$ in Equation 3.56, the δW_{rev} can be formulated as:

$$\delta W_{rev} = -dU - P_0 dV + T_0 dS + \sum_{k} \mu_{k,0} \delta N_k$$
 (3.58)

Species k can be divided into environmental species i and non-environmental species j. The general transformation reaction of species j can be formulated as:

$$v_j N_j \to \sum_i v_{ij} N_i \tag{3.59}$$

where v_j is the stoichiometric value of species j, and v_{ij} is the molecular transfer from species j into species i. If during species transfer, it is assumed that the quantity of species i is proportional to the change of species j, it leads to the relation $\sum_{j} \left(\frac{v_{ij}}{v_j} dN_j \right)$, scaled by the stoichiometric ratio $\frac{v_{ij}}{v_j}$. Additionally, species i can also change independently, expressed as dN_i . Finally, the balance of environmental species i and non-environmental species j can be formulated as:

$$\delta N_i = dN_i + \sum_j \left(\frac{v_{ij}}{v_j} dN_j\right) \tag{3.60}$$

Note that no entropy is considered to be generated from the species transformation. Substituting δN_i from Equation 3.60 into Equation 3.58, the maximum useful work (or reversible work) can be described using:

$$\delta W_{rev} = -dU - P_0 dV + T_0 dS + \sum_{i} \mu_{i,0} dN_i + \sum_{i} \mu_{i,0} \sum_{j} \left(\frac{v_{ij}}{v_j} dN_j \right)$$
(3.61)

The right side of Equation 3.61 has exact differentials with constant coefficients, so its integration is path independent; hence, it can be integrated using two paths:

1. At fixed composition to the thermo-mechanical dead state (restricted), with no reaction or diffusion permitted.

2. At fixed thermo-mechanical state, with reaction and diffusion permitted to the environmental true dead state (unrestricted).

Thus:

$$X = \int_{\text{Resource state}}^{\text{Restricted dead state}} (-dU - P_0 dV + T_0 dS)$$

$$+ \int_{\text{Restricted dead state}}^{\text{True dead state}} (-dU - P_0 dV + T_0 dS)$$

$$+ \sum_{i} \mu_{i,0} dN_i + \sum_{i} \mu_{i,0} \sum_{j} \left(\frac{v_{ij}}{v_j} dN_j\right)$$

$$(3.62)$$

where the first integral is the thermo-mechanical exergy X_{TM} , and the second integral is the chemical exergy X_{CH} . Hence, the internal exergy of the resource becomes $X_{int} = X_{TM} + X_{CH}$. Adding the external exergy in the form of kinetic energy KE and potential energy PE, the internal exergy gives the total exergy of a resource $X = X_{TM} + X_{CH} + KE + PE$. Note that no reaction occurs for the thermo-mechanical exergy X_{TM} . Moreover, X_{TM} can be rewritten as:

$$X_{TM} = \int_{\text{Resource state}}^{\text{Restricted dead state}} (-dU - P_0 dV + T_0 dS)$$

$$= (U - U_{TM}) + P_0 (V - V_{TM}) - T_0 (S - S_{TM})$$

$$= (U + P_0 V - T_0 S) - (U_{TM} + P_0 V_{TM} - T_0 S_{TM})$$
(3.63)

where the thermo-mechanical exergy is stated as the difference between the availability with Gibbs energy $X_{TM} = A - G_{TM}$ at the thermo-mechanical dead state with fixed original chemical composition. The availability can be grouped in the same way:

$$A(P,T) = U + P_0V - T_0S = H - T_0S$$
(3.64)

where H and S are enthalpy and entropy, respectively. The availability A is usually considered to be the same as exergy X. The difference is that availability A is the system state evaluation with respect to initial conditions (P_0 and T_0),

whereas the exergy X relates between the system and its surroundings, concurrently evaluating the availability change between two states.

The second term of Equation 3.62 represents the chemical exergy, which integrates to:

$$X_{CH} = \int_{\text{Restricted dead state}}^{\text{True dead state}} \left(-dU - P_0 dV + T_0 dS \right) + \sum_{i} \mu_{i,0} dN_i + \sum_{i} \mu_{i,0} \sum_{j} \left(\frac{v_{ij}}{v_j} dN_j \right)$$

$$= (U_{TM} - U_0) + P_0 (V_{TM} - V_0) - T_0 (S_{TM} - S_0)$$

$$- \sum_{i} \mu_{i,0} (N_{i,TM} - N_{i,0}) - \sum_{i} \mu_{i,0} \sum_{j} \left(\frac{v_{ij}}{v_j} (N_{i,TM} - N_{i,0}) \right)$$
(3.65)

Cancelling the environmental intensive states with unknown extensive composition gives:

$$X_{CH} = (U_{TM} + P_0 V_{TM} - T_0 S_{TM}) - \sum_{i} \sum_{i} \mu_{i,0} \left(\frac{v_{ij}}{v_j} N_j\right)$$
(3.66)

where the chemical exergy X_{CH} is the chemical potential of the resource at the thermo-mechanical dead state and the chemical potential of the environmental species j formed from the species originally present in the system j at the true dead state. The chemical exergy is defined as the difference between the chemical potential (the Gibbs function) of the resource before and after it has reacted and diffused to be part of the environment, all at the true dead state, thus:

$$X_{CH} = G_{TM} - G_0 (3.67)$$

Finally, the total exergy is formulated as:

$$X = X_{TM} + X_{CH} = (A - G_{TM}) + (G_{TM} - G_0) = A - G_0$$
 (3.68)

Note that there are two references used in the previously derived equations: the restricted dead state and the true dead state. The difference is that the composition of the restricted dead state is fixed as the initial reservoir composition (no reaction or diffusion), while the mixture composition of the true dead state is in equilibrium with the environmental surroundings (Figure 3.7). Both the restricted and true

dead states are at P_0 and T_0 . The transition to the true dead state with a typical air composition would involve further interaction with the environment, in terms of diffusion of the molecular species and chemical reactions [218]. The environmental conditions are assumed to be the true dead state conditions. For ICEs applications, the environmental pressure and temperature are mostly set to 1.01 bar and 298 K, respectively. The molar concentrations of the species are set to be: 20.35% O_2 , 75.67% O_2 , 0.03% O_2 , 3.03% O_2 0, 3

The thermodynamic properties for each species are based on curve fitting of the thermodynamic data [113]. The assumptions are that the unburned mixture has unchanging composition and that the burned mixture is in equilibrium. The specific heat, standard state enthalpy, standard state entropy, and specific internal energy are calculated using the polynomials shown in Equations 3.69–3.71, to determine unburned and burned mixture properties:

$$\frac{c_p(T)}{R} = a_1 + a_2T + a_3T^2 + a_4T^3 + a_5T^4 \tag{3.69}$$

$$\frac{h(T)}{R} = a_1 + \frac{a_2T}{2} + \frac{a_3T^2}{3} + \frac{a_4T^3}{4} + \frac{a_5T^4}{5} + \frac{a_6}{T}$$
 (3.70)

$$\frac{s(T)}{R} = a_1 \ln T + a_2 T + \frac{a_3 T^2}{2} + \frac{a_4 T^3}{3} + \frac{a_5 T^4}{4} + a_7 \tag{3.71}$$

The internal energy is given by:

$$u = h - RT (3.72)$$

Values for coefficients a for H₂, O₂, N₂, and H₂O [113] are given for two temperature ranges. The first range, from 300 K to 1000 K, is appropriate for the unburned mixture properties, and the range from 1000 K to 5000 K is used for the burned mixture properties.

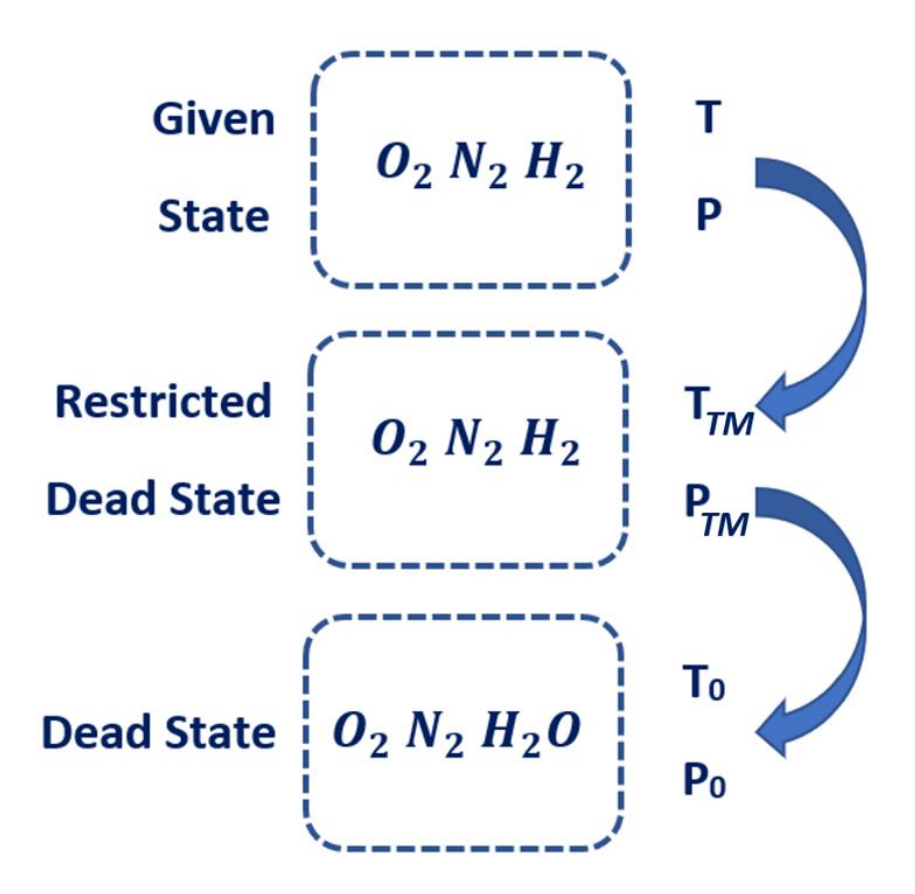


Figure 3.7: Illustration of the system at a given state, restricted dead state, and true dead state. To calculate the physical exergy, a process occurs which changes the temperature and pressure of the system to the restricted dead state; however, the system's chemical composition is not changed by this process. To calculate the chemical exergy of the system, another process occurs where the chemical composition changes, but the pressure and temperature of the system remain constant $(P_{TM} = P_0 = 1 \text{ bar and } T_{TM} = T_0 = 298.15 \text{ K}).$

3.6.1 Exergy transfers

The exergy transfer to indicated work is:

$$\frac{dX_{Work}}{d\theta} = (P - P_0)\frac{dV}{d\theta} \tag{3.73}$$

where P is the instantaneous in-cylinder pressure, P_0 is the pressure at the restricted dead state, and V is the volume of the cylinder. The in-cylinder pressure was taken from the two-zone hydrogen combustion model.

The exergy transfer to heat between the in-cylinder mixture and chamber wall is:

$$\frac{dX_{Heat}}{d\theta} = -\left(1 - \frac{T_0}{T}\right)\frac{dQ_{ht}}{d\theta} \tag{3.74}$$

where T_0 and T are the initial and in-cylinder mixture temperatures, respectively. The convective heat loss Q_{ht} is modeled using the Woschni correlation [170].

The hydrogen chemical exergy is:

$$X_{CH} = (U_{TM} + P_0 V_{TM} - T_0 S_{TM}) - \sum_{i} \sum_{i} \mu_{i,0} \left(\frac{v_{ij}}{v_j} N_j\right)$$
(3.75)

where the chemical exergy X_{CH} is the chemical potential of the resource at the thermo-mechanical dead state and the chemical potential of the environmental species j formed from the species originally present in the system i at the environmental dead state.

The exergy destruction due to combustion irreversibility was calculated as a function of the reaction rate and the difference between the chemical potential of the reactants and products. The entropy generation is formulated as:

$$\frac{dX_{Comb}}{d\theta} = -T_0 \frac{dS_{Gen}}{d\theta} = \frac{T_0}{T} \sum_i \mu_{i,0} \frac{dm_i}{d\theta}$$
 (3.76)

where the chemical potential μ_i is set to be X_{Chem} for the fuel, and Gibbs energy G_i for other gases.

The exergy expelled by exhaust was calculated as the thermo-mechanical exergy at the EVO:

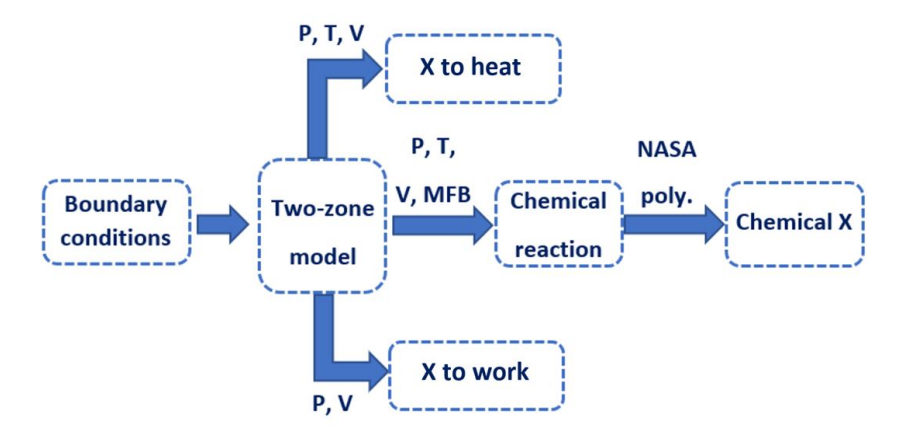


Figure 3.8: Schematic of the methodology for the exergy analysis where the symbols have their usual meaning and NASA poly. are empirical correlations to calculate mixture thermodynamic properties taken from [113].

$$X_{exh} = X_{(\theta = EVO)} \tag{3.77}$$

The in-cylinder exergy was calculated using Equation 3.62 when the specific internal energy, volume, and entropy of the gas are known.

The combustion and exergy models were developed in MATLAB (version 2021). The code was run on a Dell Precision 3660 desktop with a 13th Gen Intel(R) Core(TM) i7-13700K CPU running at 3.4 GHz, featuring 16 cores and 24 logical processors, supported by 32 GB of physical RAM. The simulations, which involved solving ordinary differential equations using MATLAB's ode45 solver, were performed very quickly, with each run completing in seconds. A summary of the modeling approach is outlined in Figure 3.8.

3.6.2 Combined top-down and bottom-up exergy approach

In the bottom-up approach, the irreversibility due to heat transfer, combustion, and exhaust are summed. In contrast, the top-down approach calculates the total engine irreversibility by taking the difference between the exergy input and the output. It should be noted that the top-down approach is a global method that does not identify or quantify losses; it solely depends on the exergy flow crossing the control volume boundary. A combined bottom-up and top-down approach has been applied,

where the inefficiencies of the hydrogen engine operating at various conditions were identified and quantified using the bottom-up approach. However, the efficiency was calculated using the top-down approach because unidentified exergy was present, leading to the use of the lower engine efficiency.

Chapter 4

Single-zone model of a hydrogen SI engine

Single-zone engine combustion models are simple but can yield useful results as a step in the design process for developing alternative fuel systems. The basic single-zone thermodynamic model described in Section 3.1 of the methodology is advanced by implementing a laminar flame speed (LFS) sub-model to investigate combustion, an extended Zeldovich mechanism for NO emissions, and incorporating the Livengood-Wu integral model for knock characteristics.

4.1 Incorporating the laminar flame speed sub-model

The single-zone model is modified by incorporating LFS to predict the combustion duration with respect to the reference operating conditions by using the inverse relative change in the LFS [202]. When the total combustion duration $(\Delta\theta)$ is linear with burn duration $(\Delta\theta_0)$, then:

$$\Delta\theta = \Delta\theta_0 \, g_{SL} = \Delta\theta_0 \, \frac{g_{SL}}{g_{SL,0}} \tag{4.1}$$

where the function g incorporates the influence of LFS on burn duration. The determined combustion duration for each operating case is used in the Wiebe function (Equation 4.2), giving the gross energy released by the hydrogen-air mixture as a function of crank angle:

$$x_b = 1 - \exp\left[-a\left(\frac{\theta - \theta_{soc}}{\Delta\theta}\right)^{m+1}\right] \tag{4.2}$$

where θ is the instantaneous crank angle, θ_{soc} is the start-of-combustion crank angle, a (set at 6.9) and m are efficiency and form factors, respectively, and $\Delta\theta$ is the combustion duration (Equation 4.1). The experimental data for the combustion duration and shape factor m is fitted using the least-square method. The maximum error between the experimental and simulated value of m at various operating conditions was found to be 12% ($R^2 = 0.895$).

A correlation of LFS for a hydrogen-air mixture as a function of equivalence ratio, pressure, and temperature [162] is:

$$S_L = S_{L,0}(\phi) \left(\frac{T_u}{T_o}\right)^{\alpha} \left(\frac{P}{P_o}\right)^{\beta} \tag{4.3}$$

where $S_{L,0}$ is the LFS measured at ambient conditions at a given equivalence ratio ϕ when T_u corresponds to ambient temperature T_o , and P corresponds to ambient pressure P_o , and α and β are mixture strength-dependent constants. Moreover, P and T_u are the pressure and temperature at the start of the combustion for each operating condition and are obtained using the polytropic relation. The effect of residual gases on the LFS is not considered since it did not vary the ratio in Equation 4.1. Due to the flammability limits of hydrogen, the computation of LFS is performed for a wide range of equivalence ratios to validate the model against the available experimental studies [157, 219, 220, 221]. However, few studies are available at the relevant conditions [149, 150, 152]. The derived analytical correlations of hydrogen LFS at elevated temperatures and pressures for equivalence ratios are shown in Table 4.1, and are easily implemented into spark ignition engine simulations [222]. The laminar flame speed empirical correlations are valid only within their specified ranges presented in Table 4.1; using them outside those limits may lead to inaccurate results due to the nature of polynomial fitting

Comparing the experimental data of LFS [157, 221, 219, 220] with predictive calculations using the correlations of [149, 150, 223], the laminar burning velocity shows similar behavior for a range of equivalence ratios from 0.5 to 3.0, with peak

Table 4.1: Hydrogen LFS correlations from various studies.

Reference	Pressure	Temperature	Equivalence
	(MPa)	(K)	Ratio (-)
Verhelst [223]	0.1 – 1.0	300-430	0.30-1.00
Verhelst et al. [152]	0.5 – 4.5	500-900	0.33 – 5.00
Ravi and Petersen [150]	0.1 – 3.0	270-620	0.50 – 5.00
Gerke et al. [149]	0.5 – 4.5	350-700	0.36 – 2.50
	0.1 - 8.0	300-900	0.40 – 3.75

burning velocities located in the rich region from 1.4 to 2.0 with magnitudes between 2.5–3.0 m/s (Figure 4.1). The computational flame speed curve accurately predicts the experimental data in the lean-burn region, but the maximum flame velocity is underestimated with respect to the data of [219].

Thermo-diffusivity and hydrodynamic instabilities are likely to be prevalent under engine operating conditions and can modulate the flame speed [157]. Thus, the computed flame speed might underpredict the burning velocity at elevated pressures. Nevertheless, the burning velocity of different mixture compositions will only be used to calculate the change of combustion characteristics at various equivalence ratios, spark timing, and intake pressure; hence it does not represent the laminar flame propagation nor the turbulent burning velocity. However, there is a trade-off between ease of use and the level of complexity of a model, and incorporating LFS is a useful addition to the single-zone model. Figure 4.2 shows that, for the equivalence ratio range used, the correlations [149, 152] are most useful due to extended lean-burn limits at wider ranges of pressures and temperatures. The LFS correlation of Verhelst et al. [152] can be incorporated in neat hydrogen spark ignition engine simulations, and the correlation provided acceptable results [222].

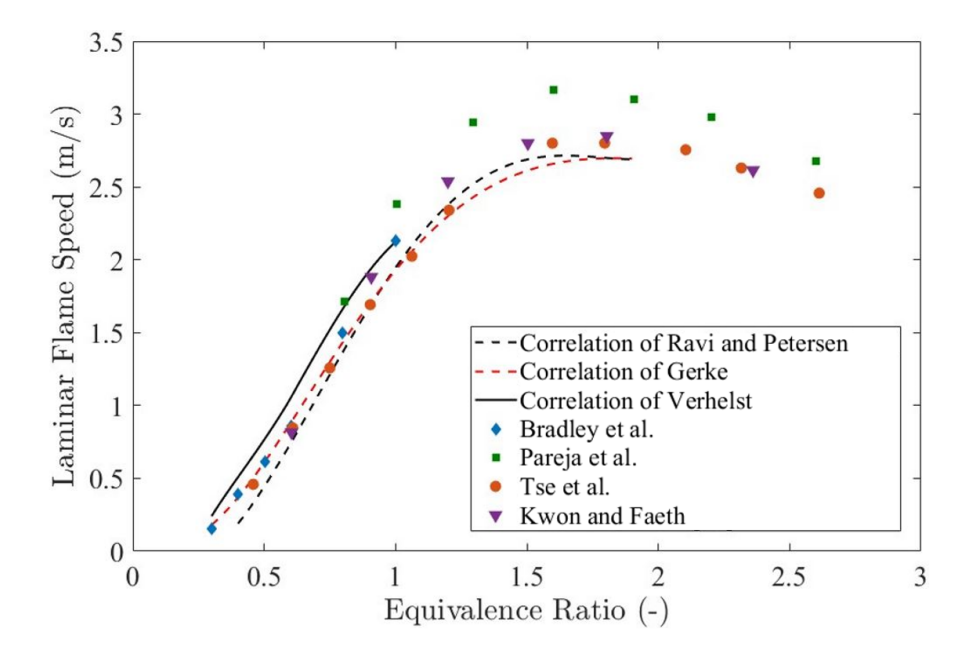


Figure 4.1: Hydrogen-air mixture laminar burning velocity as a function of equivalence ratio at engine-relevant conditions ($T_0 = 300 \,\mathrm{K}, P_0 = 1 \,\mathrm{atm}$). Experimental values [157, 221, 219, 220] are presented as symbols, while computational results are presented as lines (Correlation 2 is used from Gerke et al. [149]).

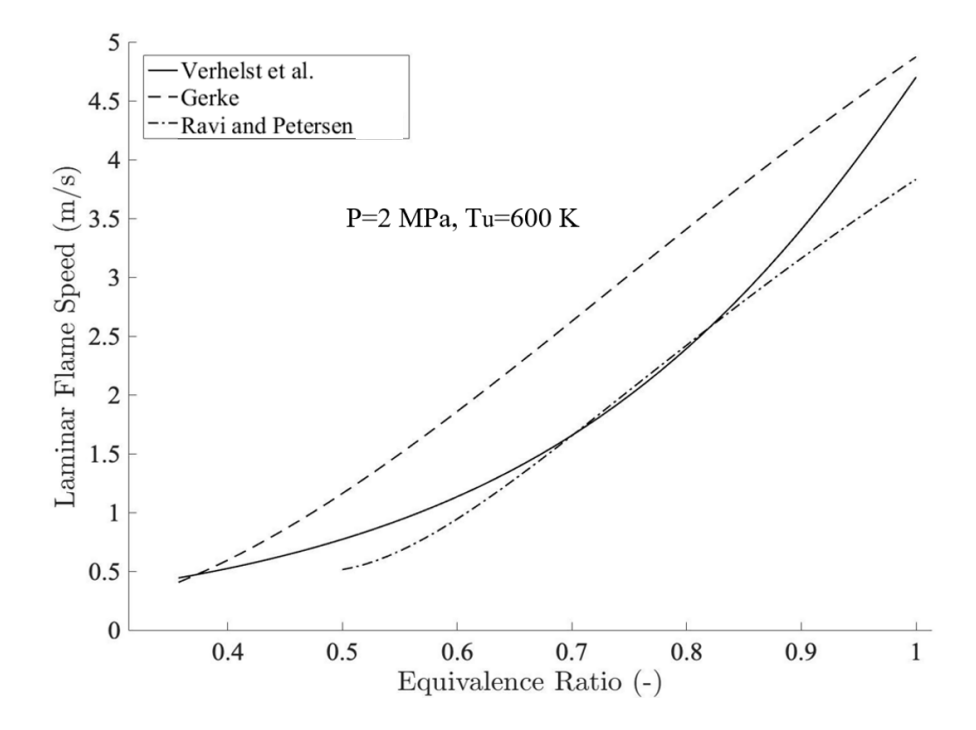


Figure 4.2: LFS of hydrogen at engine-relevant conditions for equivalence ratio at $P_0 = 0.5 \,\mathrm{MPa}, T_0 = 350 \,\mathrm{K}$ (Correlation 1 is used from Gerke et al. [149]).

4.2 Validating the single-zone combustion model

The main purpose of incorporating the LFS into the single-zone model is not to represent the laminar flame propagation or turbulent burning velocity, but to calculate the variation in the combustion characteristics across various equivalence ratios, spark timings, and intake pressures. Without the incorporation of the LFS, it is not feasible to evaluate the global performance parameters using a less complex single-zone model. The intention of this work is therefore to provide a simplified laminar flame scaling approach, yet make a useful addition to the single-zone approach. The scaling of the combustion duration with the LFS of hydrogen for varying engine operating conditions has been effective in determining the main combustion parameters through the Wiebe equation for hydrogen engines. Table 4.2 below represents the predicted shape factor m, CA50, and IMEP. It can be seen from the analysis that the simulated results are not far from reality. The model is simple yet provides accurate results for the lean-burn hydrogen SI engine. The model has been validated with the available hydrogen data of Sementa et al. [47] and Gürbüz and Akçay [92] for various engine-relevant conditions.

Table 4.2: Simulated IMEP

λ (-)	ST (bTDC)	IMEP (bar)	m coefficient	m simulated	Simulated IMEP (bar)	IMEP error
						(%)
1.29	3.6	6.14	2.58	2.57	5.97	2
1.39	4.6	5.72	2.68	2.72	5.67	1
1.60	10	5.08	2.94	2.59	5.41	6
1.81	8.6	4.72	2.37	2.45	4.86	3
2.00	12.6	4.36	2.00	2.04	4.67	7
2.20	14.6	4.13	1.57	1.55	4.38	6
2.41	18.6	3.87	1.21	1.09	4.08	5
2.60	20.6	3.66	0.79	0.82	3.77	3

Additionally, to assess the single-zone model, the in-cylinder pressure at various operating conditions was compared to two previously published experimental data for a hydrogen-fuelled SI engine. For the baseline results, the equivalence ratio and the Wiebe function parameters were adjusted to match the simulated results with the available experimental engine data. The simulation results for in-cylinder

pressure and heat release rate at different equivalence ratios, spark timings, and engine speeds were validated using the published experimental data of Sementa et al. [47]. The corresponding specifications of their single-cylinder engine are given in Table 4.3. The effects of lean-burn operation and intake air pressure boosting on engine performance were validated with the study of Gürbüz and Akçay [92].

Table 4.3: SI engine specifications used in simulations.

Characteristic	Sementa et al. [47]	Gürbüz and Akçay [92]		
Bore x Stroke [mm]	72.0×60.0	85.7 x 82.6		
Displacement Volume $[cm^3]$	244.3	476.5		
Speed [rpm]	2000	1600		
Compression Ratio [-]	11.5	8.0		

The in-cylinder pressure data was selected to assess the effectiveness and reliability of the numerical model. Figure 4.3 presents the experimental and numerical results for the in-cylinder pressure and heat release rate variations at two lean operating conditions ($\lambda=1.30$ and $\lambda=2.00$) at 2000 rpm and a compression ratio of 11.5. The model predictions were satisfactory during the compression and expansion processes, but a difference of more than 2σ was observed during the combustion process. The simulated in-cylinder combustion pressure profile was under-predicted due to the lack of detailed chemical reaction mechanisms, assuming that the burning velocity is laminar, and not accounting for the effect of thermal diffusivity and pressure attributed to Darrieu-Landau instabilities [157]. The quantitative variation between the experimental data and model results was evaluated, and the standard error (ε) was found to be 3% for $\lambda=1.30$ and $\lambda=2.00$ conditions with a maximum deviation value $d_{\rm max}$ of 142 kPa. Moreover, the heat release rate for both lean operating conditions at $\lambda=1.30$ and $\lambda=2.00$ was predicted satisfactorily by the current model, which also accounts for heat loss.

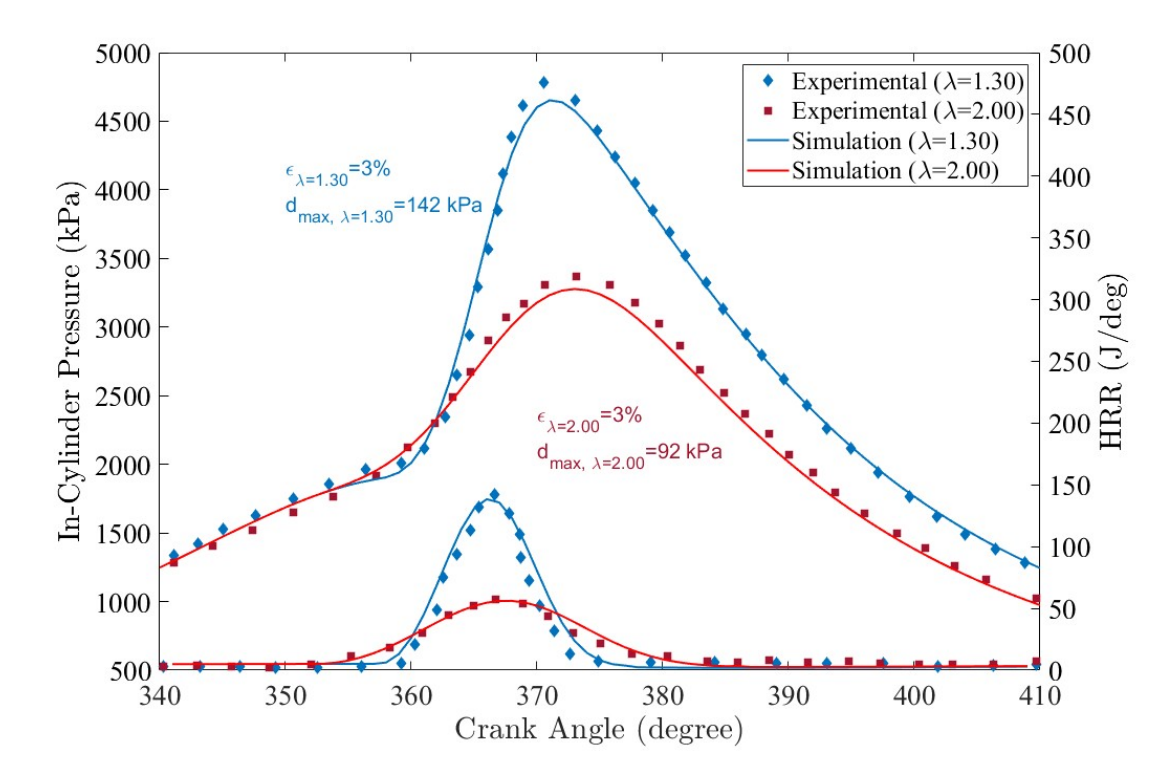


Figure 4.3: In-cylinder pressure and heat release rate of the hydrogen-air mixture; experimental values [47] are presented as symbols, while computational results are presented as a solid line (MAP = 84 kPa, CR = 11, N = 2000 rpm, $ST_{\lambda=1.30}$ = 3°CA bTDC, $ST_{\lambda=2.00}$ = 12°CA bTDC).

Figure 4.4 shows the validation of simulated indicated mean effective pressure and maximum in-cylinder pressure at various spark timings from 30° bTDC to TDC for different intake pressures. The simulation results were compared with the experimental work of Gürbüz and Akçay [92]. The maximum error of the simulated results was 3%, which is within the cycle-to-cycle variation of the experimental conditions. The fuel mass flow rate was calculated based on the density changes associated with increasing the intake MAP, and it has been validated with experimental data as shown in Figure 4.5. Note that the density fuel mass flow rate in the ITE calculations was incorporated.

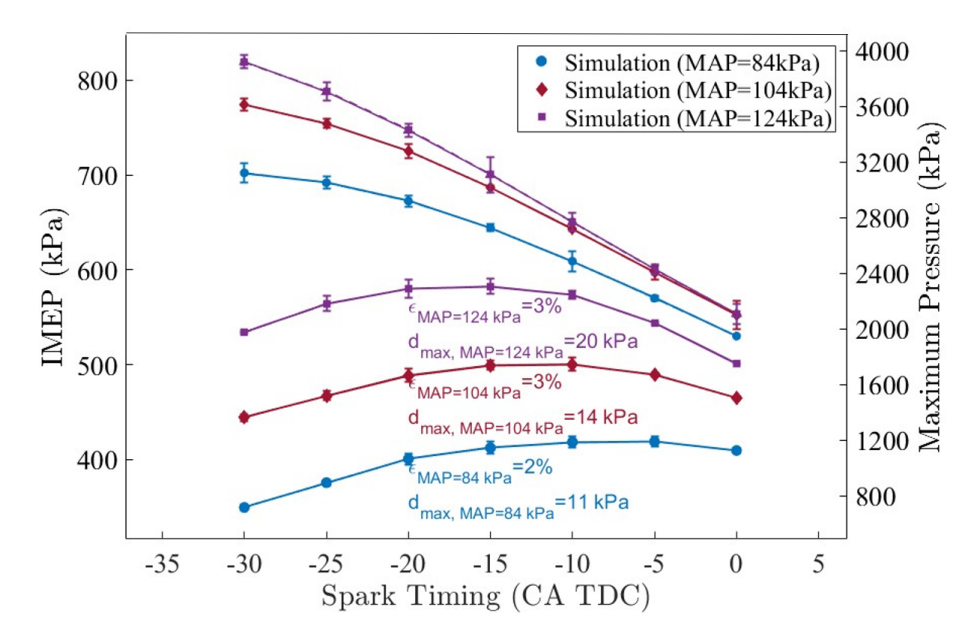


Figure 4.4: Experimental and simulated results for indicated mean effective pressure and maximum in-cylinder pressure at an equivalence ratio of 0.6. Experimental values [92] are presented with error bars, while computational results are presented as a solid line (CR = 8.1, N = 1600 rpm).

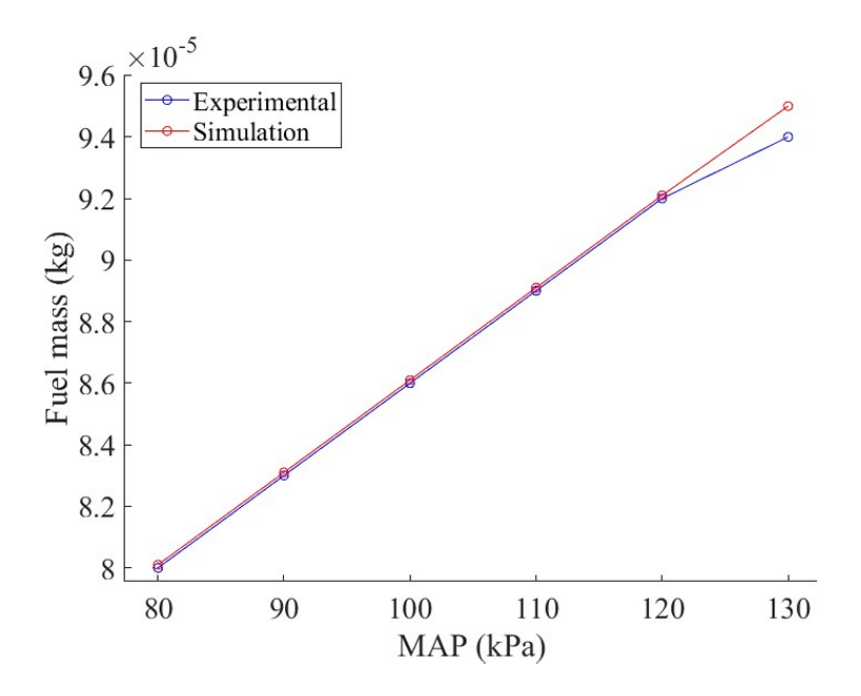


Figure 4.5: Comparison of the simulated fuel mass variation with MAP with experimental data of [92].

4.3 Hydrogen SI engine combustion performance

The initial and boundary conditions for the numerical model are directly related to the experimental data of a single-cylinder four-stroke hydrogen SI engine [47]. The values for boosted intake pressure, equivalence ratio, and spark timing on the combustion and emission characteristics are given in Table 4.4. All the simulations were carried out at a fixed compression ratio of 11.5 at an engine speed of 2000 rpm.

Table 4.4: Operating conditions used for the simulations. Data sources: [103, 37, 224, 47].

Parameters	Values		
Spark Timing (°CA bTDC)	30 to 0		
Equivalence ratio (-)	0.385 to 0.770		
MAP (kPa)	84 to 134		

The operation of naturally aspirated hydrogen IC engines under lean mixture conditions could lead to performance reduction; therefore, it is beneficial to boost the manifold air pressure to achieve power comparable to existing gasoline engines [44]. The boost pressure supplied to the engine, either by a supercharger or turbocharger at the inlet, is further amplified during compression, which is a function of the compression ratio and temperature. The application of increased intake air pressure affects the combustion characteristics. Figure 4.6 shows the variation of the simulated in-cylinder pressure traces at different manifold air pressures (MAP = 84 kPa, MAP = 114 kPa, MAP = 134 kPa) and excess air ratios ($\lambda = 1.54$, $\lambda = 2.00$). The simulation does not account for the mechanical losses incurred by the charger. Increasing the intake air pressure affects the in-cylinder pressure, where the pressure at the end of compression changes from 1.39 MPa for a MAP of 84 kPa to 2.22 MPa for the MAP of 134 kPa at $\lambda = 1.54$ at 2000 rpm. This is mainly due to an increase in volumetric efficiency caused by an increase in the amount of air compressed at higher pressure, altering the combustion process. Hence, for $\lambda = 1.54$ operation, the peak in-cylinder pressure increased from 4.42 MPa to 57.52 MPa when the MAP was increased from 84 kPa to 134 kPa. The observed increase in combustion performance from increasing the intake air pressure for $\lambda = 1.54$ operation was not the same for leaner mixtures due to an increase in the amount of air inside the chamber. Operating conditions that correspond to mixtures leaner than $\lambda = 2.00$ result in a reduction in burning speeds; hence, the spark timing had to be advanced to compensate for the longer combustion duration. The instantaneous heat release rate shows the characteristics of the combustion process. The heat release rate decreased significantly with much leaner mixtures due to the lower amount of fuel in the mixture and slower combustion speed caused by the increase of air. Additionally, note from the inset plot in Figure 4.6 that the peak heat release rate shifted slightly with boosting pressure under $\lambda = 1.54$ operating condition. However, under lean mixture operation ($\lambda = 2.00$), the peak heat release rate shifted significantly by 20 °CA from 360 °CA to 380 °CA, and the peak magnitude also decreased from 31 J/°CA to 15 J/°CA. The total amount of heat release increased with increasing boosting pressure at $\lambda = 1.54$ due to the increased amount of fuel required to maintain constant λ . For leaner mixtures ($\lambda = 2.00$), the total magnitude of heat did not vary significantly with higher boost pressures. This was due to the reduction of in-cylinder pressure caused by the longer combustion duration due to the increased amount of leaner mixture inside the chamber.

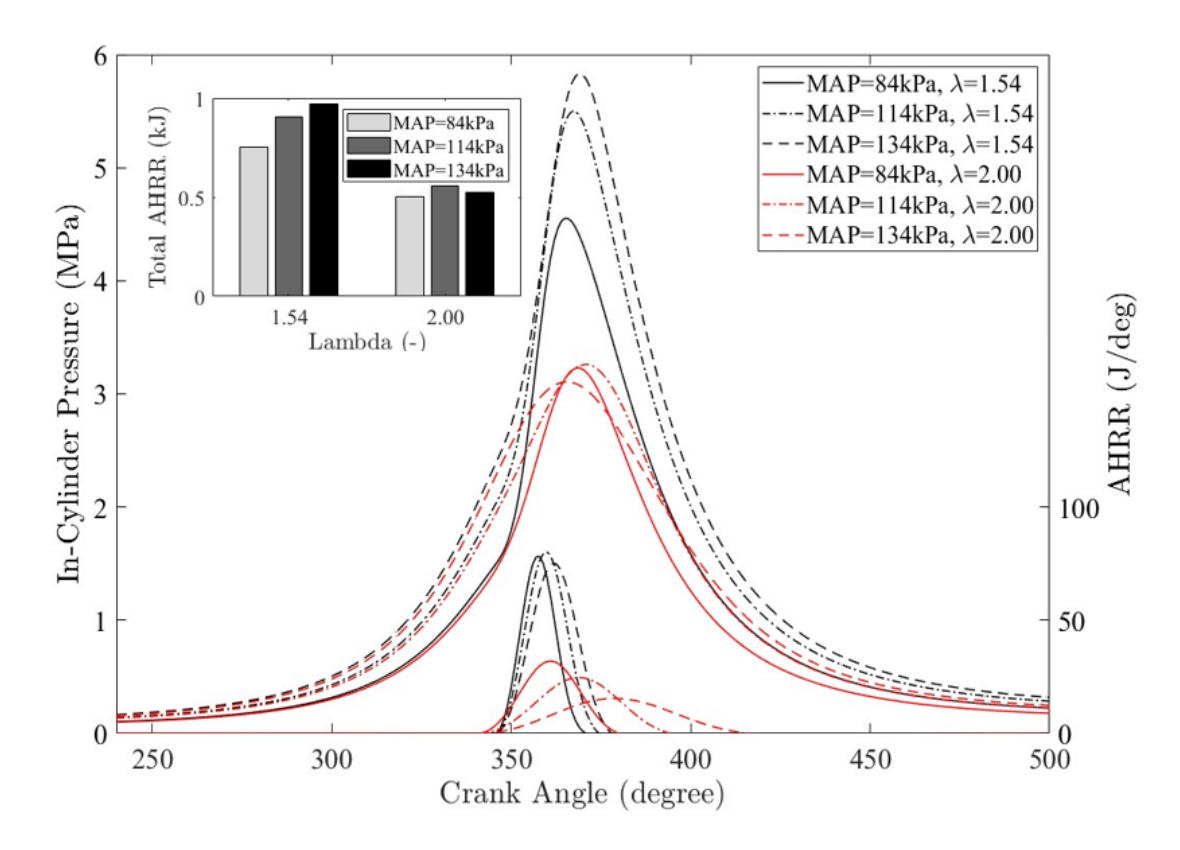


Figure 4.6: Results for in-cylinder pressure and apparent heat release rate (AHRR) curves with boosting pressures of 84 kPa, 114 kPa, and 134 kPa, and excess air variation ($\lambda = 1.54, 2.00$), to compare the effect of charging pressure at different lean conditions (CR = 11.5, $N = 2000 \,\mathrm{rpm}$, ST = 10°CA bTDC).

Figure 4.7 shows the simulated peak in-cylinder pressure for various λ and MAP cases for MBT timing at 2000 rpm. The peak cylinder pressure increases linearly for $\lambda < 1.82$ because of the increasing amount of hydrogen in the fuel-air mixture. As the boost pressure increases, the energy supply increases, resulting in higher peak in-cylinder pressure values, with a maximum observed at a MAP of 134 kPa and $\lambda = 1.30$ with a magnitude of 7.14 MPa. Furthermore, for $\lambda > 1.82$, any increase in the intake air pressure results in lower peak cylinder pressure due to the lower burning speed caused by air dilution and the reduced amount of hydrogen in the mixture. The simulated peak cylinder pressure of 7.14 MPa for the hydrogen engine did not exceed the values found for a gasoline-fuelled SI engine under the same operating conditions [225]. The maximum peak pressure rise can be controlled by adjusting the spark timing, but the data correspond to MBT timing for each

operating condition.

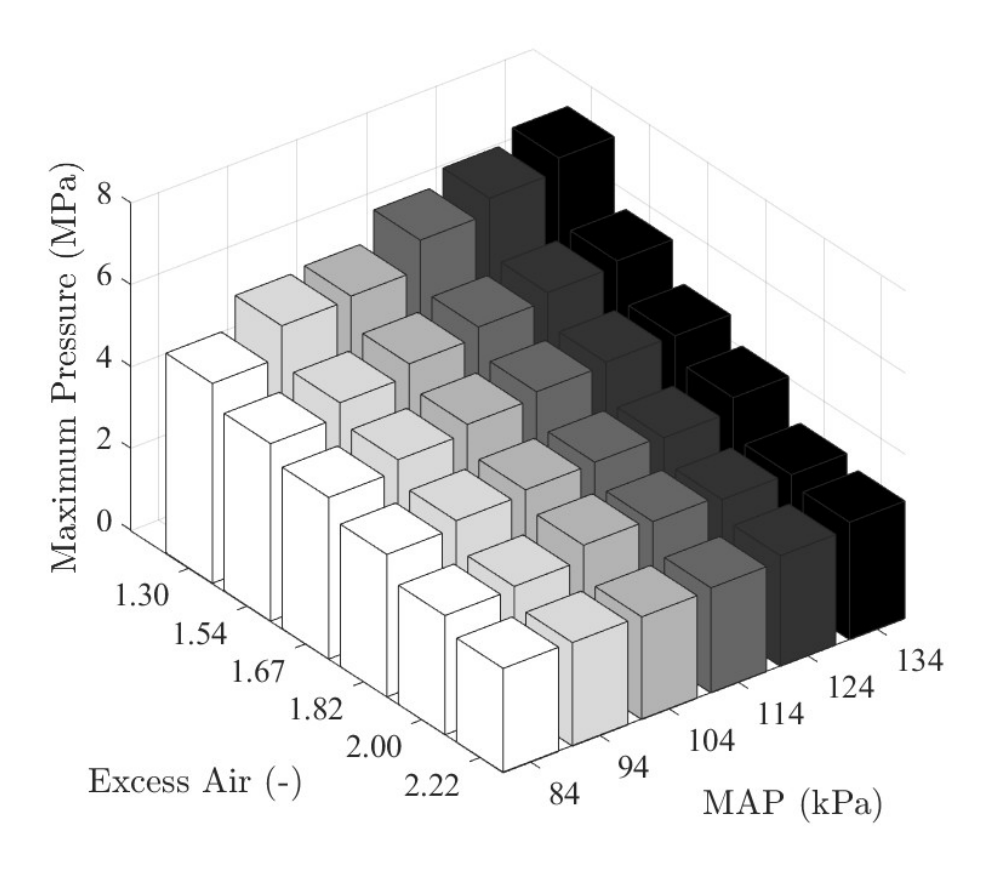


Figure 4.7: Maximum in-cylinder pressure values for boosted pressures varying from 10 kPa to 50 kPa with 10 kPa increments at lean-burn conditions from $\lambda = 1.30$ to $\lambda = 2.22$ (CR = 11.5, ST = MBT).

The mass fraction of fuel burned (MFB) and the location of end-gas autoignition are required to determine the knocking intensity, i.e., the instantaneous mass fraction burned per crank angle for each operating condition. Figure 4.8 shows the mass fraction profile as a function of crank angle for each boosted condition for $\lambda = 1.82$ at a fixed spark timing of 15° CA bTDC. The hydrogen-air mixture burns at a fast rate after the spark discharge, peaks around halfway through combustion, and then drops to near zero towards the end of combustion. Hence, the MFB period increases with increasing intake pressure due to the increased amount of hydrogen-air mixture [92]. As a result of added air intake pressure, the combustion duration is prolonged, increasing the knocking tendency [226].

Since combustion duration was found to be a good indicator of knock occurrence, it is reasonable to use the mass fraction burned curves to characterize the combustion stages by their duration in terms of crank angles. Combustion duration (CA10-90) is the crank angle interval required to burn the bulk of the mixture, defined as the time between the start of flame development (10% mass fraction burned) and the end of flame propagation (90% mass fraction burned). Figure 4.9 shows the combustion duration of the hydrogen-air mixture under varying MAP and λ . A leaner mixture results in an increase in CA10-90 due to slower burning velocity and increased flame development angle (CA0-10). This is caused by the slower LFS due to the reducing equivalence ratio [113]. This means that CA10-90 is not only a factor affecting combustion efficiency, but the entire flame propagation depends on the flame kernel initiation process.

In addition, the MAP has a greater impact on leaner mixture operation due to the increased air volume. For a MAP of 134 kPa, the combustion duration increases significantly up to 53° CA when the mixture was leaner than $\lambda = 2.22$, and the combustion duration increased by 60% when MAP was increased from 104 kPa to 134 kPa. Also, the crank angle at which 50% of fuel burned (CA50) must be located between 8 to 10° CA aTDC for optimum performance [140, 227].

Figure 4.10 shows that CA50 shifts away from the optimal location when the mixture becomes leaner. For the naturally aspirated condition at a MAP of 84 kPa, the CA50 location shifts significantly away from the optimal location for $\lambda > 2.22$. However, for higher boosted pressures, the increase of CA50 occurs after $\lambda = 2.00$ for the MAP of 104 kPa and 114 kPa, and just after $\lambda = 1.82$ for the MAP of 134 kPa. This is mainly due to less fuel in the mixture, hence slower flame speed resulting in longer combustion durations. Therefore, the combustion location of CA50 could not be centred at 8-10° CA after TDC. Furthermore, slower-burning mixtures require increased spark advance to achieve the optimal indicated thermal efficiency.

Figure 4.11 shows how the load is affected by the CA50 point at different MAP values. The load increases as the CA50 is positioned at the optimal location around 8-10° CA aTDC and reduces as the CA50 shifts away from the optimal position. Increasing the intake pressure increases the in-cylinder temperature, which increases

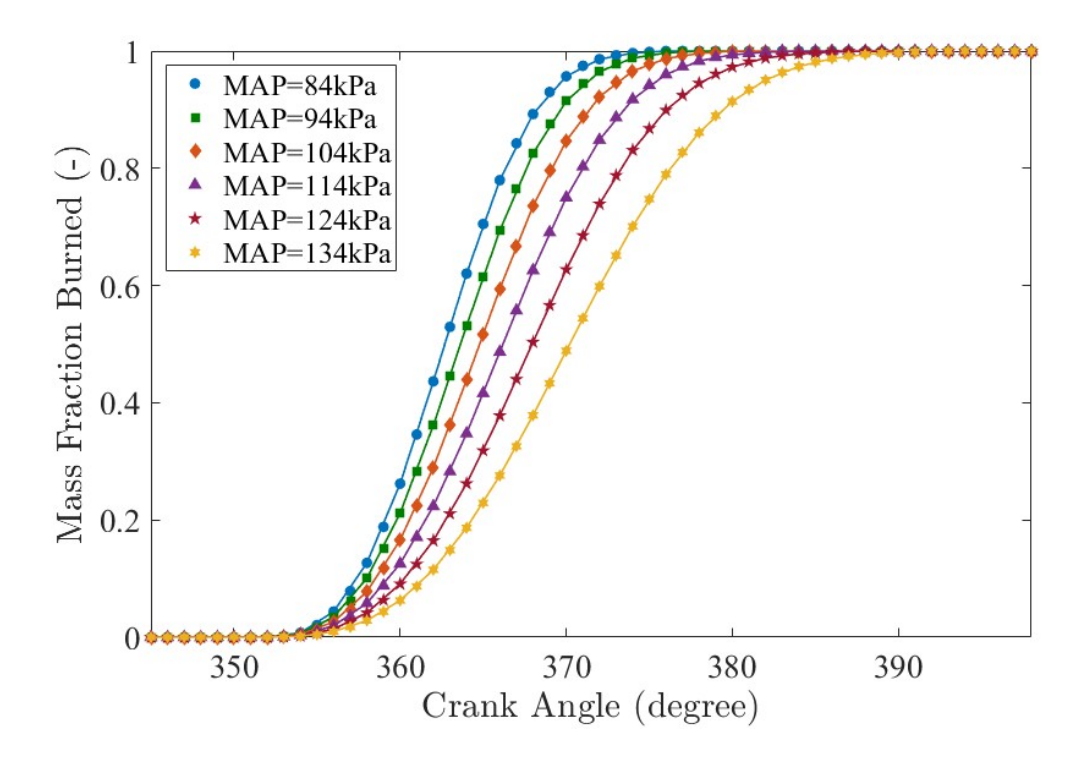


Figure 4.8: Results for mass fraction burned profile as a function of crank angle for MAP at $\lambda = 1.82$ (CR = 11.5, N = 2000 rpm, ST = 15°CA bTDC).

the burn rate. The discussion in this part pertains to an increase in the inducted amount of leaner hydrogen-air charge caused by higher boost pressure, which results in an increase in the burn duration. The increase in burn duration is reflected in a relatively slower burn rate compared to lower boost pressure operating conditions.

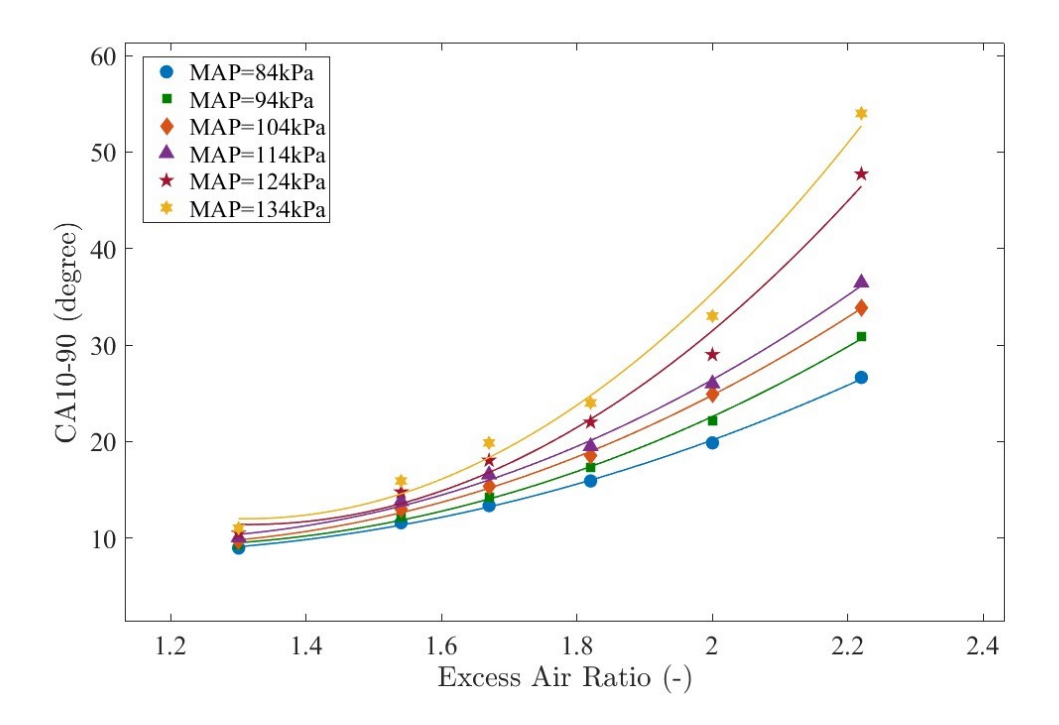


Figure 4.9: Combustion duration (CA10-90) for various λ and MAP values at MBT timing for each operating condition. The lines represent least-squares fits.

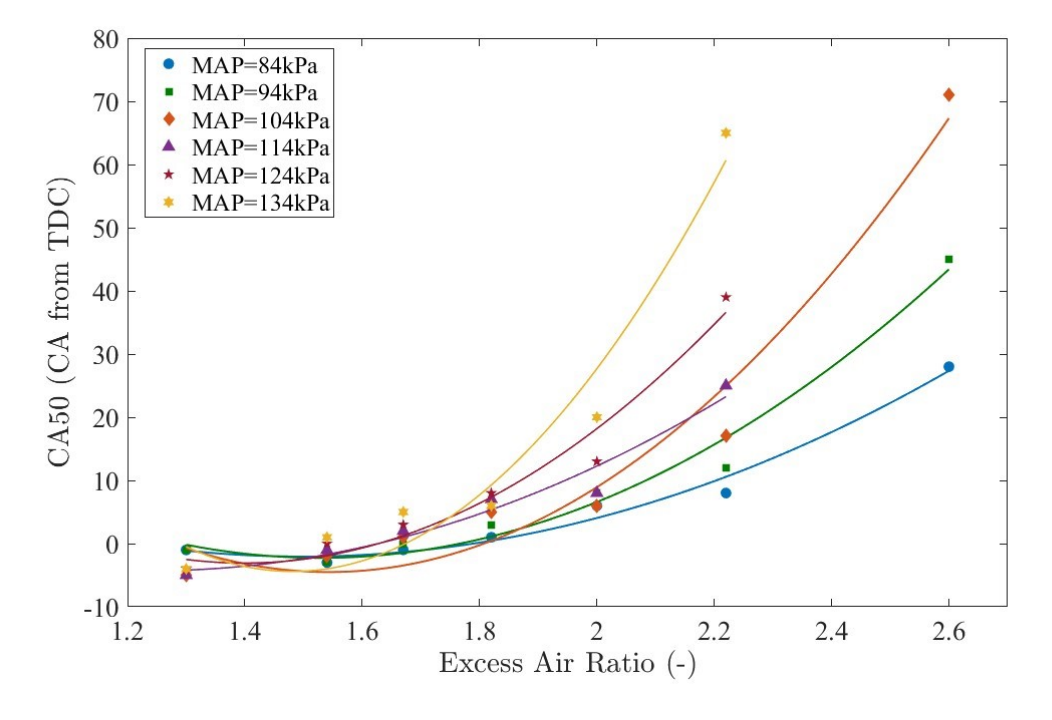


Figure 4.10: Location of CA50 for various λ and MAP values at MBT timing for each operating condition. The lines represent least-squares fits.

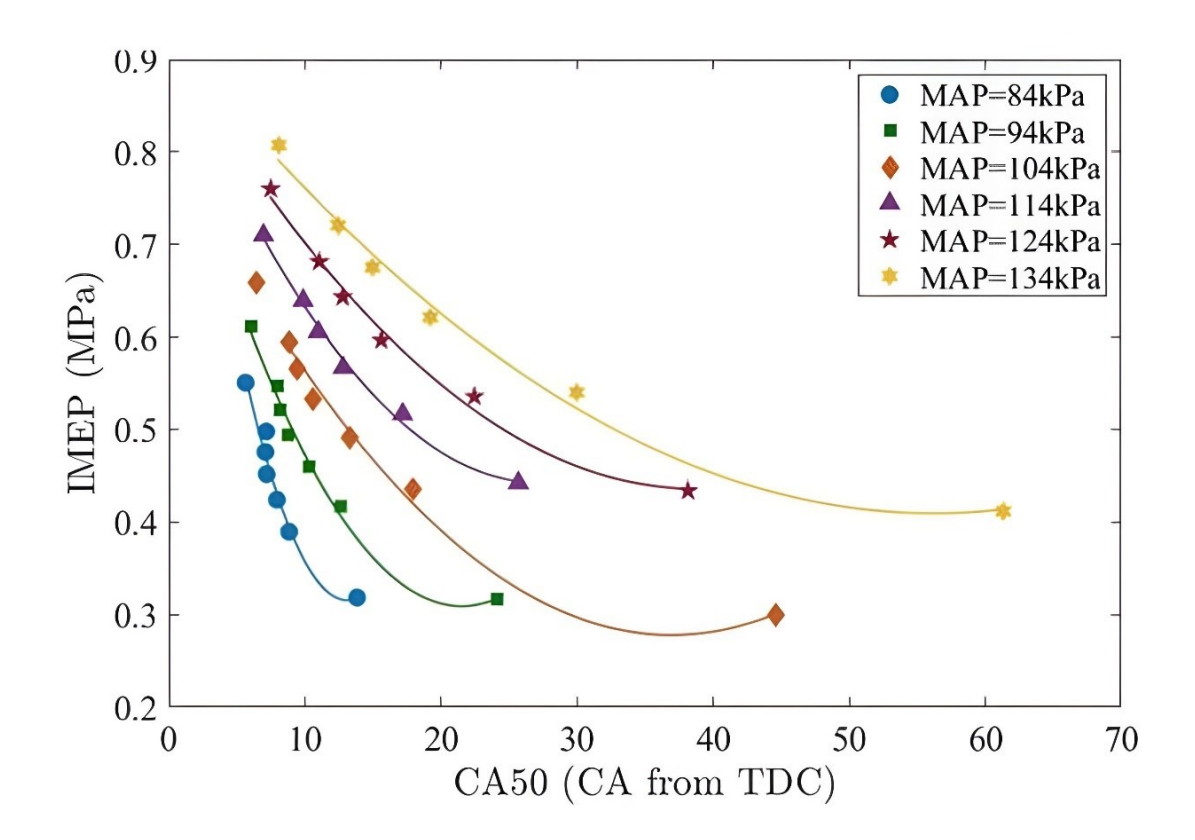


Figure 4.11: Location of CA50 at different loads for various λ and MAP values at MBT timing for each operating condition. The lines represent least-squares fits.

4.4 Knock model

To evaluate the chemical effects on the autoignition delay time, the hydrogen reaction mechanism of Li et al. [228] is solved using chemical kinetics, where a premixed hydrogen-air mixture was maintained at different equivalence ratios and different ambient temperature and pressure. In Figure 4.12(a), the simulated autoignition time for a stoichiometric hydrogen-air mixture maintained at an ambient pressure of 2 atm was compared with the available values from [229]. Comparison of the newly calculated autoignition delay-time using chemical kinetic results with previous Arrhenius correlations (gasoline model), along with the simulation results of Zhao et al. [230], is shown in Figures 4.12(a) and 4.12(b).

Figure 4.13(a) depicts the influence of pressure on the hydrogen autoignition delay time while keeping the equivalence ratio constant. The results indicate that

there is negligible variation in the autoignition delay time when the pressure was increased from 30 to 50 atm. However, it was noticed in Figure 4.13(b) that for different equivalence ratios there was an observable difference in the autoignition delay time for different pressures. Nevertheless, for the engine operating conditions of a fixed equivalence ratio, the pressure variation effect on the autoignition delay time is negligible; therefore, a representative pressure was chosen to simulate the autoignition delay time of all the conditions, as shown in Table 4.5.

Table 4.5: Representative pressures used for each operating condition.

λ (-)	1.30	1.54	1.67	1.82	2.00	2.22
Pressure (atm)	60	50	44	38	30	26

A least-square fit was performed on the calculated chemical kinetic values to determine the best-fit expression, which was then used to calculate the autoignition delay time for the unburnt mixture temperatures T_u relevant to engine operating conditions. Therefore, the equivalence ratio was incorporated into the hydrogen reaction simulations to enhance the accuracy of the autoignition delay time predictions.

Using the operating conditions in Table 4.5 with the Livengood-Wu knock model, Figure 4.14 shows the knock integral for various manifold air pressures and equivalence ratios at MBT timing, 10° CA retardation, and advance from MBT timing. It can be seen that knock did not pass unity at MBT timing conditions. This is in agreement with the previous work of Lee et al. [110], which showed that knocking did not occur for equivalence ratios lower than 0.6 ($\lambda > 1.67$) for hydrogen-fuelled SI engines. However, knocking was observed when the spark timing was advanced, where the knock integral exceeded unity for the MAP of 134 kPa and $\lambda = 1.30$. This operating regime shows a tendency to knock due to the increasing charge density caused by the additional air inducted into the engine. Figure 4.14 also shows a reduction in the tendency to knock when the spark timing was retarded, which could reduce the end-gas temperature and lengthen the autoignition delay time. However, retarding spark timing could lower thermal efficiency, hence knocking might prevent the engine from running with the optimal spark timing.

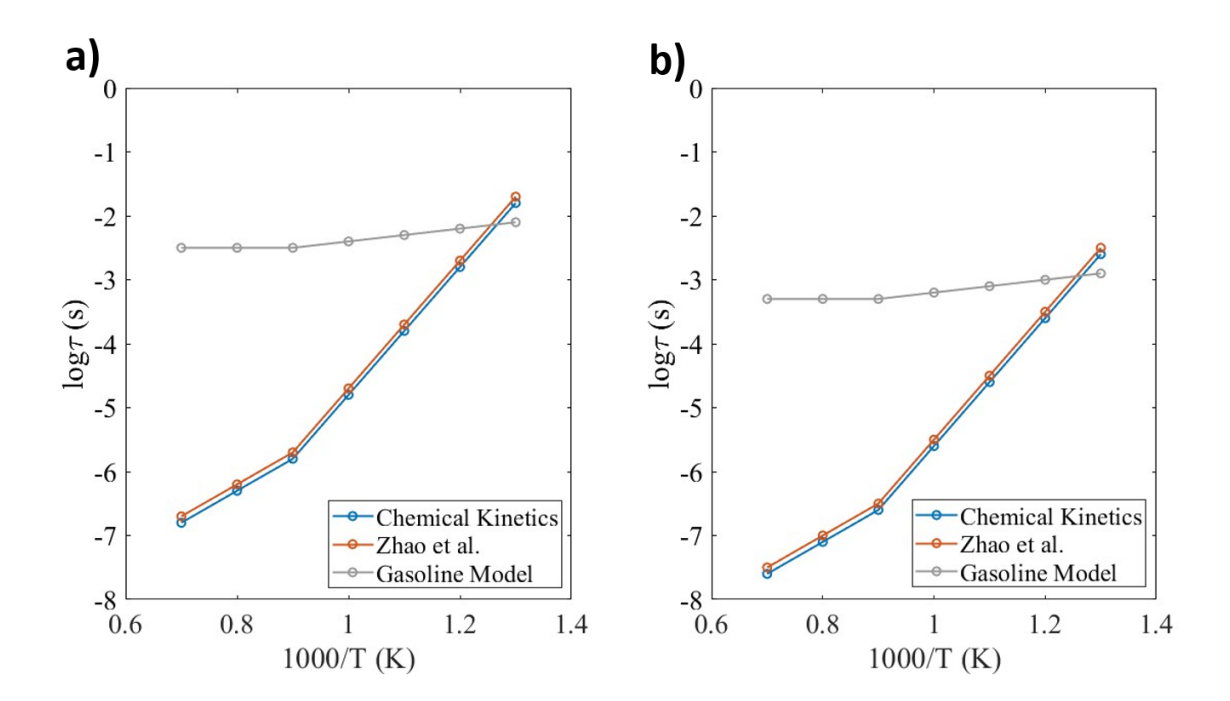


Figure 4.12: Hydrogen autoignition delay time at different temperatures at 10 atm (a) and 50 atm (b) for a stoichiometric hydrogen-air mixture compared to the gasoline model and with Zhao et al. [230].

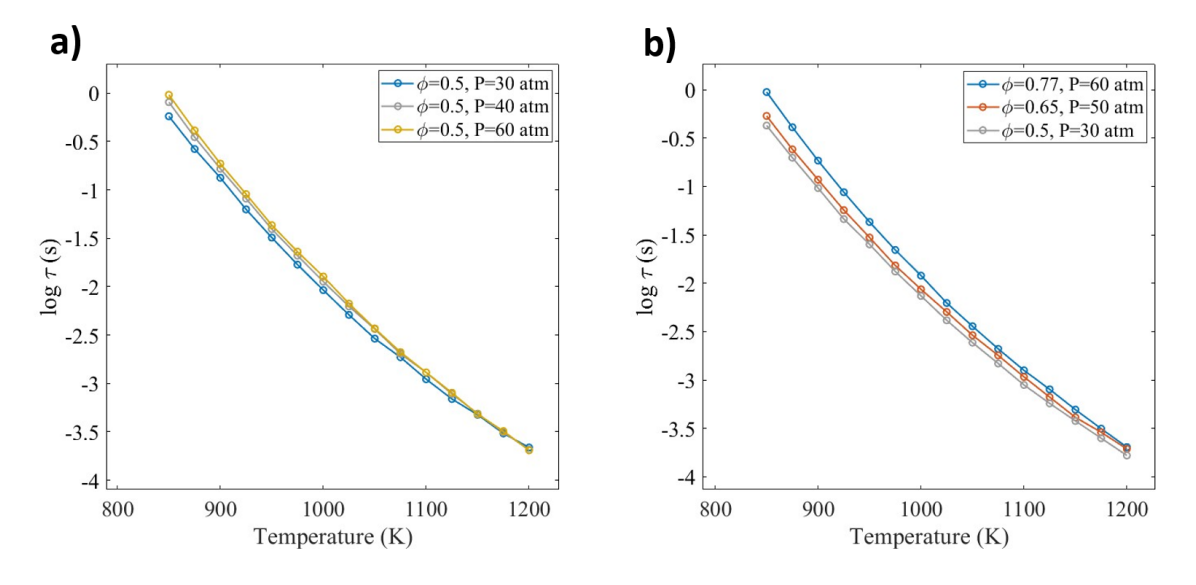


Figure 4.13: (a) Hydrogen autoignition delay time at different pressures and temperatures for $\phi = 0.5$, (b) Hydrogen autoignition delay time for three equivalence ratios at different temperatures.

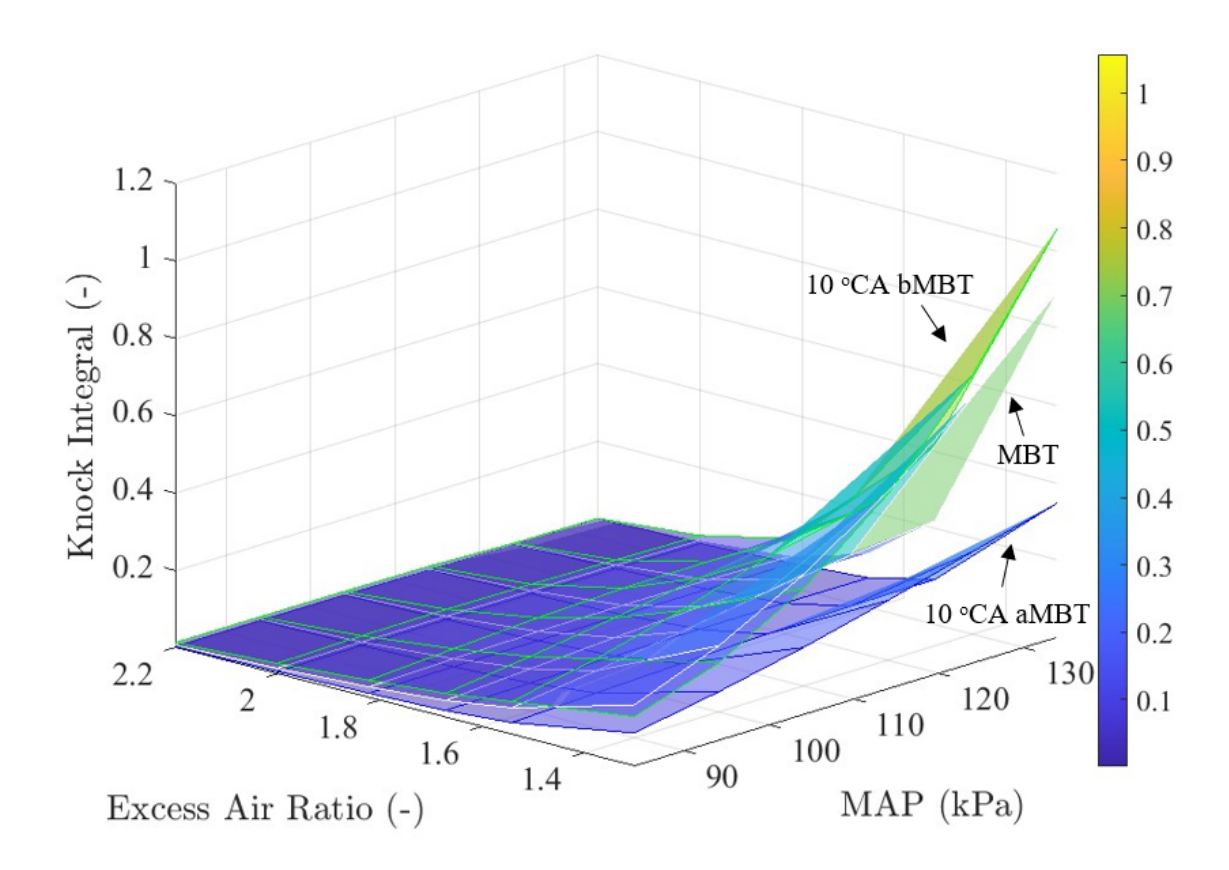


Figure 4.14: Knock integral (KI) for different operating conditions and spark timings, showing the tendency of knock occurrence.

4.5 Hydrogen engine load

The optimal spark timing of the engine is mainly determined by the nature of the flame propagation within the combustion chamber, with important parameters including engine speed, engine load, engine temperature, intake temperature, fuel composition, and air excess ratio [113]. The spark timing is fixed at the minimum spark advance for best torque (MBT) location and is evaluated as a function of equivalence ratio and boosting pressure to ensure maximum thermal efficiency under all operating conditions.

Therefore, MBT timing for the highest indicated mean effective pressure (IMEP) is determined by varying spark timing for $\lambda = 1.82$, and for boosting pressures varying between 84 kPa and 134 kPa (Figure 4.15). For the naturally aspirated conditions of MAP up to 114 kPa, the MBT timing was found to be at 15° CA

bTDC, then it increases to 20° CA bTDC. With increasing intake air pressure, the minimum advance for best torque shifts away from TDC due to increasing charge density for higher manifold air pressures. For boosting pressures less than 114 kPa, the MBT timing was not affected noticeably by increasing intake air pressure (advances $<2^{\circ}$ CA). As the intake pressure increases from 84 kPa to 114 kPa, the peak value of IMEP initially increases by approximately 1.2 bar; thereafter, the IMEP increases only marginally (by ≈ 0.7 bar). Thus, the power increase is explained by the additional charge inside the cylinder [231].

The MBT timing shifts from TDC when the charge becomes leaner (Figure 4.16). At $\lambda = 1.30$, the MBT timing is at 10° CA bTDC, but under ultra-lean conditions ($\lambda = 2.60$), it is at 20° CA bTDC. This shift is explained by the increasing combustion duration due to the decreasing burning velocity (less hydrogen in the mixture). The IMEP was reduced by operating under leaner mixtures due to lower burning speed. Figure 4.16 also shows that IMEP is reduced by up to 42% when the excess air ratio is doubled from $\lambda = 1.30$ to $\lambda = 2.60$ at their respective MBT timings under naturally aspirated operating conditions. The in-cylinder mixture composition λ was the most influential parameter on MBT timing, consistent with previous work [224].

Figure 4.17 shows the calculated IMEP with respect to λ and MAP at their respective MBT spark timing. The maximum IMEP (0.81 MPa) is reached for $\lambda=1.30$ and a MAP of 134 kPa due to increasing burning velocity. Operating under very lean conditions ($\lambda>2.22$), the IMEP varied only by up to 6% when the charge was boosted (MAP = 84-134 kPa). Under relatively lower excess air-ratio operation ($\lambda=1.30$), IMEP varied by up to 32% when MAP was boosted from 84 kPa to 134 kPa, but when operating at very lean conditions, boosting had a negligible effect on IMEP. This may be due to the reduction of the flame speed. Furthermore, increasing charging pressures had little effect on IMEP for mixtures leaner than $\lambda=2.00$. To achieve higher loads comparable to a gasoline engine, the boosted hydrogen SI engine could be run at equivalence ratios closer to stoichiometric operation with exhaust gas recirculation to mitigate knock and reduce NO emissions [44].

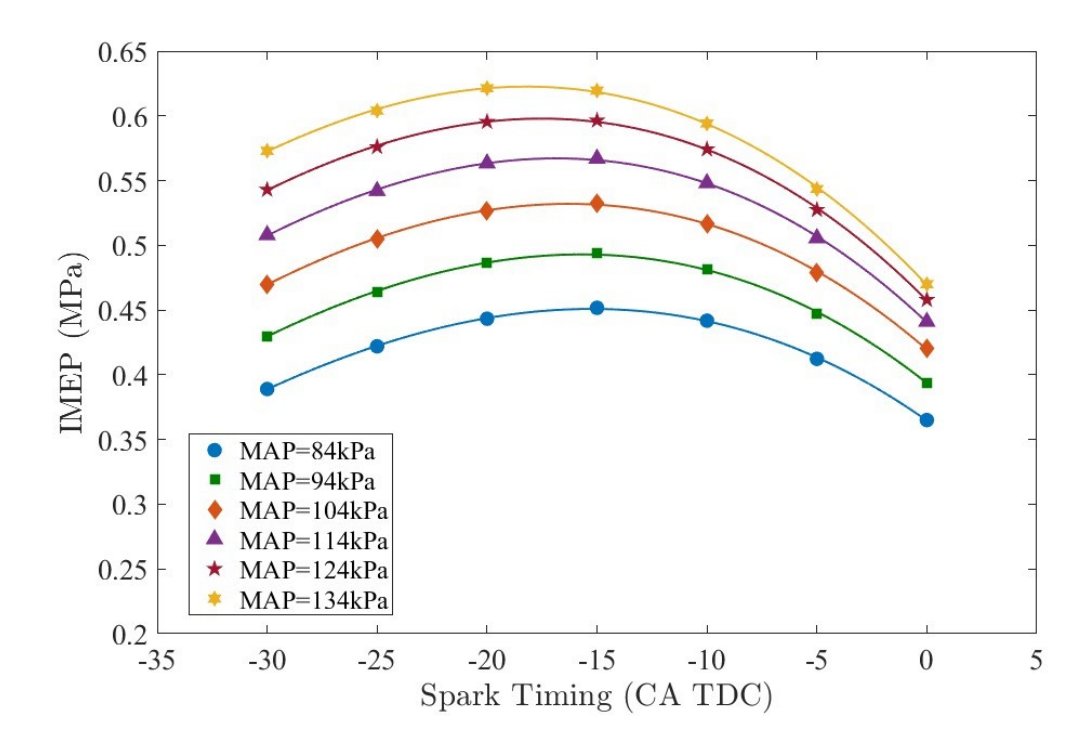


Figure 4.15: Variation of IMEP at various spark timings with MAP under $\lambda = 1.82$. The lines represent least-squares fits.

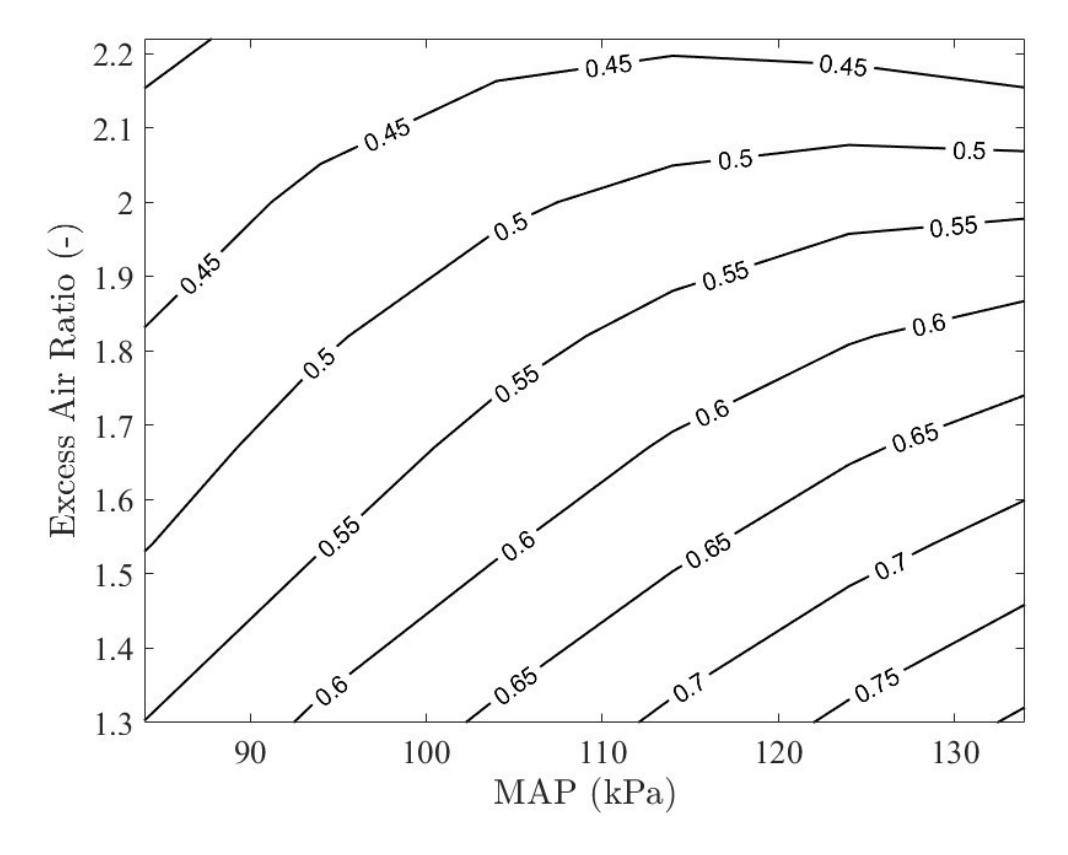


Figure 4.17: Variation of IMEP (MPa) at various spark timings for different λ under naturally aspirated conditions (MAP = 849kPa, CR = 11.5, $N = 2000 \, \text{rpm}$).

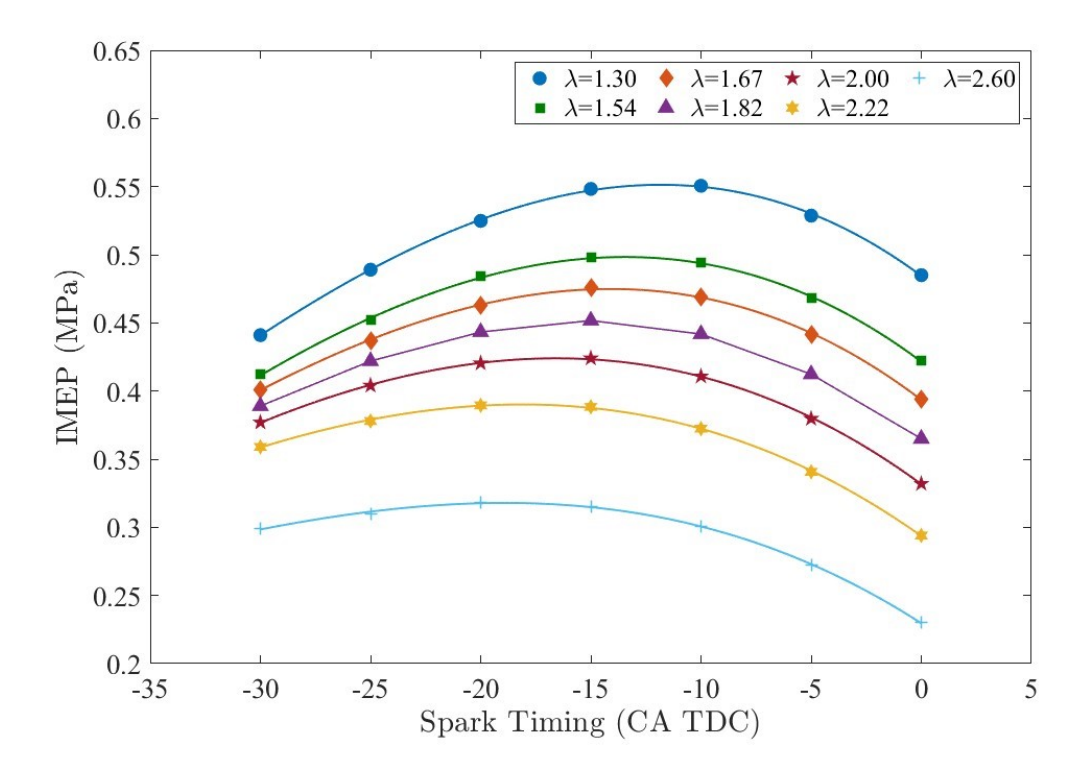


Figure 4.16: Variation of IMEP at various spark timings at different λ for naturally aspirated conditions (MAP = 84 kPa, CR = 11.5, N = 2000 rpm). The lines represent least-squares fits.

4.6 Indicated thermal efficiency and indicated specific fuel consumption

Indicated thermal efficiency (ITE) shows how effectively the chemical energy of the fuel is converted into mechanical work. Figure 4.18 shows the effect of λ and MAP on ITE at the optimum spark timing for best torque at an engine speed of 2000 rpm. The ITE increases proportionally with boosted pressure, reaching about 39% for $\lambda = 1.82$ at a MAP of 84 kPa, whereas it reaches 42% with an increment of intake pressure by 40 kPa. For boosting pressures less than 94 kPa, ITE increases linearly with increasing λ . For naturally aspirated conditions (MAP = 84 kPa), ITE increases by approximately 21% with the excess air ratio increasing from $\lambda = 1.30$ to $\lambda = 2.22$. When the charging pressure increases beyond 114 kPa, the ITE peaks around $\lambda = 1.82$. This is in agreement with Luo et al. (2019), where the highest thermal efficiency was achieved for equivalence ratios between 0.65 and 0.80 ($\lambda =$ 1.53-1.25). Likewise, for mixtures leaner than $\lambda = 2.22$, boosting pressure did not increase ITE beyond boost pressure values of 94 kPa. The maximum simulated ITE—approximately 42%—occurs at $\lambda = 1.82$ at a MAP of 124 kPa. This study does not include the effect of unburned hydrogen emissions, which might result in a reduction of ITE [75].

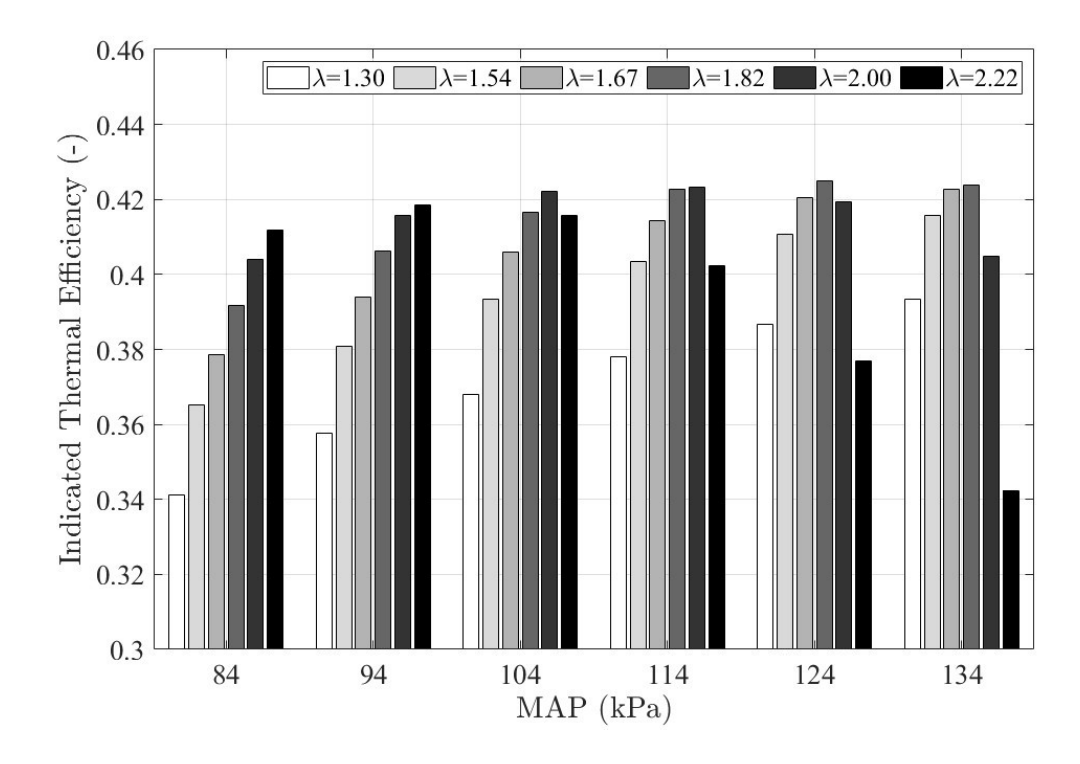


Figure 4.18: Indicated thermal efficiency at various MAP (84–134 kPa) and lean conditions ($\lambda = 1.30$ –2.22) at various loads, to estimate optimal efficiency for different operating conditions (CR = 11.5, N = 2000 rpm).

Indicated specific fuel consumption (ISFC) evaluates how effectively the thermal power of the fuel is converted to indicated power. Figure 4.19 shows that under naturally aspirated conditions of 84 kPa MAP, the ISFC was reduced by 17% when the engine operation was varied from $\lambda=1.30$ to $\lambda=2.22$. As for the boosting effect, ISFC reduced as MAP increased for the naturally aspirated condition at $\lambda=1.30$. For a MAP of 84 kPa, the ISFC increases as the mixture becomes leaner than $\lambda=2.22$. Whereas for MAP values of 114 kPa and 134 kPa, the ISFC increases when the mixture becomes leaner beyond $\lambda=2.00$ and $\lambda=1.82$, respectively. These findings correlate well with the shift of CA50 and agree with previous studies [96]. Figure 4.20 depicts the spark timing effect on ISFC at various λ under naturally aspirated conditions (MAP = 84 kPa). The optimal ISFC value occurs when the spark timing approaches MBT timing (the highest indicated power output). In general, the increase in manifold air pressure reduces fuel consumption for mixtures with $\lambda < 1.82$ (Figure 4.21). This reduction in fuel consumption results

from the changes in the mixture composition. As MAP increases from 84 kPa to 94 kPa, the ISFC decreases (except for $\lambda=2.60$), where the load was found to decrease when the MAP was increased from 84 kPa to 94 kPa. This observation was due to a significant increase in the combustion duration caused by increased air dilution at boost pressures for lean-burn mixtures ($\lambda=2.60$). For $\lambda=1.30$ and $\lambda=1.82$, the ISFC reduces by 13% and 7%, respectively, when MAP increases from 84 kPa to 134 kPa.

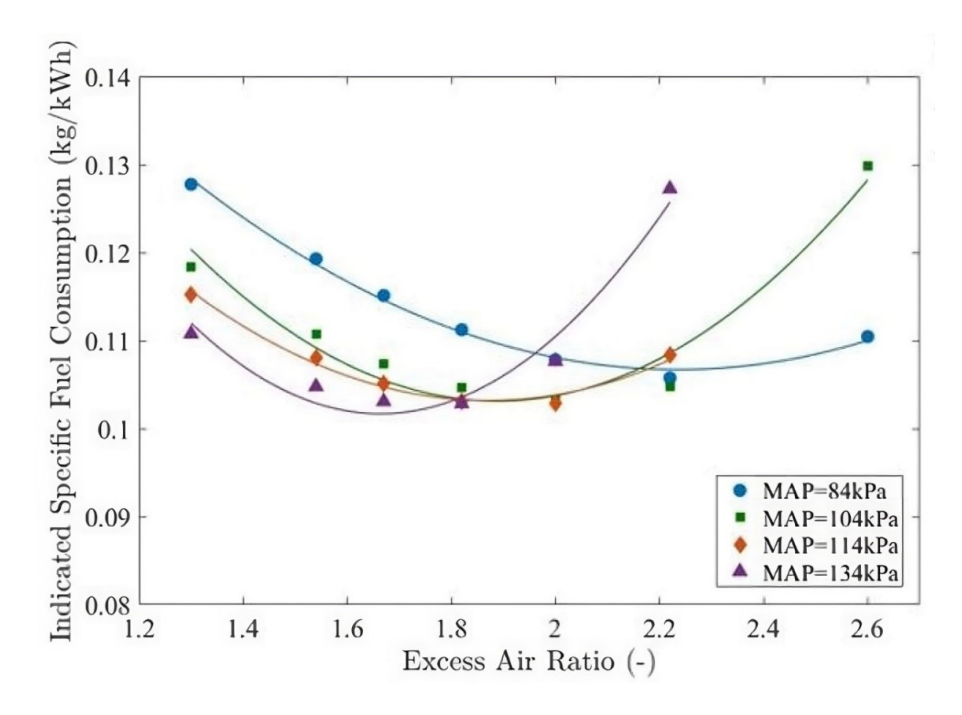


Figure 4.19: ISFC values at different λ and MAP at MBT timing. The lines represent least-squares fits.

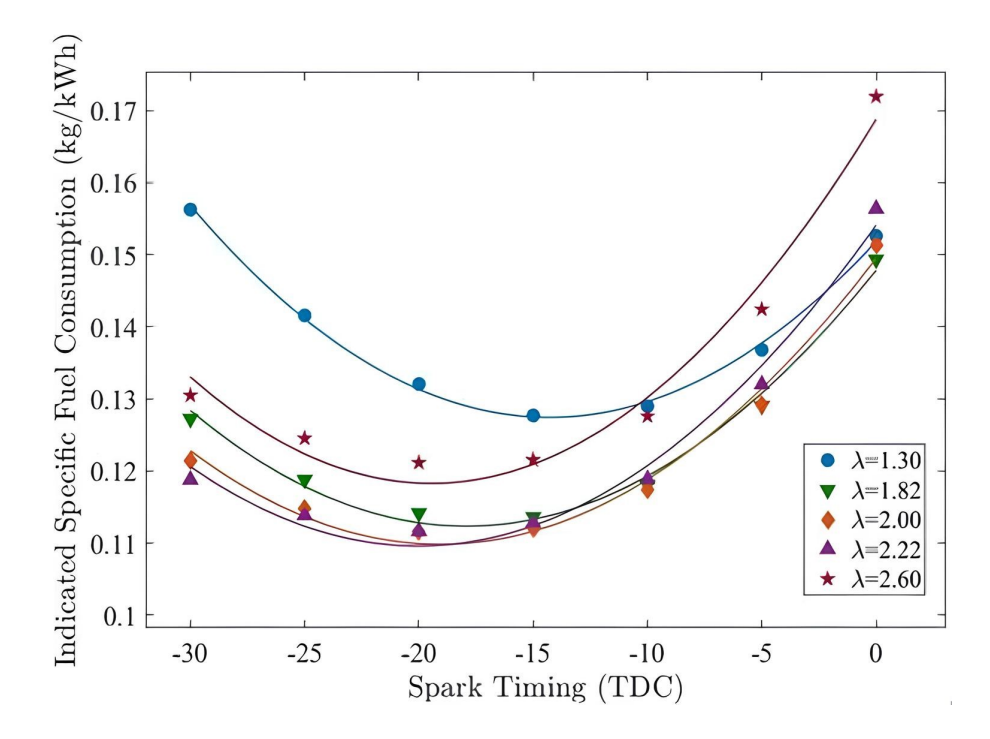


Figure 4.20: ISFC values at different λ and spark timings for MAP = 84 kPa. The lines represent least-squares fits.

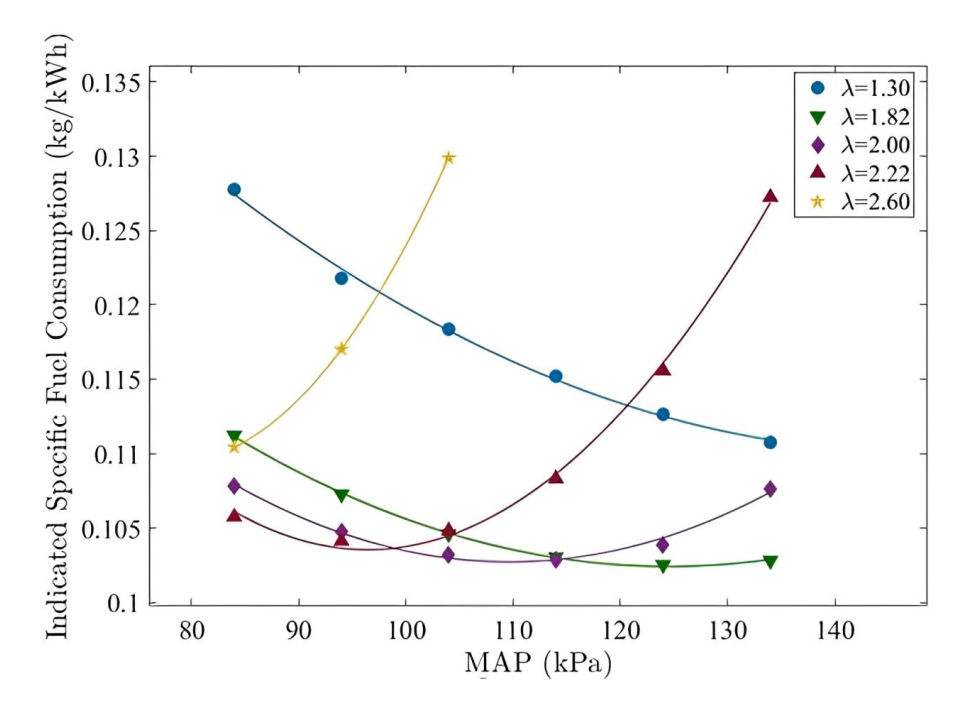


Figure 4.21: ISFC values at different λ and MAP at MBT timing. The lines represent least-squares fits.

4.7 Nitric oxide emissions

This section explores a strategy to reduce NO emissions of hydrogen engines by operating under lean conditions. The simulated results of boost pressure (MAP) on NO emissions at different λ are shown in Figure 4.22. Boosting the intake pressure increases NO emissions, and this effect is prominent when the engine is operated with $\lambda < 2.00$. The increase in NO emissions is explained by the in-cylinder temperature rise caused by supercharging, as NO formation depends on high local temperature and excess oxygen. Operating beyond $\lambda = 2.22$, NO emissions reduce for higher boosted pressures (MAP of 134 kPa) (Figure 4.22). This reduction occurs because increasing $\lambda > 2.22$ causes the temperature to decrease significantly, reducing NO formation to nearly zero, which agrees with previous work [232]. Reductions in NO emissions occur with increasing λ for the corresponding MAP values (Figure 4.23). NO emissions are also reduced by retarding the spark timing with respect to MBT timing (Figure 4.24), mainly due to reducing the global in-cylinder temperature. For $\lambda = 1.82$ and MAP of 134 kPa, NO emissions reduce by up to 68% when the spark is retarded by 10° CA (from 15 to 5° CA bTDC). However, retarding the spark timing marginally reduces ITE (Figure 4.25). For $\lambda = 1.82$ and $MAP = 84 \, kPa$, NO emissions reduce by 55% and ITE reduces by 6% when spark timing is retarded by 5° CA from MBT. Further retarding the spark timing by 10° CA results in NO emissions dropping almost to zero and ITE reducing by 14%. Figure 4.25 also shows that the reduction in NO emissions was more pronounced by varying the mixture composition, as it influences the in-cylinder temperature and inhibits the NO formation process to almost zero levels under ultra-lean-burn operation of the SI hydrogen engine.

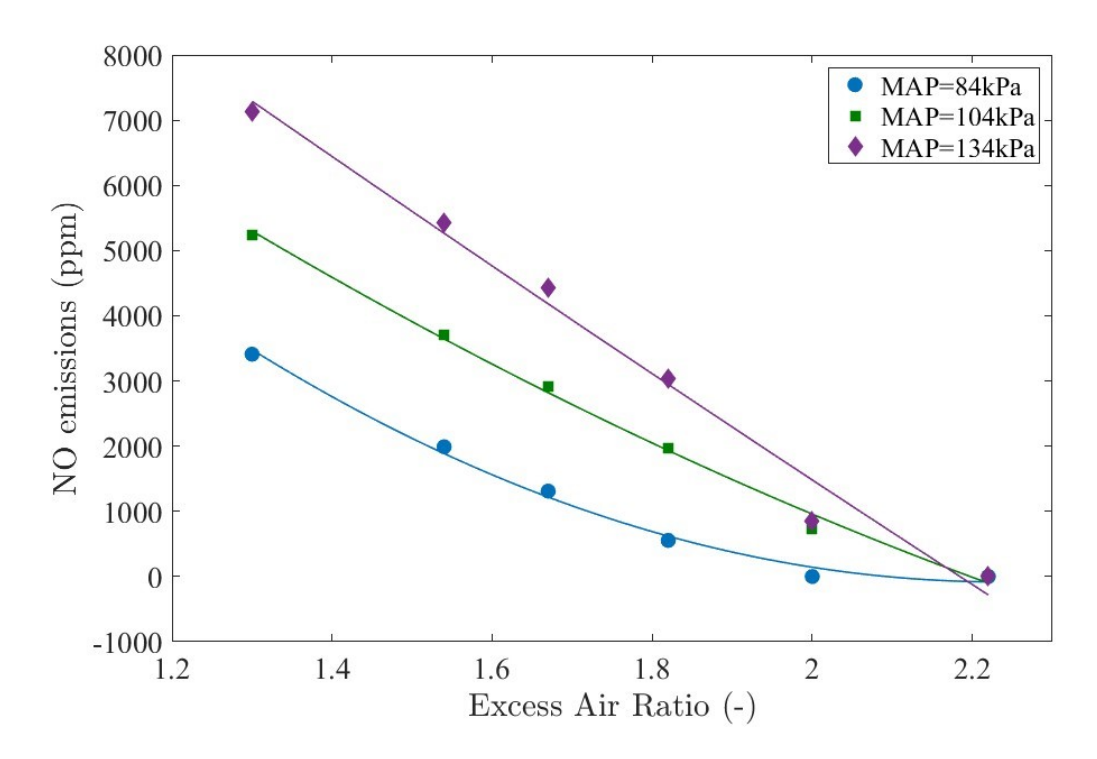


Figure 4.22: NO emissions (a) at various λ and MAP at MBT timing. The lines represent least-squares fits.

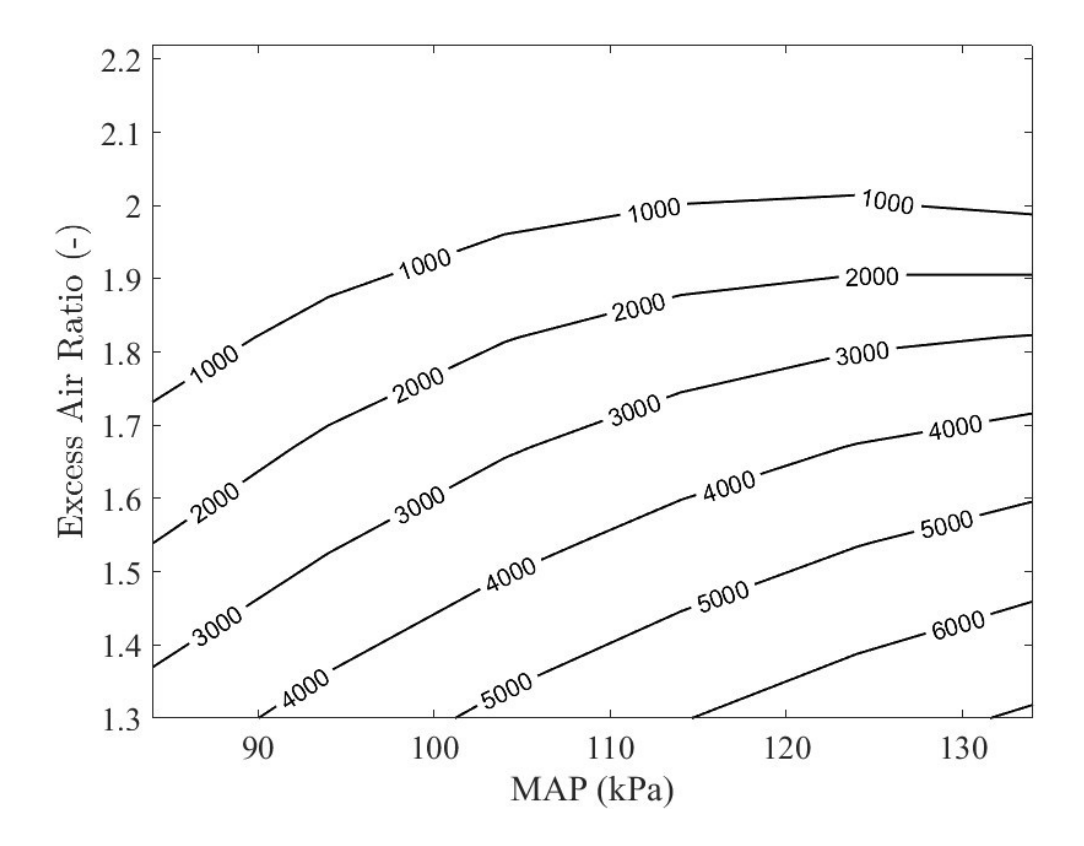


Figure 4.23: NO emissions at various λ and MAP at MBT timing.

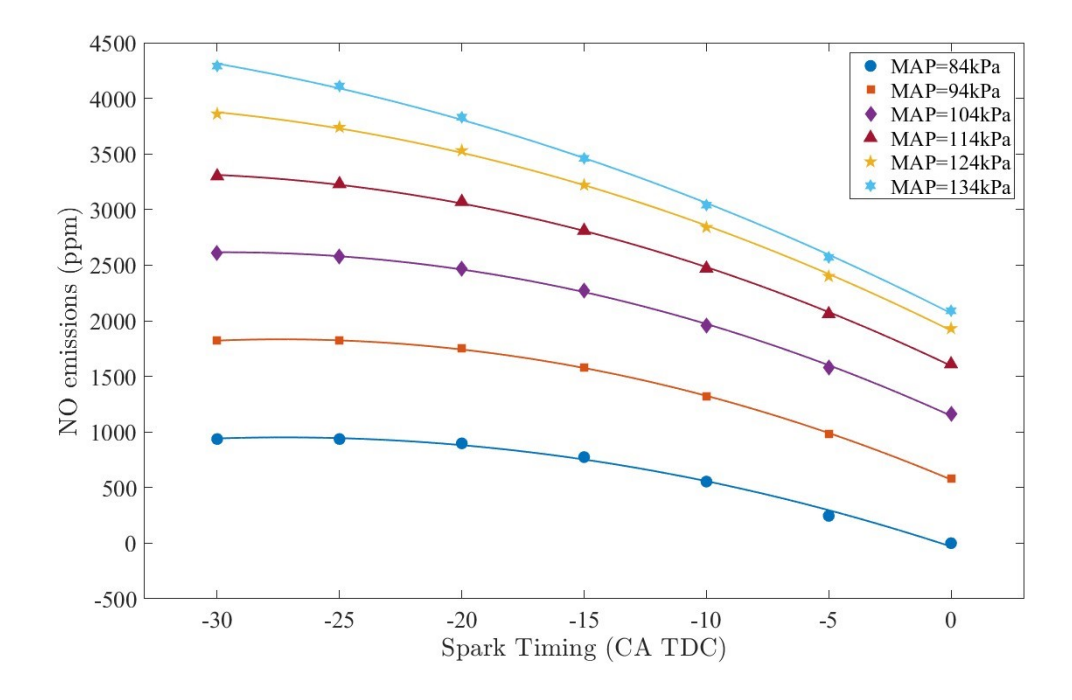


Figure 4.24: NO emissions at $\lambda=1.82$ for different spark timings and MAP values. The lines represent least-squares fits.

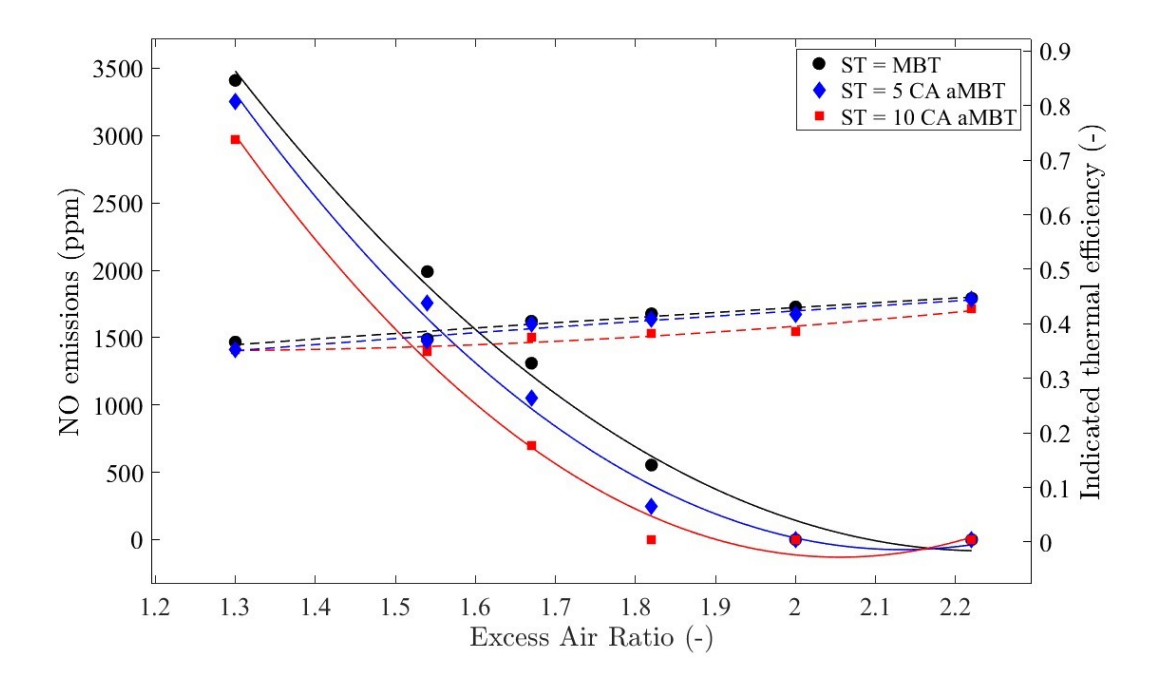


Figure 4.25: NO emissions and indicated thermal efficiency at different λ operating at a MAP of 84 kPa (naturally aspirated) with different spark timings: MBT, 5° CA, and 10° CA retardation with respect to MBT timing. The lines represent least-squares fits.

4.8 Mapping hydrogen SI engine

The model and simulations described can be drawn together to describe how NO emissions from a hydrogen ICE can be controlled using in-cylinder combustion processes. The IMEP and NO emissions reduce while ITE increases (Figure 4.26), with ITE peaking at around 42% for an absolute intake pressure of 124 kPa at $\lambda = 1.82$. By increasing the intake manifold air pressure further than 124 kPa, the engine operates at higher loads, but the ITE reduces because the CA50 combustion location cannot be centred on 8° CA aTDC due to the retardation of spark timing to mitigate knock. The IMEP and NO emission variation with spark timing (for $\lambda = 1.82$, Figure 4.27) shows that the highest ITE is achieved at the MBT timing for each operating condition due to the highest power output. ITE and load vary proportionally with spark timing; hence, NO emissions can be reduced by retarding spark timing at a slightly reduced IMEP. This also mitigates knock (Figure 4.14). Figure

4.27 also shows that the reduction of NO emissions is more pronounced by varying the mixture composition, as it influences the in-cylinder temperature and inhibits the NO formation process to almost zero levels under ultra-lean-burn operation of the SI hydrogen engine.

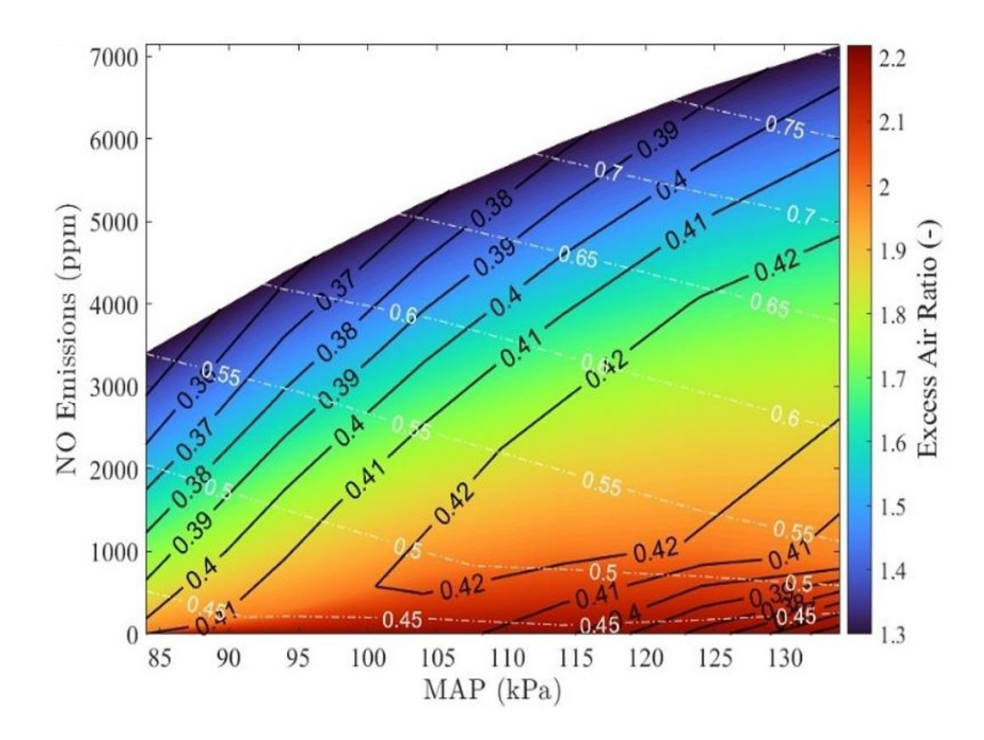


Figure 4.26: The operation of hydrogen SI engines to control NO emissions for various MAP, λ , and the knock region.

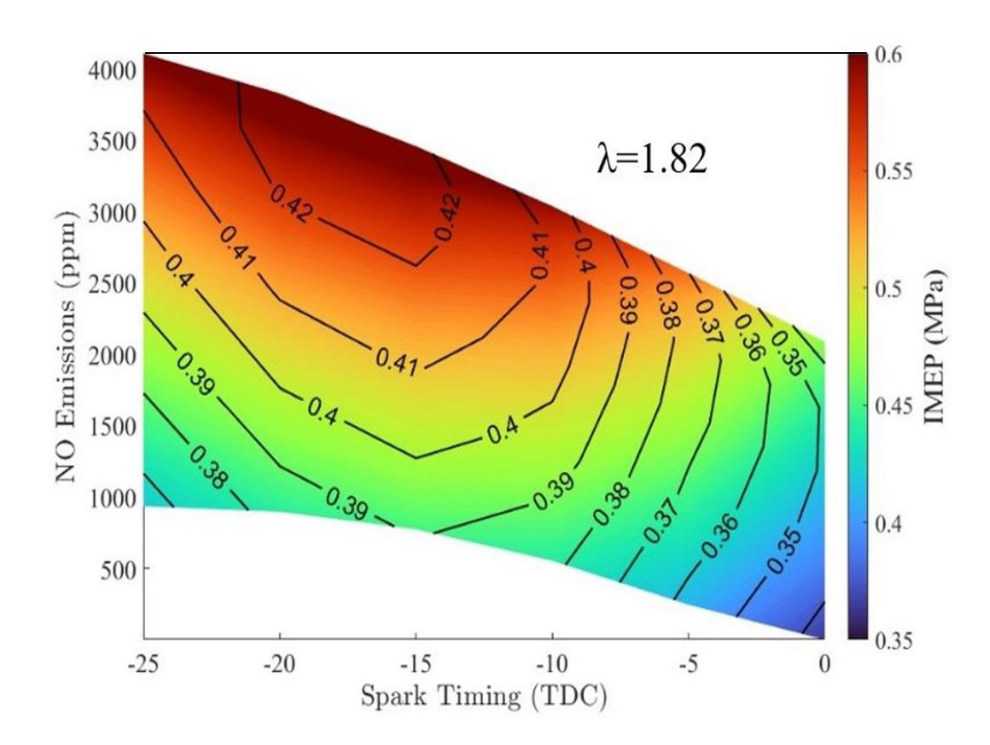


Figure 4.27: The operation of hydrogen SI engines to control NO emissions for various IMEP and spark timings at $\lambda=1.82$. ITE is shown as a heat map and contour lines, whilst the dashed white line represents IMEP.

4.9 Summary

Improvements to the single-zone combustion model include incorporating LFS to investigate NO emissions and the knocking characteristics of boosted lean-burn hydrogen combustion. The simulated cylinder pressure, heat release rate, and peak cylinder pressure are validated with experimental results, agreeing to within the standard error of cycle-to-cycle fluctuations. The simulations show that a naturally aspirated hydrogen-fuelled SI engine can operate at $\lambda = 1.30$ to $\lambda = 2.60$. However, CA50 could not be centred at the optimal position for mixtures operating leaner than $\lambda = 2.22$, particularly when the boost pressure exceeds 114 kPa. This is because high dilution leads to a longer combustion duration. The simulations indicated that boosted lean-burn operation improves the indicated thermal efficiency (ITE) by up to 42% (at $\lambda = 1.82$ under manifold air pressure of 124 kPa at a load of 6 bar IMEP). Once validated, the NO emissions model shows that emissions increase

with boost pressure; however, optimizing the start of combustion and the excess air ratio curtails this increase. For $\lambda=1.82$, the NO emissions reduce by 55%, almost dropping to zero, but this reduction impacts ITE only marginally. Further experimental work is required to substantiate the proposed boosted lean-burn hydrogen SI engine technology.

Chapter 5

Laminar flame speed correlation

Experimental data on hydrogen flame speed at elevated pressures are scarce due to the instability of the flames. Nonetheless, the properties of stable hydrogen flames can be predicted using chemical kinetics models. The injection of water could offer several benefits to combustion and emissions performance as it modulates the laminar flame speed (LFS) within the combustion chamber, but this effect has not been completely understood. Currently, no correlation exists to predict the LFS of hydrogen-air combustion with water addition under lean mixture engine operating conditions. In this chapter, a new correlation will be developed to predict the LFS of hydrogen-air with water addition under lean mixture engine operating conditions. Preferential diffusion effects, particularly those associated with hydrogen's high diffusivity and low Lewis number, can influence flame propagation and combustion characteristics in lean hydrogen-air mixtures. In this work, laminar flame speeds were obtained from detailed chemical kinetic simulations using mixture-averaged transport properties. While this approach does not fully capture multi-component diffusion or Lewis number-dependent transport, it was sufficient to provide accurate inputs for the zero-dimensional combustion models and to establish trends in the effects of hydrogen content and excess air ratio on performance and emissions.

The developed hydrogen LFS with water addition will be used to develop a two-zone combustion model to investigate the effect of water addition in a hydrogen spark ignition (SI) engine in Chapter 6. The LFS is a physiochemical property of the combustible mixture and is defined as the speed at which a premixed, steady, planar flame front propagates in a direction normal to the plane. A flame results from a self-sustaining chemical reaction occurring within a space referred to as the flame front, which heats the reactants and concurrently converts the unburned mixture into products. The flame front consists of two regions:1. The preheated zone and 2. The reacting zone. In the preheated zone, the temperature of the reactants is raised through heat conducted from the reacting zone. The temperature gradient between the two zones is not considered significant, as no substantial energy release or reaction occurs [113]. Hence, due to the combustible charge being burned, a critical temperature will be reached, and an exothermic reaction will occur. Flames will not be stable in any combustion application, and no experimental setup exists to measure the perfectly planar propagating flame. Thus, for every measurement, the approximation of the one-dimensional planar flame front is assumed by considering the deviation from its planar flame geometry. Moreover, all experimental hydrogen LFS values used in this study are assumed to be stretch-free. The laminar burning velocity is formulated as the mass burning rate per unit surface area of the unburned mixture:

$$S_l = \frac{1}{A\rho_u} \frac{dm}{dt} \tag{5.1}$$

where A is the flame front surface area, ρ_u is the unburned mixture density, and $\frac{dm}{dt}$ is the mass burning rate. It is necessary to distinguish between the laminar flame speed and the burning velocity. The LFS refers to the flame propagating in a fixed frame of reference, whereas the burning velocity refers to the flame spherically growing from the spark or its specified ignition point. Hence, the flame speed is equal to the sum of the burning velocities and the rate of expansion of the burned gases.

5.1 Chemical kinetic simulations

The laminar premixed flame structure consists of two primary zones: the preheat zone and the reaction zone. The preheat zone occupies most of the thermal flame thickness, where the fresh hydrogen with air mixture is gradually heated by thermal

diffusion and radical transport from the reaction zone. In this region, the reaction rate is low, but the temperature and species gradients are steep. The reaction zone is thinner in comparison and is the zone where the chemical reactions accelerate rapidly which lead to the formation of intermediate radicals and combustion products. The dominant reaction mechanisms include both bimolecular and chain-branching reactions involving H, O, and OH radicals. The flame speed was determined by the balance between thermal diffusion and chemical reaction rates across these zones. The chemical kinetic mechanism of a freely propagating hydrogen flame, consisting of 19 elementary reversible reaction mechanisms developed by Li et al. [233], was used to calculate the laminar flame speed (LFS) of hydrogen-air combustion under various pressures ranging from 10 bar to 70 bar, temperatures from 400 to 800 K, equivalence ratios from 0.35 to 1, and for 0 to 20% molar fraction of water. More than 5000 LFS values were calculated through CONVERGE [215] in a well-stirred reactor for the selected range of conditions. These data were used to develop a new correlation capable of predicting the LFS of hydrogen-air combustion with water addition in any practical power generation device.

The model by Li et al. [233] has been validated against published experimental LFS data for hydrogen-air combustion for temperatures ranging from 298 to 3000 K, pressures from 0.3 to 87 atm, and equivalence ratios from 0.25 to 5. The experimentally measured values of the LFS were obtained either through burner flame stabilization [234] or spherical flame propagation in a chamber [221, 223]. The main difference between these two techniques is that the burner flames did not consider the stretch rate effect, resulting in higher values than those obtained through spherical flame propagation, where the results were corrected based on the flame stretch rate. A comparison of published experimental results of hydrogen burning speeds [234, 235, 221, 236] with the calculated LFS from the Li et al. model at different equivalence ratios is shown in Figure 5.1. The simulated values of LFS show good agreement with the experimentally measured stretch-free burning velocities [221, 236] under lean operating regions of $\Phi < 1$.

The comparison of published experimental data of Koroll and Mulpuru [235] and Lyu et al. [120] with simulations performed under 1 atm pressure and at a

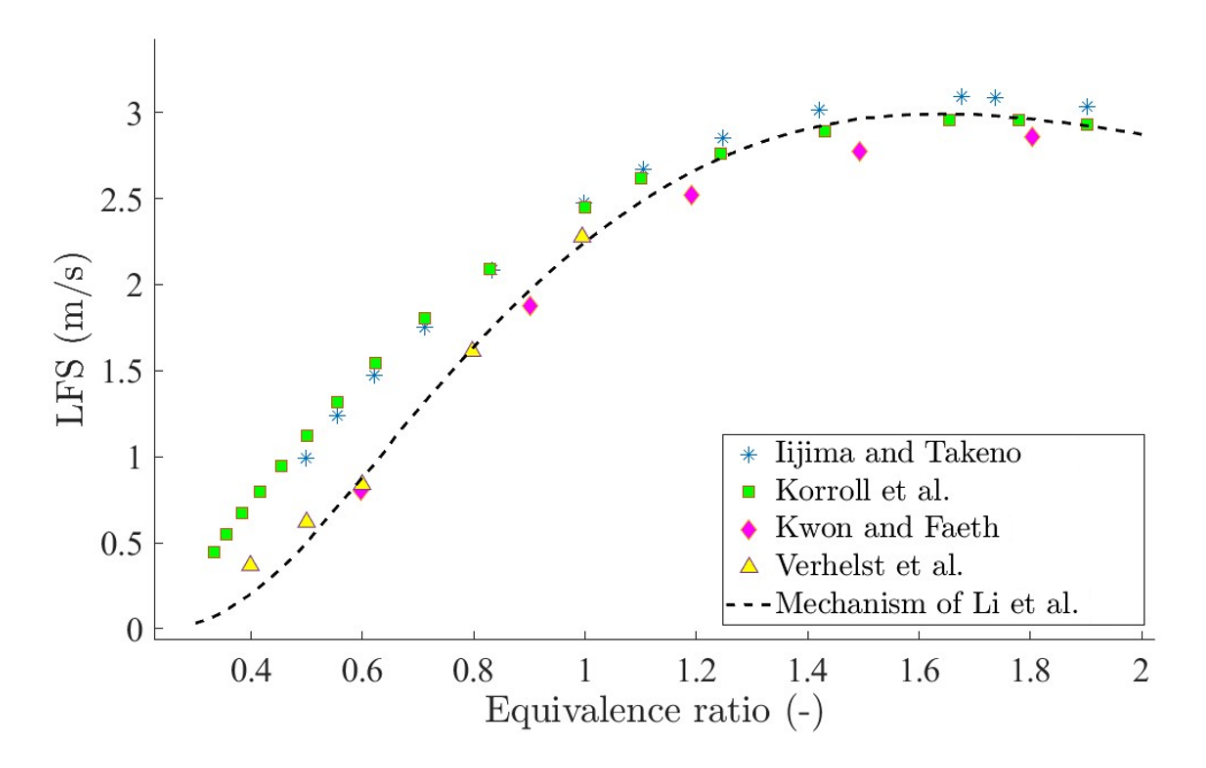


Figure 5.1: Laminar burning velocities at different equivalence ratios at P of 1 atm and T of 300 K. The markers represent the experimental data values [234, 237, 221, 223]. The dashed line represents the hydrogen LFS calculated from the detailed chemical kinetics with the mechanism of [228].

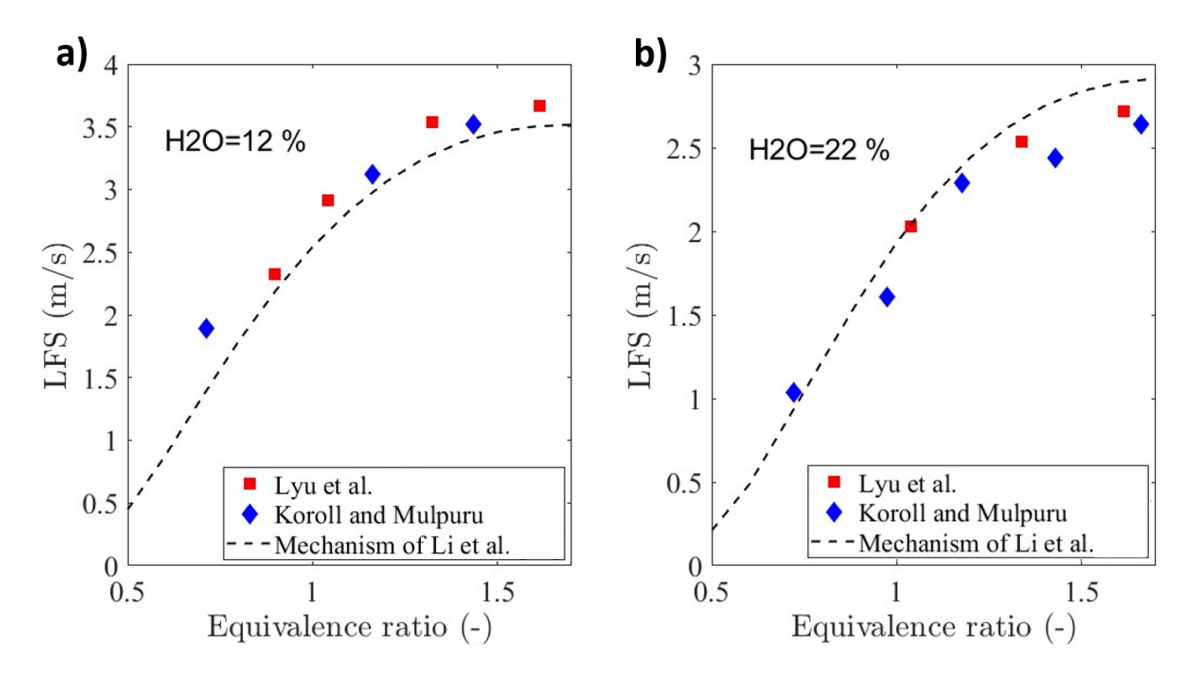


Figure 5.2: Laminar flame speed of hydrogen with 12% and 22% water addition at various equivalence ratios (P=1 atm, T=373 K). The dashed line is the simulated LFS using the Li et al. mechanism [233], and the markers represent experimental data [235, 120].

temperature of 373 K, with varied equivalence ratios of the hydrogen-air mixture from 0.5 to 1.7 for steam dilutions at 12% and 22% by volume, are shown in Figure 5.2. Both the experimental and simulated LFS exhibit the similar global trend with varying equivalence ratios. The simulated LFS results are within a maximum of 11% and 6% error margins when compared to the experimental data of Koroll and Mulpuru [235] and Lyu et al. [120], respectively. The data presented in Figures 5.1 and 5.2 show that the hydrogen kinetic mechanism is in good agreement with experimental data for neat hydrogen-air lean mixture combustion [221, 223], and for water addition under lean hydrogen combustion [235, 120]. Therefore, the Li et al. [233] chemical kinetic model was used in this work as the basis to calculate the lean-burn water-diluted hydrogen LFS values under high pressure engine-relevant operating conditions.

5.2 LFS correlation

Generation of LFS data from chemical kinetic models for different sets of operating conditions is time-consuming. Therefore, it is useful to develop a correlation for hydrogen that can predict the LFS under complex engine operating conditions with a high degree of accuracy, particularly for water injection strategies favoring NOx reduction [82]. The formulation [152] used to fit the hydrogen with water addition LFS is

$$S_{l}(\phi, P, T_{u}, \chi) = S_{l0}(\phi, P, T_{u}) \left(\frac{T_{u}}{T_{0}}\right)^{\alpha(\phi, P, T_{u})} (1 - \chi F(\phi, P, T_{u}, \chi))$$
 (5.2)

where the parameters S_{l0} , α , and F were fitted using polynomials of least order ($R^2 = 0.99$). A reference pressure ($P_0 = 5$ bar) and a reference temperature ($T_0 = 600$ K) were set to make the pressure and temperature non-dimensional. Initially, just over 2500 LFS data points were fitted using the Levenberg-Marquardt algorithm for S_{l0} (Equation 5.2) at various pressures and equivalence ratios at a fixed temperature of 600 K. The correlation was tested to ensure that no spurious values were generated, confirmed by conducting a non-negative constrained multivariate regression analysis. The Akaike Information Criterion (AIC) [238] was adopted to explore different combinations of the predictors to determine the most optimized fitting model:

$$S_{l0} = a_1 \phi^2 + a_2 \phi^3 + a_3 \log(\phi) + a_4 \log\left(\frac{P}{P_0}\right) + a_5 \exp(-\phi) + a_6 \phi \log\left(\frac{P}{P_0}\right) + a_7 \log(\phi) \left(\frac{P}{P_0}\right) + a_8 \exp(-\phi) \left(\frac{P}{P_0}\right)$$
 (5.3)

The corresponding fitting coefficients a_i are shown in Table 5.1. Figure 5.3 shows the comparison of the calculated initial S_{l0} values obtained from the chemical kinetics model with the newly developed correlation (Equation 5.3). It can be seen that the correlation predicted S_{l0} with good accuracy, where 98% of data fitted well within 10% error. However, the inset plot in Fig. 5.3 shows that the values for the

LFS lower than 0.3 m/s did not fit within the 10% error margin. This was due to the weighting factor which could not be increased further since it tended to reduce the correlation accuracy for the entire operating condition range.

Table 5.1: Coefficients a_i to be used in Equation 5.3, coefficients b_i to be used in Equation 5.4, coefficients c_i to be used in Equation 5.5, and coefficients d_i to be used in Equation 5.6, for conditions of $P_0 = 5$ bar and $T_0 = 600$ K.

C.	Value	C.	Value	C.	Value	C.	Value
a_1	13.7528	b_1	-1.2354	c_1	9.294	d_1	4.9667
a_2	-4.3159	b_2	0.0000345	c_2	-27.86	d_2	-3.0818
a_3	-1.2832	b_3	0.10518	c_3	30.70	d_3	0.4600
a_4	1.0261	b_4	-0.5332	c_4	-14.76	d_4	-0.2508
a_5	-3.4574	b_5	4.3181	c_5	2.853	d_5	0.4331
a_6	-3.7039	b_6	1.8539			d_6	3.2483
a_7	0.1490	b_7	-0.5166			d_7	-3.0087
a_8	0.2545	b_8	-0.6528			d_8	-8.5907
		b_9	3.2115			d_9	0.1448

To explore the dependence of pressure, temperature, and equivalence ratio on the exponent term α , a polynomial was developed for $\alpha(P, \phi, T)$ by fitting it with a set of 2000 hydrogen LFS data generated at different conditions. Most of the available LFS correlations [149, 150] considered the exponent α only to be dependent on equivalence ratio. Figure 5.4 shows the power coefficient α calculated from Equation 5.2 once the S_{l0} was known from Equation 5.3. It can be seen that α is not only dependent on ϕ but also influenced by pressure and temperature; all three parameters are intercoupled. Due to the power coefficient α being completely dependent on pressure, temperature, and equivalence ratio, α in Equation 5.2 has been expressed to account for the effects of pressure and equivalence ratio. Then the temperature effect on the hydrogen LFS was accounted for by including an exponential term that relates to temperature and equivalence ratio through the exponent β , which was previously considered to be solely dependent on the equivalence ratio. This third order polynomial of α consisting of 9 coefficients b_i was fitted (R² = 0.99).

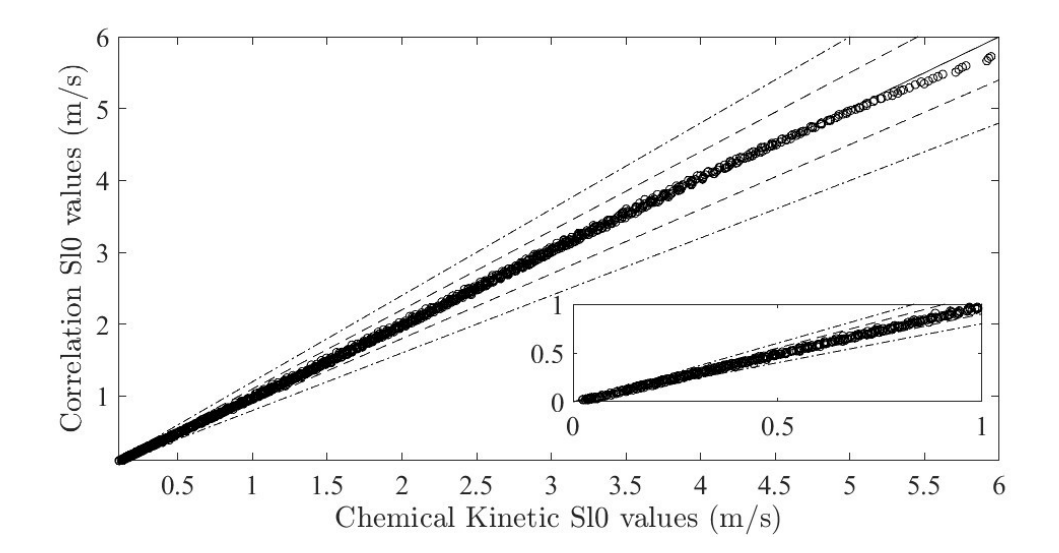


Figure 5.3: Chemical kinetic values of S_{l0} compared to correlation S_{l0} values using Equation (3), with lines of 10% and 20% deviation (P=10-70 bar, $\phi = 0.35 - 1$, T=600 K, and $\chi = 0$).

The attained polynomial expression for α is shown in Equation 5.4, and the fitting coefficients for b_i are presented in Table 5.1.

$$\alpha = \left(b_1 \phi^3 + b_2 \left(\frac{P}{P_0}\right)^3 + b_3 \phi^3 \left(\frac{P}{P_0}\right) + b_4 \log \left(\frac{P}{P_0}\right) + b_5 \exp(-\phi) + b_6 \phi \log \left(\frac{P}{P_0}\right) + b_7 \log(\phi) \left(\frac{P}{P_0}\right) + b_8 \exp(-\phi) \left(\frac{P}{P_0}\right) + b_9 \phi \exp\left(-\frac{P}{P_0}\right)\right)$$

$$\cdot \exp\left(\beta \frac{T}{T_0}\right)$$
(5.4)

where β is dependent only on the equivalence ratio, and it is given in the form of

$$\beta = c_1 \phi^4 + c_2 \phi^3 + c_3 \phi^2 + c_4 \phi + c_5 \tag{5.5}$$

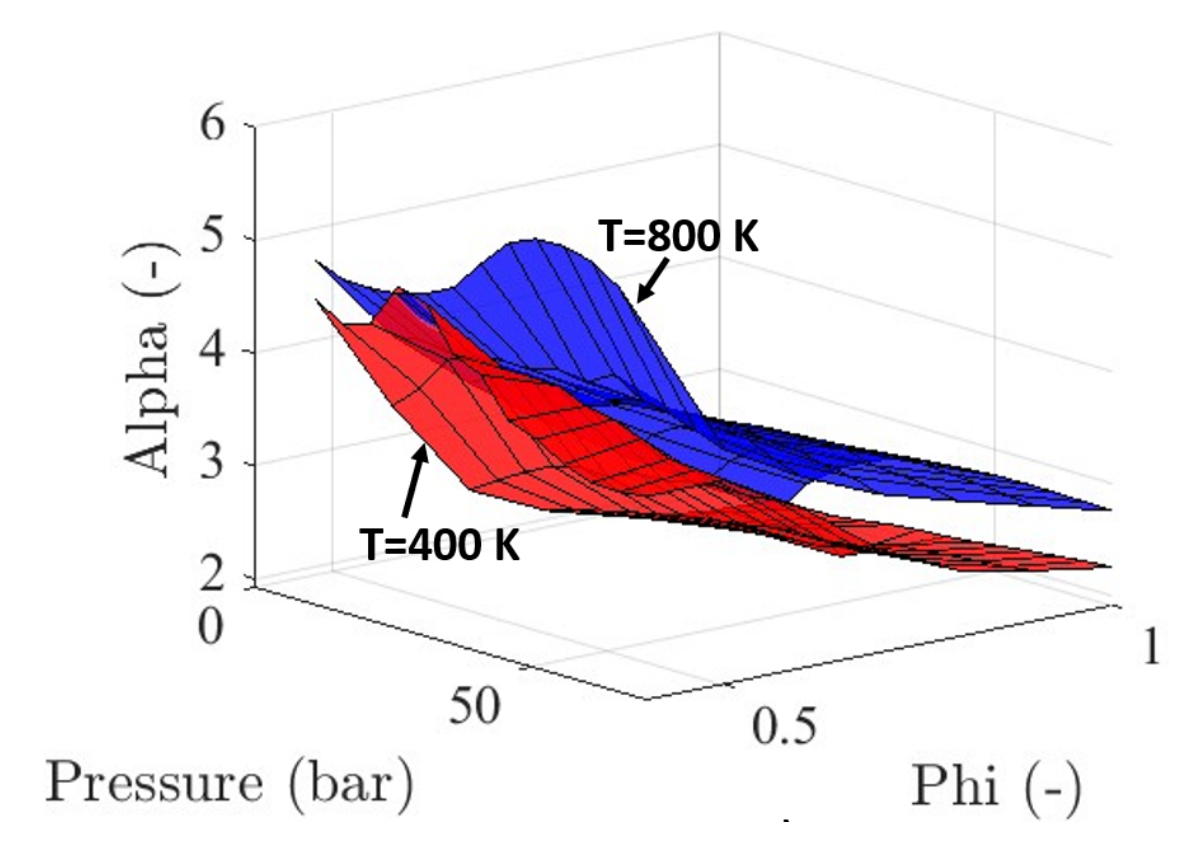


Figure 5.4: Alpha at various equivalence ratios and pressures for temperatures of 400 K and 800 K for hydrogen.

The accuracy of the α term in Equation 5.3 due to the inclusion of the temperature effect on the hydrogen-air LFS was compared with the chemical kinetic model [233] for 3000 data points (Figure 5.5). The improvement in accuracy for the hydrogen-air flames through the incorporation of the term $\exp\left(\frac{\beta T}{T_0}\right)$ in α (Equation 5.4, black markers) is compared with the fitting accuracy without the proposed term $\exp\left(\frac{\beta T}{T_0}\right)$ (red markers). The accuracy improved significantly for LFS values greater than 3 m/s; furthermore, most of the data points are within a $\pm 10\%$ margin.

5.3 LFS correlation with water addition

Injecting water into the intake manifold of the hydrogen-fuelled engine modulates the LFS and the local equivalence ratio within the combustion chamber. The new LFS correlation of hydrogen-air combustion (Eqs. 5.2 and 5.4) can now be extended to include the effects of the molar fraction of water on hydrogen combustion under

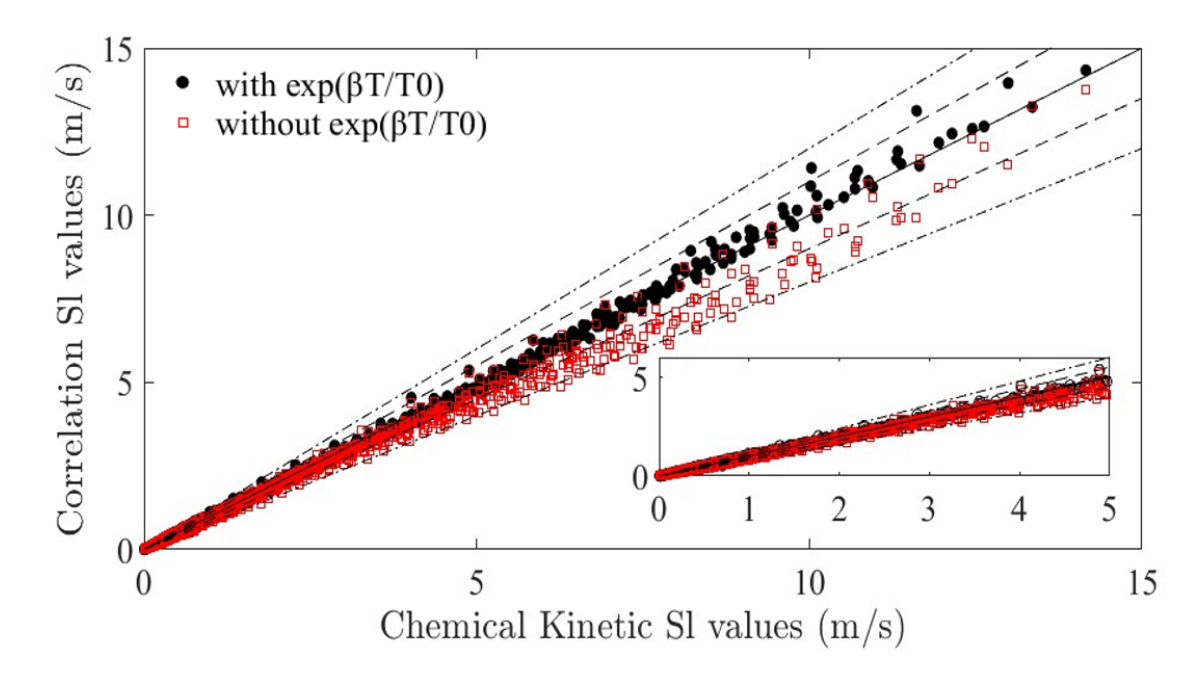


Figure 5.5: Chemical kinetic values of LFS compared to the new correlation LFS values with 10% and 20% uncertainty bands. Black markers show LFS values by calculating α (Eq. 4), and the red markers are the LFS values without using the new term.

engine-relevant conditions. The residual volume fraction term F in the hydrogen flame speed correlation combines the effects of pressure and equivalence ratio in the correction term [152].

In this work, the water addition was incorporated into the flame speed correlation by including the molar fraction of water χ in the term F in Equation 5.2. Note that the equivalence ratios used in this study only considered fuel and air, and not the global equivalence ratio that is affected by the dilution of the reactive mixture by water vapor. The term F was fitted dependently on pressure, temperature, equivalence ratio, and water addition:

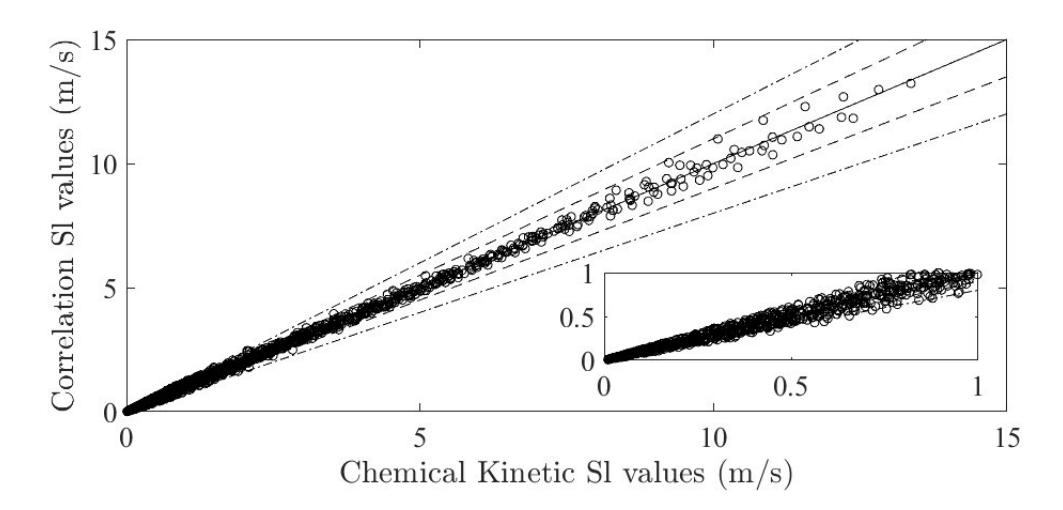


Figure 5.6: Chemical kinetic values of LFS compared to correlation values with 10% and 20% deviation, including the term $\exp\left(\frac{\beta T}{T_0}\right)$ ($\chi=0-20\%,\ P=10-70$ bar, T=400-800 K, $\phi=0.35-1$).

$$F = d_1 + d_2 \left(\frac{P}{P_0}\right) \chi^2 + d_3 \log\left(\frac{P}{P_0}\right)$$

$$+ d_4 \left(\frac{P}{P_0}\right)^2 \chi^2 + d_5 \left(\frac{T}{T_0}\right)^2$$

$$+ d_6 \left(\frac{P}{P_0}\right) \left(\frac{T}{T_0}\right) \chi^2 + d_7 \phi \left(\frac{T}{T_0}\right)$$

$$+ d_8 \chi^2 \left(\frac{T}{T_0}\right) + d_9 \phi^2 \left(\frac{P}{P_0}\right)$$

$$(5.6)$$

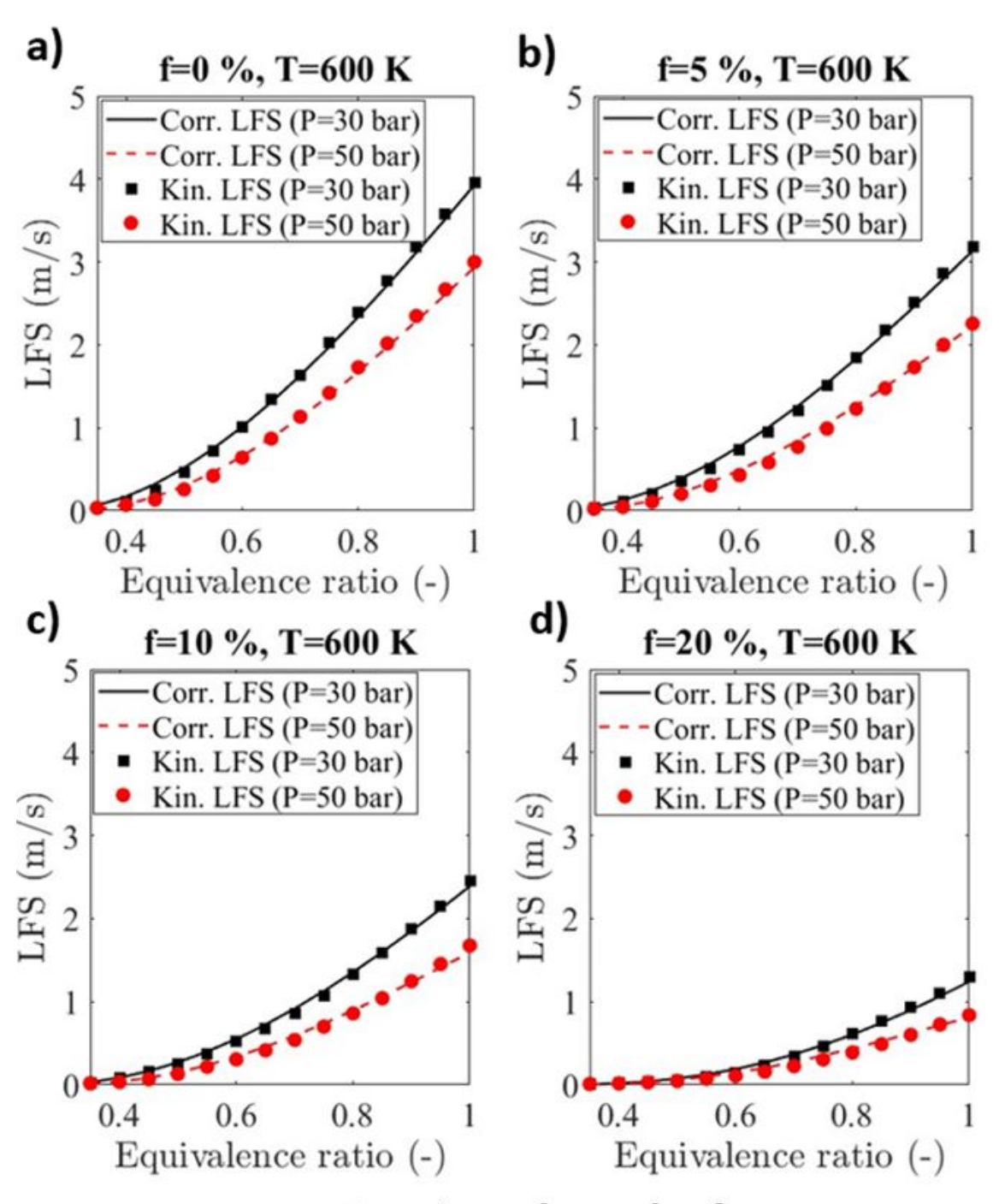
where the coefficients d_i are given in Table 5.1. The comparison of values obtained from the correlation and the chemical kinetic model at different pressures, temperatures, and equivalence ratios with water addition ranging from 0 to 20% molar fraction is shown in Figure 5.6. About 84% of data fitted within 10% and around 97% of data fitted within the 20% error margin. These data points correspond to the operating conditions used in this study.

5.4 Hydrogen with water addition LFS at enginerelevant conditions

Figure 5.7 shows the hydrogen LFS values obtained from the new correlation compared with the calculated chemical kinetic flame speed values. This comparison was made for equivalence ratios ranging from 0.35 to 1 with 0 to 20% (at 5% increment) of water addition, whilst the whole mixture was maintained at pressures of 30 and 50 bar, and temperatures between 400 and 800 K. The correlation was accurate for all cases (Figures 5.7 (a-c) and 5.7 (e-h)) except for the 20% water addition case. In the 20% water addition case, particularly for equivalence ratios greater than 0.8 and at a pressure of 30 bar and a temperature of 400 K (Figure 5.7 (h)), the correlation underpredicted the LFS values. For pressures of 30 bar and 50 bar, at a temperature of 600 K, and with 20% water addition at equivalence ratios less than 0.7, the correlation slightly overpredicted the LFS values, with the largest deviation being within 13% and 18%, respectively (Figure 5.7 (d)). Figures 5.7 (a-d) also reveal that the LFS predicted by the correlation decreased with an increase in water addition from 0 to 20%. The pure hydrogen LFS decreased by 67% and 72% for 20% water addition at 30 and 50 bar, respectively. For a pressure of 30 bar at ambient reactive mixture temperatures of 400 K and 800 K, the LFS decreased by 60% and 74%, respectively. Figures 5.7 (a-d) show that by increasing the pressure from 10 to 30 bar, the LFS decreased by 27%, 29%, 32%, and 35% for water additions of 0%, 5%, 10%, and 20%, respectively. Whereas, when the temperature was increased from 400 to 800 K (Figures 5.7 (e-h)), the LFS increased significantly by 313%, 467%, 525%, and 685% for water additions of 0%, 5%, 10%, and 20%, respectively. It is clear that the new correlation preserves the global trend of the chemical kinetic LFS values at all operating conditions presented in Figure 5.7.

5.5 Effect of water addition on LFS correlation

Figure 5.8 shows the effect of water addition on the LFS correlation at various pressures and equivalence ratios, and it can be seen that the LFS reduces with



Continued overleaf

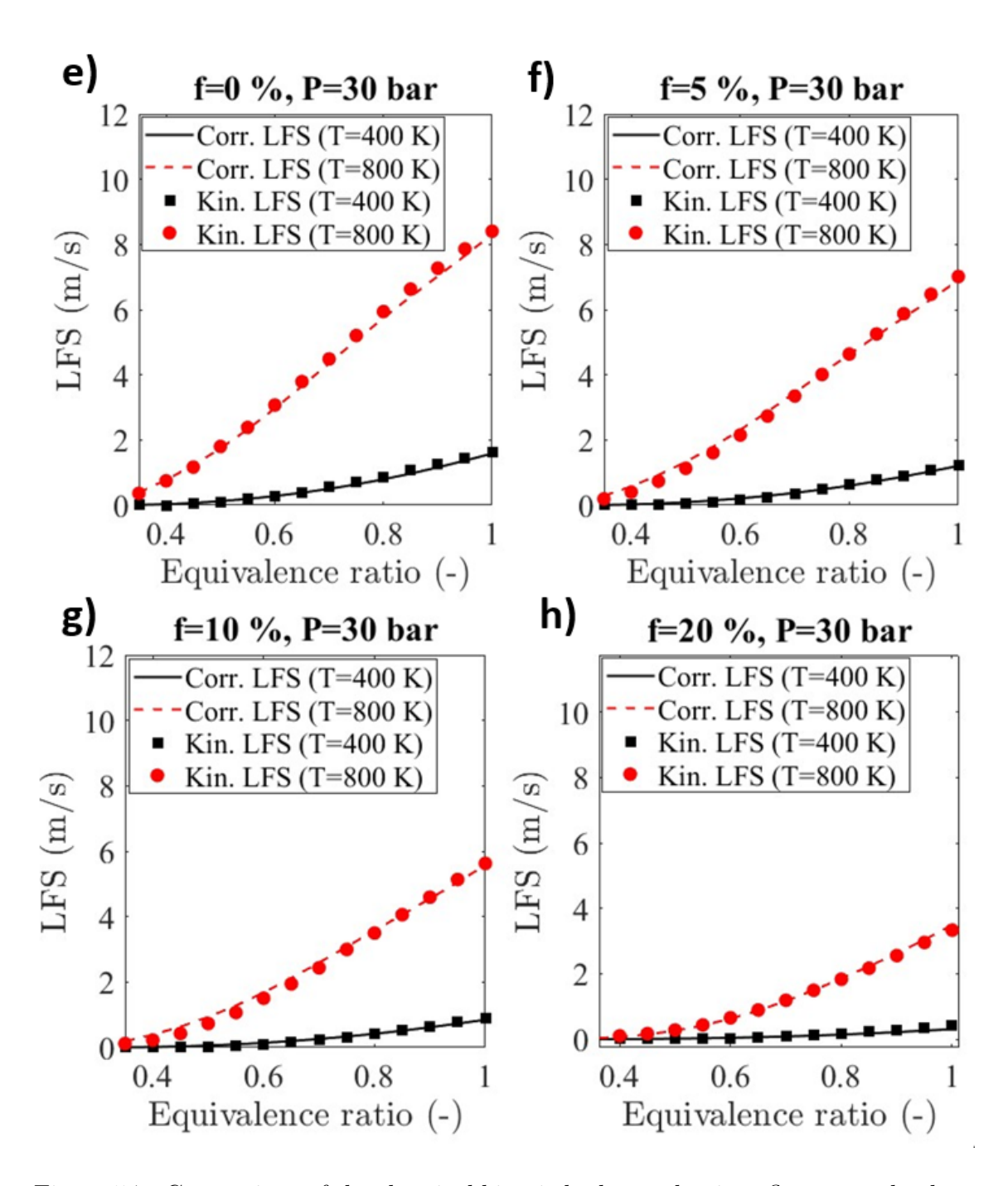


Figure 5.7: Comparison of the chemical kinetic hydrogen laminar flame speed values with correlation values at various operating conditions.

increasing pressure. This is in agreement with previous work [239], where it was shown that at water addition of less than 20% by mole fraction, the LFS of hydrogen initially increased and then decreased with increasing pressure. The inflection point occurred at a pressure of 10 atm. Since this study focuses on engine-relevant higherpressure operating conditions, pressures less than 10 bar were not simulated; hence only a monotonic reduction of the LFS with an increase in pressure was observed. The observed monotonic reduction in flame speeds with pressure could be associated with the reaction order n being less than two due to steam being considered as a third-body in the reaction, hence $S_L \sim P^{(n/2-1)}$ causes the flame speed to reduce with higher pressures, as discussed in [240]. For neat hydrogen, the LFS decreased by 73%, 66%, and 58% when the pressure was varied from 10 to 70 bar for equivalence ratios of 0.6, 0.8, and 1, respectively (Figures 5.8 (a - c)). The new correlation and its analysis revealed that pressure has a more pronounced effect on LFS for leaner hydrogen mixtures due to relatively lower energy content in the reactive mixture, which was insufficient to counteract the effect of increased pressure. It is interesting to note that for higher percentages of water addition, specifically at 20% by mole, the LFS was not significantly affected by pressure at levels above 40 bar for mixtures leaner than 0.8 (Figures 5.8 (a-b)). This phenomenon occurs due to the reduction in global temperature resulting from increased dilution and higher heat capacity of the charge; hence, the dissociation reactions were not initiated under higher percentages of water addition. It has been shown experimentally [120] that water addition controls the reaction, which causes deflagration of the hydrogen flame at various equivalence ratios, as well as slowing the rise in pressure. The new correlation predicts this behavior (Figure 5.8) under all pressures and equivalence ratios, due to an increase in heat capacity of the mixture caused by steam dilution [241]. The equivalence ratio effect on the LFS was consistently seen in all the presented data. Under leaner mixture conditions, both with and without water addition, an increase in the equivalence ratio caused the LFS to increase (Figures 5.8 (a – c)). For the case of pure hydrogen at a pressure of 30 bar and a temperature of 700 K, the hydrogen LFS increased by 94% and 201% when the equivalence ratio was raised from 0.6 to 0.8 and 1, respectively. Whereas for water addition of 20% at the same conditions, the LFS increased by 179% and 457% when the equivalence ratio was raised from 0.6 to 0.8 and 1, respectively. Though the LFS increases significantly with an increase in equivalence ratio for 20% water addition relative to neat hydrogen combustion, on an absolute scale, the magnitude of the hydrogen LFS with water addition is much lower than that of neat hydrogen combustion. Additionally, the new correlation provides LFS values very close to those predicted by chemical kinetics, except for an equivalence ratio of 0.6, where the correlation slightly overpredicts the LFS values (Figure 5.8 (a)) with the greatest deviation of approximately 11%. However, as the equivalence ratio increased beyond 0.6, the accuracy of the correlation also improved. This is attributable to the higher magnitudes of LFS associated with the equivalence ratio.

Figure 5.9 shows that the LFS decreases linearly with increasing water addition for all pressures and temperatures, but the rate of decrease of the LFS of hydrogen is more pronounced at higher ambient temperatures of the reactive mixture. The correlation also reveals that the linear rate of decrease of LFS is evident even at lower ambient mixture temperatures of 400 K and an equivalence ratio $\Phi = 1$ (Figures 5.9 (c-d)). However, the rate of decrease of flame speed is not significant at $\Phi < 1$ at the same lower ambient mixture temperatures of 400 K (Figures 5.9 (a-b)). The new correlation closely matches chemical kinetic LFS values, with exceptions at an equivalence ratio of 0.5 and pressures of 30 bar and 50 bar (Figures 5.9 (a-b)), respectively. In these cases, the new correlation slightly overpredicts the LFS values, with the greatest deviation being approximately 13% (Figure 5.9 (b)). However, as the equivalence ratio increases to the stoichiometric condition, the accuracy of the new correlation improves for various temperatures, pressures, and water additions (Figures 5.9 (c-d)). The linear decrease in the rate of the LFS is noted with the addition of water, but there appears to be a limit to the amount of water addition for effective control of hydrogen combustion, beyond which it tends to be detrimental to engine performance. This is due to a decrease in the global reaction temperature caused by the high heat capacity of the water vapor in the reactive mixture [242]. The LFS values increase with increasing temperature, a trend captured by the power α used in the correlation (Equation 5.2). As explained in subsection 5.2.2, α captures not only the effect of temperature but also the influence of the equivalence ratio and the coupled effect of pressure and temperature on the hydrogen LFS. The new correlation for hydrogen LFS, with a reduced order of polynomial and a reduced number of coefficients, shows that more than 97% of data are within the 20% accuracy level across various temperatures, pressures, equivalence ratios, and water addition conditions. The new correlation is sufficiently sensitive to predict variations of LFS under different conditions of pressure, temperature, equivalence ratio, and water additions. Error analysis of this correlation is discussed in the next section.

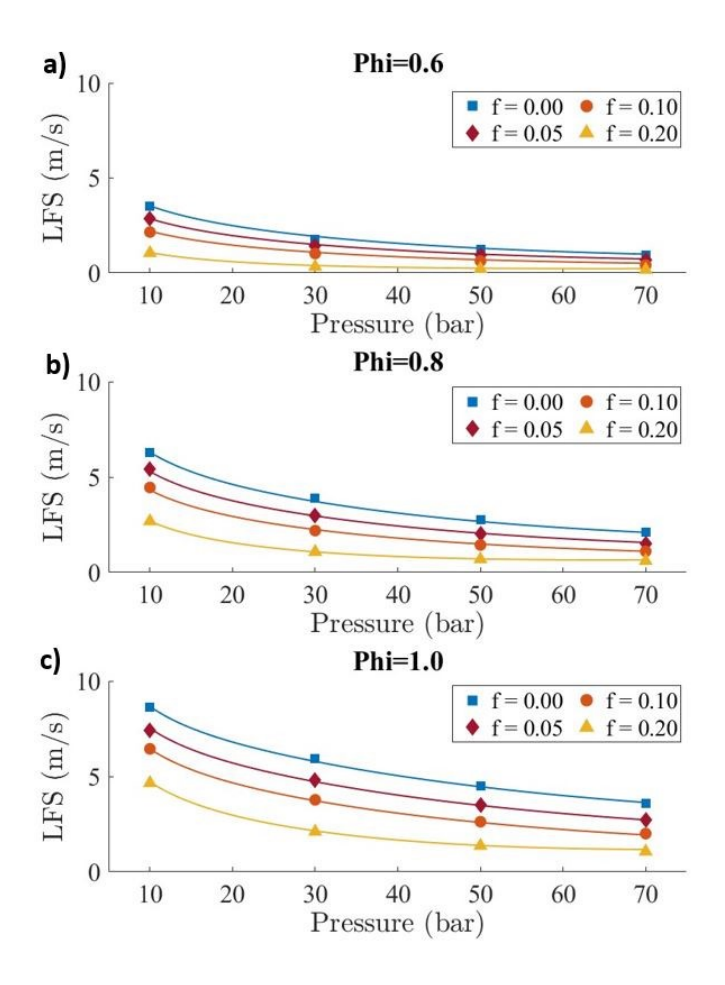


Figure 5.8: Laminar flame speed values for various water additions (0 - 20%) at different pressures: (a) at an equivalence ratio of 0.6; (b) at an equivalence ratio of 0.8; and (c) at an equivalence ratio of 1 at a temperature of 700 K. Solid lines represent correlation values and markers denote the chemical kinetic values.

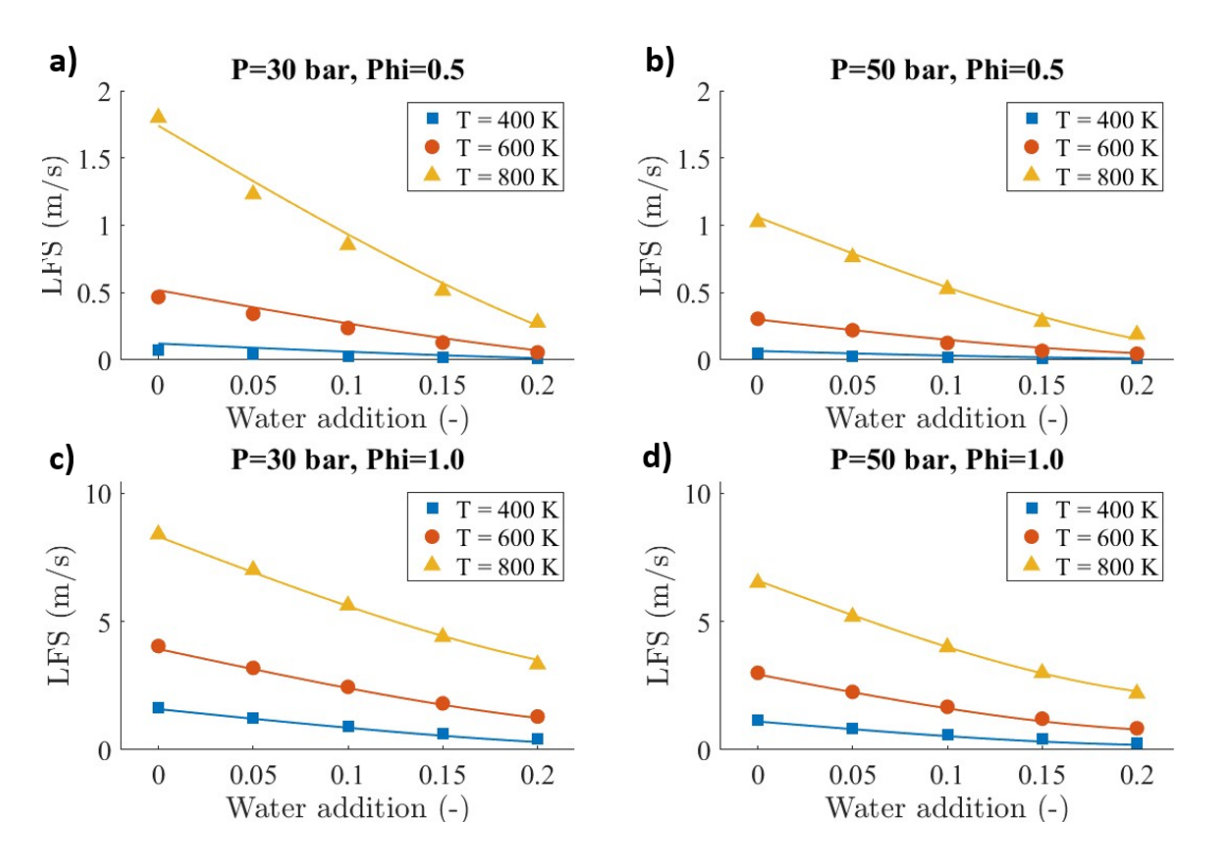


Figure 5.9: Laminar flame speed values of hydrogen with various water additions at different temperatures, pressures, and equivalence ratios. Solid lines represent correlation values, and markers denote the chemical kinetic values.

5.6 Residual analysis

Figure 5.10 (a) illustrates the LFS error across a wide range of pressures from 10 to 70 bar, temperatures from 400 to 800 K, and equivalence ratios from 0.35 to 1. The accuracy of the pure hydrogen LFS values predicted from the new correlation is consistent with previous studies [150, 152], as more than 99% of the data are within a 20% error margin. Furthermore, around 87% of the data were within a 10% deviation. To quantify the relative error, residuals between the chemical kinetics and the correlation flame speed values were calculated for selected operating conditions. The average mean error was within 5% for water additions of 5% and 10%, within 4% for water addition of 15%, and within 7% for water addition of 20%. A comparison was also made between the LFS values obtained from Equation 5.4 with and without the term $\exp\left(\frac{\beta T}{T_0}\right)$ as shown in Figure 5.10. A significant number of data points

had their residuals reduced significantly by incorporating the temperature-pressure coupling effect term into the new LFS correlation. Without the inclusion of the new term in α (Equation 5.4), the LFS values would be underestimated, leading to residuals shifting to higher values. The addition of the temperature-pressure coupling term successfully refined the power α , minimizing the value of the residuals. These residuals were used to generate a histogram for various operating conditions of hydrogen with water addition (Figure 5.11), and were found to be unimodal, with the accuracy assessed using the mean and standard deviation. For each level of water addition, the histogram shape remained unimodal for all concentrations of water additions, with a peak at zero. The absolute values of mean residual were 0.1033, 0.1002, 0.0665, and 0.0887 m/s for 5%, 10%, 15%, and 20% water addition, respectively. When the molar fraction of water in the mixture increased, the residual magnitudes were reduced, correlating well with the decrease in LFS values due to the water addition, as shown in Figures 5.8 and 5.9. Note that bars with less than 4 data points have not been included in Figures 5.10 and 5.11.

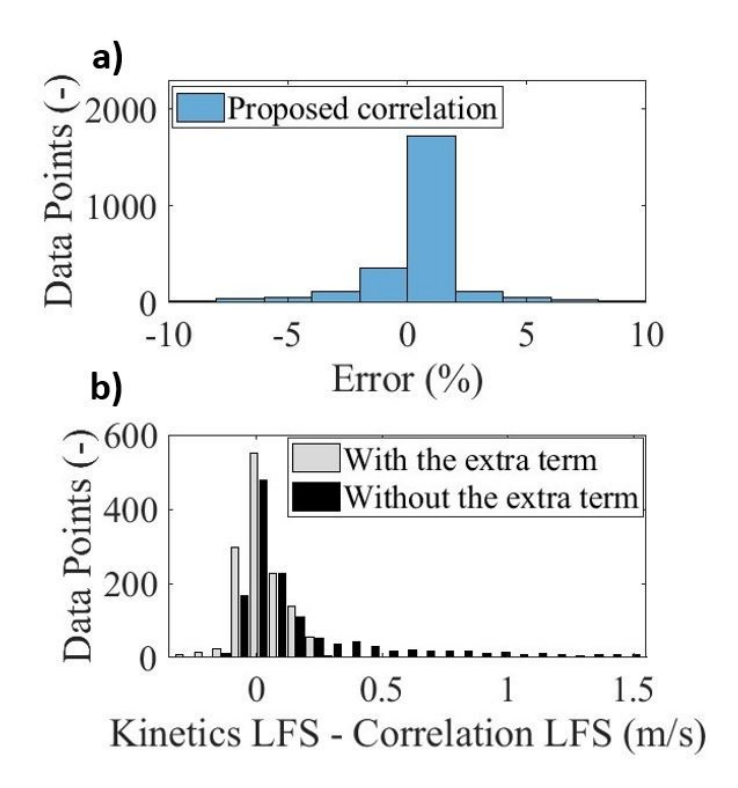


Figure 5.10: (a) The standard error for the new LFS correlation at various operating conditions ($\phi = 0.35 - 1$, P = 10 - 70 bar, and T = 400 - 800 K); (b) The histogram of the residuals with and without the exp $\left(\frac{\beta T}{T_0}\right)$ term.

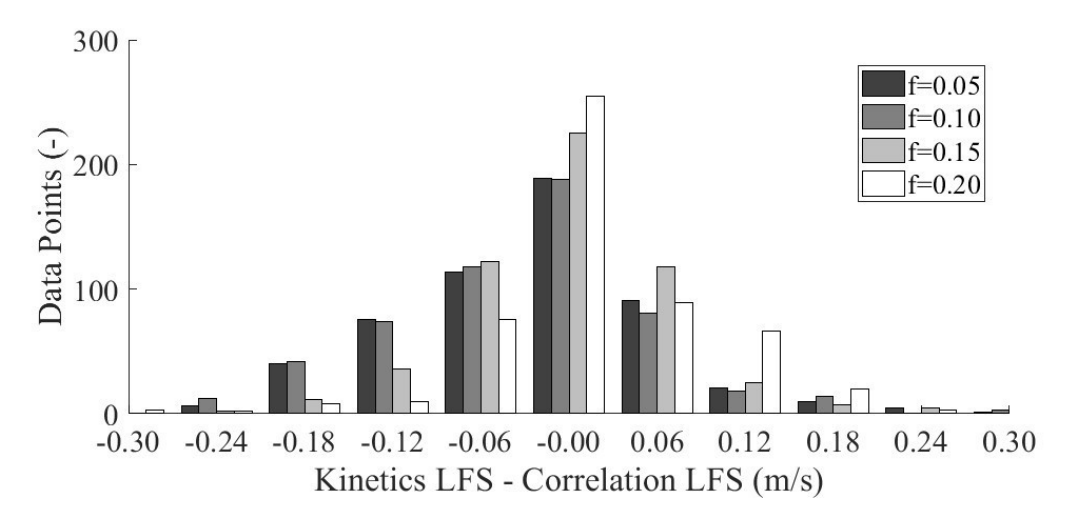


Figure 5.11: The histogram of the residuals calculated as the difference between chemical kinetics and correlation LFS values (m/s) against the number of data points at different water additions (1-20%) and operating conditions ($\phi = 0.35 - 1$, P = 10 - 70 bar, and T = 400 - 800 K).

5.7 Summary

The LFS is important for modeling internal combustion engines (ICEs), but generating these from experiments or chemical kinetic simulations can be costly and time-consuming. A new correlation accurately predicting LFS with water addition at engine-relevant operating conditions has been developed. The LFS correlation was validated for pressure ranges from 10 to 70 bar, temperature ranges from 400 to 800 K, equivalence ratio ranges from 0.35 to 1, and water addition by mole from 0 to 20%. The LFS of hydrogen-air mixtures, with and without water addition, were simulated using an accepted chemical kinetic model. Polynomial expressions of reduced order and number of terms were developed with optimized values of coefficients to predict the LFS under lean mixture operation and high-pressure conditions. The variation between the simulated values from the chemical kinetic model and the predicted values from the new correlations of reduced order resulted in an R^2 of 0.99. A new term was added to the power term α in the correlation to capture the coupled effects of pressure, equivalence ratio, and temperature on LFS under engine-relevant lean-burn, water-diluted operating conditions.

Chapter 6

An improved and extended two-zone model to study the effect of water dilution

The injection of water modulates hydrogen combustion, but there are trade-offs to be optimized between the amount of water used and engine performance, emission reduction, and knocking regions. This new validated two-zone combustion model predicts the performance of a boosted lean-burn hydrogen SI engine with water addition. The thermodynamic model incorporates water-diluted hydrogen LFS, an extended Zeldovich mechanism for nitric oxide emissions, and the Livengood-Wu integral model for knock characteristics based on advanced chemical kinetics.

6.1 Model validation

The results for in-cylinder pressure at different equivalence ratios and spark timings are validated using published data [47]. Both the simulated and experimental incylinder pressures exhibit similar trends as the crank angle increases from 340 to 410 °CA. This alignment is illustrated in Figure 6.1, which compares the experimental data (shown as markers) with the simulation results (shown by lines). In Figure 6.1, the blue markers and line represent the data for an equivalence ratio $\phi = 0.77$, while the red markers and line correspond to $\phi = 0.50$. The in-cylinder pressure

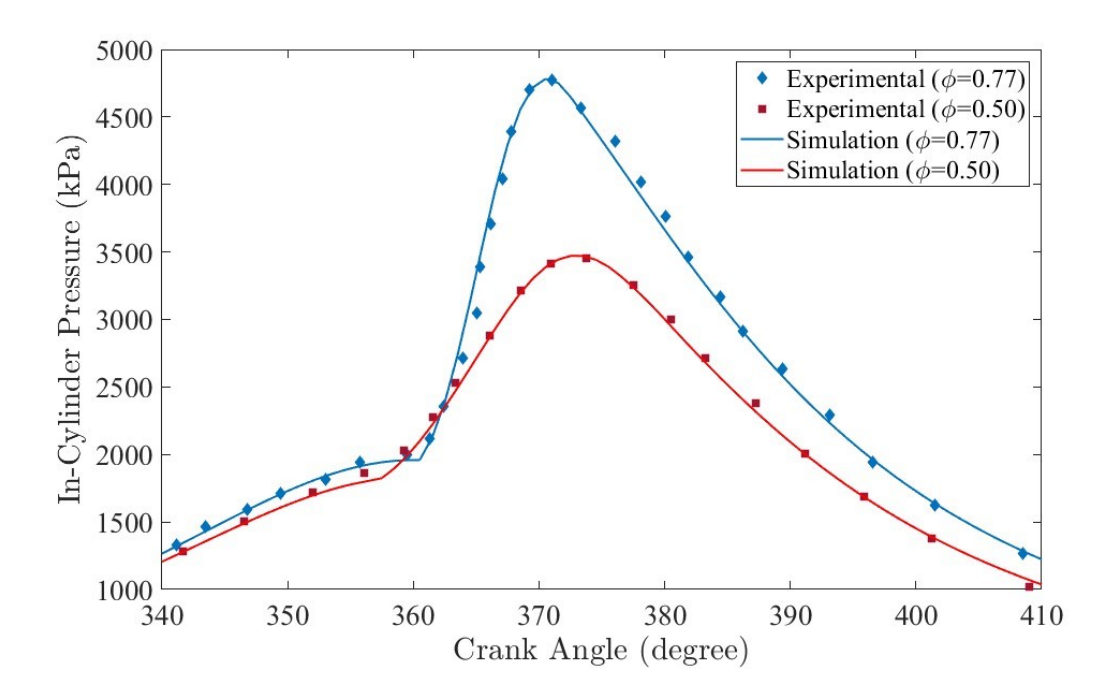


Figure 6.1: The simulated in-cylinder pressure compared to experimental values of [47] (MAP = 84 kPa, CR = 11.5, N = 2000 rpm, $ST_{\phi=0.77}$ = 3 °CA bTDC, $ST_{\phi=0.50}$ = 12 °CA bTDC).

peaks observed in the experimental hydrogen data are captured by the simulation using the two-zone hydrogen combustion model, to assess the accuracy of the hydrogen numerical model compared to experimental values. The in-cylinder pressure shows that as the equivalence ratio decreases from 0.77 to 0.50, there is a significant reduction in the peak in-cylinder pressure as well as a shift in the crank angle corresponding to the peak in-cylinder pressure away from top dead centre. This was mainly caused by the reduction of the hydrogen flame speed for greater air-diluted mixtures. At $\phi=0.77$, the peak pressure reaches approximately 4600 kPa, whereas at $\phi=0.50$, the peak pressure is around 3300 kPa. This reduction in peak pressure with decreasing equivalence ratio is consistent between the experimental hydrogen values and the simulated values. For both equivalence ratios, the pressure starts rising sharply around 350 °CA, peaks between 360 and 370 °CA, and then decreases as the crank angle approaches 410 °CA. This is due to the initiation of the spark event at 10 °CA bTDC and demonstrates that the two-zone hydrogen combustion model predicts the in-cylinder pressure well at various fuel-to-air ratios.

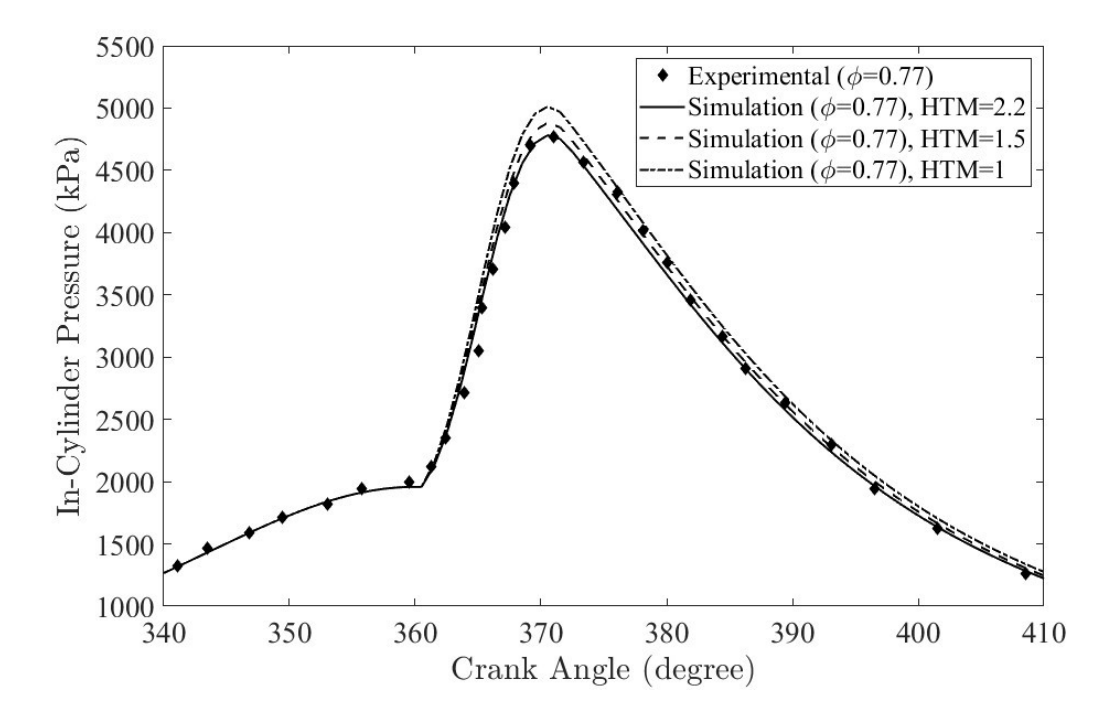


Figure 6.2: The simulated in-cylinder pressure compared to experimental values of [47] for different heat transfer coefficients (MAP = 84 kPa, CR = 11.5, N = 2000 rpm, $ST_{\phi=0.77} = 10$ °CA bTDC).

Due to significant differences in properties of hydrogen compared to that of petrol and diesel, it is necessary to choose an appropriate heat transfer model to accurately predict the performance of the engine. The in-cylinder heat flux is greater for hydrogen in comparison with a carbon-based fuel. In addition, the analysis of the heat transfer model in an engine is typically conducted using the correlations suggested by Woschni [170]. However, it has been shown [177] that by multiplying the heat transfer coefficient in the Woschni correlation by a factor of 2.2, the correlation was able to predict the performance accurately under different operating conditions. In Figure 6.2, the in-cylinder pressure is shown for an equivalence ratio of 0.77 at a spark timing of 3 °CA bTDC at different heat transfer multipliers, demonstrating the multiplier of 2.2 to be the most accurate for an equivalence ratio of 0.77. This comparison illustrates the importance of selecting an appropriate hydrogen heat transfer model.

6.1.1 Comparing the performance of the single- and two-zone models

The models were assessed by comparing the in-cylinder pressure and mass fraction burned profiles since all other results derive from these two parameters. Figure 6.3 shows that the two-zone combustion model predicted the experimental data with greater accuracy, mainly due to the inclusion of the turbulence sub-model. Turbulence was calculated using the k-epsilon model. The initial turbulent kinetic energy was calculated using an analytical fitting created by the turbulent kinetic energy values simulated using a three-dimensional computational fluid dynamic model at the crank angle position of intake valve closing. This difference affected the mass fraction profile between the single-zone and two-zone hydrogen combustion models.

Empirical correlations can provide the flame speed of the mixture under different engine operating conditions, but this requires knowing the unburned pressure and temperature, as well as the chemical composition. Given that the flame was presumed to be moving at the speed of the local laminar flame and considering that the eddies produced during the intake process continue to exist during combustion, it is assumed that the charge is uniform. The combustion process can be represented as the movement of a flame front with a limited thickness. The propagation rate is determined by the entrainment rate of the eddies. Additionally, the flame front was previously taken to be of zero thickness, leading to the assumption that the fuel mass is consumed instantaneously within the flame front. At greater loads, it is expected that the eddies result in higher in-cylinder pressures. To achieve the same load or in-cylinder pressure from the two models, it is required that the combustion duration be shorter or the flame speed be increased at a particular fuel mixture at a particular equivalence ratio, temperature, pressure, and exhaust gas recirculation ratio.

The two-zone model provides a slightly higher level of accuracy when predicting the engine performance because of the greater capability of capturing the water effect on the hydrogen combustion. The addition of water in hydrogen-air combustion has three primary impacts: 1) the dilution effect, which decreases the LFS, and

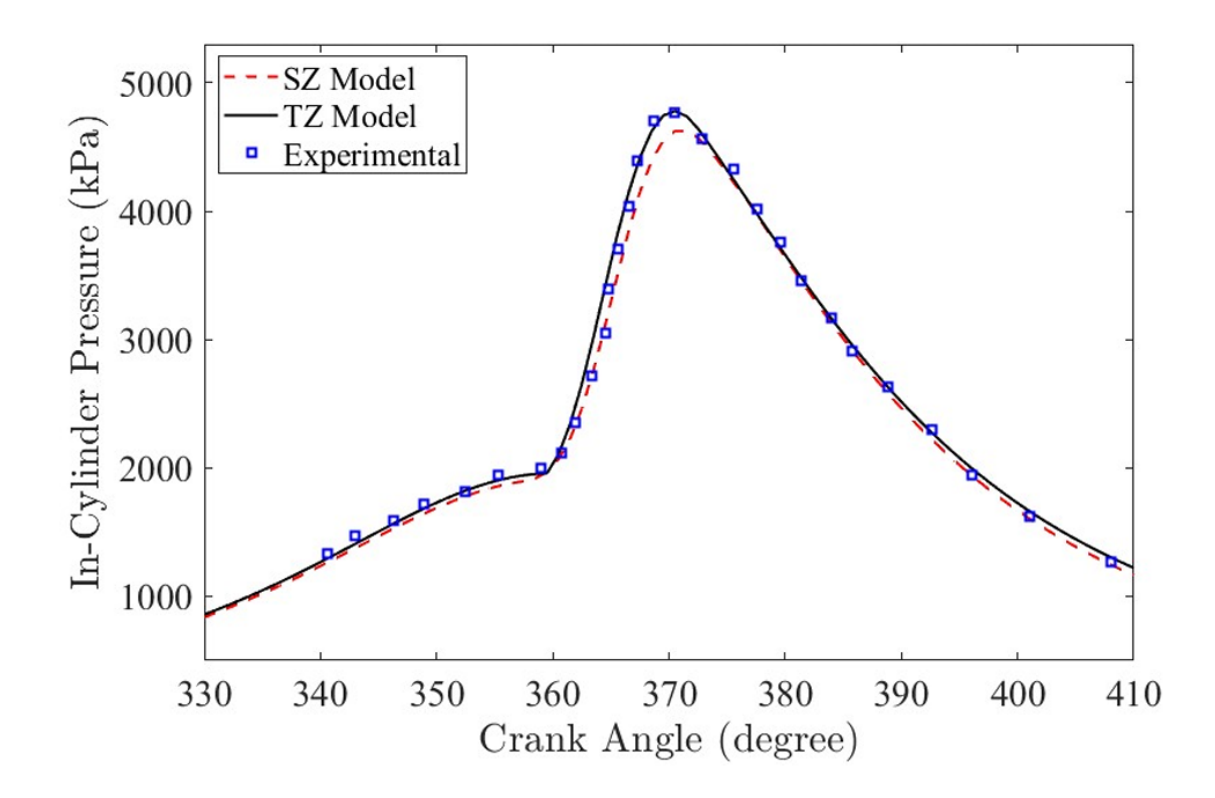


Figure 6.3: Simulated in-cylinder pressure using single zone (SZ) and two zone (TZ) hydrogen combustion models compared to experimental data of [47].

the 2) thermal-diffusion effect, which modifies the thermodynamic and transport characteristics of the reactive in-cylinder mixture. The single-zone model captures only the first effect, whereas the two-zone model captures both water effects on the hydrogen combustion. Nevertheless, the single-zone model is effective at predicting the pure hydrogen combustion at various spark timings, equivalence ratios, and manifold air pressures with good accuracy.

6.2 Hydrogen engine model performance

The two-zone model integrates sub-models for NO emissions and knock integral prediction to study the NO emissions from a boosted lean-burn hydrogen-fuelled SI engine with water addition. The combustion performance was investigated under the operating conditions shown in Table 6.1 by analysing the in-cylinder pressure and load. The numerical initial and boundary conditions are verified and validated

with experimental conditions [47]. The simulations were conducted with a constant compression ratio of 11.5 and an engine speed of 2000 rpm. The two-zone model performance is evaluated by considering the LFS and in-cylinder characteristics at engine-relevant conditions.

Table 6.1: Conditions used in the hydrogen engine numerical model.

Parameters	Values		
Spark Timing (°CA bTDC)	20 to 0		
Equivalence ratio (-)	0.5 to 0.9		
MAP (kPa)	80 to 120		
Compression ratio (-)	11.5		
Water addition (% by volume)	0 to 8		

6.2.1 Laminar flame speed at engine relevant conditions

Laminar flame speed is the most influential parameter for engine numerical modelling. The water-diluted hydrogen LFS correlation was calculated based on the empirical correlation proposed in Chapter 4. Figure 6.4 shows the hydrogen LFS values at different temperatures and equivalence ratios at a pressure of 3 MPa (Figure 6.4a), 5 MPa (Figure 6.4b), and 7 MPa (Figure 6.4c). It can be seen that the LFS decreases significantly with decreasing equivalence ratio. At a pressure of 5 MPa and a temperature of 600 K, the hydrogen laminar flame speed decreased by 47%, 58%, and 84% when the equivalence ratio was decreased from 0.9 to 0.7, 0.65, and 0.5, respectively. This was due to the reduction of the energy content when the mixture became leaner. Additionally, Figures 6.4(a-c) show that the LFS decreases with increasing pressure for the equivalence ratios used. For an equivalence ratio of 0.9 at a temperature of 700 K, the LFS decreased by 24% and 40% when the pressure was increased from 3 MPa to 5 MPa and 7 MPa, respectively. This reduction is explained by the reaction order n being less than two, given as $S_L \sim P^{(0.5n-1)}$. This was in agreement with previous studies [239]. Conversely, it can be seen from Figures 6.4(a-c) that the LFS increased monotonically with increasing temperature

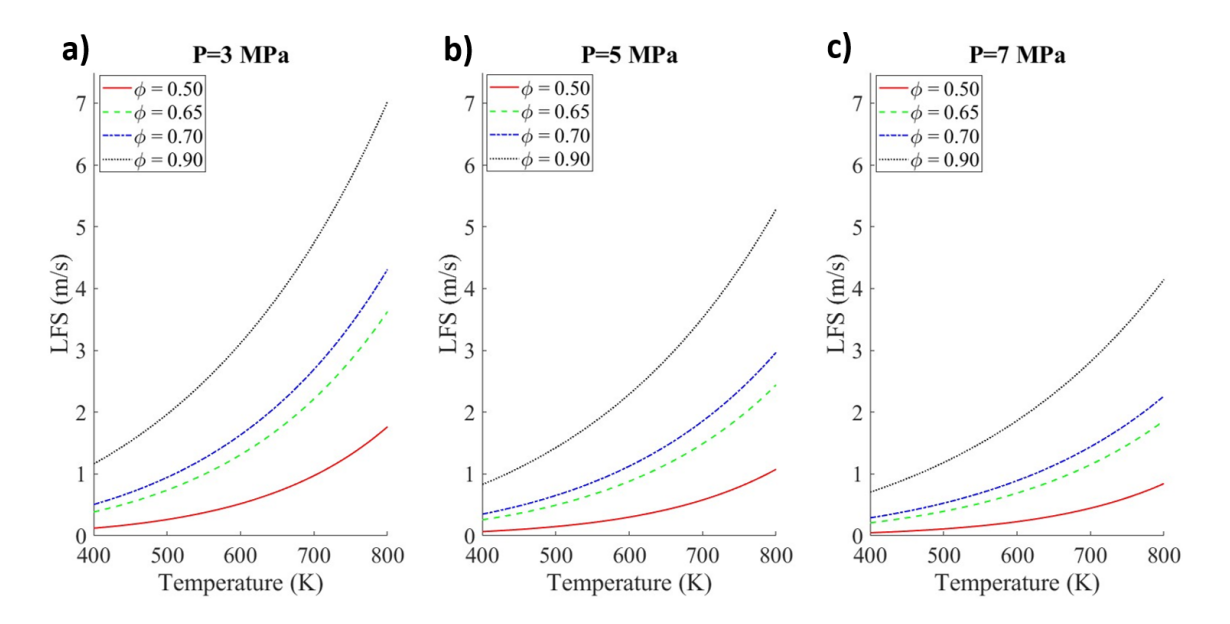


Figure 6.4: Hydrogen laminar flame speed values at different temperature, pressure, and equivalence ratio. Calculated using the hydrogen laminar flame speed empirical correlation proposed in Chapter 4.

under all presented equivalence ratios and pressures. For a pressure of 5 MPa and an equivalence ratio of 0.9, the LFS increased by more than six times when the temperature was increased from 400 K to 800 K. This was because the rate of the chemical reactions increases exponentially with increasing temperature based on the Arrhenius equation [113]. Figure 6.5 shows the LFS values of water-diluted hydrogen at various water additions and temperatures at an equivalence ratio of 0.5 (Figure 6.5a), 0.65 (Figure 6.5b), 0.7 (Figure 6.5c), and 0.9 (Figure 6.5d). It can be seen that the addition of water reduces the LFS. For an equivalence ratio of 0.9 at a pressure of 40 bar, the LFS was reduced by 4%, 13%, 21%, and 33% when 1%, 3%, 5%, and 8% water was added, respectively. This was mainly due to the reduction of the global temperature and increased heat capacity of the mixture with the added water [120].

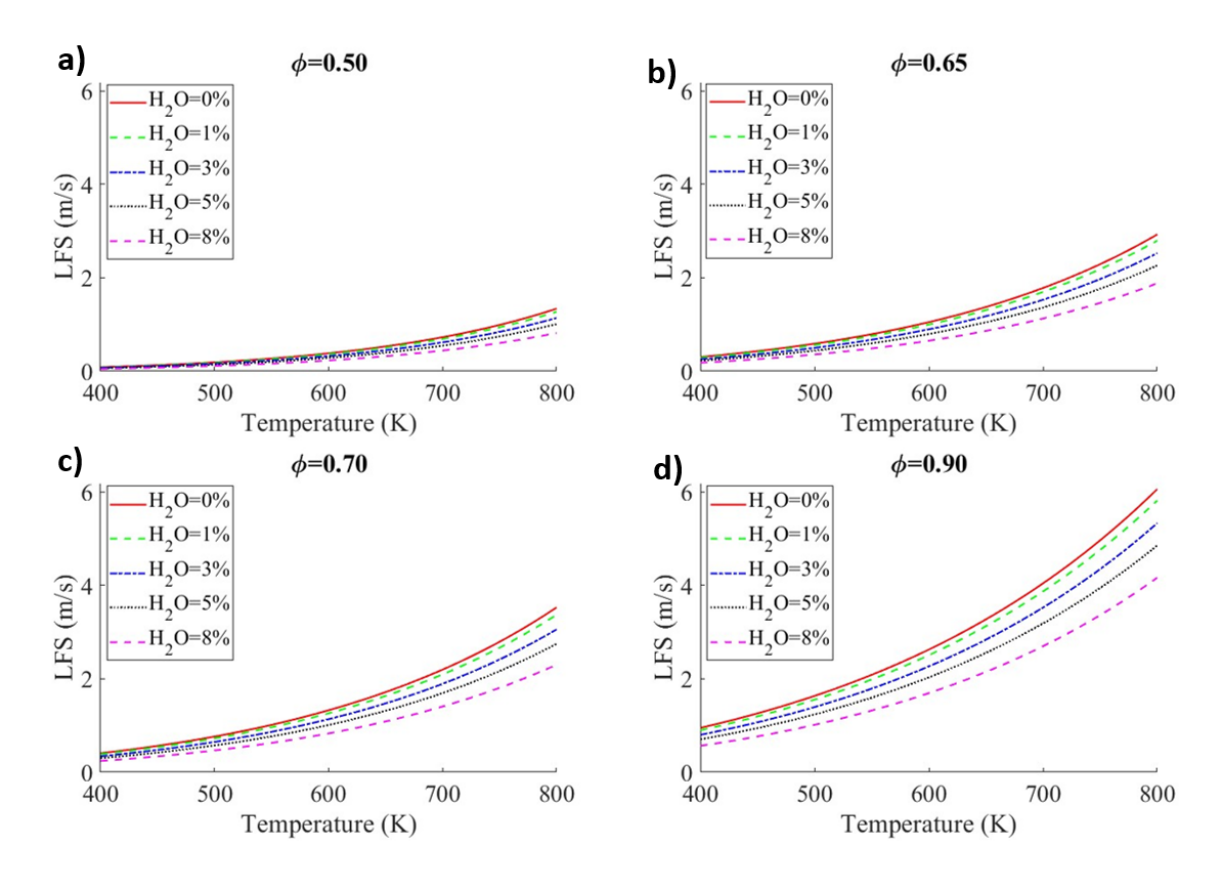


Figure 6.5: Hydrogen LFS values at various equivalence ratios, temperature, and water addition (P=4 MPa) calculated using the new hydrogen laminar flame speed empirical correlation.

6.2.2 In-cylinder characteristics

Figure 6.6 shows that the peak in-cylinder pressure and total apparent heat release rate (AHRR) decrease with increasing water addition, and that the crank angle associated with peak in-cylinder pressure shifted marginally away from the top dead centre (TDC). For an equivalence ratio of 0.9, the crank angle corresponding to the maximum in-cylinder pressure shifted around 3 °CA away from TDC for 8% water addition compared to the pure hydrogen operation, and the magnitude of the peak also decreased from 5.52 MPa to 4.92 MPa. This decrease in the in-cylinder magnitude and the shift of the corresponding peak crank angle location were caused by the reduction of the flame speed. The water addition causes the deflagration of lean-burn hydrogen flames, eventually reducing the pressure rise [120].

For the same reason, Figure 6.6 also shows that the AHRR peak decreased with

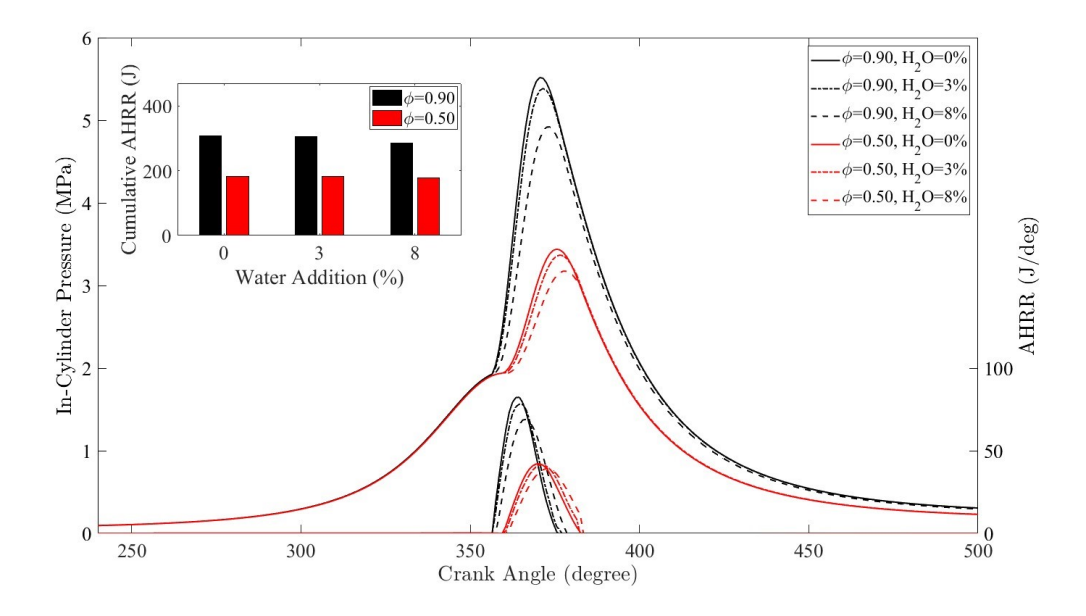


Figure 6.6: Simulated hydrogen engine in-cylinder pressure and AHRR for various ϕ at different water additions.

increasing air dilution; the peak AHRR decreased by 48% when the ϕ was decreased from 0.9 to 0.5. Similarly, for $\phi = 0.9$, the peak AHRR decreased by 5% and 16% when 3% and 8% water were added, respectively. Furthermore, the peak AHRR location shifted away from TDC with water addition by 2°CA and 3°CA when 3% and 8% water were added, respectively.

It can also be noted from the inset plot in Figure 6.6 that the total AHRR decreased with decreasing equivalence ratio. For pure hydrogen operation, the total AHRR decreased when the ϕ was decreased from 0.9 to 0.5 because of the reduction in flame speed for leaner hydrogen mixtures. The total AHRR also decreased with water addition. For $\phi = 0.9$, the total AHRR decreased by 1% and 7% when 3% and 8% water were added, respectively. This was because of the reduced flame speed combined with the increase of the in-cylinder charge heat capacity with water addition.

Figure 6.7 shows that the maximum in-cylinder pressure reduces monotonically with increasing water addition for any given equivalence ratio. For an equivalence ratio of 0.9, the maximum in-cylinder pressure reduced by 1%, 4%, 6%, and 10% when 1%, 3%, 5%, and 8% water were added, respectively. Whereas, the maximum

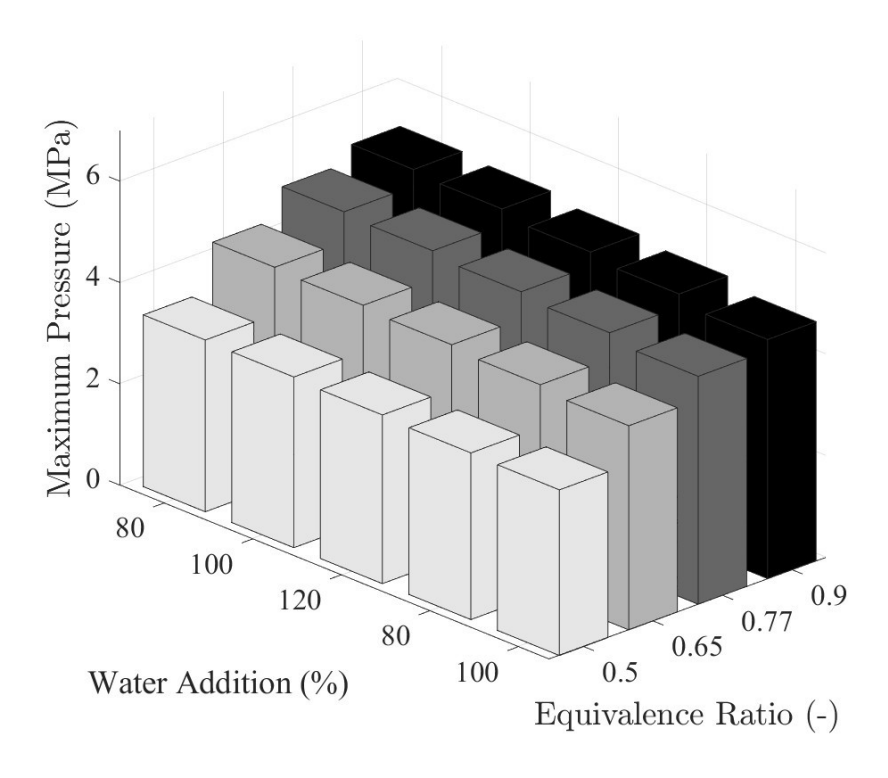


Figure 6.7: The maximum in-cylinder pressure at various ϕ and water additions at naturally aspirated condition, MAP = 80 kPa.

in-cylinder pressure increases with increasing equivalence ratio under all simulated cases of water addition, which was due to the increased in-cylinder energy content from the higher concentration of hydrogen present in the mixture. For pure hydrogen operation, the maximum in-cylinder pressure increased by 27%, 45%, and 55% when the equivalence ratio shifted from 0.5 to 0.65, 0.77, and 0.9, respectively.

Similarly, Figure 6.8 shows that the maximum in-cylinder combustion pressure increases with an increase in the manifold absolute pressure (MAP) due to the increased in-cylinder charge density. For an equivalence ratio of 0.9, the maximum in-cylinder pressure increased by 8% and 16% when MAP was increased from 80 kPa to 100 kPa and 120 kPa, respectively. The peak in-cylinder pressure magnitude of 6 MPa was found under an equivalence ratio of 0.9 for 40 kPa boosting.

The optimal location of spark timing in an engine is mainly determined by the characteristics of the flame propagation within the combustion chamber and the associated engine parameters such as load, fuel composition, intake pressure, intake

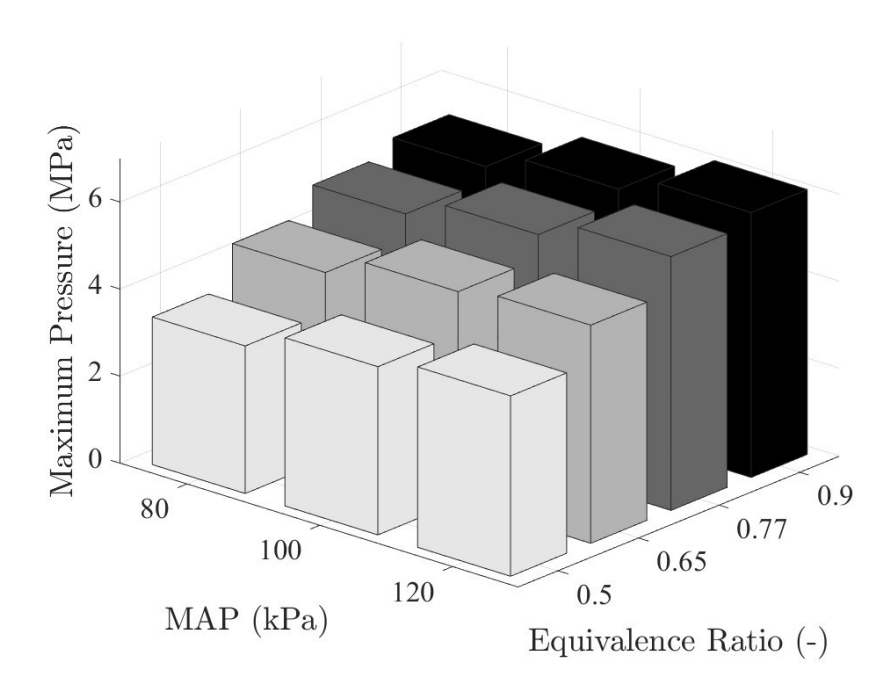


Figure 6.8: The maximum in-cylinder pressure of pure hydrogen at various ϕ and MAP (ST = MBT, CR = 11.5).

temperature, and engine speed. The spark timing was fixed at the minimum spark advance for the best torque (MBT) location to ensure maximum thermal efficiency under all operating conditions. Therefore, the MBT timing at the highest indicated mean effective pressure (IMEP) was determined by varying the spark timing for naturally aspirated (MAP = 80 kPa) condition at various equivalence ratios (Figure 6.9a). The MBT shifts away from the TDC when the mixture becomes leaner. At $\phi = 0.9$, the MBT timing was at 4 °CA bTDC, whereas, for $\phi = 0.5$, it was at 10 °CA bTDC. This can be explained by an increase in combustion duration due to the reduction of flame speed for leaner mixtures.

Figure 6.9a also shows that the IMEP was reduced by 41% when the ϕ was reduced from 0.9 to 0.5 at their respective MBT timings under the naturally aspirated condition. Figure 6.9b shows the variation of load at different MAP for different spark timing under $\phi = 0.77$. As MAP increased, the MBT timing shifted towards TDC due to the increase of the charge density at higher MAP values. When the MAP increased from 80 kPa to 100 kPa and 120 kPa, the IMEP at MBT timing increased by an order of 5 and 10 bar, respectively. The power increase is explained

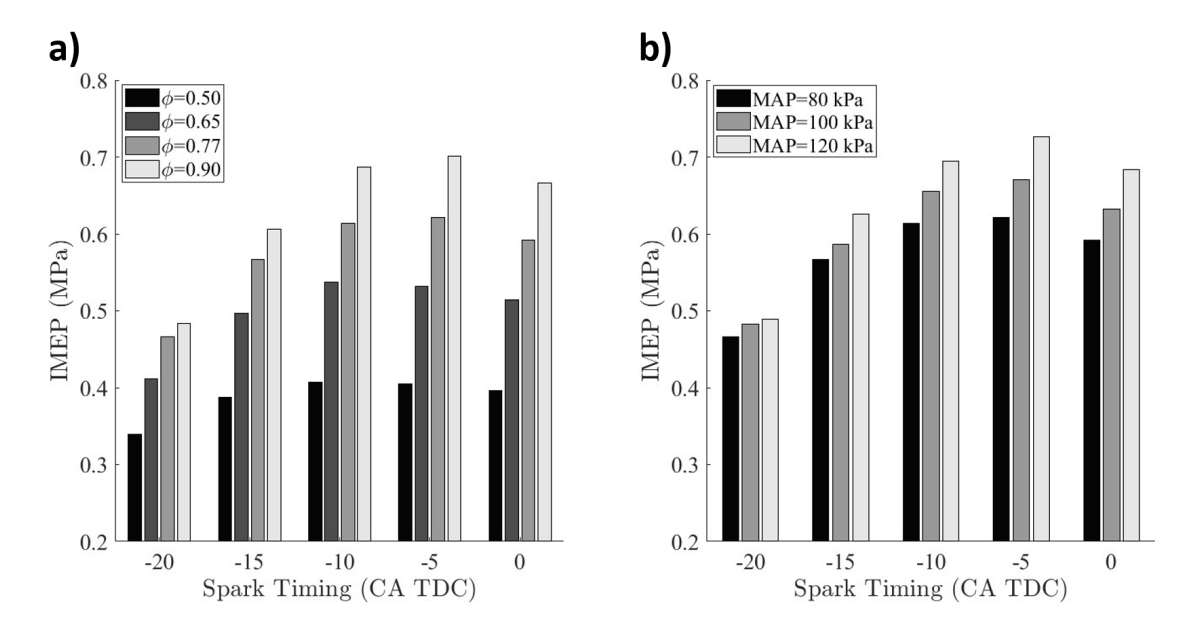


Figure 6.9: a) Simulated IMEP at different spark timings for various equivalence ratios (MAP = 80 kPa) and b) simulated IMEP at different spark timings for various manifold air pressures ($\phi = 0.77$).

by an increase in in-cylinder charge density for higher intake manifold air pressures [30].

In Figure 6.10, the IMEP for different water additions under various spark timings for the $\phi=0.77$ shows that by adding water into the hydrogen reactive mixture, the MBT timing was advanced. For pure hydrogen under $\phi=0.77$ the MBT timing was found to be at 6 °CA bTDC, whereas, when 3% and 8% water was added, the MBT shifted marginally to 7 and 8 °CA bTDC, respectively. This was caused by the increase in combustion duration with water addition, due to the reduction in the flame speed.

The instantaneous mass fraction burned per crank angle for various equivalence ratios at a fixed spark timing of 5 °CA bTDC under naturally aspirated conditions are shown in Figure 6.11a. As air dilution in the hydrogen/air mixture increases, so does the combustion duration. The mass fraction burned is a good indicator of engine performance. It is reasonable to use the mass fraction burned curves to characterize the combustion stages as a function of crank angles. The crank angle location for 50% (CA50) mass burn fraction shifted by 1, 2, and 6 °CA away with respect to $\phi = 0.9$ condition, when the mixture tends to become leaner for

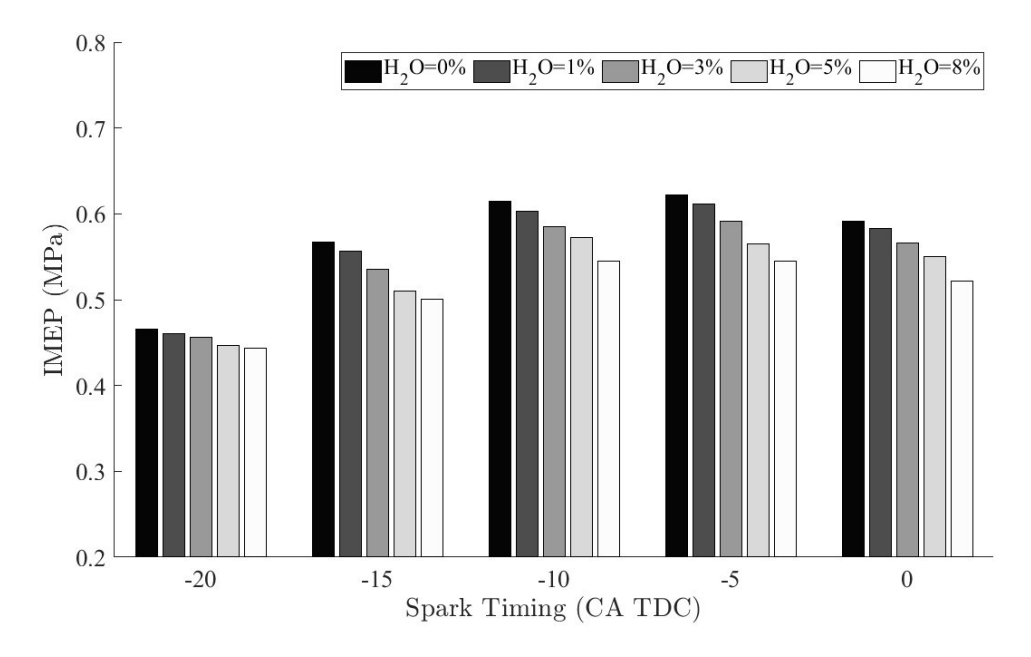


Figure 6.10: Simulated IMEP at different spark timings for various percentages of water additions under $\phi = 0.77$ under naturally aspirated condition (MAP = 80 kPa).

equivalence ratios of 0.77, 0.65, and 0.5, respectively. In general, the CA50 location shifted away from TDC for leaner mixtures. This was caused by the slower burning flame velocity at increased air dilution and the increased flame development angle. The effect of the water addition on the hydrogen mass fraction burned has been shown in Figure 6.11b. It can be seen that when water was added under naturally aspirated conditions at $\phi = 0.77$, the combustion duration only marginally increased. The water addition reduces the flame speed, mostly due to the high heat capacity of water, hence greater amounts of heat were absorbed by the water species inside the chamber. Therefore, the CA50 location shifted only by 3 °CA when 8% water was added into the mixture. The water addition effect in the two-zone hydrogen combustion model was captured not only by the flame speed effect, but also from the thermal property variation caused by water addition.

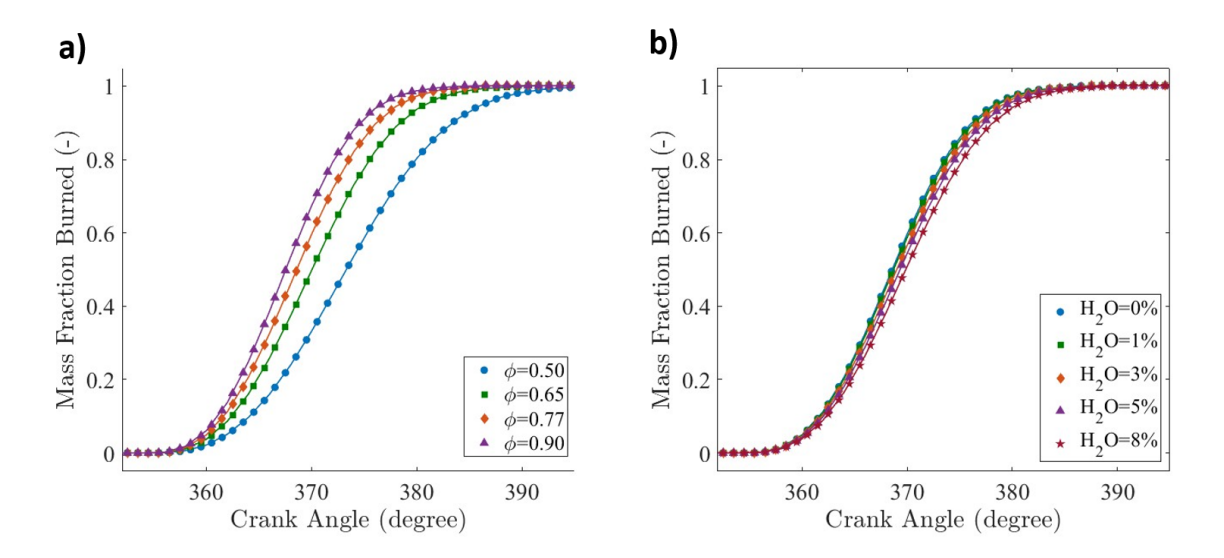


Figure 6.11: Simulated mass fraction burned profile for various equivalence ratios at MAP = 80 kPa (CR = 11.5, N = 2000 rpm, ST = 5 °CA bTDC) and b) Simulated mass fraction burned profile for various water additions at MAP = 80 kPa (CR = 11.5, N = 2000 rpm, ST = 5 °CA bTDC).

6.3 IMEP and ITE

The IMEP of the lean-burn hydrogen engine at various MAP and ϕ are given in Figure 6.12a and show that boosting is effective by increasing the IMEP under all presented ϕ values. For $\phi=0.9$, the IMEP increases by 6% and 13% when MAP increases from 80 kPa to 100 kPa and 120 kPa, respectively. For $\phi=0.45$, when the MAP increases from 80 kPa to 100 kPa, the IMEP increases by approximately 4 bar. When the MAP was further increased to 120 kPa from 100 kPa, the IMEP increased by approximately 5 bar. Figure 6.12b shows the addition of water caused the lean-burn hydrogen engine load to decrease monotonically for all the presented equivalence ratios. This is due to the reduction in the flame speed with water addition, which increases the combustion duration, leading to lower in-cylinder pressures. This effect was captured in the new two-zone combustion model only by incorporating a water-diluted hydrogen LFS correlation. In Figure 6.12b the rate of IMEP reduction with water addition is predominant for greater equivalence ratio values. For $\phi=0.9$, the IMEP was reduced by 2%, 6%, 10%, and 15% when 1%, 3%, 5%, and 8% water was added, respectively. For the leaner ϕ value of 0.45, IMEP

was affected less by the water addition; the IMEP was reduced by 1%, 3%, 5%, and 10% when 1%, 3%, 5%, and 8% water was added, respectively. This decrease can be explained by the reduction of the global reaction temperature caused by the increase in heat capacity due to water vapor addition to the reactive mixture [242]. Additionally, the results also captured the lean-burn hydrogen-specific heat capacity variations caused by water addition through incorporating thermodynamic data [113]. The engine load reduction with water addition also indicates a limit on the amount of water dilution on the stability of hydrogen combustion for leaner mixtures.

Quantifying thermal energy conversion into mechanical work is done using the indicated thermal efficiency (ITE). The range of ITE for various MAP and ϕ in Figure 6.13a shows that ITE increases with increasing air dilution in the hydrogen engine. Under naturally aspirated conditions, the ITE increases by 4%, 6%, and 8% when ϕ varies from 0.9 to 0.77, 0.65, and 0.5, respectively. The increase in ITE with decreasing fuel/air ratio is due to the greater expansion of leaner mixtures caused by the variation of the specific heat ratio [47]. Figure 6.13a also shows that the ITE of lean-burn hydrogen SI engines increases with MAP boosting. For $\phi = 0.9$, the ITE increases by 3% and 7% when MAP was increased from naturally aspirated condition to 100 kPa and 120 kPa, respectively. This increase relates to the load increase with boosting (Figure 6.10). The peak ITE of almost 42% occurs at $\phi = 0.5$ and 40 kPa boosting, and is in agreement with other studies [92, 93, 96, 97]. In Figure 6.13b, it can be seen that water addition reduces ITE because of the reduction in load caused by the higher heat capacity of water combined with the prolonged combustion duration due to the reduced flame speed. For $\phi = 0.9$, ITE reduces by 1%, 4%, 6%, and 10% when 1%, 3%, 5%, and 8% water is added, respectively.

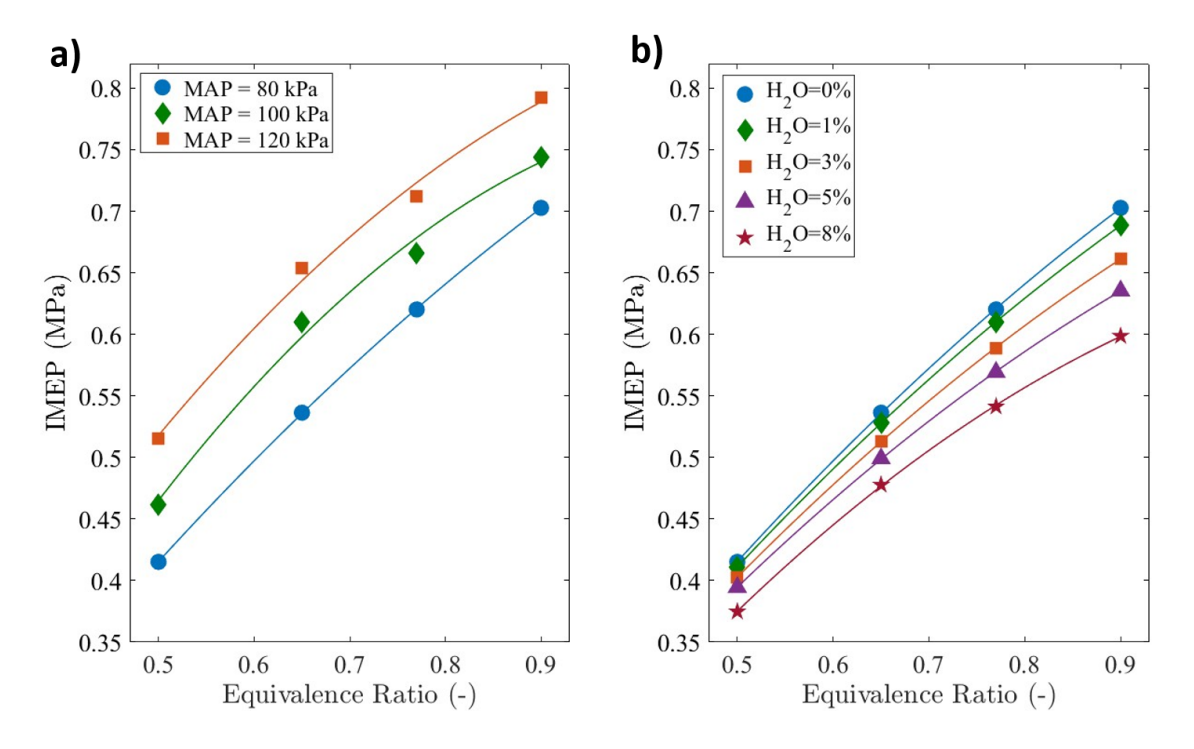


Figure 6.12: a) IMEP at various MAP and ϕ , and b) IMEP at various water additions and ϕ at naturally aspirated condition (CR = 11.5, MAP = 80 kPa, ST = MBT). The lines represent least-squares fits.

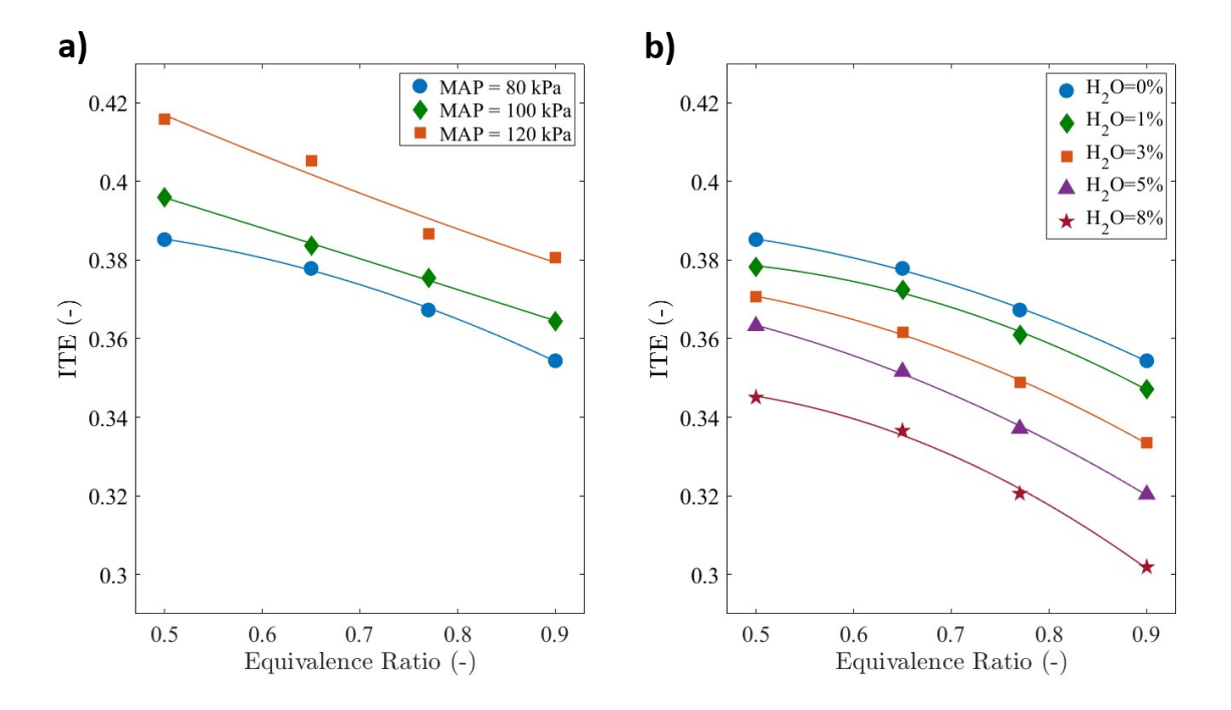


Figure 6.13: a) ITE at various MAP and ϕ , and b) ITE at various water additions and ϕ at naturally aspirated condition (CR = 11.5, MAP = 80 kPa, ST = MBT). The lines represent least-squares fits.

6.4 Indicated specific fuel consumption and NO emissions

The indicated specific fuel consumption (ISFC) measures the effectiveness of the thermal fuel conversion to indicated power. Figure 6.14a shows that operating the hydrogen engine leaner reduces the ISFC. This is because of the reduction of the amount of hydrogen in the in-cylinder mixture. Furthermore, increasing the MAP reduces the ISFC. For $\phi = 0.9$, the ISFC reduced by 3% and 8% when the MAP was increased from 80 to 100 and 120, respectively. The reduction in ISFC with boosting MAP is due to an increase in indicated power at higher values of MAP, which also increases the in-cylinder charge density [231]. This is in agreement with boosted lean-burn hydrogen SI engine experimental data [92]. In Figure 6.14b, it can be seen that water addition under naturally aspirated conditions increases the ISFC monotonically under all presented equivalence ratios. This is explained by the engine load decreasing with water addition, due to higher heat capacity and reduction of the flame speed introduced by the water addition [242]. Boosting decreases the ISFC, but increases NO emissions. Under $\phi = 0.9$, NO emissions increase by 5% and 23% when the MAP was increased from 80 kPa to 100 kPa and 120 kPa, respectively. The increase in NO emissions with boosting is due to an increase in the in-cylinder charge density brought by greater energy content for higher MAP values at a given ϕ [62]. Hence, when the in-cylinder energy content reduces by decreasing the equivalence ratio, for a given MAP, significant reductions in NO emission were observed (Figure 15a). For naturally aspirated conditions of 80 kPa, NO emissions reduce by 39%, 55%, and 83% when the ϕ varies from 0.9 to 0.77, 0.65, and 0.5, respectively.

Additionally, for the lean-burn hydrogen engine the addition of water increases ISFC but NO emissions reduce. This can be seen from Figure 6.15b, where the NO emission decreases with decreasing values of ϕ and increasing values of water addition. For $\phi = 0.9$, NO emissions reduce by 6%, 16%, 26%, and 38% when 1%, 3%, 5%, and 8% water is added, respectively. This is mainly due to reducing the global in-cylinder temperature with the water addition [126]. With current hydrogen SI engine technology, a compromise of load and NO emissions could be possible with

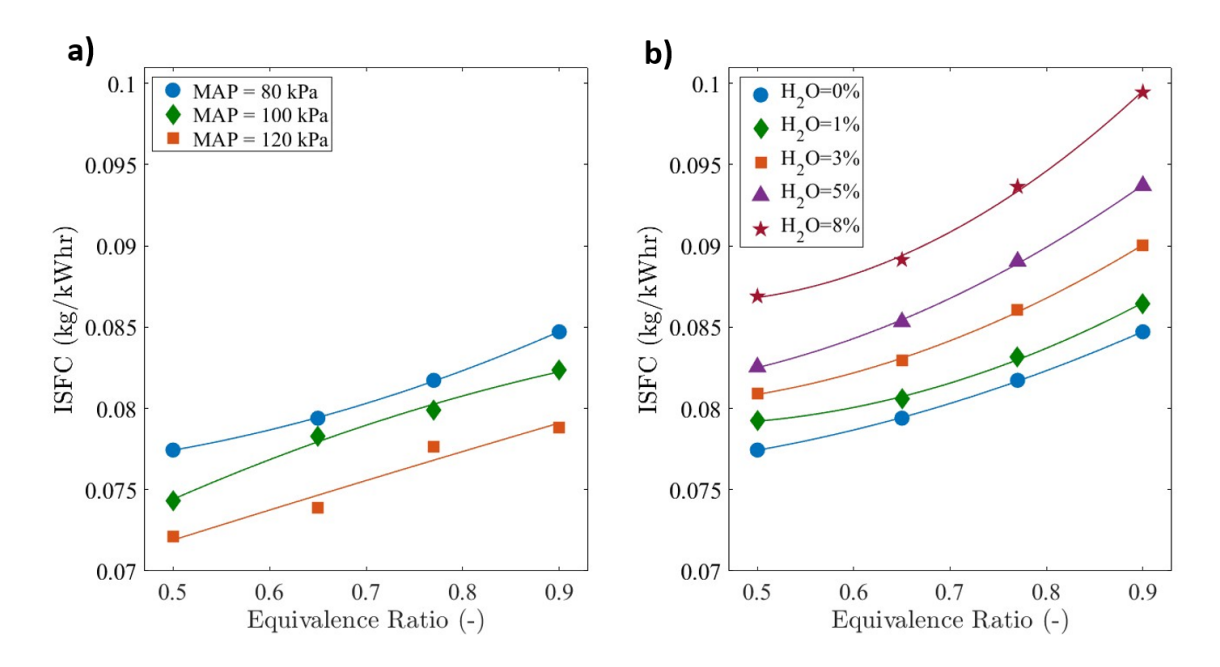


Figure 6.14: a) ISFC at various MAP and ϕ , and b) ISFC at various water additions and ϕ at naturally aspirated condition (CR = 11.5, MAP = 80 kPa, ST = MBT). The lines represent least-squares fits.

the introduction of water into the combustion chamber.

6.5 Knock prediction

The autoignition delay time is important for modelling combustion abnormalities. For the premixed fuel and oxidizer mixture, the ignition delay time is defined as the time from the start of spark to the initiation of chain-branching reactions [243]. The ignition delay time in engines depends on equivalence ratio, pressure, temperature, and in-cylinder mixture concentration. The autoignition causes a rapid rise in the cylinder pressure, and this abnormal combustion is termed as knock [113]. In Figure 6.16, the knock integral for lean-burn hydrogen operation was calculated for various MAP and ϕ using the Livengood-Wu integral [114]. No end gas autoignition was observed for the operating conditions shown in Table 1, as none of the values exceeded unity and this was in agreement with experimental studies [110, 112, 62, 39, 73]. It is clear that when MAP is boosted, the knock integral increases significantly due to increasing charge density as additional air is inducted into the combustion

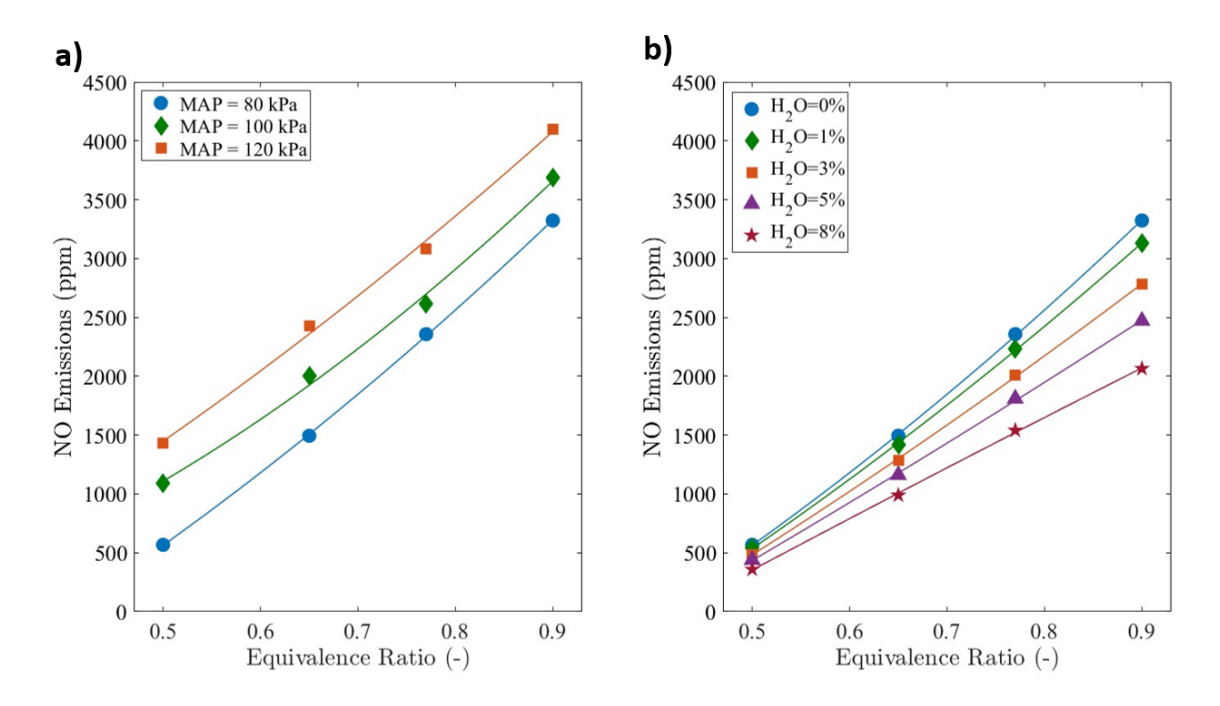


Figure 6.15: a) NO emissions at various MAP and ϕ , and b) NO emissions at various water additions and ϕ at naturally aspirated condition (CR = 11.5, MAP = 80 kPa, ST = MBT). The lines represent least-squares fits.

chamber. Additionally, knock can be mitigated by increasing air dilution [112]. In Figure 6.16, under MAP of 120 kPa, the knock integral reduces by 8%, 16%, and 27% when ϕ varies from 0.9 to 0.77, 0.65, and 0.5, respectively. This reduction of the knock integral is caused by the increase of the hydrogen autoignition delay time (Figure 6.17). The autoignition delay time increases for higher levels of air-diluted hydrogen mixtures due to the reduction of the available energy in a reactive mixture.

The knock integral also decreases monotonically with water dilution (Figure 6.18) under all presented equivalence ratios for MAP of 120 kPa. For ϕ of 0.9, the knock integral reduces by 2%, 6%, 9%, and 14% when 1%, 3%, 5%, and 8% water is added, respectively. A slightly lower reduction was observed for a leaner mixture; for ϕ of 0.5, the knock integral reduces by 2%, 4%, 6%, and 10% when 1%, 3%, 5%, and 8% water is added, respectively. The increasing autoignition delay time as water is added influences the knock integral reduction (Figure 6.19). The autoignition delay time increases because of the increasing absorption of heat due to the high heat capacity of water. Nevertheless, knocking and NO emissions in hydrogen-fuelled

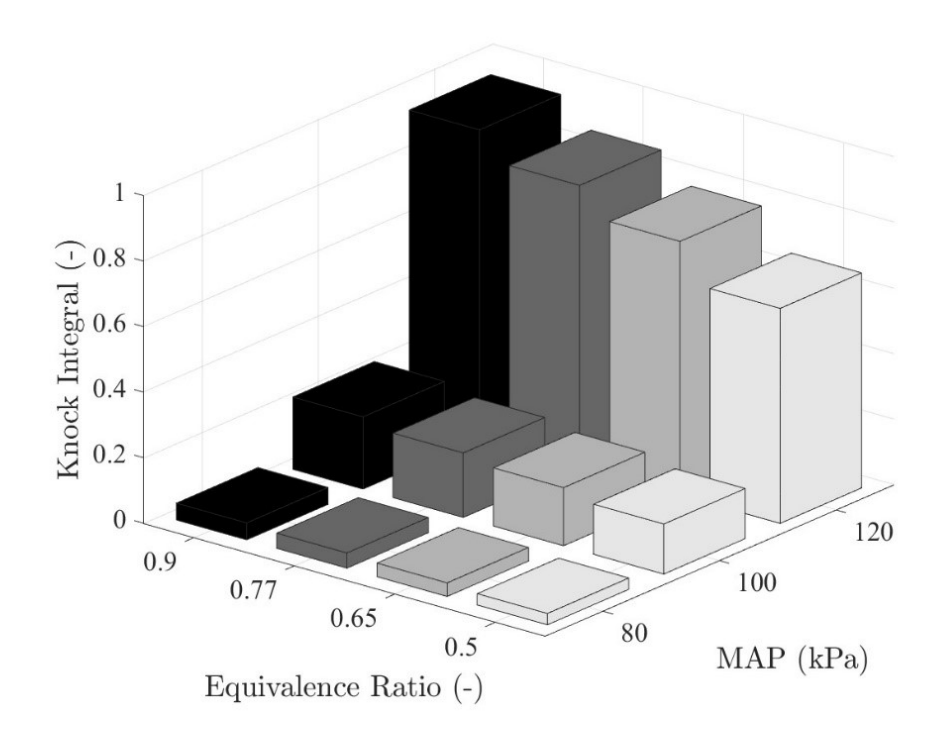


Figure 6.16: Knock integral, KI, at various MAP and ϕ for a hydrogen-fuelled SI engine at MBT timing (N=2000 rpm, CR=11.5).

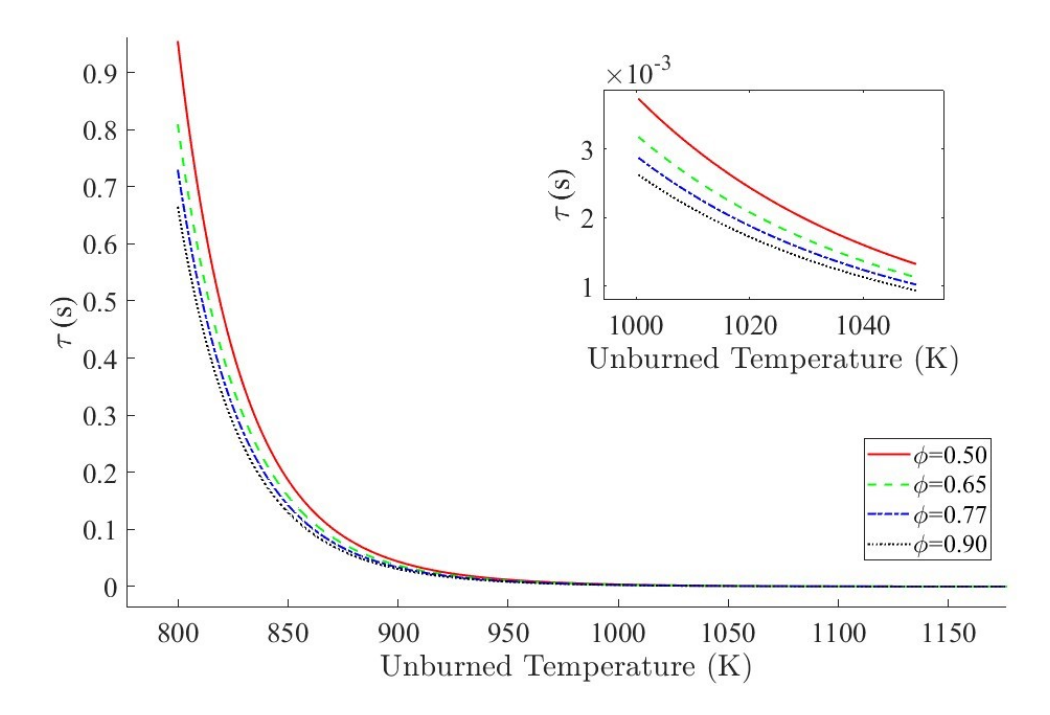


Figure 6.17: Hydrogen autoignition delay time at various unburned gas temperatures and ϕ (P=4 MPa).

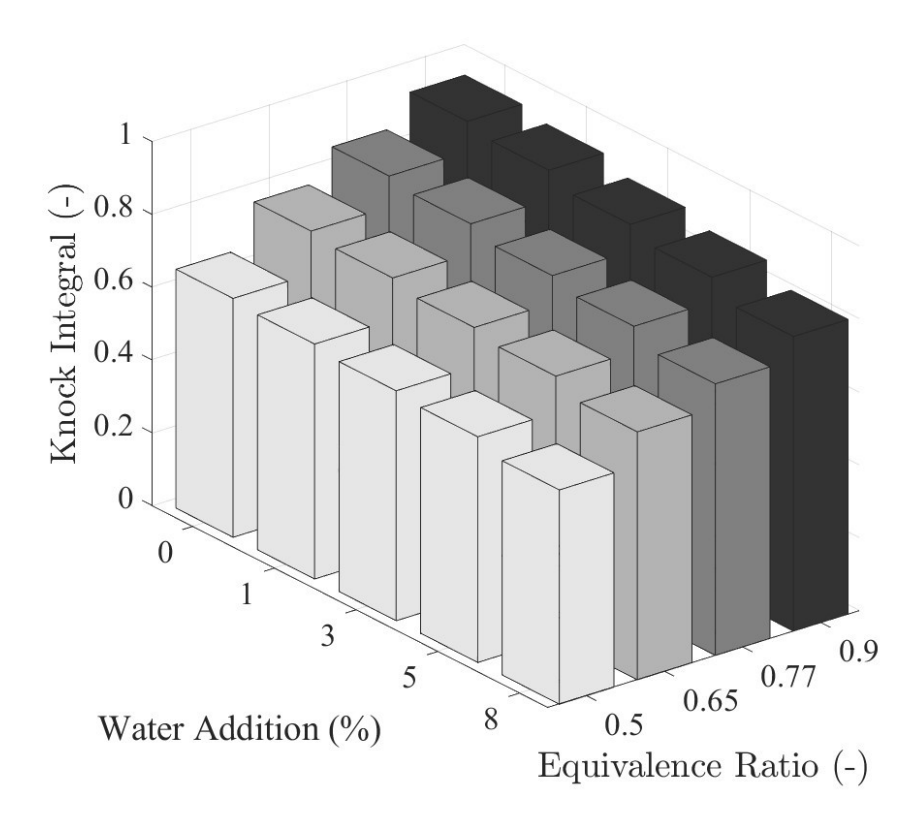


Figure 6.18: Knock integral, KI, at various water additions and ϕ for a hydrogen-fuelled SI engine at MBT timing for naturally aspirated condition (CR=11.5, MAP=120 kPa).

engines could be reduced, but at the cost of performance. For a ϕ of 0.9 under a MAP of 120 kPa, if 1% water was added, the knock integral and NO emissions reduce by 2% and 5%, respectively, while ITE reduces by 2%.

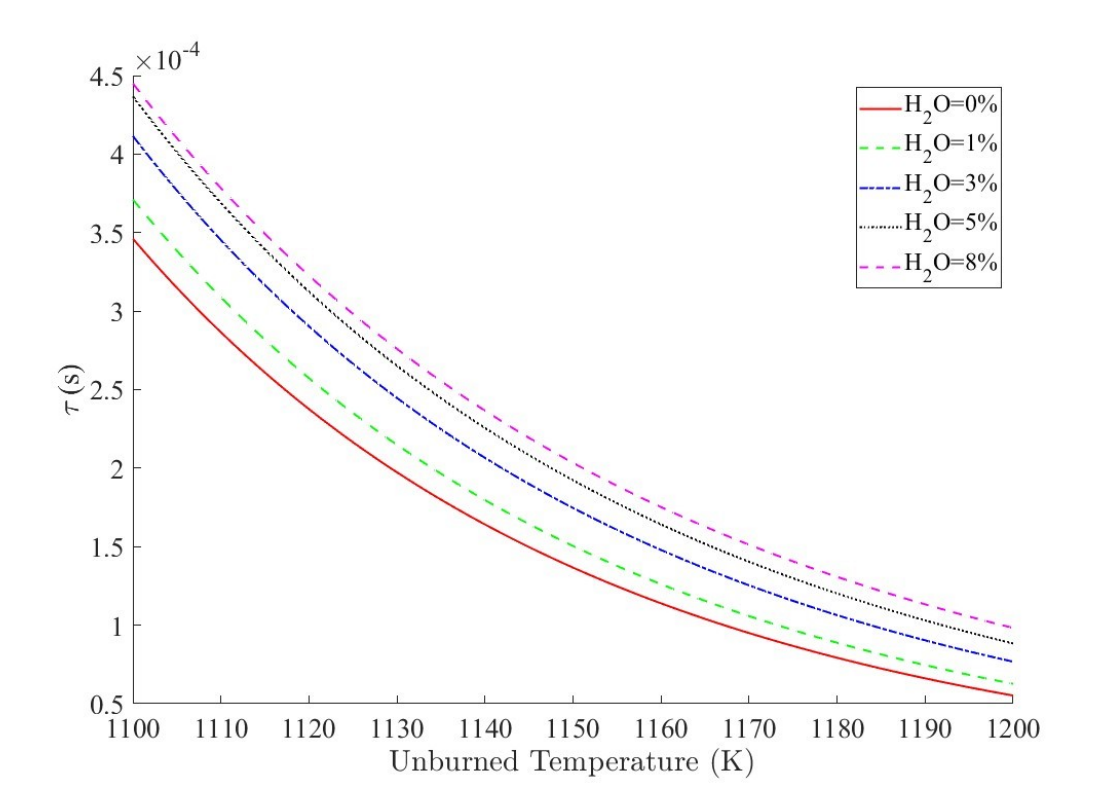


Figure 6.19: Hydrogen autoignition delay time at various unburned gas temperatures and water additions (P=4 MPa, ϕ =0.9).

6.6 Hydrogen operating regimes

Drawing together the outcomes from the new two-zone hydrogen combustion model with water addition describes the engine performance, emissions, and combustion abnormalities. Figure 6.20 illustrates the interaction between NO emissions, ISFC, IMEP, and the equivalence ratio of a hydrogen engine with different levels of water addition at a MAP of 120 kPa (Figure 6.20) and a MAP of 80 kPa (Figure 6.21). Both maps show that NO emissions and ISFC have an inversely proportional relationship when water is added. This is because thermal efficiency reduces due to the decrease in flame speed and an increase in the heat capacity of the in-cylinder charge. As the percentage level of water addition increases, the NO emissions decrease significantly, a trend evident at all equivalence ratios.

Under ϕ of 0.9 at a MAP of 120 kPa (Figure 6.20), the NO emissions reduce from 4102 ppm to 2646 ppm with an 8% water addition. This was because of the cool-

ing effect due to water addition, lowering the in-cylinder combustion temperature, thereby reducing the formation of NO emissions. However, reducing NO emissions with water addition comes at the cost of increasing ISFC due to the reduction of the ITE, indicated by the dashed horizontal white lines in Figures 6.20 and 6.21. This reduction of thermal efficiency is due to lower combustion efficiency caused by higher values of specific heat capacity of the in-cylinder charge resulting from water addition and slower flame speeds.

The trade-off between ISFC and NO emissions is more pronounced for richer mixtures, and it can be seen from the operational maps that the relationship between ISFC and NO becomes linear as the hydrogen mixture becomes leaner. The colour map (Figures 6.20 and 6.21) represents the IMEP; higher IMEP values are associated with higher equivalence ratios, MAP, and lower percentages of water addition, whereas ITE increases with decreasing equivalence ratio. In Figures 6.20 and 6.21, the condition at which the knock integral exceeds unity is highlighted as the knocking region. In Figure 6.20, the Livengood knock integral values show that the knocking tendency increases with increasing equivalence ratio and load, whereas it decreases with water addition under all operating conditions. This is mainly due to the increase in hydrogen autoignition delay time as water is added.

Hence, water injection could benefit the hydrogen engine by expanding the knockfree operating conditions at higher loads by reducing the knock tendency, but it comes with the trade-off of reduced thermal efficiency, thereby increasing the ISFC.

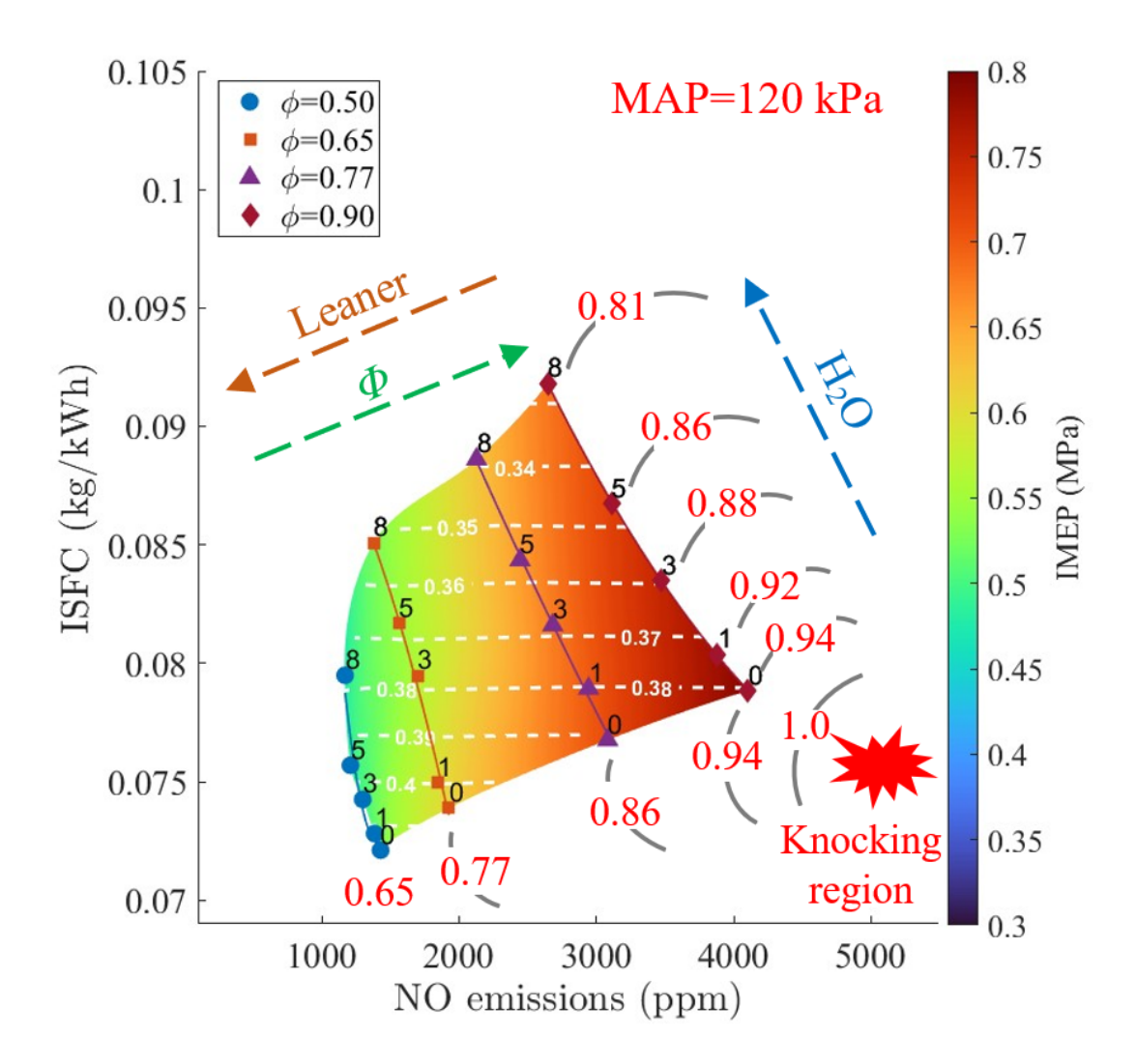


Figure 6.20: Plots for the operation of a boosted lean-burn hydrogen SI engine with water addition at MAP of 120 kPa. IMEP is shown as a heat map, symbols with the value on top represent the water addition percentage, the white dashed lines represent ITE, and the solid lines represent knock integral values.

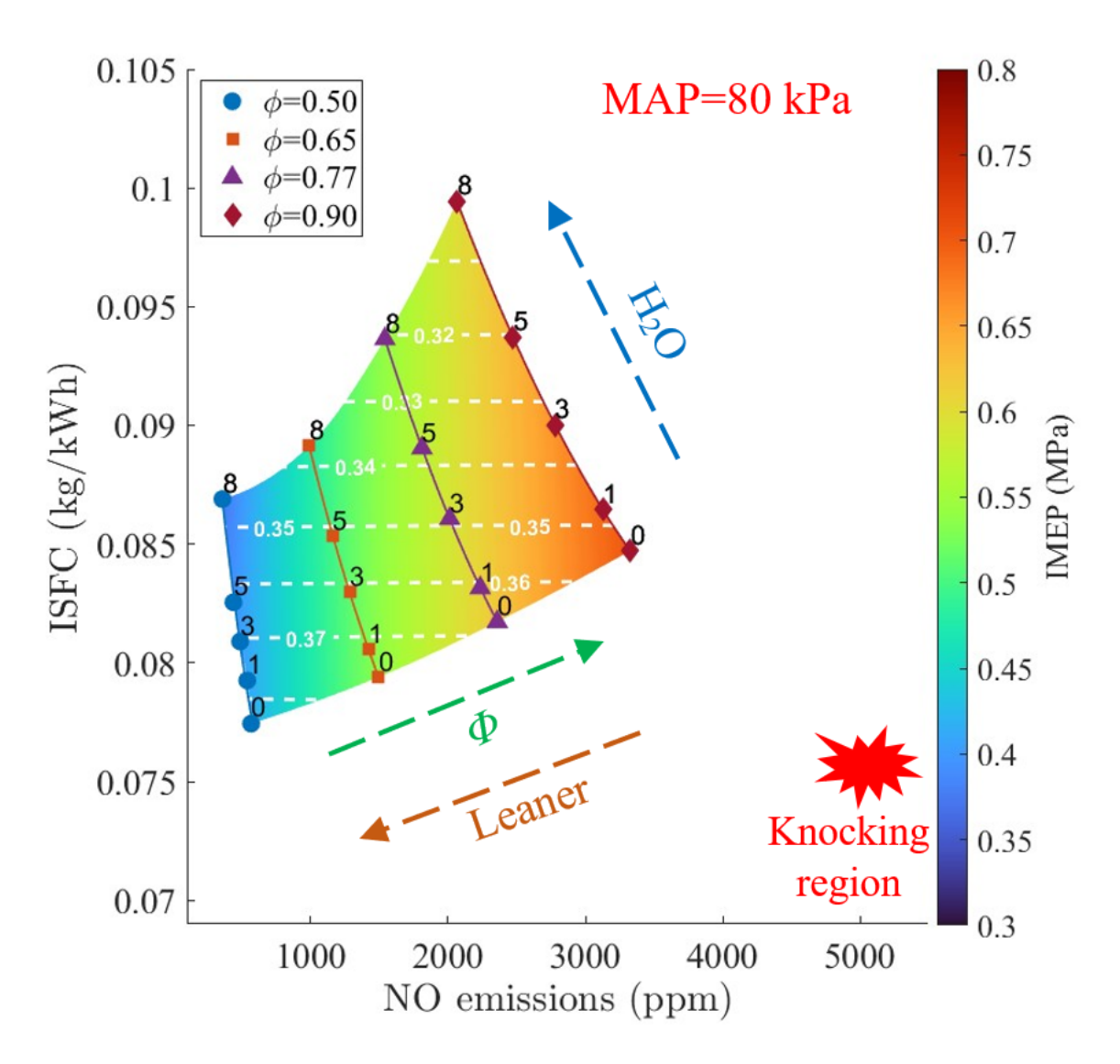


Figure 6.21: Plots for the operation of a boosted lean burn hydrogen SI engine with water addition at MAP of 80 kPa. IMEP is shown as a heat map, symbols with the value on top represent the water addition percentage, the white dashed lines represent ITE, and the solid lines represent knock integral values.

6.7 Summary

The thermodynamic model was advanced by incorporating water-diluted hydrogen LFS, an extended Zeldovich mechanism for nitric oxide emissions, and the Livengood-Wu integral model for knock characteristics based on advanced chemical kinetics. A comprehensive analysis of a hydrogen-fuelled engine at various manifold air pressures, equivalence ratios, and water addition was undertaken. Finally, the

chapter underlines the importance of optimizing the water injection amount to balance the trade-offs between engine performance, emission reduction, and knocking regions.

Chapter 7

Exergy analysis of the lean-burn hydrogen SI engine

Exergy analysis is a method for investigating the fundamental origins of losses, the limits to efficiency, and the engineering trade-offs required to reduce losses. Using the improved two-zone model (Chapter 6), this comprehensive exergy analysis investigates the processes of exergy destruction under real-world conditions.

7.1 Entropy generation

Hydrogen allows for high dilution rates with air or exhaust-gas recirculation (EGR). Although reducing NOx emissions [75], this also reduces engine power output and potentially limits hydrogen use in high-density powered applications. Moreover, the lower power of lean-burn hydrogen operation reduces the in-cylinder temperature, increasing the combustion irreversibility ratio. This increase in irreversibility—the destruction of available energy—is directly proportional to the rate of entropy generation. Entropy can be generated by processes such as unrestrained chemical reactions, friction, heat transfer across different temperature zones, and mixing of different gases [192], but exergy transfer does not necessarily mean exergy destruction. Entropy generation (exergy destruction) must be reduced to improve the fuel conversion efficiency.

The entropy generation $(S_{\text{gen}} = S_{\text{products}} - S_{\text{reactants}})$ at various operating condi-

tions is calculated by assuming adiabatic, constant volume, and closed combustion chamber conditions. As mixtures become leaner (ϕ of 0.90 to 0.45), entropy generation increases (Figure 7.1) because the lean combustion with excess air provides a greater quantity of product species, leading to an increase in the chemical component of entropy. The entropy generation increases significantly when the /phi was reduced from 0.90 to 0.45.

In agreement with previous work using hydrocarbon fuels [194], increasing the reactant temperature monotonically reduces entropy generation. For ϕ of 0.90 under a pressure of 30 bar, entropy generation was reduced by 61% and 86% at a temperature of 1800 K when the reactant temperature was increased from 300 K to 500 K and 900 K, respectively. This is explained by the reduction of the difference between the reactant and product temperatures, directly reducing combustion entropy generation. This entropy reduction could reduce combustion irreversibility if it were possible to keep the reactant temperature as close as possible to product temperatures just before combustion starts. This could be achieved by high compression of the fresh charge [197], but raising the reactant temperature increases the likelihood of combustion abnormalities and NOx emissions.

In Figure 7.1, the reactant pressure has a modest effect on entropy generation for constant internal energy-volume combustion, mainly due to the suppression of product dissociation [194]. However, the pressure influence on entropy generation was more noticeable when the pressure rose from 10 to 30 bar, but less significant for engine-relevant combustion pressures (>30 bar).

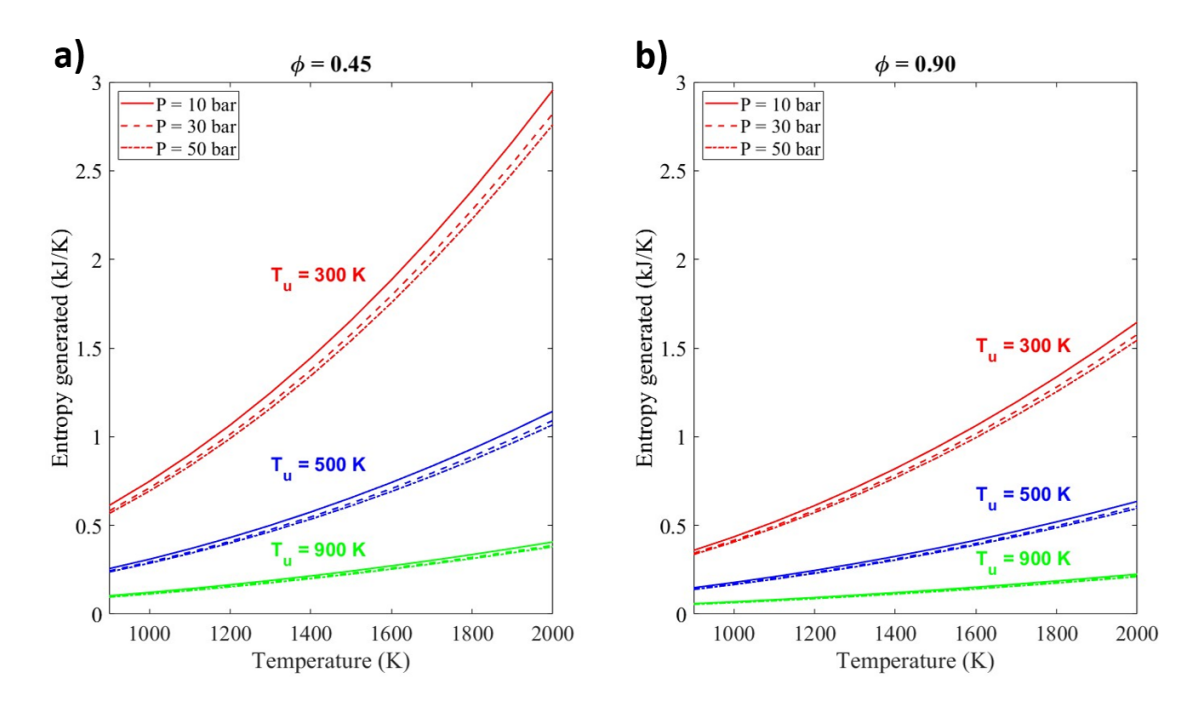


Figure 7.1: Entropy generated by combustion at various pressures and temperatures in a hydrogen-fuelled SI engine for equivalence ratios a) 0.45, and b) 0.90.

Water addition to a hydrogen SI engine reduces NO emissions and mitigates knock, allowing the engine to operate at higher loads (Chapter 6). Therefore, it is logical to assess the effect of diluents on entropy generation of hydrogen combustion. Increasing the diluent ratio (e.g., nitrogen, oxygen, and water) increases combustion-generated entropy due to the reduction in reactant entropy caused by the decreased fuel amount (Figure 7.2). Water addition has the greatest effect on entropy generation, while nitrogen has the least influence.

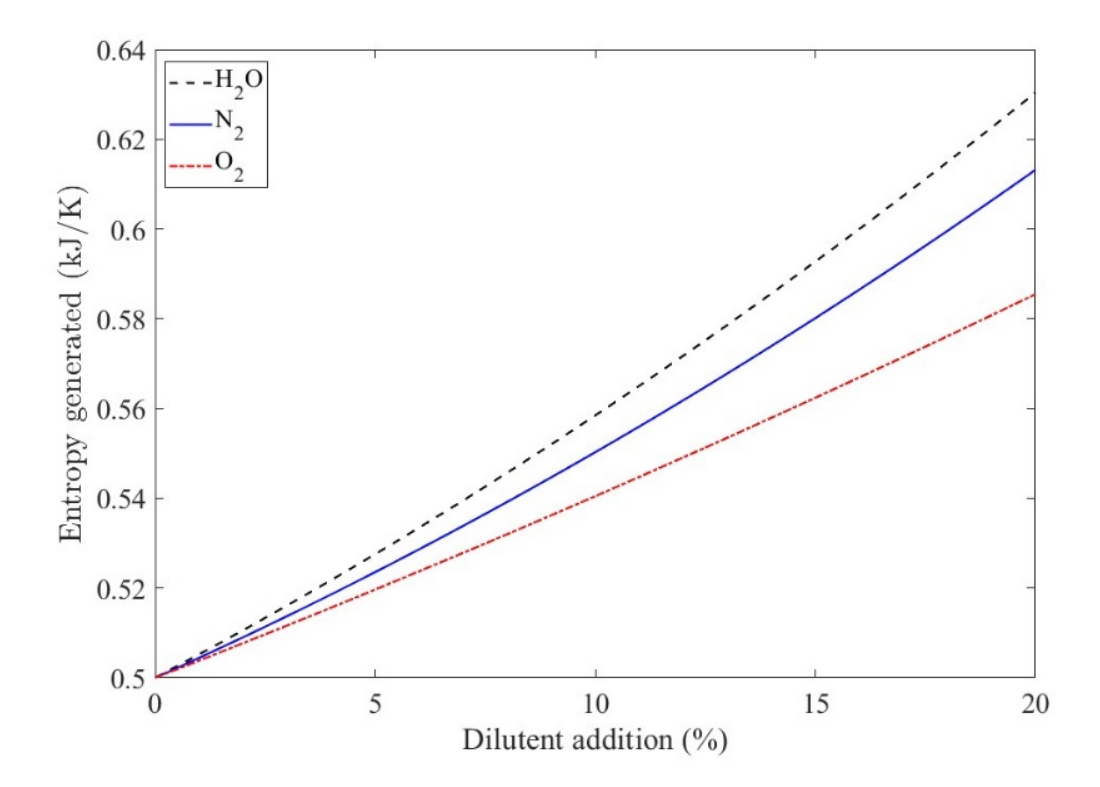


Figure 7.2: Entropy generated by combustion at diluent additions at an ϕ of 0.9 (P=30 bar, T=300 K).

7.1.1 Hydrogen SI engine exergy

The exergy is destined for either work, heat, irreversibility, or exhaust, and the proportions of this 'exergy split' are a function of crank angle (Figure 7.3). The initial and boundary conditions for the numerical model are directly related to the experimental data of a single cylinder four stroke hydrogen SI engine [47]. The values for boosted intake pressure, equivalence ratio and spark timing on the combustion and emission characteristics are given in Table 6.1. All the simulations were carried at a fixed compression ratio of 11.5 at an engine speed of 2000 rpm. At the intake valve closure (IVC) at 240°CA, the total input exergy equals the chemical exergy with a small addition from the thermo-mechanical exergy. During the compression process, work is supplied by the piston to the mixture (negative work exergy values):

• the in-cylinder pressure and temperature increase, thus the in-cylinder thermomechanical exergy increases,

- the exergy transfer to heat is negligible, and
- the pressure and temperature of the premixed hydrogen/air charge is not sufficient to start the oxidation; therefore, the chemical exergy is constant.

In Figure 7.3a, the start of combustion is at 4°CA bTDC, after which the chemical exergy drops rapidly as the fuel burns, while the thermo-mechanical exergy increases due to the significant rise in in-cylinder pressure and temperature. During combustion, expansion occurs, and exergy transfers to work and heat, eventually decreasing the total in-cylinder exergy. After the end of combustion as the piston approaches bottom dead centre (BDC), the total in-cylinder exergy continues decreasing because of the exergy transfer to heat, work, and combustion-related exergy destruction. The remaining exergy of the in-cylinder mixture at the end of the expansion process is defined as the exergy expelled by the exhaust gases because the pressure and temperature at the instant of exhaust valve opening (EVO) are greater than those of the dead state.

At leaner conditions of ϕ of 0.45 (Figure 7.3b), the chemical exergy at IVC decreases due to the reduced quantity of fuel. This reduction in hydrogen significantly lowers the exergy transfer to work and heat, as it reduces the in-cylinder pressure and temperature. However, combustion-related irreversibility increases with the leaner mixture, primarily due to the reduction in reactant entropy.

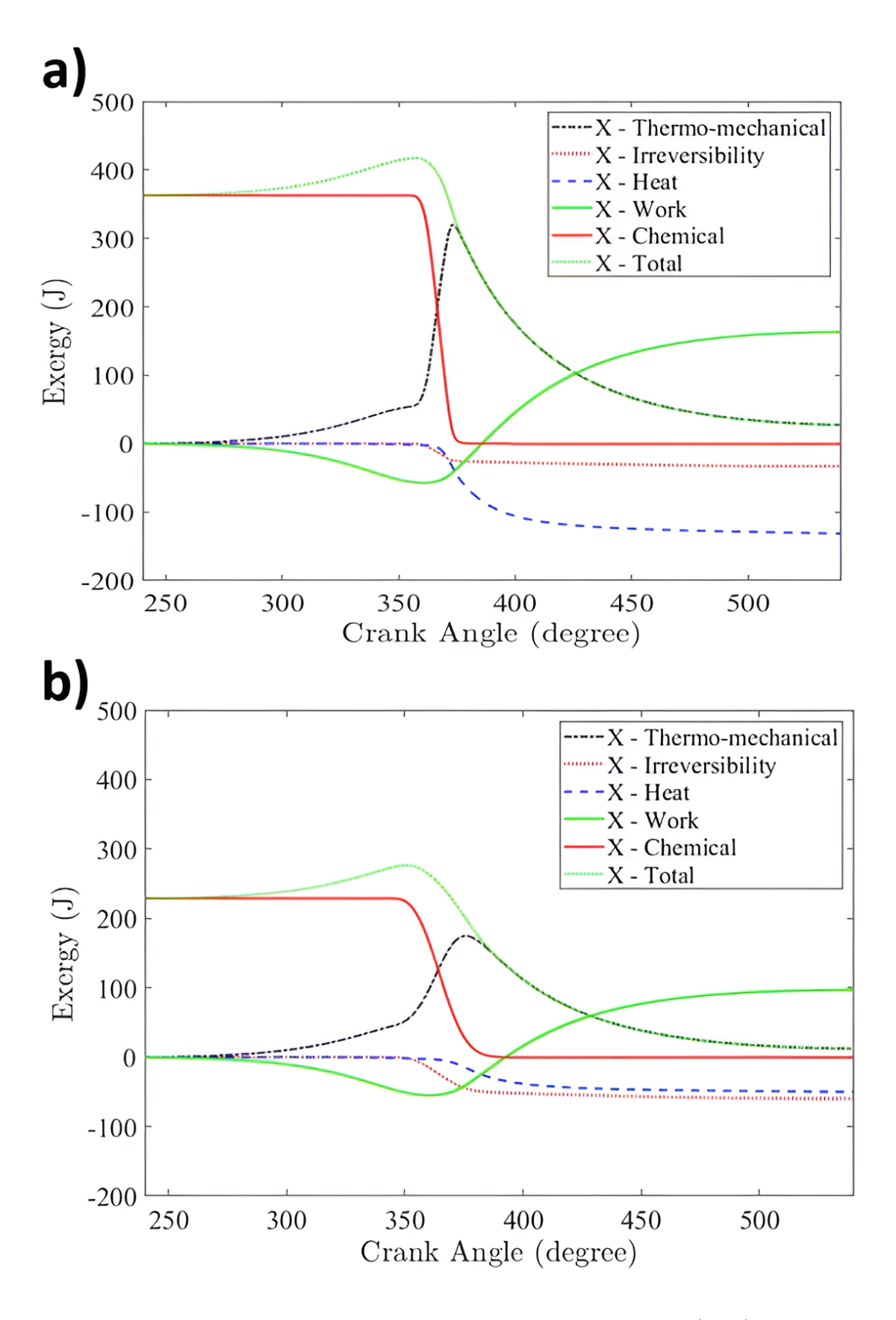


Figure 7.3: In-cylinder exergy balance from intake valve closing (IVC) to exhaust valve opening (EVO) a) under equivalence ratio of 0.9 at ST=355 °CA bTDC and b) under equivalence ratio of 0.45 at ST=345 °CA bTDC (MAP=80 kPa, N=2000 rpm, CR=11.5).

The destinations of exergy — work, heat, combustion, and exhaust — for a boosted lean-burn hydrogen SI engine at MBT timing are shown in Figure 7.4. The largest proportion of exergy was associated with reversible work, under all operating conditions. Moreover, the proportion of reversible work increases with increasing dilution ratios. When ϕ reduces from 0.90 to 0.45, the useful work ratio increases by 4%. This increase was mainly due to the exhaust enthalpy being diverted into reversible work, which eventually increases the efficiency due to a better expansion ratio. The exergy transfer to work correlates with the ITE. Conversely, the exergy to heat transfer and exhaust reduces by 35% and 64% when ϕ reduces from 0.90 to 0.45, respectively.

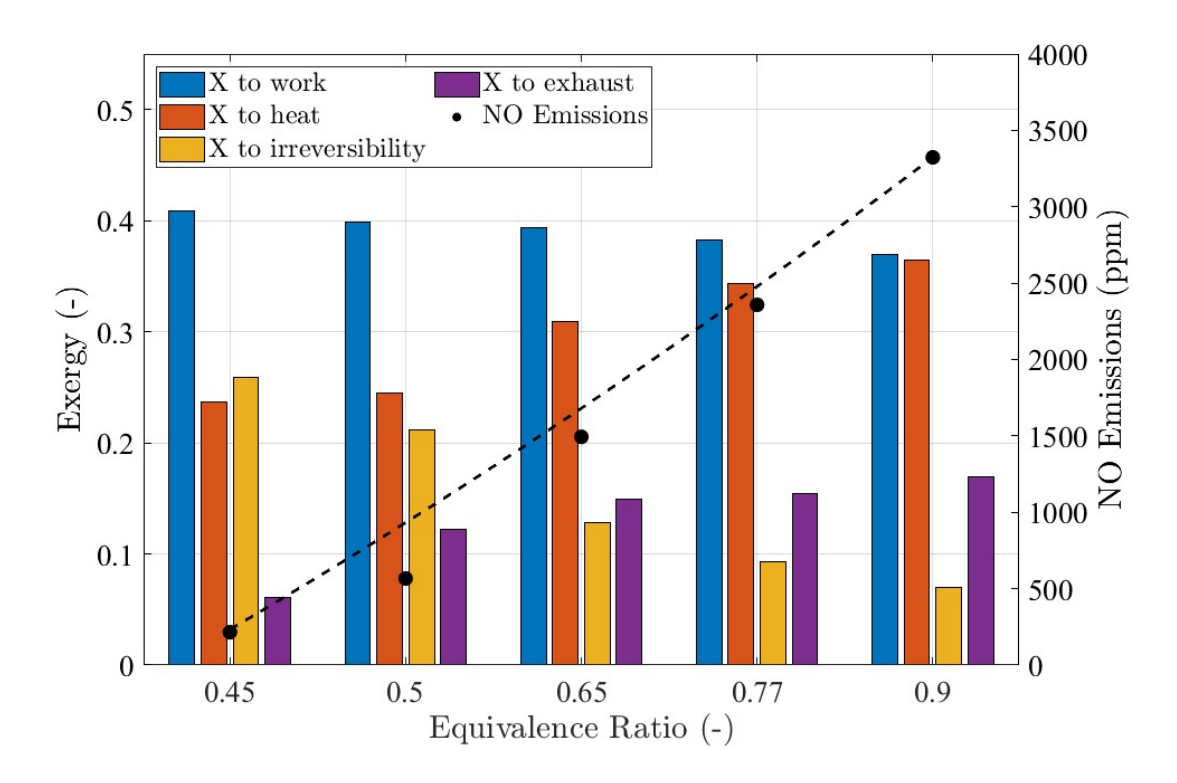


Figure 7.4: Exergy split to work, heat, irreversibility, and exhaust NO emissions at MBT timing for various equivalence ratios (MAP=80 kPa, CR=11.5).

The reduction in exergy transfer to heat results from reducing the difference between the mixture and chamber wall temperatures for leaner hydrogen mixtures. This study does not account for any unburned hydrogen residuals which might reduce thermal efficiency [48]. Furthermore, for ϕ of 0.90 the exergy transfer to heat

accounted for 36% of the exergy input. This was because of the greater difference between the in-cylinder temperature and the combustion chamber wall. In cases where exergy transfer to heat was dominant, heat reduction technologies such as the low heat rejection method [244] might improve hydrogen-fuelled engine performance. However, this approach might be less beneficial for leaner mixtures ($\phi < 0.50$), where the exergy to heat transfer was not as significant. For ϕ of 0.45, the exergy transfer to heat accounts for 23%. The exhaust exergy available represents the in-cylinder available exergy at EVO. Once the exhaust exergy is transferred to the environment, it is destroyed as it equilibrates with the environment. Increasing the air dilution rates reduces exhaust exergy.

The exergy destruction of combustion increases for leaner hydrogen/air mixtures since the difference between the reactant and product entropy increases due to the reduced amount of hydrogen in higher air-diluted mixtures. Additionally, the combustion reaction generates more entropy because of the lower burn temperatures for leaner hydrogen mixtures (see Section 7.1). The efficiency of ultra-lean hydrogen mixtures ($\phi < 0.50$) may be limited due to the increase of the combustion-related irreversibility. The increased air ratio reduces the exhaust exergy by increasing combustion exergy destruction rather than using the exhaust to benefit work output. However, the fact that lean burn hydrogen results in lower NO emissions cannot be overlooked. Lower temperatures lead to less NO formation, and if the temperature remains below 1800 K, NO emissions would be significantly reduced. From Figure 7.4, it is evident that for the naturally aspirated hydrogen engine, NO emissions were reduced by 30% and 87% when ϕ shifted from 0.90 to 0.77 and from 0.77 to 0.45, respectively. This reduction is attributed to the significant decrease in in-cylinder temperature at higher air dilution rates.

7.1.2 Effect of spark timing on exergetic processes

For ϕ of 0.77 and 0.9, Figures 7.5a and 7.5b show that the exergy associated with heat transfer decreases, but that the exhaust exergy increases as the spark timing shifts away from MBT timing. However, the magnitudes of exergy transfer associated with heat and exhaust are greater for ϕ of 0.90 compared to the leaner case ϕ of

0.77. The difference between energy and exergy analyses of exhaust is the inability of energy analysis to distinguish useful exhaust energy which could be recovered, from irreversibility which cannot (only minimized). As the spark timing shifts away from MBT timing, the exergy associated with heat transfer and work transfer is reduced due to reductions in the hydrogen engine IMEP. Reducing exergy transfer to work and heat causes increases in the exergy expelled by the exhaust gases and is commensurate with the second law of thermodynamics which states that the system rejects the unused exergy and generated entropy. Therefore, reducing the exergy transfer to work and heat necessitates that the remaining exergy be expelled at the exhaust. When ϕ was 0.77, the exergy expelled at EVO doubled when the spark timing was advanced by 10° CA from the corresponding MBT timing. However, the exergy associated with combustion irreversibility did not vary significantly (< 2%) with spark timing, as combustion-related irreversibility is influenced most by mixture composition. Figures 7.5a and 7.5b show that NO emissions were reduced when the spark timing was advanced or retarded from the corresponding MBT timing, which is due to the reduction of the in-cylinder temperature.

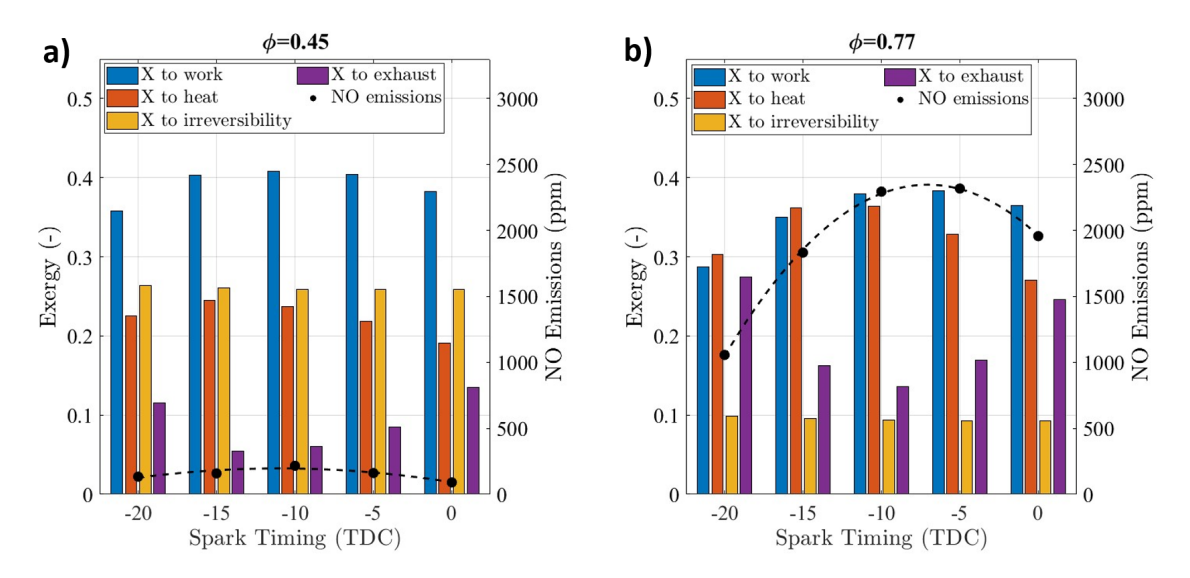


Figure 7.5: The exergy split to work, heat, irreversibility, and exhaust and NO emissions for various spark timings for ϕ of 0.77 and 0.90 (MAP=80 kPa, CR=11.5, N=2000 rpm).

7.1.3 MAP effect on the exergy split

The hydrogen SI engine requires an increase in MAP to compete with the load capabilities of a gasoline engine [44]. Figure 7.6 shows that at MBT timing, the exergy transfer to reversible work increases with increasing MAP. For ϕ of 0.90, the exergy to work transfer increases by 7% when MAP increases from 80 to 100 and 120 kPa. This increase is caused by the greater charge density associated with boosting, resulting in a larger difference between the in-cylinder temperature and combustion chamber walls, as indicated by the increase in exergy associated with heat transfer. For ϕ of 0.90 (Figure 7.6c), the exergy associated with heat transfer increases by 8% as MAP rises from 80 to 120 kPa. In contrast, the exergy expelled at exhaust decreases as MAP increases because of the increase in exergy transferred to work and heat. Specifically, exhaust exergy reduces by 70% and 22% as MAP increases from 80 to 120 kPa for ϕ of 0.45 (Figure 7.6a) and ϕ of 0.90 (Figure 7.6c), respectively.

Meanwhile, the exergy associated with combustion irreversibility slightly reduces with increasing MAP but is not significantly affected, suggesting the exergy transfer to combustion irreversibility mainly depends on the equivalence ratio. When ϕ shifts from 0.45 to 0.90 for the naturally aspirated condition (MAP of 80 kPa), exergy due to irreversibility reduces by 72% because the combustion product entropy reduces as ϕ becomes richer. This is coupled with increasing in-cylinder temperature. The exergy transfer to work increases with increasing MAP mainly because of the significant exhaust exergy losses and some contribution from reductions in combustion irreversibility. Consequently, the increase in efficiency and the reduction of the exhaust exergy with increasing MAP are promising; however, these benefits are counteracted by an increase in NO emissions (Figures 7.6(a-c)). For all modelled ϕ , NO emissions increase when MAP shifts from 80 to 120 kPa, highlighting a trade-off between improving engine performance and managing emissions.

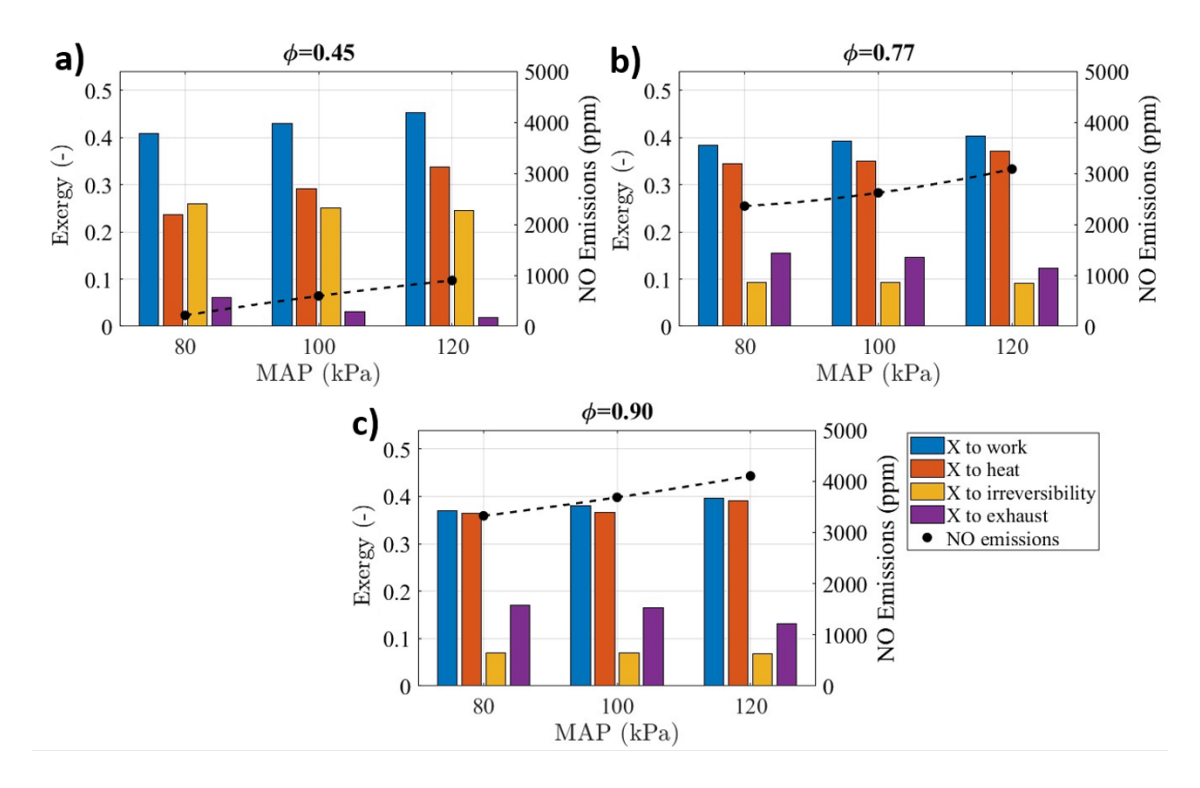


Figure 7.6: The exergy split to work, heat, irreversibility, and exhaust for various MAP, ϕ , and NO emissions at MBT timing (MAP=80 kPa, CR=11.5, N=2000 rpm).

7.1.4 Compression ratio effect on the exergy split

Increasing the compression ratio raises the reactant temperature, influencing entropy generation, hence potentially reducing the irreversibility losses associated with combustion. Whether this rise in reactant temperature is sufficient to influence the exergy due to combustion irreversibility of a hydrogen-fuelled engine is not understood. Increasing the compression ratio also increases the likelihood of combustion abnormalities occurring [228], but these are not modelled in this study. In Figure 7.7, the effect of increasing the compression ratio from 11.5 to 13.0 shows exergy transfer to work increases by 9%, 7%, 6%, 4%, and 3% for ϕ of 0.45, 0.50, 0.65, 0.77, and 0.90, respectively. The peak exergy transfer to work (44%) occurs at ϕ of 0.45. The load increase with compression ratio is explained by the increase in pressure and temperature during compression, which increases the flame speed and decreases the combustion duration. The exergy associated with combustion irreversibility did not

vary significantly with the increase of the energy state (by increasing the compression ratio). For ϕ of 0.90 under naturally aspirated conditions, exergy associated with combustion irreversibility plateaus around 7%, even though the energy state increases with increasing compression ratio or by reducing heat loss (see Section 7.2.4). Whereas, for ϕ of 0.45, exergy transfer to combustion-related irreversibility could not be reduced by more than 25%.

However, increasing the compression ratio is more effective at reducing the exergy at exhaust compared to combustion-related losses. Exhaust exergy reduces by 88%, 41%, and 37% when the compression ratio increases (from 11.5 to 13.0) for ϕ of 0.45, 0.77, and 0.90, respectively. Concurrently, the increase of the in-cylinder energy state increases the NO emissions by 229% and 36% for ϕ of 0.45 and 0.90, respectively. This illustrates the trade-off where enhancements in performance may increase emissions.

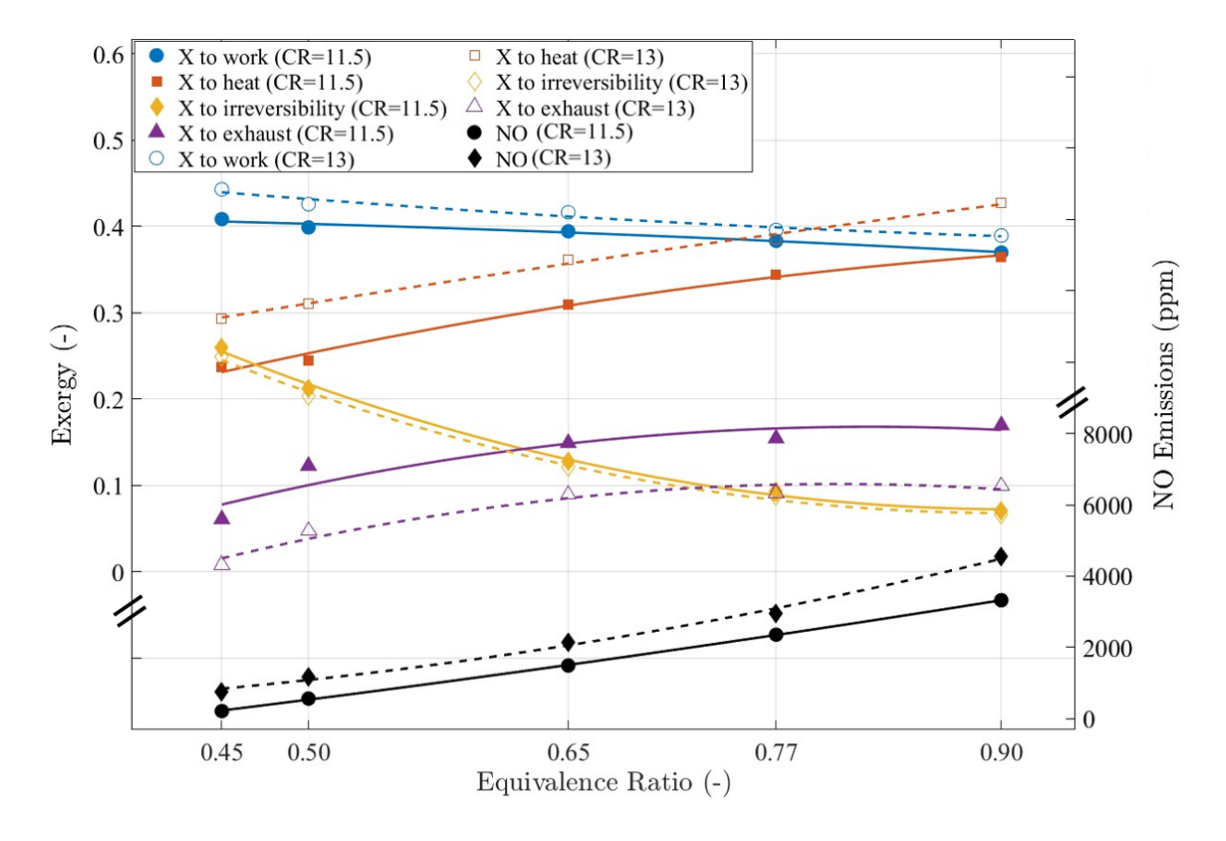


Figure 7.7: Compression ratio effect on the exergy split to work, heat, irreversibility, and exhaust for MAP=80 kPa NO emissions at MBT timing for various equivalence ratios. The lines represent least-squares fits.

7.1.5 Low heat rejection effect on the exergy split

To better understand the coupling of the exergy contributors, reductions in heat transfer were studied to understand which needs to be minimized to improve engine performance. It is important to distinguish between an adiabatic and a no-heat-transfer engine. An adiabatic engine does not have heat transfer (which is impossible based on the definition), whereas a no-heat-transfer engine allows balanced heat transfer in and out of the gas [113]. While there will be no net heat transfer, exergy destruction occurs due to the temperature difference between the burned and unburned mixture [178]. Reductions in heat transfer could be feasible by improving the insulation of the combustion chamber walls, and is known as a low heat rejection (LHR) engine [244].

The heat from the burned mixture could be used to increase the expansion work, thus increasing engine power output. For ϕ of 0.45 (Figure 7.8a), work efficiency increases by 37%, 24%, and 9% for 50%, 60%, and 80% heat-loss reductions, respectively. However, it also increases exergy transfer to the exhaust where the expelled exergy increases by 60%, 42%, and 28% for 50%, 60%, and 80% heat-loss reductions, respectively. This trend is observed for all ϕ (Figures 7.8(a-c)) and is consistent with the second law of thermodynamics, which states that a steady-state system must reject the input and generated entropy. Therefore, reducing entropy generated by heat transfer by reducing heat-loss, requires the entropy to be rejected at exhaust. Without mechanical modifications, the reduction of heat-loss increases exergy transfer to the exhaust, increasing the exhaust temperature and therefore the temperature difference with the environment. However, the work and efficiency increase. From Figure 7.8, it can be seen that the combustion-related irreversibility reduces with decreasing heat-loss. This was mainly due to increasing in-cylinder temperature caused by raising the energy state by reducing the heat-loss.

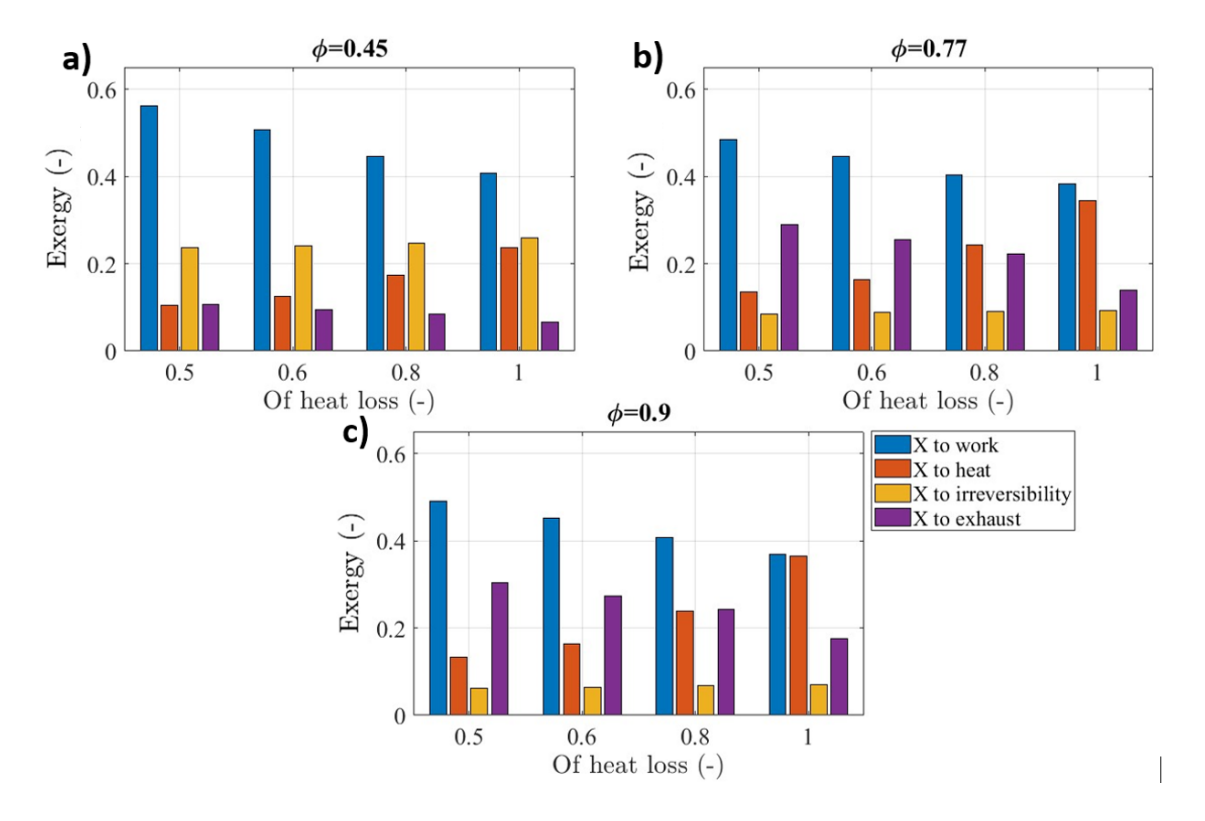


Figure 7.8: The exergy split to work, heat, irreversibility, and exhaust for various ϕ and heat-loss percentages (MAP=80 kPa, ST=MBT, CR=11.5, N=2000 rpm).

7.1.6 Effect of water addition on the exergy split

The addition of water to hydrogen alters the specific heat capacity of the combustible mixture, affecting its thermodynamic behaviour. The inset plot of Figure 7.9 shows water increases the chemical exergy due to its chemical potential. However, after combustion begins at 5 °CA bTDC, the chemical exergy decreases. This drop is less pronounced with higher water additions, primarily due to water's high specific heat capacity. The high specific heat capacity of water also reduces exergy transfer to work (Figure 7.10a), leading to lower engine power output. Similarly, exergy transfer to heat decreases significantly (Figure 7.10b), suggesting a potential approach to managing exergy loss to heat. However, Figure 7.10c shows that combustion-related exergy destruction increases with water addition, mainly due to the reduction in in-cylinder temperature caused by the added water.

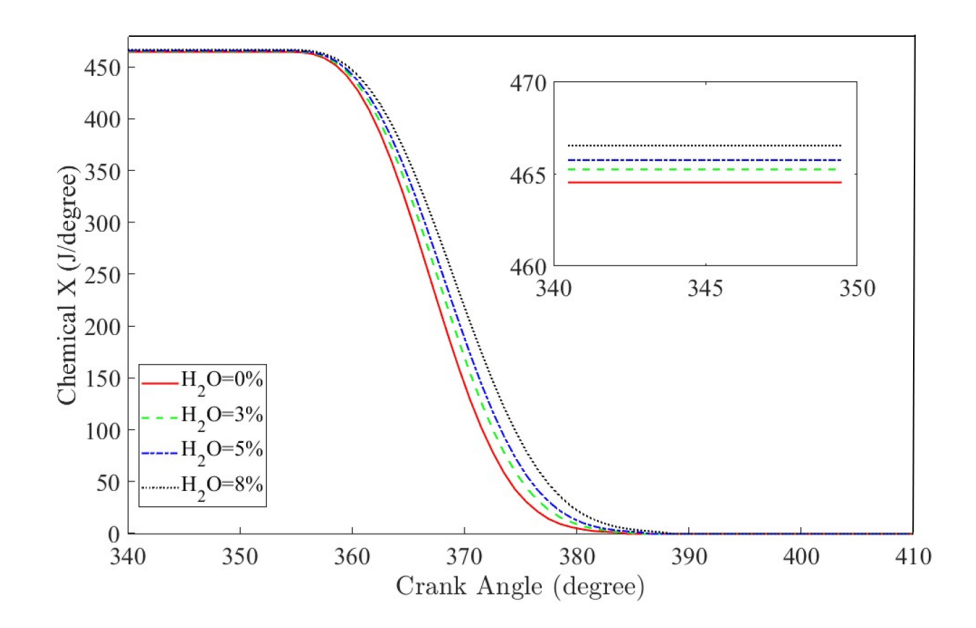


Figure 7.9: Hydrogen/air chemical exergy at different water additions for naturally aspirated condition under an equivalence ratio of 0.9 (ST=5 °CA bTDC, MAP=80 kPa, N=2000 rpm).

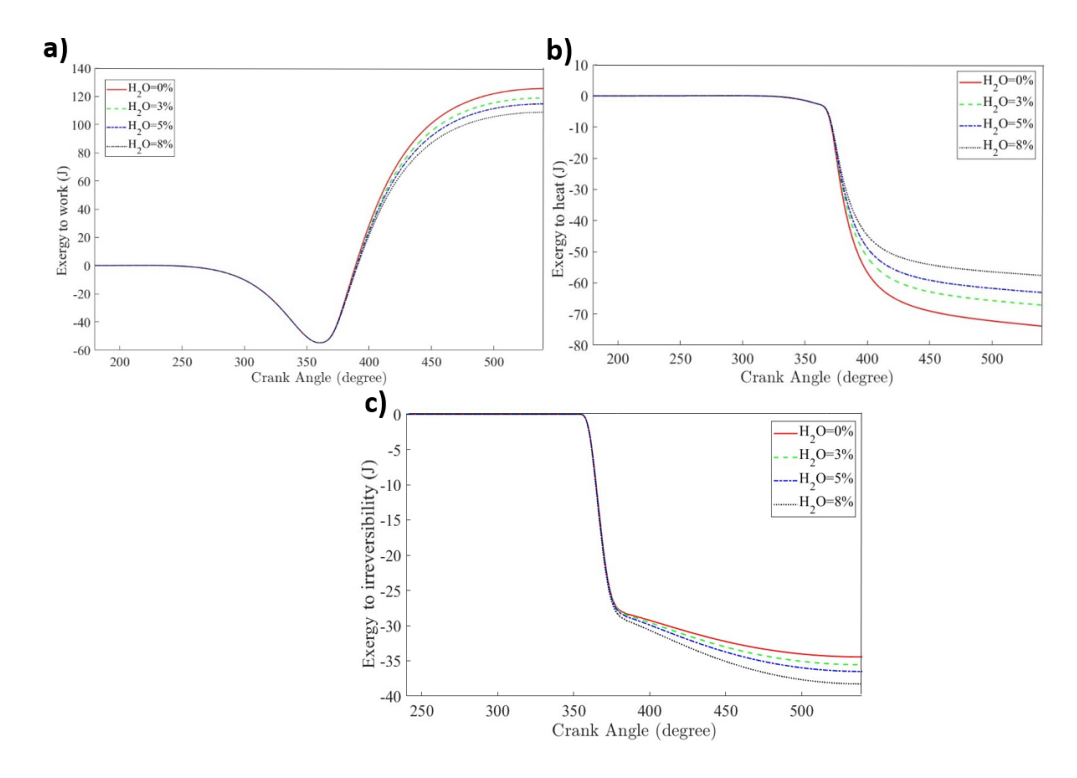


Figure 7.10: The exergy split to a) work, b) heat, and c) irreversibility for ϕ of 0.9 for various water additions (ST=5 °CA bTDC).

Figure 7.11 presents the exergy transfer to work, heat, irreversibility, and exhaust for a hydrogen-fuelled SI engine at various equivalence ratios (ϕ) and water addition levels. As water addition increases, exergy transfer to work decreases due to reduced in-cylinder pressure. For a ϕ of 0.45 (Figure 11a), the exergy transfer to work decreases by 9%, 11%, 12%, and 14% with 1%, 3%, 5%, and 8% water addition, respectively. Similarly, as water addition increases, exergy transfer to heat decreases due to the drop in in-cylinder temperature, with reductions of 2\%, 5\%, 7\%, and 11\% for the same levels of water addition. Conversely, exergy destroyed by combustionrelated irreversibility increases with water addition. This is attributed to the rise in product entropy and the decrease of in-cylinder temperature. Exergy-loss to irreversibility increases by 1\%, 2\%, and 4\% with 3\%, 5\%, and 8\% water addition, respectively. As exergy transfers to work and heat decrease, the remaining exergy must be expelled through the exhaust. For ϕ of 0.45, the exergy expelled by the exhaust gases increases by 18%, 51%, 81%, and 121% with 1%, 3%, 5%, and 8%water addition, respectively. This suggests a potential for using exergy in the exhaust of water-diluted hydrogen SI engines.

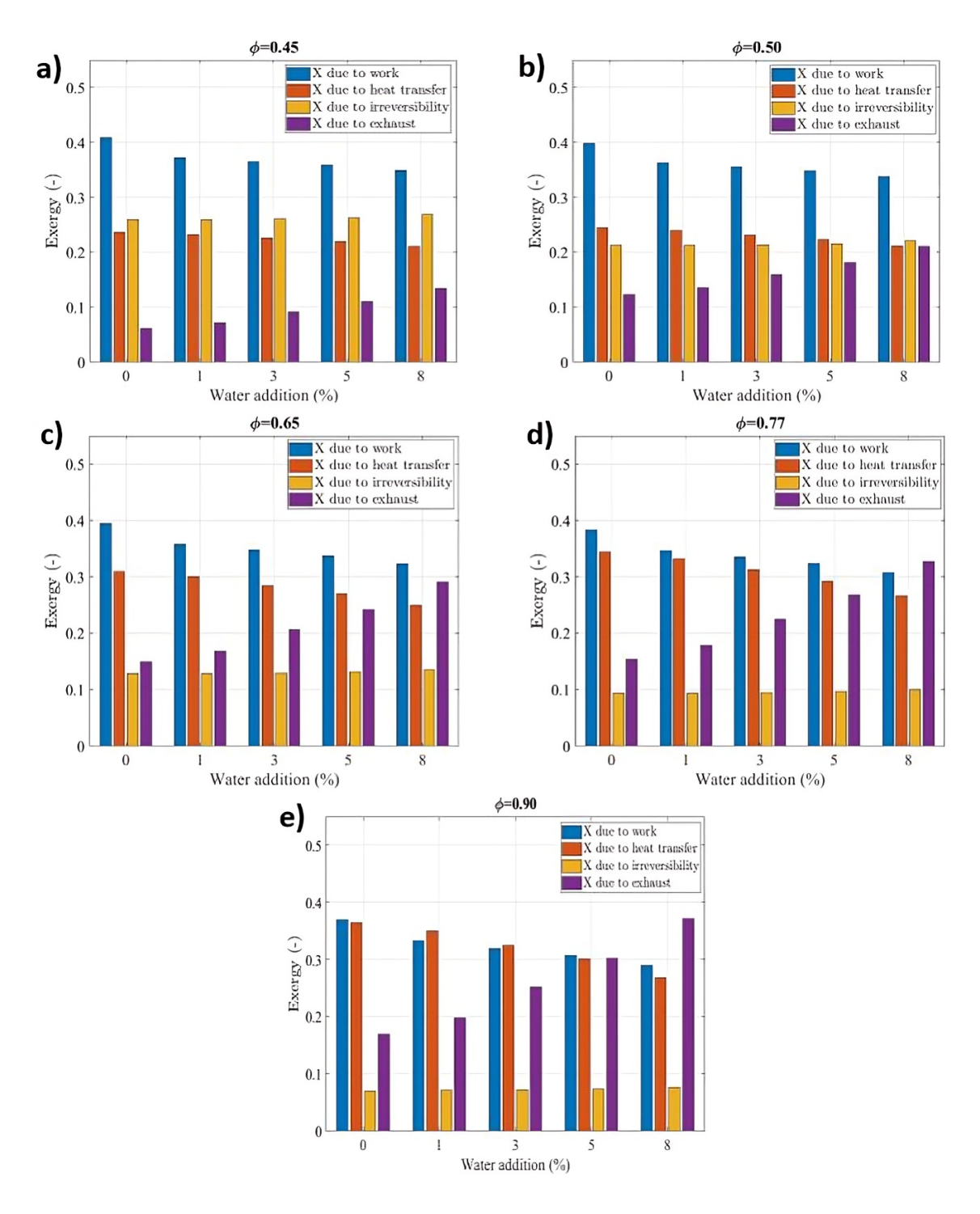


Figure 7.11: The exergy split for a lean-burn hydrogen engine at various water additions and equivalence ratios (N=2000 rpm, CR=11.5, ST=MBT).

7.2 Combined top-down and bottom-up approach

The efficiency of a hydrogen-fuelled engine at a ϕ of 0.90 is calculated using two approaches: 1) the bottom-up approach, and 2) the top-down approach (Table 7.1).

In the bottom-up approach, the irreversibility due to heat transfer, combustion, and exhaust are summed. Whereas, the top-down approach calculates the total engine irreversibility by taking the difference between the exergy input and output. The top-down approach is a global method that does not identify or quantify losses, but depends solely on the exergy flows crossing the control volume boundary. The bottom-up and top-down exergy methods differ by approximately 11 J in the total irreversibility, which is defined as unaccounted exergy. This unaccounted exergy could be due to mechanical friction [178].

Table 7.1: Exergy balance for the case of ϕ of 0.90 under the naturally aspirated condition MAP=80 kPa (CR=11.5, N=2000 rpm, ST=4 °CA bTDC).

Process	Description	Bottom-Up (J)	Top-Down (J)
Exergy input	Fuel Chemical Exergy	465	465
Irreversibility	Heat Transfer	170	170
	Combustion	33	33
	Exhaust	79	79
Exergy output	Reversible Work	172	172
Exergy input - Exergy output		292	292
Total Irreversibility		282	293
Efficiency (%)	1 - Irreversibility/Exergy input	39%	37%

7.3 Summary

This chapter offers a comprehensive exergy analysis of a boosted lean-burn hydrogen spark-ignition engine, investigating the processes involving exergy destruction under real-world conditions. Using an improved two-zone engine model to study incylinder processes, the results indicate that increasing air dilution enhances exergy transfer to work, due mainly to diverting exhaust exergy into reversible work. However, increasing air dilution also increases combustion-related exergy destruction due

to greater entropy generation for leaner mixtures, but reducing heat loss decreases combustion-related irreversibility. Higher manifold air pressures and compression ratios increase the quantity of exergy directed to work and heat, while reducing exergy expelled to exhaust. Gaining an understanding of the thermodynamic mechanisms of the routes by which the work potential is lost potentially assists in engineering improvements to minimize exergy losses, and to increase efficiency and work output.

Chapter 8

Conclusions and future work

Hydrogen has the potential to replace fossil fuels to significantly reduce tailpipe emissions, so improving air quality. Hydrogen also has the potential to reduce wellto-wheel GHG emissions, if carbon-free production can be achieved. The motivation for this work is to advance the efficiency of the ICE to meet future emissions targets set for automotive manufacturers in many nations. Hydrogen may also offer advantages in combustion properties compared to traditional fossil fuels, so understanding in detail the end-to-end processes for its combustion in an ICE is an important step to improving engine design. A general point is that due to hydrogen's low charge density, the operation of naturally aspirated hydrogen ICEs might produce lower loads than standard gasoline ICEs. The hydrogen ICE load can be increased by boosting the manifold air pressure (MAP), which can be done using a turbocharger or supercharger at the inlet. Experiments are costly and time-consuming, so modelling these processes under realistic conditions is a useful contribution. This work focuses on improving the quality and performance of models for the hydrogen-fuelled spark-ignition ICE to understand advanced combustion strategies. Hydrogen combustion was analysed using improved single- and two-zone combustion models, and by exploiting the second law of thermodynamics to understand the exergy losses. The single- and two-zone hydrogen combustion models were validated for premixed spark-ignition engine operation across equivalence ratios from 0.4 to 1.0 and manifold air pressures ranging from 80 to 140 kPa. Validation was performed by comparing simulated in-cylinder pressure, IMEP, and thermal efficiency against published experimental data under varying spark timings and intake conditions.

8.1 Single-zone model

Single-zone combustion models underpredict the burning velocity at elevated pressures due to thermo-diffusivity and hydrodynamic instabilities at realistic engine operating conditions. The single-zone combustion model was advanced by incorporating the laminar flame speed (LFS) to predict the combustion duration with respect to the reference operating conditions. This was implemented by using the inverse relative change in the LFS. There is a trade-off between ease of use and the level of complexity of a model, but incorporating LFS is a useful addition to the single-zone model. The burning velocity of different mixture compositions was only used to calculate the change of combustion characteristics at various equivalence ratios, spark timings, and intake pressures, hence it does not represent the laminar flame propagation nor the turbulent burning velocity. The new single-zone model was assessed by comparing the in-cylinder pressure at various operating conditions to previously published experimental data. For the baseline results, the equivalence ratio and the Wiebe function parameters were adjusted to match the simulated results with the available experimental engine data. Satisfactory accuracy was achieved between the simulation and experimental values for various equivalence ratios, manifold air pressures, and spark timings.

The results indicate that increasing the intake MAP improves thermal efficiency, primarily due to enhanced volumetric efficiency from increased compressed air at higher pressures. For an equivalence ratio of 0.65, the indicated mean effective pressure (IMEP) increased by one-third when the MAP was raised from 84 kPa to 134 kPa. However, this IMEP increase with rising MAP is less pronounced for mixtures leaner than 0.65 due to the greater amount of air in the combustion chamber. For equivalence ratios below 0.5, the effect of increasing MAP diminishes because the significant increase in air inside the combustion chamber reduces the LFS, resulting in longer combustion durations. To offset the longer combustion durations, the spark timing has to be advanced. For instance, the minimum spark timing for best torque

(MBT) for an equivalence ratio of 0.77 was at 10 °CA bTDC, whereas it shifted to 20 °CA bTDC for ultra-lean mixtures (ϕ <0.5). Thus, in hydrogen SI engines, the spark timing event should be adjusted for varying charge densities and burning velocities to maintain high efficiency. For ultra-lean mixtures ($\phi < 0.5$), the combustion location could not be centred at the optimal position of 8-10 °CA aTDC due to the slow burning speed of the hydrogen/air mixture. Furthermore, the hydrogen SI engine peak thermal efficiency up to 42%, was reached at an equivalence ratio of 0.55and a manifold air pressure of 124 kPa. Further increases in thermal efficiency were limited by the tendency for knocking and nitric oxide emissions at higher manifold air pressures. The Livengood-Wu integral indicates the knocking tendency for MAP values greater than 124 kPa at an equivalence ratio of 0.77. However, knock was mitigated by retarding spark timing which reduces the end-gas temperature and lengthened the auto-ignition delay time. However, retarding spark timing lowers thermal efficiency, hence knocking might prevent the engine from running with the optimal spark timing. Varying the mixture composition changes the NO emissions, as composition influences the in-cylinder temperature. But, when boosting is applied in the hydrogen SI engine, particularly for mixtures richer than 0.5, it leads to higher NO emissions due to increase in-cylinder temperatures. Additionally, NO emissions can be reduced by retarding spark timing; at an equivalence ratio of 0.55 and a MAP of 134 kPa, retarding spark timing by 10 °CA reduces NO emissions by 68%. Under naturally aspirated conditions (MAP = 84 kPa), a 5 °CA spark timing retardation results in a 55% reduction in NO emissions, with a 6% decrease in indicated thermal efficiency. The results indicate that NO emissions are significantly influenced by varying the equivalence ratio, as it affects the in-cylinder temperature substantially and inhibits NO formation to nearly zero under ultra-lean-burn operation of the SI hydrogen engine.

8.2 Laminar flame speed correlation

There are other strategies for mitigating combustion abnormalities and reducing nitric oxide emissions, such as low-temperature combustion through lean burn with

water injection. In this case, as the exhaust composition contains significant levels of water vapour, it was reasonable to study the effect of water addition on hydrogen combustion. Besides the thermal and chemical effects of water on the reactive mixture, it modulates the LFS, which is one of the most important inputs to numerical combustion models. Experimental data on hydrogen LFS at elevated pressures are scarce because of the instability of the flames. Nevertheless, the stable hydrogen flame speed could be predicted using chemical kinetic models. Generating the LFS data from chemical kinetic models for different sets of operating conditions could be time-consuming. Moreover, since no correlation exists in the literature to predict the LFS of hydrogen-air combustion with water addition under lean mixture engine operating conditions, this thesis offers a newly developed LFS correlation for hydrogen-air combustion extended to account for the effects of water addition under engine-relevant conditions by calculating the chemical kinetic LFS values. The LFS correlation was validated for pressure ranges from 10 to 70 bar, temperature ranges from 400 to 800 K, equivalence ratio ranges from 0.35 to 1, and water addition by mole from 0 to 20%. Polynomial expressions of reduced order and number of terms were developed with optimized values of coefficients to predict the LFS under lean mixture operation and high-pressure conditions. For creating the LFS correlation, a reference pressure of 5 bar and a reference temperature of 600 K were set to make pressure and temperature non-dimensional. Firstly, over 2500 hydrogen LFS data points were fitted using the Levenberg-Marquardt algorithm at various pressures and equivalence ratios at a fixed temperature of 600 K. A non-negative constrained multivariate regression analysis was performed to avoid spurious values. The Akaike Information Criterion (AIC) was used to find the most optimized combination of the predictors for the correlation. For the fixed temperature of 600 K, the LFS correlation showed good accuracy, where 98% of the data fitted within a 10% error margin. However, the correlation did not meet the 10% error criteria for LFS values smaller than 0.3 m/s, as the weighting factor could not improve the accuracy for these smaller LFS values, as it would reduce the accuracy of the overall operating condition range.

To explore the dependence of pressure, temperature, and equivalence ratio on

the temperature-dependent exponent, α , 2000 hydrogen LFS data points at various operating conditions were used. The power exponent α was shown to be dependent on pressure, temperature, and equivalence ratio. These effects were captured by including an exponential term that relates to temperature and equivalence ratio through the exponent β , which was previously in literature considered to be solely dependent on the equivalence ratio. The results show that the incorporation of the temperature-dependent exponential term in the exponential power improves the accuracy of the hydrogen LFS prediction when compared to the chemical kinetic model across 3000 data points. The improvement was more notable for LFS values above 3 m/s, where most of the data points fell within a $\pm 10\%$ error margin. The variation between the simulated values from the chemical kinetic model and the predicted values from the new correlations of reduced order resulted in an R^2 of 0.99. The newly developed hydrogen LFS correlation was extended to incorporate the effects of water addition, to allow accurate prediction of hydrogen combustion under engine-relevant conditions. This extended correlation showed strong accuracy, with 84% of data points fitting within a 10% error margin and 97% within a 20% error margin when compared to a chemical kinetic model, covering a range of pressures, temperatures, equivalence ratios, and up to 20% water addition.

The new correlation revealed that pressure has a more pronounced effect on hydrogen LFS for leaner hydrogen mixtures due to relatively lower energy content in the reactive mixture, which was insufficient to counteract the effect of increased pressure. For higher percentages of water addition, specifically at 20% by mole, the LFS was not significantly affected by pressure at levels above 40 bar for mixtures leaner than 0.8. This was because of the reduction in global temperature from increased dilution and higher heat capacity of the charge, hence the dissociation reactions were not initiated under higher percentages of water addition. Though the LFS increased significantly with an increase in equivalence ratio for 20% water addition relative to neat hydrogen combustion, on an absolute scale, the magnitude of the hydrogen LFS with water addition is much lower than neat hydrogen combustion. The LFS decreases linearly with increasing water addition for all pressures and temperatures, but the rate of decrease of the LFS of hydrogen was more pronounced at higher

ambient temperatures of the reactive mixture. The linear decrease in the rate of the LFS was noted with the addition of water, but there appears to be a limit to the amount of water addition for effective control of hydrogen combustion, beyond which it tends to be detrimental to engine performance.

8.3 Two-zone model

The applicability of the newly developed LFS empirical correlation was proven by incorporating it into a two-zone combustion model to predict the performance, combustion abnormalities, and nitric oxide emissions of a boosted lean-burn hydrogen SI engine under a water injection environment. The injection of water modulates hydrogen combustion, but there are trade-offs to be optimized between the amount of water used and engine and emission performance. The model showed that water addition extended the combustion duration by reducing the LFS. Adding 8% water at an equivalence ratio of 0.7 shifted CA50 by 3°CA, showing that the two-zone model captures the effect of LFS reduction. The reduction of in-cylinder pressure with water addition could cause reductions in indicated thermal efficiency (ITE) and IMEP. At an equivalence ratio of 0.9, the IMEP decreased by 2\%, 6\%, 10\%, and 15% with 1%, 3%, 5%, and 8% water addition, respectively, highlighting a more significant impact on richer hydrogen mixtures. Whereas, at an equivalence ratio of 0.9, the ITE reduced by 1%, 4%, 6%, and 10% with 1%, 3%, 5%, and 8% water addition, respectively, due to increased heat capacity and slower rate of combustion. Conversely, increasing the MAP and equivalence ratio increased the in-cylinder pressure. However, the reduction in ITE and IMEP could become an advantage since water addition allows the engine to operate at higher MAP and compression ratios, so mitigating combustion abnormalities and NO emissions. As increasing MAP raises NO emissions, for an equivalence ratio of 0.9, the NO emissions increased by 5% and 23% as MAP increased from 80 to 120 kPa. Lower equivalence ratios lead to significant NO reductions, with naturally aspirated NO emissions decreasing by up to 83% when the equivalence ratio decreased from 0.9 to 0.5. Water addition further reduces NO emissions; for an equivalence ratio of 0.9, adding 8% water re-

duced NO by 38% due to lower global in-cylinder temperatures. Autoignition delay time is critical to modelling combustion abnormalities because it determines when chain-branching reactions occur, which can lead to knock. The autoignition delay time is influenced by equivalence ratio, pressure, temperature, and mixture concentration. The results show that the Livengood-Wu integral increases significantly with increasing MAP due to higher charge density, though air dilution mitigates this effect. For instance, under MAP of 120 kPa, the knock integral reduces by 8\%, 16%, and 27% as ϕ decreases from 0.9 to 0.5. Water addition also lowers the knock integral by increasing the autoignition delay time through heat absorption. At ϕ = 0.9 and MAP = 120 kPa, 8% water addition reduces the knock integral by 14%, with slightly smaller reductions for leaner mixtures. Thus, optimized water addition could mitigate NO emissions and combustion abnormalities while maintaining a reasonable engine load in lean-burn hydrogen engines due by increasing MAP and compression ratio. For a ϕ of 0.9 under a MAP of 120 kPa, the addition of 1% water caused the knock integral and NO emissions to reduce by 2\% and 5\%, respectively, while ITE was reduced by 2%. Thus, water addition could benefit hydrogen engine emission control and knock mitigation, but careful optimization is required to avoid significantly reducing thermal efficiency. The engine operation map based on ISFC, NO, ITE, ϕ , and water addition obtained through this new two-zone model has the potential to advance combustion strategies in hydrogen ICEs.

8.4 Understanding the fundamentals of ICE energy losses

With the completion of the improved two-zone model, it is possible to investigate the origins of the losses by undertaking exergy analysis and to examine the resulting trade-offs. Since the physical and chemical properties of pure hydrogen differ significantly from those of hydrocarbon fuels, it is beneficial to understand the exergy split into work, heat, irreversibility, and exhaust of hydrogen combustion under realistic engine operating conditions. Due to hydrogen's higher burning speed compared to that of hydrocarbon fuels the exergy transfer to work and heat might be greater than

that of hydrocarbon fuels. Meanwhile, the exergy destroyed by combustion-related irreversible processes could be lower than that for hydrocarbon fuels, due to lower reactant and product entropy changes. Lower entropy generation for hydrogen is attributed to its simpler combustion pathway compared to that of hydrocarbon fuels. Also, compared to hydrocarbon fuels hydrogen allows high dilution rates, reducing NO emissions, this also reduces engine power output. Moreover, the lower power of lean-burn hydrogen operation reduces the in-cylinder temperature, increasing the combustion irreversibility ratio. This increase in irreversibility—the destruction of available energy—is directly proportional to the rate of entropy generation. Entropy generation increased significantly with leaner mixtures; for $\phi = 0.45$, the generation rose due to the increased product entropy from excess air. Increasing the reactant temperature reduces entropy generation significantly, showing a 61% and 86% reduction when the temperature increases from 300 K to 500 K and 900 K, respectively. At leaner equivalence ratios, the exergy transfer to work increases as the exhaust enthalpy is redirected into reversible work. At $\phi = 0.45$, work exergy transfer increased by 4%, while heat and exhaust exergy transfers reduced by 35% and 64%, respectively. For $\phi = 0.9$, 36% of the exergy input is transferred to heat. Increasing MAP boosts the exergy transfer to work, with a 7% increase observed when MAP rises from 80 kPa to 120 kPa at $\phi = 0.9$. The exhaust exergy decreases by 70% and 22% for $\phi = 0.45$ and 0.9, respectively, with MAP increase. Raising the compression ratio from 11.5 to 13 increases exergy transfer to work by up to 9\%, peaking at 44\% for $\phi = 0.45$. However, exhaust exergy reduces by 88%, 41%, and 37% for ϕ of 0.45, 0.77, and 0.9, respectively. Reducing heat loss by 50-80\% increases work efficiency by 9-37% but also raises exhaust exergy by 28-60%. For $\phi = 0.45$, reducing heatloss enhances work efficiency but increases exhaust exergy due to higher in-cylinder temperatures. The amount of exergy transferred to work increases with decreasing equivalence ratio, as the exhaust enthalpy is diverted into reversible work. However, the combustion-related irreversibility rate increases due to the reactant and product entropy difference arising from the reduced amount of hydrogen fuel. When the spark timing shifts away from the corresponding MBT timing, the exergy associated with work and heat decreases because of the reducing IMEP. Reductions in exergy

transfer to work and heat cause the exergy expelled by the exhaust gases to increase. Additionally, increasing the MAP or compression ratio reduces the exergy expelled at exhaust, as the exergy used for work and heat transfer leave less exergy to be expelled. This is consistent with the second law of thermodynamics which states that a steady-state system must reject the input and generated entropy. Therefore, reducing the entropy generated by heat transfer by reducing heat loss requires the entropy to be rejected by the exhaust stage of the cycle. Without mechanical modifications, reducing heat loss increases exergy transfer to the exhaust, increasing the exhaust temperature and therefore the temperature difference with the environment. In contrast, exergy associated with combustion irreversibility was not significantly affected by spark timing, MAP, or compression ratio. However, it was caused by the equivalence ratio because of the difference between the reactant and product entropy. For a ϕ of 0.45, approximately 26% of the incoming exergy was lost due to the irreversibility of the combustion reaction, limiting the maximum possible efficiency of the hydrogen-fuelled SI engine to 74%. While this theoretical approach showed potential benefits for hydrogen engine efficiency, the improvements in exhaust enthalpy must be further addressed to maximize the benefit from entropy reductions by reducing heat loss. Improvements to using or converting exhaust heat into useful energy may enhance the overall engine performance and efficiency.

8.5 Limitations and future work

The results presented provide support for developing hydrogen-fuelled ICEs. However, experimental work is required to substantiate the proposed boosted lean-burn hydrogen SI engine strategies. Boosting intake air pressure enhances thermal efficiency but increases the likelihood of combustion abnormalities. The proposed knock model only captures the autoignition of the unburned mixture at the end-gas, but hot spots or emissions from unburned hydrogen from the previous cycle can cause pre-ignition. Pre-ignition was not considered since the hot spots could not be identified using a zero-dimensional combustion model. Therefore, future work should investigate the formation of hot spots in hydrogen-fuelled SI engines to reduce nitric

oxide emissions without significantly compromising thermal efficiency. The combustion abnormalities in hydrogen ICEs could be controlled by the injection system. Higher hydrogen injection pressures allow for shorter injection durations, improving mixing and atomization. This could improve engine load and mitigate emissions and combustion abnormalities, making it a reasonable topic for future investigation using a suitable numerical model. The two-zone model does not consider heat transfer between the burned and unburned zones, which may lead to overprediction of unburned zone temperatures and underestimation of heat loss. Additionally, model validation was constrained to limited operating conditions due to experimental data availability, which may affect the generalizability of the results across broader engine regimes. The single- and two-zone combustion models could be extended to predict the performance of other fuels in ICEs once the thermodynamic properties, laminar flame speed, and autoignition delay time are remodelled for the specific fuel. Although developed for hydrogen, the models are built on a framework that combines energy and exergy analysis making the methodology suitable for future work on strategy development and optimization of alternative-fuelled SI engines. The single-zone and two-zone combustion models used in this study do not incorporate a dedicated ignition model. Ignition is assumed to occur instantaneously or is initiated based on empirical correlations or predefined spark timing, and therefore the models do not resolve the detailed physics of ignition delay. The empirical correlation to predict the LFS of hydrogen was developed using chemical kinetics. It would be interesting to investigate whether a machine learning technique could develop the correlation based on experimental values, bypassing chemical kinetic simulations. Regarding water addition to hydrogen engines, it would be interesting to investigate the spatial effect of water addition on the mixing of the reactive in-cylinder mixture, which could not be done using the methodology applied in this work. The exergy analysis considered work, heat, combustion irreversibility, and exhaust to indicate the relative size and importance. There is a space for a more detailed examination of the physics and chemistry processes, however, moving beyond the zero-dimensional engine model would be a significant, but difficult step. Furthermore, there are many advantages of using less complex model. One way forward would be to use fluid

dynamics simulations to provide deeper insights into the loss mechanisms within engine processes and components, offering a clearer path to minimize exergy losses and enhance overall engine performance. Since the physical and chemical properties of traditional hydrocarbon fuels differ significantly from those of hydrogen, it would be beneficial to understand their exergy split into work, heat, irreversibility, and exhaust. As each fuel has its own thermodynamic properties and chemical structure, this could affect the exergy split into work, heat, irreversibility, and exhaust. As the exergy analysis across various fuels could reveal areas where ICE efficiency might be improved, it could thereby propose design and optimization strategies. Further research should also explore the application of second law-based control strategies in various engine configurations, incorporating advanced predictive control methods and neural network approximations for real-time implementation in hardware-in-the-loop setups. The benefits of incorporating exergy into control algorithms could pave the way for next generation ICE technologies.

References

- [1] UNFCCCC. The Paris Agreement. Tech. rep. Bonn, Germany, 2016.
- [2] IEA. Greenhouse Gas Emissions from Energy Data Explorer. Tech. rep. 2023.
- [3] IEA. World Energy Outlook. Tech. rep. 2023.
- [4] J. Zhai et al. "Impact of Ship Emissions on Air Quality in the Greater Bay Area in China under the Latest Global Marine Fuel Regulation". Environmental Science & Technology. 5733. 12341–12350. 2023. DOI: 10.1021/acs.est.3c03950.
- [5] A. Maragkogianni, S. Papaefthimiou, and C. Zopounidis. "Shipping Industry and Induced Air Pollution". In: *Mitigating Shipping Emissions in European Ports*. Cham: Springer International Publishing, 2016, 1–9. DOI: 10.1007/ 978-3-319-40150-8_1.
- [6] S. Yeh et al. "Tradable performance standards in the transportation sector". Energy Economics. 102. 105490. 2021. DOI: 10.1016/j.eneco.2021.105490.
- [7] T. Smith, C. Axon, and R. Darton. "The impact on human health of carrelated air pollution in the UK, 1995–2005". Atmospheric Environment. 77. 260–266. 2013. DOI: 10.1016/j.atmosenv.2013.05.016.
- [8] L. Zhang et al. "Energy, exergy and economic (3E) study on waste heat utilization of gas turbine by improved recompression cycle and partial cooling cycle". Energy Sources, Part A: Recovery, Utilization, and Environmental Effects. 452. 4127–4145. 2023. DOI: 10.1080/15567036.2023.2202626.

- [9] S. Manavalla et al. "System Design, Optimization and 2nd Law Analysis of a 100 MWe Double Reheat s-CO2 Power Plant at Full Load and Part Loads". Sustainability. 1520. 14677. 2023. DOI: 10.3390/su152014677.
- [10] N. Gray et al. "Decarbonising ships, planes and trucks: An analysis of suitable low-carbon fuels for the maritime, aviation and haulage sectors". *Advances in Applied Energy*. 1. 100008. 2021. DOI: 10.1016/j.adapen.2021.100008.
- [11] F. Leach et al. "The scope for improving the efficiency and environmental impact of internal combustion engines". *Transportation Engineering*. 1. 100005. 2020. DOI: 10.1016/j.treng.2020.100005.
- [12] J. Turner et al. "On the Application of Joule-Cycle-Based Waste Heat Recovery to Heavy-Duty Vehicles". en. In: Detroit, Michigan, United States, 2024, 2024–01–2589. DOI: 10.4271/2024-01-2589.
- [13] A. Boretti. "Advances in hydrogen compression ignition internal combustion engines". *International Journal of Hydrogen Energy*. 3619. 12601–12606. 2011. DOI: 10.1016/j.ijhydene.2011.06.148.
- [14] Y. Mogi et al. "Effect of high compression ratio on improving thermal efficiency and NOx formation in jet plume controlled direct-injection near-zero emission hydrogen engines". International Journal of Hydrogen Energy. 4773. 31459–31467. 2022. DOI: 10.1016/j.ijhydene.2022.07.047.
- [15] M. Mohamed et al. "Exploring the benefits of hydrogen-water injection technology in internal combustion engines: A rigorous experimental study". *International Journal of Engine Research*. 14680874241288624. 2024. DOI: 10.1177/14680874241288624.
- [16] S. Khalili et al. "Global Transportation Demand Development with Impacts on the Energy Demand and Greenhouse Gas Emissions in a Climate-Constrained World". Energies. 1220. 3870. 2019. DOI: 10.3390/en12203870.
- [17] J. Hofmann et al. "Assessment of electrical vehicles as a successful driver for reducing CO2 emissions in China". *Applied Energy*. 184. 995–1003. 2016. DOI: 10.1016/j.apenergy.2016.06.042.

- [18] C. Gerbaulet et al. "European electricity sector decarbonization under different levels of foresight". Renewable Energy. 141. 973-987. 2019. DOI: 10. 1016/j.renene.2019.02.099.
- [19] A. Nedjalkov et al. "Blueprint and Implementation of Rural Stand-Alone Power Grids with Second-Life Lithium Ion Vehicle Traction Battery Systems for Resilient Energy Supply of Tropical or Remote Regions". *Materials*. 1216. 2642. 2019. DOI: 10.3390/ma12162642.
- [20] S. Olówósejéjé, P. Leahy, and A. P. Morrison. "A practical approach for increased electrification, lower emissions and lower energy costs in Africa". Sustainable Futures. 2. 100022. 2020. DOI: 10.1016/j.sftr.2020.100022.
- [21] A. Ajanovic. "On the Integration of Electric Vehicles into the Energy System". In: 2019 8th Mediterranean Conference on Embedded Computing (MECO). Budva, Montenegro: IEEE, 2019, 1–1. DOI: 10.1109/MECO.2019.8760185.
- [22] Y. Wu and L. Zhang. "Can the development of electric vehicles reduce the emission of air pollutants and greenhouse gases in developing countries?" Transportation Research Part D: Transport and Environment. 51. 129–145. 2017. DOI: 10.1016/j.trd.2016.12.007.
- [23] D. Rathore et al. "Sustainability of biohydrogen as fuel: Present scenario and future perspective". *AIMS Energy*. 71. 1–19. 2019. DOI: 10.3934/energy. 2019.1.1.
- [24] C. Bae and J. Kim. "Alternative fuels for internal combustion engines". *Proceedings of the Combustion Institute*. 363. 3389–3413. 2017. DOI: 10.1016/j.proci.2016.09.009.
- [25] C. Axon and R. Darton. "A systematic evaluation of risk in bioenergy supply chains". Sustainable Production and Consumption. 47. 128–144. 2024. DOI: 10.1016/j.spc.2024.03.028.
- [26] EEA. Transport and mobility. Tech. rep. 2023.

- [27] G. Kalghatgi. "Is it the end of combustion and engine combustion research? Should it be?" *Transportation Engineering*. 10. 100142. 2022. DOI: 10.1016/j.treng.2022.100142.
- [28] F. Barbir. "Transition to renewable energy systems with hydrogen as an energy carrier". Energy. 343. 308–312. 2009. DOI: 10.1016/j.energy.2008.07.007.
- [29] S. K. Dash, S. Chakraborty, and D. Elangovan. "A Brief Review of Hydrogen Production Methods and Their Challenges". *Energies*. 163. 1141. 2023. DOI: 10.3390/en16031141.
- [30] T. Sinigaglia et al. "Production, storage, fuel stations of hydrogen and its utilization in automotive applications-a review". International Journal of Hydrogen Energy. 4239. 24597–24611. 2017. DOI: 10.1016/j.ijhydene.2017. 08.063.
- [31] A. M. Abdalla et al. "Hydrogen production, storage, transportation and key challenges with applications: A review". *Energy Conversion and Management*. 165. 602–627. 2018. DOI: 10.1016/j.enconman.2018.03.088.
- [32] A. Alaswad et al. "Developments in fuel cell technologies in the transport sector". *International Journal of Hydrogen Energy*. 4137. 16499–16508. 2016. DOI: 10.1016/j.ijhydene.2016.03.164.
- [33] C. Acar and I. Dincer. "The potential role of hydrogen as a sustainable transportation fuel to combat global warming". *International Journal of Hydrogen Energy.* 455. 3396–3406. 2020. DOI: 10.1016/j.ijhydene.2018.10.149.
- [34] M. Granovskii, I. Dincer, and M. A. Rosen. "Environmental and economic aspects of hydrogen production and utilization in fuel cell vehicles". *Journal of Power Sources*. 1571. 411–421. 2006. DOI: 10.1016/j.jpowsour.2005.07.044.
- [35] S. E. Hosseini and B. Butler. "An overview of development and challenges in hydrogen powered vehicles". *International Journal of Green Energy*. 171. 13–37. 2020. DOI: 10.1080/15435075.2019.1685999.

- [36] S. Falfari et al. "Hydrogen Application as a Fuel in Internal Combustion Engines". *Energies.* 166, 2545, 2023, DOI: 10.3390/en16062545.
- [37] J. Gao et al. "Lean-burn characteristics of a turbocharged opposed rotary piston engine fuelled with hydrogen at low engine speed conditions". *International Journal of Hydrogen Energy*. 461. 1219–1233. 2021. DOI: 10.1016/j.ijhydene.2020.09.167.
- [38] S. Verhelst. "Hydrogen engine-specific properties". International Journal of Hydrogen Energy. 269. 987–990. 2001. DOI: 10.1016/S0360-3199(01)00026-X.
- [39] S. Szwaja, K. Bhandary, and J. Naber. "Comparisons of hydrogen and gasoline combustion knock in a spark ignition engine". *International Journal of Hydrogen Energy*. 3218. 5076–5087. 2007. DOI: 10.1016/j.ijhydene.2007. 07.063.
- [40] R. Tkatchenko. "The evolution of the car-making industry". Vezetéstudomány
 / Budapest Management Review. 38–45. 2011. DOI: 10.14267/VEZTUD.2011.
 04.03.
- [41] R. O. King and M. Rand. "The Hydrogen Engine". Nature. 1744438. 975–976.1954. DOI: 10.1038/174975a0.
- [42] H. Pfriem. "Overview of the cooperative program on hydrogen storage, conversion and safety of the international energy agency". *International Journal of Hydrogen Energy*. 165. 329–338. 1991. DOI: 10.1016/0360-3199(91)90169-J.
- [43] C. White, R. Steeper, and A. Lutz. "The hydrogen-fueled internal combustion engine: a technical review". *International Journal of Hydrogen Energy*. 3110. 1292–1305. 2006. DOI: 10.1016/j.ijhydene.2005.12.001.
- [44] M. Berckmüller et al. "Potentials of a Charged SI-Hydrogen Engine". In: 2003, 2003–01–3210. DOI: 10.4271/2003-01-3210.

- [45] V. Dhyani and K. Subramanian. "Experimental investigation on effects of knocking on backfire and its control in a hydrogen fueled spark ignition engine". *International Journal of Hydrogen Energy*. 4314. 7169–7178. 2018. DOI: 10.1016/j.ijhydene.2018.02.125.
- [46] G. Maio et al. "Experimental and numerical investigation of a direct injection spark ignition hydrogen engine for heavy-duty applications". *International Journal of Hydrogen Energy*. 4767. 29069–29084. 2022. DOI: 10.1016/j.ijhydene.2022.06.184.
- [47] P. Sementa et al. "Exploring the potentials of lean-burn hydrogen SI engine compared to methane operation". *International Journal of Hydrogen Energy*. 4759. 25044–25056. 2022. DOI: 10.1016/j.ijhydene.2022.05.250.
- [48] S. Verhelst. "Recent progress in the use of hydrogen as a fuel for internal combustion engines". *International Journal of Hydrogen Energy*. 392. 1071–1085. 2014. DOI: 10.1016/j.ijhydene.2013.10.102.
- [49] P. Deboer, W. Mclean, and H. Homan. "Performance and emissions of hydrogen fueled internal combustion engines". *International Journal of Hydrogen Energy*. 12. 153–172. 1976. DOI: 10.1016/0360-3199(76)90068-9.
- [50] H. S. Homan, P. C. T. Deboer, and W. J. Mclean. "The Effect of Fuel Injection on NOx Emissions and Undesirable Combustion for Hydrogen-Fueled Piston Engines". In: 1978, 780945. DOI: 10.4271/780945.
- [51] C. Bleechmore and S. Brewster. "Dilution Strategies for Load and NOx Management in a Hydrogen Fuelled Direct Injection Engine". In: 2007, 2007–01–4097. DOI: 10.4271/2007-01-4097.
- [52] A. Mohammadi et al. "Performance and combustion characteristics of a direct injection SI hydrogen engine". *International Journal of Hydrogen Energy*. 322. 296–304. 2007. DOI: 10.1016/j.ijhydene.2006.06.005.
- [53] H. Wei et al. "Experimental study of thermal efficiency and NOx emission of turbocharged direct injection hydrogen engine based on a high injection pres-

- sure". International Journal of Hydrogen Energy. 4834. 12905—12916. 2023. DOI: 10.1016/j.ijhydene.2022.12.031.
- [54] T. Wallner et al. "Fuel economy and emissions evaluation of BMW Hydrogen 7 Mono-Fuel demonstration vehicles". *International Journal of Hydrogen Energy*. 3324, 7607–7618, 2008, DOI: 10.1016/j.ijhydene.2008.08.067.
- [55] H. Knorr. "The man hydrogen propulsion system for city buses". *International Journal of Hydrogen Energy*. 233. 201–208. 1998. DOI: 10.1016/S0360-3199(97)00045-1.
- [56] R. Gopalakrishnan et al. "Engineering the Ford H2 IC Engine Powered E-450 Shuttle Bus". In: 2007, 2007–01–4095. DOI: 10.4271/2007-01-4095.
- [57] Z. Yang et al. "Effects of injection mode on the mixture formation and combustion performance of the hydrogen internal combustion engine". *Energy*. 147. 715–728. 2018. DOI: 10.1016/j.energy.2018.01.068.
- [58] B. Fan et al. "Effect of hydrogen injection strategies on mixture formation and combustion process in a hydrogen direct injection plus natural gas port injection rotary engine". Energy Conversion and Management. 160. 150–164. 2018. DOI: 10.1016/j.enconman.2018.01.034.
- [59] Y. Li et al. "Effects study of injection strategies on hydrogen-air formation and performance of hydrogen direct injection internal combustion engine". *International Journal of Hydrogen Energy.* 4447. 26000–26011. 2019. DOI: 10.1016/j.ijhydene.2019.08.055.
- [60] A. Hamzehloo and P. Aleiferis. "Computational Study of Hydrogen Direct Injection for Internal Combustion Engines". In: 2013, 2013–01–2524. DOI: 10.4271/2013-01-2524.
- [61] R. Hari Ganesh et al. "Hydrogen fueled spark ignition engine with electronically controlled manifold injection: An experimental study". Renewable Energy. 336. 1324–1333. 2008. DOI: 10.1016/j.renene.2007.07.003.

- [62] D. Nguyen et al. "Effect of supercharger system on power enhancement of hydrogen-fueled spark-ignition engine under low-load condition". *International Journal of Hydrogen Energy.* 469. 6928–6936. 2021. DOI: 10.1016/j.ijhydene.2020.11.144.
- [63] G. Prabhukumar, B. Nagalingam, and K. Gopalakrishnan. "Theoretical studies of a spark-ignited supercharged hydrogen engine". *International Journal of Hydrogen Energy*. 106. 389–397. 1985. DOI: 10.1016/0360-3199(85)90065-5.
- [64] R. K. Maurya and M. R. Saxena. "Characterization of ringing intensity in a hydrogen-fueled HCCI engine". *International Journal of Hydrogen Energy*. 4319. 9423–9437. 2018. DOI: 10.1016/j.ijhydene.2018.03.194.
- [65] B. D. Gowda and T. Echekki. "Complex injection strategies for hydrogen-fueled HCCI engines". Fuel. 97. 418–427. 2012. DOI: 10.1016/j.fuel.2012. 01.060.
- [66] M. Mohamed Ibrahim and A. Ramesh. "Investigations on the effects of intake temperature and charge dilution in a hydrogen fueled HCCI engine". International Journal of Hydrogen Energy. 3926. 14097–14108. 2014. DOI: 10.1016/j.ijhydene.2014.07.019.
- [67] V. M. Domínguez et al. "Hydrogen or hydrogen-derived methanol for dual-fuel compression-ignition combustion: An engine perspective". Fuel. 333. 126301.
 2023. DOI: 10.1016/j.fuel.2022.126301.
- [68] C. Gong et al. "Experimental investigation of equivalence ratio effects on combustion and emissions characteristics of an H2/methanol dual-injection engine under different spark timings". Fuel. 262. 116463. 2020. DOI: 10.1016/j.fuel.2019.116463.
- [69] B. Ma et al. "Multiple combustion modes existing in the engine operating in diesel methanol dual fuel". Energy. 234. 121285. 2021. DOI: 10.1016/j. energy.2021.121285.

- [70] N. N. Mustafi, R. R. Raine, and S. Verhelst. "Combustion and emissions characteristics of a dual fuel engine operated on alternative gaseous fuels". Fuel. 109. 669–678. 2013. DOI: 10.1016/j.fuel.2013.03.007.
- [71] J. Wang et al. "Effect of partially premixed and hydrogen addition on natural gas direct-injection lean combustion". *International Journal of Hydrogen Energy.* 3422. 9239–9247. 2009. DOI: 10.1016/j.ijhydene.2009.09.018.
- [72] H. L. Yip et al. "A Review of Hydrogen Direct Injection for Internal Combustion Engines: Towards Carbon-Free Combustion". Applied Sciences. 922.
 4842. 2019. DOI: 10.3390/app9224842.
- [73] H. Xu et al. "Experimental and numerical investigation on effects of preignition positions on knock intensity of hydrogen fuel". *International Journal of Hydrogen Energy*. 4652. 26631–26645. 2021. DOI: 10.1016/j.ijhydene. 2021.05.154.
- [74] N. S. Matthias, T. Wallner, and R. Scarcelli. "A Hydrogen Direct Injection Engine Concept that Exceeds U.S. DOE Light-Duty Efficiency Targets". SAE International Journal of Engines. 53. 838–849. 2012. DOI: 10.4271/2012-01-0653.
- [75] M. Oikawa et al. "Effect of supercharging on improving thermal efficiency and modifying combustion characteristics in lean-burn direct-injection near-zero-emission hydrogen engines". International Journal of Hydrogen Energy. 472. 1319–1327. 2022. DOI: 10.1016/j.ijhydene.2021.10.061.
- [76] A. Wimmer et al. "H2-Direct Injection A Highly Promising Combustion Concept". In: 2005, 2005–01–0108. DOI: 10.4271/2005-01-0108.
- [77] T. Shudo et al. "Reduction of Cooling Loss in Hydrogen Combustion by Direct Injection Stratified Charge". In: 2003, 2003–01–3094. DOI: 10.4271/ 2003-01-3094.
- [78] W. Vera-Tudela et al. "Study on the ignitability of a high-pressure directinjected methane jet using a diesel pilot, a glow-plug, and a pre-chamber".

- International Journal of Engine Research. 242. 360–372. 2023. DOI: 10.1177/14680874211048144.
- [79] S. Szwaja and K. Grab-Rogalinski. "Hydrogen combustion in a compression ignition diesel engine". *International Journal of Hydrogen Energy*. 3410. 4413–4421. 2009. DOI: 10.1016/j.ijhydene.2009.03.020.
- [80] R. Zhang et al. "Optical study on the effects of the hydrogen injection timing on lean combustion characteristics using a natural gas/hydrogen dual-fuel injected spark-ignition engine". *International Journal of Hydrogen Energy*. 4639. 20777–20789. 2021. DOI: 10.1016/j.ijhydene.2021.03.171.
- [81] A. Boretti. "Hydrogen internal combustion engines to 2030". *International Journal of Hydrogen Energy*. 4543. 23692-23703. 2020. DOI: 10.1016/j.ijhydene.2020.06.022.
- [82] J. Mortimer et al. "Extending the knock limits of hydrogen DI ICE using water injection". Fuel. 335. 126652. 2023. DOI: 10.1016/j.fuel.2022. 126652.
- [83] J. K. Pandey and K. Gn. "Studying the effects of manifold pressure boosting and EGR on combustion and NO $_{\rm x}$ emission of hydrogen-fueled SI engine". International Journal of Engine Research. 248. 3492–3504. 2023. DOI: 10. 1177/14680874231153209.
- [84] K. Ravi, J. Pradeep Bhasker, and E. Porpatham. "Effect of compression ratio and hydrogen addition on part throttle performance of a LPG fuelled lean burn spark ignition engine". Fuel. 205. 71–79. 2017. DOI: 10.1016/j.fuel. 2017.05.062.
- [85] M. Naruke et al. "Effects of hydrogen addition on engine performance in a spark ignition engine with a high compression ratio under lean burn conditions". International Journal of Hydrogen Energy. 4429. 15565–15574. 2019.
 DOI: 10.1016/j.ijhydene.2019.04.120.

- [86] G. Lim et al. "Effects of compression ratio on performance and emission characteristics of heavy-duty SI engine fuelled with HCNG". International Journal of Hydrogen Energy. 3811. 4831–4838. 2013. DOI: 10.1016/j.ijhydene. 2013.01.188.
- [87] P. Boettcher et al. "The effect of heating rates on low temperature hexane air combustion". Fuel. 96. 392–403. 2012. DOI: 10.1016/j.fuel.2011.12.044.
- [88] R. Schefer. "Hydrogen enrichment for improved lean flame stability". *International Journal of Hydrogen Energy*. 2810. 1131–1141. 2003. DOI: 10.1016/S0360-3199(02)00199-4.
- [89] F. Ma et al. "A Quasi-Dimensional Combustion Model for SI Engines Fuelled by Hydrogen Enriched Compressed Natural Gas". In: 2008, 2008–01–1633. DOI: 10.4271/2008-01-1633.
- [90] R. J. Natkin et al. "Hydrogen IC Engine Boosting Performance and NOx Study". In: 2003, 2003–01–0631. DOI: 10.4271/2003-01-0631.
- [91] S. Verhelst and T. Wallner. "Hydrogen-fueled internal combustion engines". Progress in Energy and Combustion Science. 356, 490-527, 2009. DOI: 10. 1016/j.pecs.2009.08.001.
- [92] H. Gürbüz and İ. H. Akçay. "Evaluating the effects of boosting intake-air pressure on the performance and environmental-economic indicators in a hydrogen-fueled SI engine". *International Journal of Hydrogen Energy.* 4656. 28801–28810. 2021. DOI: 10.1016/j.ijhydene.2021.06.099.
- [93] J. Lee et al. "High power performance with zero NOx emission in a hydrogen-fueled spark ignition engine by valve timing and lean boosting". Fuel. 128. 381–389. 2014. DOI: 10.1016/j.fuel.2014.03.010.
- [94] C. R. Leite, R. Oung, and P. Brequigny. "Combustion Cycle-To-Cycle Variation Analysis in Diesel Baseline Hydrogen-Fueled Spark-Ignition Engines". SAE Technical Paper. 2023. DOI: 10.4271/2023-01-0290.

- [95] J. P. Bhasker and E. Porpatham. "Effects of compression ratio and hydrogen addition on lean combustion characteristics and emission formation in a Compressed Natural Gas fuelled spark ignition engine". Fuel. 208. 260–270. 2017. DOI: 10.1016/j.fuel.2017.07.024.
- [96] Q.-h. Luo et al. "Effect of equivalence ratios on the power, combustion stability and NOx controlling strategy for the turbocharged hydrogen engine at low engine speeds". *International Journal of Hydrogen Energy*. 4431. 17095—17102. 2019. DOI: 10.1016/j.ijhydene.2019.03.245.
- [97] S. Verhelst et al. "Increasing the power output of hydrogen internal combustion engines by means of supercharging and exhaust gas recirculation". International Journal of Hydrogen Energy. 3410. 4406–4412. 2009. DOI: 10. 1016/j.ijhydene.2009.03.037.
- [98] T. Wallner and H. Lohse-Busch. "Performance, Efficiency, and Emissions Evaluation of a Supercharged, Hydrogen-Powered, 4-Cylinder Engine". In: 2007, 2007–01–0016. DOI: 10.4271/2007-01-0016.
- [99] A. Rao, Y. Liu, and F. Ma. "Study of NOx emission for hydrogen enriched compressed natural along with exhaust gas recirculation in spark ignition engine by Zeldovich' mechanism, support vector machine and regression correlation". Fuel. 318. 123577. 2022. DOI: 10.1016/j.fuel.2022.123577.
- [100] J. Duan et al. "Study on the NOx emissions mechanism of an HICE under high load". International Journal of Hydrogen Energy. 4234. 22027–22035. 2017. DOI: 10.1016/j.ijhydene.2017.07.048.
- [101] D. Lou et al. "Study on the Effects of EGR and Spark Timing on the Combustion, Performance, and Emissions of a Stoichiometric Natural Gas Engine".

 ACS Omega. 541. 26763–26775. 2020. DOI: 10.1021/acsomega.0c03859.
- [102] K. Nakata et al. "Engine Technologies for Achieving 45% Thermal Efficiency of S.I. Engine". SAE International Journal of Engines. 91. 179–192. 2015. DOI: 10.4271/2015-01-1896.

- [103] V. De Bellis et al. "Experimental and 0D Numerical Investigation of Ultra-Lean Combustion Concept to Improve the Efficiency of SI Engine". In: 2021, 2021–01–0384. DOI: 10.4271/2021-01-0384.
- [104] J. A. Goldwitz and J. B. Heywood. "Combustion Optimization in a Hydrogen-Enhanced Lean-Burn SI Engine". In: 2005, 2005–01–0251. DOI: 10.4271/ 2005-01-0251.
- [105] Y.-F. Liu et al. "Performance and emission characteristics of a hydrogenenriched compressed-natural-gas direct-injection spark ignition engine diluted with exhaust gas recirculation". Proceedings of the Institution of Mechanical Engineers, Part D: Journal of Automobile Engineering. 2261. 123–132. 2012. DOI: 10.1177/0954407011413047.
- [106] P. A. Dennis et al. "Performance of a Port Fuel Injected, Spark Ignition Engine Optimised for Hydrogen Fuel". In: 2012, 2012–01–0654. DOI: 10. 4271/2012-01-0654.
- [107] S. Oh et al. "Investigation on the operable range and idle condition of hydrogen-fueled spark ignition engine for unmanned aerial vehicle (UAV)". *Energy*. 237. 121645. 2021. DOI: 10.1016/j.energy.2021.121645.
- [108] L. Guo, H. Lu, and J. Li. "A hydrogen injection system with solenoid valves for a four-cylinder hydrogen-fuelled enginefn2fn2This paper is based on L.S. Guos Ph.D. dissertation in the Department of Energy Engineering, Zhejiang University, Hangzhou, 310027, P.R. China." *International Journal of Hydrogen Energy*. 244. 377–382. 1999. DOI: 10.1016/S0360-3199(98)00035-4.
- [109] J. Gao et al. "Review of the backfire occurrences and control strategies for port hydrogen injection internal combustion engines". Fuel. 307. 121553. 2022. DOI: 10.1016/j.fuel.2021.121553.
- [110] K.-J. Lee, T. C. Huynh, and J.-T. Lee. "A study on realization of high performance without backfire in a hydrogen-fueled engine with external mixture".

 International Journal of Hydrogen Energy. 3523. 13078–13087. 2010. DOI: 10.1016/j.ijhydene.2010.04.078.

- [111] V. Dhyani and K. Subramanian. "Development of online control system for elimination of backfire in a hydrogen fuelled spark ignition engine". *International Journal of Hydrogen Energy*. 4627. 14757–14763. 2021. DOI: 10.1016/j.ijhydene.2020.08.148.
- [112] Y. Li et al. "Influence of the equivalence ratio on the knock and performance of a hydrogen direct injection internal combustion engine under different compression ratios". *International Journal of Hydrogen Energy*. 4621. 11982–11993. 2021. DOI: 10.1016/j.ijhydene.2021.01.031.
- [113] J. B. Heywood. *Internal combustion engine fundamentals*. New York: Mcgraw-Hill Education, 2018.
- [114] J. Livengood and P. Wu. "Correlation of autoignition phenomena in internal combustion engines and rapid compression machines". *Symposium (International) on Combustion*. 51. 347–356. 1955. DOI: 10.1016/S0082-0784(55) 80047-1.
- [115] V. Dhyani and K. Subramanian. "Fundamental characterization of backfire in a hydrogen fuelled spark ignition engine using CFD and experiments". International Journal of Hydrogen Energy. 4460. 32254–32270. 2019. DOI: 10.1016/j.ijhydene.2019.10.077.
- [116] T. Shudo. "Thermal efficiency analysis in a hydrogen premixed combustion engine". *JSAE Review*. 212. 177–182. 2000. DOI: 10.1016/S0389-4304(99) 00091-0.
- [117] Y. Chen and R. Raine. "Engine Knock in an SI Engine with Hydrogen Supplementation under Stoichiometric and Lean Conditions". SAE International Journal of Engines. 72. 595–605. 2014. DOI: 10.4271/2014-01-1220.
- [118] S. Zhu et al. "A review of water injection applied on the internal combustion engine". Energy Conversion and Management. 184. 139–158. 2019. DOI: 10. 1016/j.enconman.2019.01.042.

- [119] A. Boretti. "Water injection in directly injected turbocharged spark ignition engines". *Applied Thermal Engineering*. 521. 62-68. 2013. DOI: 10.1016/j.applthermaleng.2012.11.016.
- [120] Y. Lyu et al. "Effects of steam dilution on laminar flame speeds of H2/air/H2O mixtures at atmospheric and elevated pressures". International Journal of Hydrogen Energy. 4315. 7538–7549. 2018. DOI: 10.1016/j.ijhydene.2018.02.065.
- [121] Y. Zhuang et al. "Investigation of water spray evolution process of port water injection and its effect on engine performance". Fuel. 282. 118839. 2020. DOI: 10.1016/j.fuel.2020.118839.
- [122] V. Ayhan. "Investigation of electronic controlled direct water injection for performance and emissions of a diesel engine running on sunflower oil methyl ester". Fuel. 275. 117992. 2020. DOI: 10.1016/j.fuel.2020.117992.
- [123] S. Welscher et al. "A comprehensive evaluation of water injection in the diesel engine". *International Journal of Engine Research*. 241. 99–112. 2023. DOI: 10.1177/14680874211044297.
- [124] V. Subramanian, J. Mallikarjuna, and A. Ramesh. "Effect of water injection and spark timing on the nitric oxide emission and combustion parameters of a hydrogen fuelled spark ignition engine". *International Journal of Hydrogen Energy.* 329. 1159–1173. 2007. DOI: 10.1016/j.ijhydene.2006.07.022.
- [125] M. Younkins, M. S. Wooldridge, and B. A. Boyer. "Port Injection of Water into a DI Hydrogen Engine". In: 2015, 2015–01–0861. DOI: 10.4271/2015– 01-0861.
- [126] P. Xu et al. "Effects of direct water injection on engine performance in a hydrogen (H2)-fueled engine at varied amounts of injected water and water injection timing". International Journal of Hydrogen Energy. 4524. 13523—13534. 2020. DOI: 10.1016/j.ijhydene.2020.03.011.

- [127] J. Wang et al. "Numerical investigation of water injection quantity and water injection timing on the thermodynamics, combustion and emissions in a hydrogen enriched lean-burn natural gas SI engine". *International Journal of Hydrogen Energy*. 4535. 17935–17952. 2020. DOI: 10.1016/j.ijhydene. 2020.04.146.
- [128] R. Novella et al. "Numerical assessment of water injection for improved thermal efficiency and emissions control in a medium-duty hydrogen engine for transportation applications". Fuel. 359. 130455. 2024. DOI: 10.1016/j.fuel. 2023.130455.
- [129] M. N. Taxon, S. R. Brueckner, and S. V. Bohac. "Effect of Fuel Humidity on the Performance of a Single-Cylinder Research Engine Operating on Hydrogen". In: 2002, 2002–01–2685. DOI: 10.4271/2002-01-2685.
- [130] F. Payri et al. "A complete 0D thermodynamic predictive model for direct injection diesel engines". Applied Energy. 8812. 4632-4641. 2011. DOI: 10. 1016/j.apenergy.2011.06.005.
- [131] R. K. Maurya and N. Akhil. "Comparative study of the simulation ability of various recent hydrogen combustion mechanisms in HCCI engines using stochastic reactor model". *International Journal of Hydrogen Energy.* 4216. 11911–11925. 2017. DOI: 10.1016/j.ijhydene.2017.02.155.
- [132] J. Kim et al. "Assessment of Turbulent Combustion Models for Simulating Prechamber Ignition in a Natural Gas Engine". *Journal of Engineering for Gas Turbines and Power.* 1439. 091004. 2021. DOI: 10.1115/1.4050482.
- [133] U. Gerke and K. Boulouchos. "Three-dimensional computational fluid dynamics simulation of hydrogen engines using a turbulent flame speed closure combustion model". *International Journal of Engine Research*. 135. 464–481. 2012. DOI: 10.1177/1468087412438796.
- [134] S. Posch et al. "Turbulent combustion modeling for internal combustion engine CFD: A review". *Progress in Energy and Combustion Science*. 106. 101200. 2025. DOI: 10.1016/j.pecs.2024.101200.

- [135] V. Knop et al. "Modelling of combustion and nitrogen oxide formation in hydrogen-fuelled internal combustion engines within a 3D CFD code". *International Journal of Hydrogen Energy*. 3319. 5083–5097. 2008. DOI: 10.1016/j.ijhydene.2008.06.027.
- [136] R. Pyszczek et al. "Numerical Modeling of Spark Ignition in Internal Combustion Engines". Journal of Energy Resources Technology. 1422. 2020. DOI: 10.1115/1.4044222.
- [137] S. Sfriso et al. "Proposal and Validation of 3D-CFD Framework for Ultra-Lean Hydrogen Combustion in ICEs". In: *SAE Technical Paper Series*. Detroit, Michigan, United States: SAE International, 2024. DOI: 10.4271/2024-01-2685.
- [138] M. Pasternak et al. "Aspects of 0D and 3D Modeling of Soot Formation for Diesel Engines". Combustion Science and Technology. 18610-11. 1517–1535. 2014. DOI: 10.1080/00102202.2014.935213.
- [139] H. Barths, C. Felsch, and N. Peters. "Mixing models for the two-way-coupling of CFD codes and zero-dimensional multi-zone codes to model HCCI combustion". *Combustion and Flame*. 1561. 130–139. 2009. DOI: 10.1016/j.combustflame.2008.09.001.
- [140] G. Abbaszadehmosayebi and L. Ganippa. "Characterising Wiebe Equation for Heat Release Analysis based on Combustion Burn Factor (Ci)". Fuel. 119. 301–307. 2014. DOI: 10.1016/j.fuel.2013.11.006.
- [141] A. M. Shivapuji and S. Dasappa. "Experiments and zero D modeling studies using specific Wiebe coefficients for producer gas as fuel in spark-ignited engines". Proceedings of the Institution of Mechanical Engineers, Part C: Journal of Mechanical Engineering Science. 2273. 504–519. 2013. DOI: 10.1177/0954406212463846.
- [142] D. Hu et al. "Construction and verification of dual-fuel engine combustion model". *Journal of the Energy Institute*. 112. 101486. 2024. DOI: 10.1016/j.joei.2023.101486.

- [143] R. Yang, T. Xie, and Z. Liu. "The Application of Machine Learning Methods to Predict the Power Output of Internal Combustion Engines". *Energies*. 159. 3242. 2022. DOI: 10.3390/en15093242.
- [144] J. Zhu et al. "Development and Validation of a Modeling and Calibration Method for Diesel-Like Multistage Combustion Based On a Modified Multi-Wiebe Function". ACS Omega. 714. 11756-11769. 2022. DOI: 10.1021/ acsomega.1c06858.
- [145] J. J. Fagelson, W. J. McLEAN, and P. C. T. De Boer. "Performance and NO $_{\rm x}$ Emissions of Spark Ignited Combustion Engines Using Alternative Fuels—Quasi One-Dimensional Modeling I. Hydrogen Fueled Engines". Combustion Science and Technology. 181-2. 47–57. 1978. DOI: 10.1080/00102207808946838.
- [146] M. A. Al-Baghdadi and H. A. Al-Janabi. "A prediction study of a spark ignition supercharged hydrogen engine". Energy Conversion and Management. 4420. 3143–3150. 2003. DOI: 10.1016/S0196-8904(03)00127-4.
- [147] B. Salvi and K. Subramanian. "A novel approach for experimental study and numerical modeling of combustion characteristics of a hydrogen fuelled spark ignition engine". Sustainable Energy Technologies and Assessments. 51. 101972. 2022. DOI: 10.1016/j.seta.2022.101972.
- [148] G. Derrico, A. Onorati, and S. Ellgas. "1D thermo-fluid dynamic modelling of an S.I. single-cylinder H2 engine with cryogenic port injection". *International Journal of Hydrogen Energy*. 3320. 5829–5841. 2008. DOI: 10.1016/j.ijhydene.2008.05.096.
- [149] U. Gerke et al. "Derivation of burning velocities of premixed hydrogen/air flames at engine-relevant conditions using a single-cylinder compression machine with optical access". *International Journal of Hydrogen Energy*. 356. 2566–2577. 2010. DOI: 10.1016/j.ijhydene.2009.12.064.
- [150] S. Ravi and E. L. Petersen. "Laminar flame speed correlations for pure-hydrogen and high-hydrogen content syngas blends with various diluents". *International Journal of Hydrogen Energy.* 3724. 19177–19189. 2012. DOI: 10.1016/j.ijhydene.2012.09.086.

- [151] S. Verhelst and R. Sierens. "A quasi-dimensional model for the power cycle of a hydrogen-fuelled ICE". *International Journal of Hydrogen Energy*. 3215. 3545–3554. 2007. DOI: 10.1016/j.ijhydene.2007.02.011.
- [152] S. Verhelst et al. "A correlation for the laminar burning velocity for use in hydrogen spark ignition engine simulation". *International Journal of Hydrogen Energy.* 361. 957–974. 2011. DOI: 10.1016/j.ijhydene.2010.10.020.
- [153] H. Safari, S. Jazayeri, and R. Ebrahimi. "Potentials of NOX emission reduction methods in SI hydrogen engines: Simulation study". *International Journal of Hydrogen Energy*. 342. 1015–1025. 2009. DOI: 10.1016/j.ijhydene. 2008.10.029.
- [154] S. Eckart et al. "Application and comparison of multiple machine learning techniques for the calculation of laminar burning velocity for hydrogenmethane mixtures". Thermal Science and Engineering Progress. 32. 101306. 2022. DOI: 10.1016/j.tsep.2022.101306.
- [155] P. Clavin. "Dynamic behavior of premixed flame fronts in laminar and turbulent flows". *Progress in Energy and Combustion Science*. 111. 1–59. 1985. DOI: 10.1016/0360-1285(85)90012-7.
- [156] A. Lipatnikov and J. Chomiak. "Molecular transport effects on turbulent flame propagation and structure". *Progress in Energy and Combustion Science*. 311. 1–73. 2005. DOI: 10.1016/j.pecs.2004.07.001.
- [157] D. Bradley et al. "Laminar burning velocities of lean hydrogen-air mixtures at pressures up to 1.0 MPa". Combustion and Flame. 1491-2. 162-172. 2007. DOI: 10.1016/j.combustflame.2006.12.002.
- [158] X. Cai et al. "Turbulent burning velocity and its related statistics of ammoniahydrogen-air jet flames at high Karlovitz number: Effect of differential diffusion". *Proceedings of the Combustion Institute*. 394. 4215–4226. 2023. DOI: 10.1016/j.proci.2022.07.016.

- [159] A. N. Lipatnikov et al. "Transition from turbulence-dominated to instability-dominated combustion regime in lean hydrogen-air flames". Combustion and Flame. 259. 113170. 2024. DOI: 10.1016/j.combustflame.2023.113170.
- [160] P. Venkateswaran et al. "Measurements and analysis of turbulent consumption speeds of H2/CO mixtures". Combustion and Flame. 1588. 1602–1614. 2011. DOI: 10.1016/j.combustflame.2010.12.030.
- [161] L. Berger, A. Attili, and H. Pitsch. "Intrinsic instabilities in premixed hydrogen flames: Parametric variation of pressure, equivalence ratio, and temperature. Part 1 Dispersion relations in the linear regime". Combustion and Flame. 240. 111935. 2022. DOI: 10.1016/j.combustflame.2021.111935.
- [162] M. Metghalchi and J. Keck. "Laminar burning velocity of propane-air mixtures at high temperature and pressure". Combustion and Flame. 38. 143– 154. 1980. DOI: 10.1016/0010-2180(80)90046-2.
- [163] A. A. Konnov et al. "A comprehensive review of measurements and data analysis of laminar burning velocities for various fuel+air mixtures". *Progress in Energy and Combustion Science*. 68. 197–267. 2018. DOI: 10.1016/j.pecs.2018.05.003.
- [164] R. J. Varghese et al. "Measurement of laminar burning velocities of methaneair mixtures simultaneously at elevated pressures and elevated temperatures". Fuel. 257. 116120. 2019. DOI: 10.1016/j.fuel.2019.116120.
- [165] A. Harbi and A. Farooq. "Monte-Carlo based laminar flame speed correlation for gasoline". *Combustion and Flame*. 222. 61–69. 2020. DOI: 10.1016/j.combustflame.2020.08.023.
- [166] M. Del Pecchia et al. "Development of Chemistry-Based Laminar Flame Speed Correlation for Part-Load SI Conditions and Validation in a GDI Research Engine". SAE International Journal of Engines. 116, 715–741, 2018. DOI: 10.4271/2018-01-0174.

- [167] A. D'Adamo et al. "Chemistry-Based Laminar Flame Speed Correlations for a Wide Range of Engine Conditions for Iso-Octane, n-Heptane, Toluene and Gasoline Surrogate Fuels". In: 2017, 2017–01–2190. DOI: 10.4271/2017-01-2190.
- [168] B. C. Duva and E. Toulson. "Unstretched unburned flame speed and burned gas Markstein length of diluted hydrogen/air mixtures". *International Journal of Hydrogen Energy*. 4714. 9030–9044. 2022. DOI: 10.1016/j.ijhydene. 2021.12.217.
- [169] S. Meng et al. "The effects of water addition on the laminar flame speeds of CO/H2/O2/H2O mixtures". *International Journal of Hydrogen Energy*. 4125. 10976–10985. 2016. DOI: 10.1016/j.ijhydene.2016.04.251.
- [170] G. Woschni. "A Universally Applicable Equation for the Instantaneous Heat Transfer Coefficient in the Internal Combustion Engine". In: 1967, 670931.
 DOI: 10.4271/670931.
- [171] W. J. D. Annand. "A New Computation Model of Combustion in the Spark-Ignition Engine". Proceedings of the Institution of Mechanical Engineers. 1851. 119–126. 1970. DOI: 10.1243/PIME_PROC_1970_185_019_02.
- [172] G. F. Hohenberg. "Advanced Approaches for Heat Transfer Calculations". In: 1979, 790825. DOI: 10.4271/790825.
- [173] T. Tabatabaie, M. A. Ehteram, and V. Hosseini. "Investigating the effect of the heat transfer correlation on the predictability of a multi-zone combustion model of a hydrogen-fuelled spark ignition engine". Proceedings of the Institution of Mechanical Engineers, Part D: Journal of Automobile Engineering. 2301. 70–81. 2016. DOI: 10.1177/0954407015578047.
- [174] J. Demuynck et al. "On the applicability of empirical heat transfer models for hydrogen combustion engines". *International Journal of Hydrogen Energy*. 361. 975–984. 2011. DOI: 10.1016/j.ijhydene.2010.10.059.

- [175] J. Michl et al. "Derivation and validation of a heat transfer model in a hydrogen combustion engine". Applied Thermal Engineering. 98. 502–512. 2016.

 DOI: 10.1016/j.applthermaleng.2015.12.062.
- [176] T. Shudo. "Applicability of heat transfer equations to hydrogen combustion". *JSAE Review.* 233. 303–308. 2002. DOI: 10.1016/S0389-4304(02)00193-5.
- [177] J. Krishnanunni, D. Bhatia, and L. M. Das. "Experimental and modelling investigations on the performance and emission characteristics of a single cylinder hydrogen engine". *International Journal of Hydrogen Energy.* 4249. 29574–29584. 2017. DOI: 10.1016/j.ijhydene.2017.10.018.
- [178] J. Caton. "On the destruction of availability (exergy) due to combustion processes with specific application to internal-combustion engines". *Energy*. 2511. 1097–1117. 2000. DOI: 10.1016/S0360-5442(00)00034-7.
- [179] R. D. Reitz et al. "IJER editorial: The future of the internal combustion engine". *International Journal of Engine Research*. 211. 3–10. 2020. DOI: 10. 1177/1468087419877990.
- [180] C. Rakopoulos and E. Giakoumis. "Second-law analyses applied to internal combustion engines operation". *Progress in Energy and Combustion Science*. 321. 2–47. 2006. DOI: 10.1016/j.pecs.2005.10.001.
- [181] R. J. Primus et al. "An appraisal of advanced engine concepts using second law analysis techniques". In: 1984, 841287. DOI: 10.4271/841287.
- [182] C. Rakopoulos. "Evaluation of a spark ignition engine cycle using first and second law analysis techniques". Energy Conversion and Management. 3412. 1299–1314. 1993. DOI: 10.1016/0196-8904(93)90126-U.
- [183] J. A. Caton. "A Review of Investigations Using the Second Law of Thermodynamics to Study Internal-Combustion Engines". In: 2000, 2000–01–1081.
 DOI: 10.4271/2000-01-1081.
- [184] S. Mamalis et al. "A modeling framework for second law analysis of low-temperature combustion engines". *International Journal of Engine Research*. 156, 641–653, 2014, DOI: 10.1177/1468087413512312.

- [185] S. Saxena et al. "Understanding optimal engine operating strategies for gasoline-fueled HCCI engines using crank-angle resolved exergy analysis". *Applied Energy*. 114. 155–163. 2014. DOI: 10.1016/j.apenergy.2013.09.056.
- [186] L. Wang et al. "Effect of excess air/fuel ratio and methanol addition on the performance, emissions, and combustion characteristics of a natural gas/methanol dual-fuel engine". Fuel. 255. 115799. 2019. DOI: 10.1016/j.fuel.2019. 115799.
- [187] F. Meisami and H. Ajam. "Energy, exergy and economic analysis of a Diesel engine fueled with castor oil biodiesel". *International Journal of Engine Research*. 165. 691–702. 2015. DOI: 10.1177/1468087415576609.
- [188] M. Nabi and M. Rasul. "Influence of second generation biodiesel on engine performance, emissions, energy and exergy parameters". *Energy Conversion and Management*. 169. 326–333. 2018. DOI: 10.1016/j.enconman.2018.05.066.
- [189] K. D. Edwards, R. Wagner, and T. Briggs. "Investigating Potential Light-duty Efficiency Improvements through Simulation of Turbo-compounding and Waste-heat Recovery Systems". In: 2010, 2010–01–2209. DOI: 10.4271/2010-01-2209.
- [190] J. Galindo et al. "Advanced exergy analysis for a bottoming organic rankine cycle coupled to an internal combustion engine". *Energy Conversion and Management.* 126. 217–227. 2016. DOI: 10.1016/j.enconman.2016.07.080.
- [191] A. Ganguly, S. Sengupta, and S. Pramanik. "Waste heat recovery using Tesla turbines in Rankine cycle power plants: Thermofluid dynamic characterization, performance assessment and exergy analysis". Applied Thermal Engineering. 207. 118141. 2022. DOI: 10.1016/j.applthermaleng.2022.118141.
- [192] K. Nishida, T. Takagi, and S. Kinoshita. "Analysis of entropy generation and exergy loss during combustion". Proceedings of the Combustion Institute. 291. 869–874. 2002. DOI: 10.1016/S1540-7489(02)80111-0.

- [193] H. Sun et al. "Analysis of exergy loss of gasoline surrogate combustion process based on detailed chemical kinetics". *Applied Energy*. 152. 11–19. 2015. DOI: 10.1016/j.apenergy.2015.04.087.
- [194] A. A. Knizley et al. "Fuel and diluent effects on entropy generation in a constant internal energy-volume (uv) combustion process". *Energy*. 431. 315–328. 2012. DOI: 10.1016/j.energy.2012.04.024.
- [195] M. M. Namar and O. Jahanian. "Energy and exergy analysis of a hydrogen-fueled HCCI engine". Journal of Thermal Analysis and Calorimetry. 1371. 205–215. 2019. DOI: 10.1007/s10973-018-7910-7.
- [196] S. Lee et al. "Energy and exergy analyses of hydrogen-fueled spark ignition engine with various air excess ratios and ignition timings". Fuel. 349, 128588.
 2023. DOI: 10.1016/j.fuel.2023.128588.
- [197] J. S. Rawat et al. "Investigation of performance, emission and exergy parameters of a compression ignition engine fuelled with ethanol-jatropha biodiesel blend under varying hydrogen strategies". International Journal of Hydrogen Energy. 4895. 37415–37426. 2023. DOI: 10.1016/j.ijhydene.2023.06.128.
- [198] B. G. Şanli and E. Uludamar. "Energy and exergy analysis of a diesel engine fuelled with diesel and biodiesel fuels at various engine speeds". Energy Sources, Part A: Recovery, Utilization, and Environmental Effects. 4211. 1299–1313. 2020. DOI: 10.1080/15567036.2019.1635229.
- [199] M. R. Saxena and R. K. Maurya. "Exergy analysis and investigation on effect of inlet valve closing temperature and hydrogen enrichment in syngas composition in an HCCI engine". *International Journal of Hydrogen Energy*. 488. 3269–3286. 2023. DOI: 10.1016/j.ijhydene.2022.10.123.
- [200] X. Yu et al. "Energy and exergy analysis of a combined injection engine using gasoline port injection coupled with gasoline or hydrogen direct injection under lean-burn conditions". International Journal of Hydrogen Energy. 4611. 8253–8268. 2021. DOI: 10.1016/j.ijhydene.2020.12.022.

- [201] J. Liu and C. E. Dumitrescu. "Single and double Wiebe function combustion model for a heavy-duty diesel engine retrofitted to natural-gas spark-ignition". Applied Energy. 248. 95–103. 2019. DOI: 10.1016/j.apenergy.2019.04.098.
- [202] F. Lindström et al. "An Empirical SI Combustion Model Using Laminar Burning Velocity Correlations". In: 2005, 2005–01–2106. DOI: 10.4271/2005– 01-2106.
- [203] Y. Men, I. Haskara, and G. Zhu. "Multi-zone reaction-based modeling of combustion for multiple-injection diesel engines". *International Journal of Engine Research*. 216. 1012–1025. 2020. DOI: 10.1177/1468087418788488.
- [204] J. Liu, C. Ulishney, and C. E. Dumitrescu. "Application of Random Forest Machine Learning Models to Forecast Combustion Profile Parameters of a Natural Gas Spark Ignition Engine". In: *Volume 6: Design, Systems, and Complexity*. Virtual, Online: American Society of Mechanical Engineers, 2020, V006T06A003. DOI: 10.1115/IMECE2020-23973.
- [205] C. Rakopoulos, C. Michos, and E. Giakoumis. "Availability analysis of a syngas fueled spark ignition engine using a multi-zone combustion model". Energy. 339. 1378–1398. 2008. DOI: 10.1016/j.energy.2008.05.007.
- [206] A. E. Catania et al. "A Refined Two-Zone Heat Release Model for Combustion Analysis in SI Engines." JSME International Journal Series B. 461. 75–85. 2003. DOI: 10.1299/jsmeb.46.75.
- [207] X. Zhang et al. "Study on flame-vortex interaction in a spark ignition engine fueled with methane/carbon dioxide gases". Journal of the Energy Institute. 911. 133-144. 2018. DOI: 10.1016/j.joei.2016.09.005.
- [208] N. C. Blizard and J. C. Keck. "Experimental and Theoretical Investigation of Turbulent Burning Model for Internal Combustion Engines". In: 1974, 740191. DOI: 10.4271/740191.
- [209] S. Goto and J. C. Vassilicos. "Unsteady turbulence cascades". *Physical Review E.* 945. 053108. 2016. DOI: 10.1103/PhysRevE.94.053108.

- [210] R. M. McMullen, J. R. Torczynski, and M. A. Gallis. "Thermal-fluctuation effects on small-scale statistics in turbulent gas flow". *Physics of Fluids*. 351. 011705. 2023. DOI: 10.1063/5.0134870.
- [211] D. W. Carter and F. Coletti. "Scale-to-scale anisotropy in homogeneous turbulence". *Journal of Fluid Mechanics*. 827. 250–284. 2017. DOI: 10.1017/jfm.2017.496.
- [212] G. Decan et al. "Evaluation of wall heat flux calculation methods for CFD simulations of an internal combustion engine under both motored and HCCI operation". *Applied Energy*. 232. 451–461. 2018. DOI: 10.1016/j.apenergy. 2018.09.214.
- [213] A. Irimescu et al. "Development of a semi-empirical convective heat transfer correlation based on thermodynamic and optical measurements in a spark ignition engine". *Applied Energy*. 157. 777–788. 2015. DOI: 10.1016/j.apenergy.2015.02.050.
- [214] A. Sobiesiak and S. Zhang. "The First and Second Law Analysis of Spark Ignition Engine Fuelled with Compressed Natural Gas". In: 2003, 2003–01– 3091. DOI: 10.4271/2003-01-3091.
- [215] K. Richards, P. Senecal, and E. Pomraning. Converge. 2023.
- [216] N. Villenave et al. "Experimental measurements of ultra-lean hydrogen ignition delays using a rapid compression machine under internal combustion engine conditions". Fuel. 355. 129431. 2024. DOI: 10.1016/j.fuel.2023. 129431.
- [217] J. Chung, K. Min, and M. Sunwoo. "Real-time empirical NOx model based on In-cylinder pressure measurements for light-duty diesel engines". *International Journal of Automotive Technology*. 174. 549–554. 2016. DOI: 10.1007/s12239-016-0055-4.
- [218] F. Bozza et al. "Second Law Analysis of Turbocharged Engine Operation".In: 1991, 910418. DOI: 10.4271/910418.

- [219] J. Pareja, H. J. Burbano, and Y. Ogami. "Measurements of the laminar burning velocity of hydrogen-air premixed flames". *International Journal of Hydrogen Energy*. 354. 1812–1818. 2010. DOI: 10.1016/j.ijhydene.2009.12.031.
- [220] S. Tse, D. Zhu, and C. Law. "Morphology and burning rates of expanding spherical flames in H2/O2/inert mixtures up to 60 atmospheres". *Proceedings of the Combustion Institute*. 282. 1793–1800. 2000. DOI: 10.1016/S0082-0784(00)80581-0.
- [221] O. Kwon and G. Faeth. "Flame/stretch interactions of premixed hydrogen-fueled flames: measurements and predictions". Combustion and Flame. 1244. 590–610. 2001. DOI: 10.1016/S0010-2180(00)00229-7.
- [222] C. Rakopoulos, G. Kosmadakis, and E. Pariotis. "Evaluation of a combustion model for the simulation of hydrogen spark-ignition engines using a CFD code". *International Journal of Hydrogen Energy.* 3522. 12545–12560. 2010. DOI: 10.1016/j.ijhydene.2010.09.002.
- [223] S. Verhelst et al. "Laminar and unstable burning velocities and Markstein lengths of hydrogen-air mixtures at engine-like conditions". *Proceedings of the Combustion Institute*. 301. 209–216. 2005. DOI: 10.1016/j.proci.2004. 07.042.
- [224] J. Lee et al. "Effect of different excess air ratio values and spark advance timing on combustion and emission characteristics of hydrogen-fueled spark ignition engine". *International Journal of Hydrogen Energy*. 4445. 25021–25030. 2019. DOI: 10.1016/j.ijhydene.2019.07.181.
- [225] J. Stokes, T. H. Lake, and R. J. Osborne. "A Gasoline Engine Concept for Improved Fuel Economy -The Lean Boost System". In: 2000, 2000–01–2902. DOI: 10.4271/2000-01-2902.
- [226] D. Diggs. "Effect of Combustion Time on Knock in a Spark-Ignition Engine".In: 1953, 530242. DOI: 10.4271/530242.

- [227] L. Eriksson and I. Andersson. "An Analytic Model for Cylinder Pressure in a Four Stroke SI Engine". In: 2002, 2002–01–0371. DOI: 10.4271/2002-01-0371.
- [228] H. Li. "Knock in spark ignition hydrogen engines". International Journal of Hydrogen Energy. 298. 859-865. 2004. DOI: 10.1016/j.ijhydene.2003.09.
 013.
- [229] M. Slack. "Rate coefficient for H + O2 + M = HO2 + M evaluated from shock tube measurements of induction times". Combustion and Flame. 28. 241–249. 1977. DOI: 10.1016/0010-2180(77)90031-1.
- [230] Z. Zhao, Z. Chen, and S. Chen. "Correlations for the ignition delay times of hydrogen/air mixtures". Chinese Science Bulletin. 562. 215–221. 2011. DOI: 10.1007/s11434-010-4345-3.
- [231] A. Kneifel et al. "Investigations on Supercharging Stratified Part Load in a Spray-Guided DI SI Engine". SAE International Journal of Engines. 11. 171–176. 2008. DOI: 10.4271/2008-01-0143.
- [232] R. Jeeragal and K. A. Subramanian. "Experimental Investigation for NOx Emission Reduction in Hydrogen Fueled Spark Ignition Engine Using Spark Timing Retardation, Exhaust Gas Recirculation and Water Injection Techniques". *Journal of Thermal Science*. 284, 789–800, 2019. DOI: 10.1007/s11630-019-1099-3.
- [233] J. Li et al. "An updated comprehensive kinetic model of hydrogen combustion". *International Journal of Chemical Kinetics*. 3610. 566–575. 2004. DOI: 10.1002/kin.20026.
- [234] T. Iijima and T. Takeno. "Effects of temperature and pressure on burning velocity". Combustion and Flame. 651. 35–43. 1986. DOI: 10.1016/0010-2180(86)90070-2.
- [235] G. Koroll and S. Mulpuru. "The effect of dilution with steam on the burning velocity and structure of premixed hydrogen flames". Symposium (In-

- ternational) on Combustion. 211. 1811–1819. 1988. DOI: 10.1016/S0082-0784(88)80415-6.
- [236] S. Verhelst. "A study of the combustionin hydrogen-fuelled internal combustion engines". Ph.D. thesis. Belgium: Ghent University, 2005.
- [237] G. Koroll, R. Kumar, and E. Bowles. "Burning velocities of hydrogen-air mixtures". Combustion and Flame. 943. 330–340. 1993. DOI: 10.1016/0010-2180(93)90078-H.
- [238] J. E. Cavanaugh and A. A. Neath. "The Akaike information criterion: Background, derivation, properties, application, interpretation, and refinements". WIREs Computational Statistics. 113. e1460. 2019. DOI: 10.1002/wics. 1460.
- [239] M. Kuznetsov et al. "Laminar burning velocities of hydrogen-oxygen-steam mixtures at elevated temperatures and pressures". *Proceedings of the Combustion Institute*. 331. 895–903. 2011. DOI: 10.1016/j.proci.2010.06.050.
- [240] W. Zhang et al. "Laminar flame speeds of lean high-hydrogen syngas at normal and elevated pressures". Fuel. 181. 958–963. 2016. DOI: 10.1016/j.fuel. 2016.05.013.
- [241] K. Eisazadeh-Far et al. "The effect of diluent on flame structure and laminar burning speeds of JP-8/oxidizer/diluent premixed flames". Fuel. 904. 1476—1486. 2011. DOI: 10.1016/j.fuel.2010.11.020.
- [242] C. K. Law. Combustion Physics. 1st ed. Cambridge University Press, 2006.DOI: 10.1017/CB09780511754517.
- [243] K. Kuppa, A. Goldmann, and F. Dinkelacker. "Predicting ignition delay times of C1-C3 alkanes/hydrogen blends at gas engine conditions". Fuel. 222. 859– 869. 2018. DOI: 10.1016/j.fuel.2018.02.064.
- [244] A. Parlak. "The effect of heat transfer on performance of the Diesel cycle and exergy of the exhaust gas stream in a LHR Diesel engine at the optimum injection timing". Energy Conversion and Management. 462. 167–179. 2005.

 DOI: 10.1016/j.enconman.2004.03.001.

Appendix A: Pseudocode for combustion models

The pseudocode for single-zone and two-zone combustion models are presented in Table A1 and Table A2, respectively.

Table A1: Pseudocode for single-zone combustion model.

START

INPUT

Engine geometry: bore, stroke, rod length, compression ratio

Operating conditions: intake pressure, boost pressure, intake temperature, engine speed, equivalence ratio, start of combustion crank angle

CALCULATE

Crank angle array, displaced volume and clearance volume

FOR each crank angle

Calculate instantaneous cylinder volume and area

END FOR

FOR each crank angle

Calculate the motoring pressure and temperature

END FOR

CALCULATE

Reactant species: hydrogen, oxygen, nitrogen and product species: water, nitrogen, and oxygen

FOR each species

Calculate gas constant, specific heats, enthalpy and internal energy

END FOR

FOR each crank angle after start of combustion

Calculate laminar flame speed

Calculate combustion duration and mass fraction burned using Wiebe function Calculate pressure and temperature by interpolating between compression and expansion pressure and temperature.

END FOR

Continued on next page

Table A1 – continued from previous page

FOR each crank angle

Calculate indicated mean effective pressure by integrating pressure and volume, indicated power, thermal efficiency, and indicated specific fuel consumption Calculate nitric oxide formation rate using extended Zeldovich mechanism

END FOR

OUTPUT RESULTS

Mass fraction burned, pressure, mean temperature, indicated mean effective pressure, efficiency, indicated specific fuel consumption, and nitric oxide emissions

END

Table A2: Pseudocode for two-zone combustion model.

START

INPUT

Engine geometry: bore, stroke, rod length, compression ratio

Operating conditions: intake pressure, boost pressure, intake temperature, engine speed, equivalence ratio, start of combustion crank angle

CALCULATE

Crank angle array, displaced volume and clearance volume

FOR each crank angle

Calculate instantaneous cylinder volume and area

END FOR

FOR each crank angle

Calculate the motoring pressure and temperature

END FOR

CALCULATE

Reactant species: hydrogen, oxygen, nitrogen, and water and product species: water, nitrogen, and oxygen

FOR each species

Continued on next page

Table A2 – continued from previous page

Calculate gas constant, specific heats, enthalpy and internal energy

END FOR

FOR each crank angle after start of combustion

Calculate laminar flame speed, turbulence intensity and characteristic eddy burning time

Calculate entrained mass fraction and burned mass fraction

Use ODE45 to integrate burned and unburned zones then calculate pressure, unburned temperature, and burned temperature

END FOR

FOR each crank angle

Calculate indicated mean effective pressure by integrating pressure and volume, indicated power, thermal efficiency, and indicated specific fuel consumption Calculate nitric oxide formation rate using extended Zeldovich mechanism

END FOR

OUTPUT RESULTS

Mass fraction burned, pressure, unburned temperature, burned temperature, indicated mean effective pressure, efficiency, indicated specific fuel consumption, and nitric oxide emissions

END